Galaxy Distributions Within and Around Observed and Simulated Groups

Stephen David Riggs

Department of Physics and Astronomy
University of Sussex

Submitted for the degree
Doctor of Philosophy

Supervisors: Jon Loveday & Peter Thomas

May 2022

Declaration

I hereby declare that no part of this thesis has been and will not be submitted in whole or in part to another university for the award of any other degree.

The following chapters of this thesis have been undertaken in collaboration with other researchers, and some parts have been published previously.

- Chapter 2 is unpublished. I ran and analysed the semi-analytic models, and wrote the chapter. Jon Loveday came up with the idea of this project and generated and calculated the clustering for the GAMA samples. The conditional luminosity functions I generated for L-GALAXIES in this chapter were incorporated into Vázquez-Mata et al. (2020), Monthly Notices of the Royal Astronomical Society, volume 499, issue 1, pages 631-652.

- Chapter 3 is published as Riggs et al. (2021), Monthly Notices of the Royal Astronomical Society, volume 506, issue 1, pages 21-37. I performed all of the analysis and wrote the majority of the paper. Ridwan Barbhuiyan and Jon Loveday began the project by writing the code used to select the GAMA group and galaxy samples and preparing an outline of the paper. The other authors contributed to the GAMA data products used and provided comments on the paper draft.

- Chapter 4 is published as Riggs et al. (2022), Monthly Notices of the Royal Astronomical Society, volume 514, issue 4, pages 4676-4695. I performed the analysis in this project and wrote the paper draft. The idea for this project resulted from discussions I had with Jon Loveday, Peter Thomas and Annalisa Pillepich, who all subsequently provided advice during this project. The other authors contributed to the GAMA and IllustrisTNG data products used and provided comments on the paper draft.

- Chapter 5 is unpublished. I performed all of the analysis and wrote the chapter, under the supervision of Jon Loveday and Peter Thomas.

Stephen Riggs

May 2022

UNIVERSITY OF SUSSEX

STEPHEN DAVID RIGGS

DOCTOR OF PHILOSOPHY

GALAXY DISTRIBUTIONS WITHIN AND AROUND OBSERVED AND SIMULATED GROUPS

SUMMARY

This thesis explores the properties and distributions of galaxies within and around galaxy groups, making use of galaxy clustering statistics. We include both observations and simulations in this analysis.

In the first part we explore the properties of galaxies in the GAMA survey and the L-GALAXIES and SHARK semi-analytic models. We examine which elements of the models affect the predictions for galaxy stellar masses, luminosities and clustering, and find that satellite galaxy physics plays an important role in the small-scale clustering.

In the second part we determine the cross-correlation between groups and galaxies in the GAMA survey, to explore both the group profile and the large-scale bias around groups, and provide comparisons against the IllustrisTNG simulations and L-GALAXIES model. Using marked clustering statistics we find that the clustering depends strongly on the group masses, but has very little dependence on galaxy masses.

We then explore the differences in distributions of galaxies in groups in full-physics and dark matter-only simulations. Using satellites matched between the IllustrisTNG simulations and their dark matter-only equivalents, we find that the satellites reside closer to the group centre and have enhanced survival times in the full-physics simulations. We split the satellites of IllustrisTNG into those which possess dark matter-only equivalents and those which do not, and create empirical models for both of these populations.

Finally, we apply these empirical corrections in the L-GALAXIES and SHARK models, and explore the impact this has on their predictions for galaxy clustering.

Acknowledgements

I would first like to thank my supervisor Jon Loveday for guiding me throughout my PhD and for always being available to provide assistance and advice on my work.

I would next like to thank my second supervisor Peter Thomas, who provided invaluable advice on the use and interpretation of the simulations I have been analysing. I also thank my collaborators Annalisa Pillepich and Dylan Nelson who provided access to and help with the IllustrisTNG simulations. Finally I thank my examiners Cedric Lacey and Robert Smith for their comments and for the interesting discussion in the viva.

Thanks to all of the other members of the astronomy department for making it a welcoming place. I'd particularly like to thank Dan and Lucas for answering a lot of questions I had during my first year. Also thanks to Aswin, Todd and Will with whom I've had useful discussions about the data used in this thesis, and the other people I shared an office with during my time here: Cameron, Mathew and Robin.

Finally thanks to my family and friends who've helped and encouraged me prior to and during my PhD.

"If life is going to exist in a Universe of this size,
then the one thing it cannot afford to have is a sense of proportion."

DOUGLAS ADAMS, THE RESTAURANT AT THE END OF THE UNIVERSE

Contents

List of Tables

List of Figures

1

Introduction

Understanding the physics which leads to the formation of structures in the Universe requires a combination of observations, simulations and theories. Observational studies inform us about the properties of galaxies, but cannot directly be used to infer the physics involved in their formation and evolution. To achieve this, simulations are performed which can test models for the physical processes. Then in order to determine the statistical properties of galaxies we require large sample sizes, which from observations means using galaxy surveys, and from simulations requires cosmological boxes with periodic boundary conditions.

In this thesis we use a combination of observations and simulations to explore the positions and properties of galaxies in and around groups. We also explain some of the physics behind these galaxy distributions.

1.1 The structure of the Universe

1.1.1 Cosmological background

In our standard Lambda Cold Dark Matter (ΛCDM) model, the Universe consists of baryonic matter, dark matter, dark energy and radiation. The dark energy drives the expansion of the Universe and dark matter is responsible for forming structures, while the baryonic matter and radiation comprise the remainder of the Universe, including all visible components. This means that all current astronomical observations see only a small fraction of the total matter, viewing only the luminous parts of the baryonic components, and properties of the dark components can only be inferred. However, when simulating the Universe it is common to focus on the dark components, as these form the majority of the mass and their behaviour on large scales is easier to model. The differences in these approaches pose problems when trying to understand and test the physics of the Universe.

The existence of the dark components has not always been clear. In particular dark energy was not included in our standard cosmological model until the discovery that the expansion of the Universe is accelerating showed it to be necessary. This acceleration was noticed by looking at the distances to supernovae, as high-redshift supernovae were seen to be further away than is possible in a universe without dark energy (Riess et al., 1998; Perlmutter et al., 1999).

Dark matter has been included in the standard cosmological model for longer, and the primary evidence for it comes from galaxy rotation curves and weak lensing measurements around clusters. When examining the rotation of galaxies, the velocities are seen to be too high at large radii when compared to predictions assuming only the visible baryonic matter is present. This means an extra non-visible dark matter component is needed (e.g. Corbelli & Salucci, 2000). Weak lensing on the other hand refers to the modification of light travel paths due to gravity. In the case of galaxy clusters the strength of the distortions and width of the region this occurs across is inconsistent with this being just due to the baryonic matter in the galaxies, and therefore additional matter which only interacts gravitationally—dark matter—is needed (e.g. Abbott et al., 2022). Further evidence from observations of small-scale structure suggests dark matter is cold, as if dark matter was warm then this structure would be suppressed (see e.g. Bullock & Boylan-Kolchin, 2017; de Martino et al., 2020).

The ΛCDM cosmological model which includes these dark components and which we assume throughout this thesis has developed over the last 100 years from Einstein's General Relativity with the addition of the cosmological principle that the Universe is homogenous and isotropic, which means that in the Universe all spatial points are equivalent and all directions look the same for an observer. The spacetime of a simple universe fitting these criteria can be described with the Friedmann-Lemaître-Robertson-Walker metric (Friedmann, 1922; Lemaître, 1931; Robertson, 1935; Walker, 1937). For a flat spacetime this is given by

$$\mathrm{d}s^2 = -c^2\mathrm{d}t^2 + a^2(t)\left[\mathrm{d}r^2 + r^2\mathrm{d}\theta^2 + r^2\sin^2\theta\mathrm{d}\phi^2\right] \tag{1.1}$$

where c is the speed of light, $a(t)$ is the scale factor which describes the expansion of the Universe as a function of time, and the spatial part of the metric is described in terms of the comoving distance r and two angles θ and ϕ.

The scale factor can be related to time by using the redshift, z, which provides a measure of both the distance and look-back time to an object. Considering the wavelength change of a photon in an expanding universe leads to a relationship between scale and redshift of

$$a = \frac{1}{1+z}. \tag{1.2}$$

The expansion of the Universe can also be derived from General Relativity to give the two cosmological field equations for the scale factor in terms of the density, ρ, and pressure, p. These are

$$\frac{\ddot{a}}{a} = -\frac{4\pi G}{3}(\rho + \frac{3p}{c^2}) + \frac{\Lambda c^2}{3} \tag{1.3}$$

and

$$\left(\frac{\dot{a}}{a}\right)^2 = \frac{8\pi G\rho}{3} + \frac{\Lambda c^2}{3}, \tag{1.4}$$

where we have also included the cosmological constant, Λ, which is required for dark energy.

The second of the field equations leads to two further important quantities being defined.

Firstly, the Hubble parameter, where

$$H(t) = \frac{\dot{a}(t)}{a(t)}, \tag{1.5}$$

and at the present day $H(t_0)$ is defined to be $H_0 = 100h$ km s^{-1}Mpc^{-1}. The dimensionless parameter h in this is approximately 0.7, although the exact value is uncertain. The Hubble parameter can be used to determine the comoving distance to a galaxy at a given redshift, using

$$r = c\int_0^z \frac{dz'}{H(z')}. \tag{1.6}$$

Secondly, the critical density, which describes the geometry of a universe with $\Lambda = 0$ and is defined by

$$\rho_c = \frac{3H^2}{8\pi G}. \tag{1.7}$$

This is important as in a flat Universe the overall density is ρ_c. This critical density is then used to define two of the cosmological parameters we use: Ω_Λ and Ω_m. Ω_Λ gives the ratio of the dark energy density of the Universe to the critical density, while Ω_m gives the ratio of the total matter density of the Universe to the critical density. Additionally, the fraction of the baryonic matter density only is sometimes given as Ω_b. In a flat universe the Ω terms must sum to one as the density must equal ρ_c, and so observational evidence that the Universe has a low matter density and is flat provides a further demonstration of the requirement for an extra dark energy component.

Finally, we note that two further cosmological parameters are also relevant in this thesis when determining the state of the Universe. These are n_s, which determines the scale-dependence of primordial density fluctuations, and σ_8, which gives the root mean square density fluctuation in spheres of radius $8\,h^{-1}$ Mpc.

1.1.2 Structure formation

On the largest scales, structure formation is dominated by the gravitational interaction of dark matter, which draws matter into clusters, sheets and filaments, leaving voids in between. The large-scale structure was initially seeded by small perturbations in the primordial Universe, and these are proposed to grow rapidly during a period of inflation. Subsequently, large enough density perturbations are able to gravitationally collapse.

The spherical collapse model provides a description of the way in which this structure formation occurs, stating that regions with a density that is sufficiently higher than the background will evolve in the same manner as an isolated matter-dominated universe. This means these regions expand until a turn-around time after which they collapse, and the collapse continues until the matter in the region reaches an equilibrium state where it satisfies the virial theorem that the potential energy equals twice the kinetic energy. In a matter-dominated universe, the density required for this to occur is about 178 times the background density. This is frequently rounded to 200 to define halo masses as M_{200}, the mass in a spherical region where the density equals 200 times the background density.

M_{200} can be taken to be relative to either the mean density of the Universe ($M_{200\mathrm{m}}$) or to the critical density ($M_{200\mathrm{c}}$). In this thesis we usually use $M_{200\mathrm{m}}$ but we also occasionally use $M_{200\mathrm{c}}$ as some models only calculate this. Masses relative to the critical density are slightly smaller as they require a denser, and therefore smaller, spherical volume.

The final stage of structure formation is the formation of galaxies within the dark matter structures, and these galaxies consist of gas, dust and stars, and produce light which can be observed. Galaxies can have a variety of shapes and internal compositions, but are often split into an ellipsoidal bulge component and a flatter disc. Between and around the galaxies further baryonic material traces the underlying structures, in the form of the circumgalactic medium, intergalactic medium and intracluster medium.

The large-scale structure as traced by the visible galaxies is illustrated in Fig. 1.1, showing the galaxy distributions from observations by the CfA2 (Geller & Huchra, 1989), 2dFGRS (Colless et al., 2001) and SDSS (York et al., 2000) surveys and from a model using the Millennium simulation (Springel et al., 2005), where it can be seen that the galaxies are aligned as part of large-scale structures.

1.1.3 Haloes and groups

In the halo model of the Universe the large-scale structure is divided into objects known as haloes. While these haloes are complicated and potentially ill-defined, some basic assumptions and simplifications are frequently made for them. In particular, they are often assumed to be spherical and the radial distribution of matter within them is taken to follow the Navarro et al. (1997, hereafter NFW) profile.

These haloes can be identified in simulations of the Universe, but observations see galaxies and their groupings. A group of galaxies can be defined as an assembly of galaxies gravitationally bound together, whose evolution is affected by being a member of the group. The concept of a group often refers to structures with total mass $\sim 10^{13} h^{-1}\mathrm{M}_{\odot}$, but can more generally be used to describe any collection of galaxies ranging from pairs up to clusters of hundreds of galaxies with total mass $\sim 10^{15} h^{-1}\mathrm{M}_{\odot}$.

The concepts of groups and haloes can be associated, and so dark matter haloes are described as hosting the groups and the galaxies that constitute them. The structure of these haloes is hierarchical, and so they contain subhaloes which then host the individual galaxies of the group or cluster.

The constituent galaxies and subhaloes may be divided up into one central and any number of satellites. The galaxy residing at the centre of the gravitational potential of the host halo is described as the central, and will often be the most massive and brightest in the group. All the remaining galaxies and subhaloes are identified as satellites.

When the positions of galaxies are explored in the form of galaxy clustering, the halo model allows the clustering to be split into 'one-halo' and 'two-halo' terms. The one-

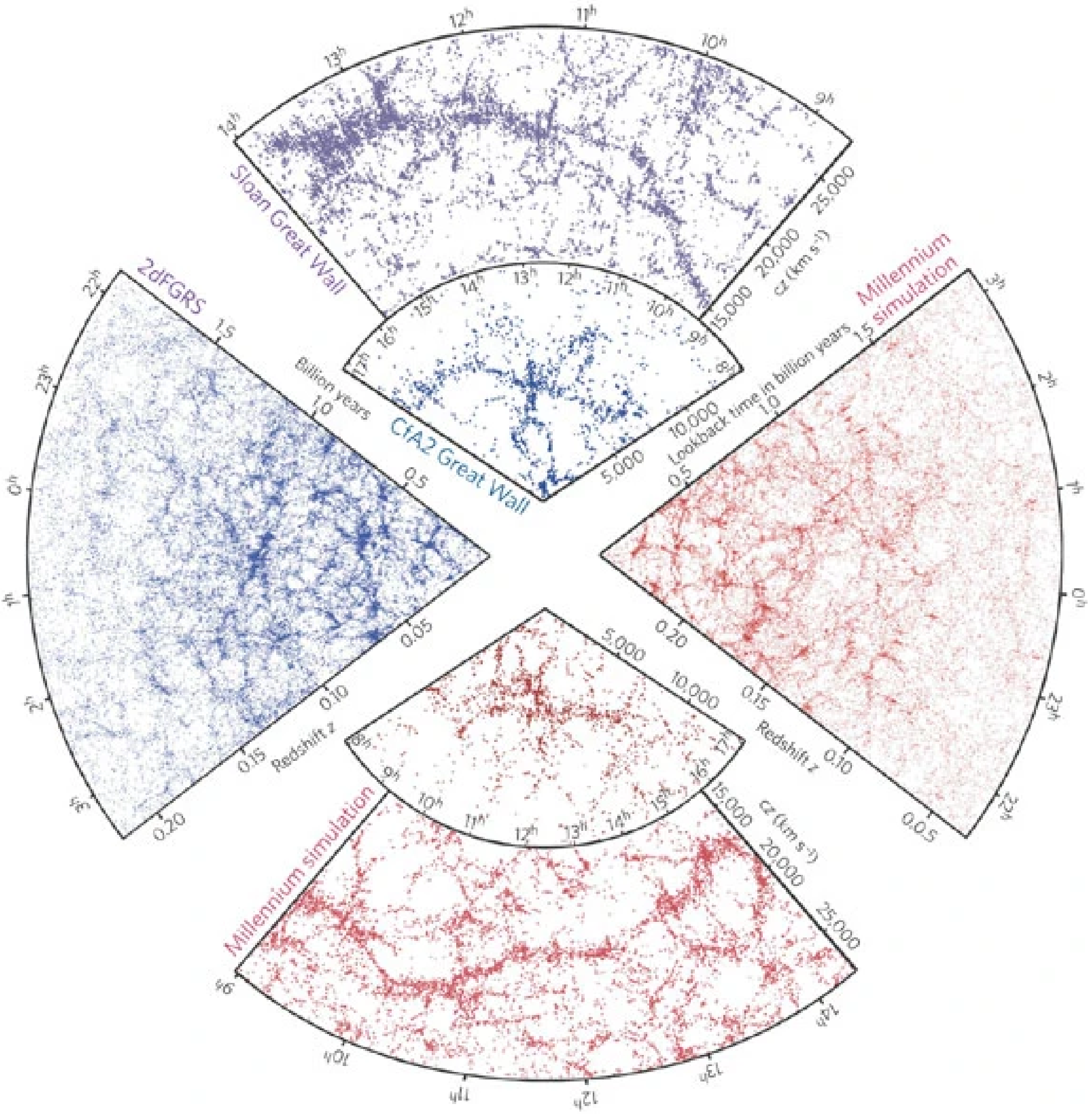

Figure 1.1: Distributions of galaxies in observations and simulations, reproduced from Springel et al. (2006). The upper and left panels show the galaxies observed by the CfA2, 2dFGRS and SDSS surveys, demonstrating the existence of filaments and clusters on the largest scales, separated by voids. The lower and right panels show galaxies placed in the Millennium simulation by a semi-analytic model.

halo term describes the associations between galaxies in the same halo, mainly resulting from the satellite galaxies, and dominates small-scale clustering. Then the two-halo term instead describes pairs of galaxies in different haloes, and gives a clustering signal on larger scales.

1.2 Statistical properties of the Universe

Galaxy clustering represents one example of a statistical property of the Universe, and is the one we focus on in this thesis. Statistical properties provide an alternative to considering individual galaxies, and can be used to explore the physics of galaxy formation and cosmology.

1.2.1 One-point functions: mass and luminosity functions

The simplest statistical properties to consider are the numbers of galaxies with different properties. These are usually expressed in the form of number densities within a sample volume.

The most fundamental of these is the stellar mass function, which shows the number density of galaxies binned by the total mass of their constituent stars. More generally, mass functions can be used to record the matter of any phase associated with objects, and examples include the baryonic mass function using the total galaxy mass in all baryonic components (stars, dust and gas), and the halo and subhalo mass functions of dark matter structures. Stellar masses are observationally given in units of $h^{-2}\mathrm{M}_{\odot}$, as they are derived from fluxes which decrease with the square of the distance to a galaxy. In simulations, stellar masses are determined in units of $h^{-1}\mathrm{M}_{\odot}$ because the critical density goes as h^2 and the simulation volume as h^{-3}, although in this thesis we usually convert masses from simulations into the observational units.

Similar to the mass functions are the luminosity functions of galaxies, which bin the galaxies using the intrinsic luminosity in different frequency bands. These frequency bands are defined by the filters of the telescopes used for observations, and so are specific to each different survey. Luminosity functions are usually given in terms of magnitudes, a logarithmic scale of flux. The absolute magnitudes, M, which we plot are related to the observed magnitudes, m, and the distance to the object, D_L, through

$$M = m - 5\log_{10}\left(\frac{D_L}{10\mathrm{pc}}\right). \tag{1.8}$$

They are given in units of $M - 5\log_{10} h$ because a factor of 100 in brightness is defined to be 5 magnitudes (giving a factor of 2.5 in base 10 logarithms) and flux decreases with the square of distance.

Despite a close relationship between the mass of an object and the light emitted, comparing either stellar mass or luminosity functions between observations of the Universe and numerical simulations poses a challenge, as the intrinsic outputs differ.

Observationally, luminosities are recorded in filter bands in the frame of the telescope, whereas in simulations it is stellar masses that are automatically available.

The usual approach to dealing with this, which we use in this thesis, is to perform analysis on both observations and simulations to give consistent definitions of masses and luminosities. However, we note that some works (e.g. Bergé et al., 2013; Herbel et al., 2017; Fagioli et al., 2018) have argued that it is instead better to take a forward modelling approach by performing all the analysis on the simulations, to reproduce what would be observed from them.

Following the standard method, the first stage of analysis on observed galaxies is to convert the observer-frame luminosities to intrinsic values. This requires accounting for the K-correction (Humason et al., 1956; Hogg et al., 2002) and e-correction (Lin et al., 1999) which result from galaxies originating at different redshifts. The K-correction accounts for the filters detecting different regions of the galaxy spectra at different redshifts due to the wavelength shift, while the optional e-correction accounts for the evolution in the star formation rates of the galaxies. Stellar masses are then estimated from the observed light, by modelling the initial stellar populations (e.g. Chabrier, 2003), the spectra that these produce (e.g. Bruzual & Charlot, 2003), and the effect of dust on these spectra (e.g. Calzetti et al., 2000). However, the extensive processing and assumptions required introduce uncertainties into the final mass estimates.

On the other hand, in simulations stellar masses are relatively simple to determine, although they are model-dependent and subject to decisions about assigning particles to objects, while luminosities are more complicated to derive. The luminosities are usually obtained by making assumptions about the stars contained in the galaxies, mimicking the procedure used to generate masses from observations.

Finally, the conversion of the resulting masses and luminosities to one-point functions is subject to some uncertainties, particularly in observations. Specifically, the one-point functions are affected by Eddington bias (Eddington, 1913), where uncertainties in the derived quantities make rarer objects appear more common. This leads to a potential overestimation of the bright end of the luminosity functions.

Once one-point functions have been measured, the form of the stellar mass and luminosity functions for galaxies is often modelled as a Schechter function (Schechter, 1976) with the form

$$\phi(L) = \phi^{\star} \left(\frac{L}{L^{\star}}\right)^{\alpha} \exp\left[-\left(\frac{L}{L^{\star}}\right)\right], \tag{1.9}$$

for luminosity (or mass) L, normalisation $\phi^{\star}$ and characteristic luminosity (or mass) $L^{\star}$. This follows a power law for faint (less massive) galaxies, then has an exponential cut-off at the bright (more massive) end. Modified forms of this function can also be used.

1.2.1.1 Conditional one-point functions

As well as considering the number density of galaxies per unit volume, it is possible to consider the number fulfilling a certain criteria. Conditional stellar mass and luminosity functions consider the number of galaxies per group, after selecting galaxies based on group mass (e.g. Yang et al., 2003). This provides a way to explore how the properties of the constituent galaxies depend on the group mass. The one-point functions of satellite galaxies in groups approximately follow a Schechter function, while the centrals follow a log-normal distribution (Yang et al., 2008, 2009)

$$\phi(L) = \phi^{\star}\exp\left[-\frac{(\log_{10} L - \log_{10} L^{\star})^2}{2\sigma^2}\right], \tag{1.10}$$

with width σ. This reflects a reasonably tight correlation between the luminosity (and mass) of the central and the total group mass.

1.2.2 Two-point functions: galaxy clustering

Galaxy clustering analysis explores the locations and grouping of galaxies. It can be related to the clustering of the underlying matter through a quantity known as the bias.

1.2.2.1 Three-dimensional clustering

The two-point correlation function is the most commonly used statistic to examine the clustering of a galaxy population. In three dimensions the two-point correlation function $\xi(r)$ describes the excess probability dP of finding a galaxy in a volume dV at a separation r from another galaxy, compared to that expected for a random distribution (Coil, 2013). It may be expressed as

$$dP = n[1 + \xi(r)]dV, \tag{1.11}$$

where n is the mean number density of galaxies (Peebles, 1980). We have expressed $\xi(r)$ in terms of the three-dimensional separation r, but for observations this is often split into components along ($r_{\parallel}$) and perpendicular to ($r_{\perp}$) the line of sight to produce $\xi(r_{\perp}, r_{\parallel})$.

The first widely used estimator of the two-point correlation function in three dimensions was that of Davis & Peebles (1983),

$$\xi(r) = \frac{n_R}{n_D}\frac{DD(r)}{DR(r)} - 1, \tag{1.12}$$

where n_D is the number of data points and n_R the number of random points. DD gives the counts of pairs of galaxies within the data catalogue and DR gives the counts of pairs between the data catalogue and a catalogue of randomly positioned galaxies. These randomly positioned galaxies are needed to convert the data pair counts to an excess probability and, by giving the random galaxies the same sky footprint and redshift distribution as the data and then choosing the right estimator, they can be used to reduce edge effects at the boundary of the sample.

Kerscher et al. (2000) compare the available estimators and show the Davis & Peebles (1983) form deviates from their reference correlation function at large scales. They find the smallest deviations come from the estimator of Landy & Szalay (1993),

$$\xi(r) = \frac{1}{RR(r)}\left(DD(r)\left(\frac{n_R}{n_D}\right)^2 - 2DR(r)\left(\frac{n_R}{n_D}\right) + RR(r)\right), \tag{1.13}$$

where RR is the count of pairs within the random catalogue. This estimator is now the most widely used.

Several codes exist in order to calculate the two-point correlation function including TreeCorr (Jarvis et al., 2004), Corrfunc (Sinha & Garrison, 2019, 2020) and CUTE (Alonso, 2012). However, some of these only perform the calculations on angular sky data and so are unsuitable for use on simulation boxes.

Simulations often use periodic boundary conditions and this simplifies the clustering calculation by removing the need for a random catalogue as the volume is not restricted at the boundaries. By assuming a random distribution of galaxies over the volume with no clustering, the random pairs may be computed as

$$RR(r) = n_D^2 \frac{v(r)}{V}, \tag{1.14}$$

where V is the total box volume and $v(r) = \frac{4}{3}\pi((r+dr)^3 - r^3)$ is the volume of a spherical shell of radius r and thickness dr (Alonso, 2012). Further, this means the estimator for the two-point correlation can be simplified to

$$\xi(r) = \frac{DD(r)}{RR(r)} - 1. \tag{1.15}$$

1.2.2.2 Projected correlation functions

The disadvantage of three-dimensional clustering when comparing observations and simulations is that the observational results include the effects of redshift space distortions (Coil, 2013). These manifest in two ways. On large scales a compression along the line of sight is seen due to the infall of galaxies onto clusters (Kaiser, 1987). On the other hand, on small scales the galaxies are seen to spread out in the "Fingers of God", due to the peculiar velocities of galaxies within groups and clusters.

To get around this, the projected correlation function in two dimensions, w_p, is frequently used as it is independent of redshift space distortion effects. Davis & Peebles (1983) derive this from the three-dimensional correlation using

$$w_p(r_\perp) = 2\int_0^\infty \xi\left((r_\perp^2 + y^2)^{1/2}\right) dy = 2\int_{r_\perp}^\infty \frac{r\xi(r)}{\sqrt{r^2 - r_\perp^2}} dr, \tag{1.16}$$

where the correlation function is projected along axis y onto $r_\perp$.

For observational data where $\xi(r_\perp, r_\parallel)$ is calculated this can be computed as

$$w_p(r_\perp) = 2\int_0^\infty \xi(r_\perp, r_\parallel) dr_\parallel, \tag{1.17}$$

where the projection is performed along the line of sight $r_\parallel$.

In practice this integral is not performed to infinity but is instead cut off at some $R_{\max}$. Loveday et al. (2018) determine it is reasonable to set this to $40h^{-1}\mathrm{Mpc}$, but Baldauf et al. (2010) demonstrate that errors are introduced at distances approaching the selected $R_{\max}$ so larger values may be beneficial. This effect is described in van den Bosch et al. (2013) as being a residual redshift space distortion, and means that on scales approaching $R_{\max}$ results from simulations and observations may not be comparable.

1.2.2.3 Cross-correlations

Another way to consider clustering is with cross-correlations between two different samples. This is commonly employed when considering the clustering of galaxy groups, but it can be generically applied to any two samples that overlap in space. Cross-correlations can be calculated with a modified form of the Landy & Szalay (1993) estimator. In the case of cross-correlation between galaxies and groups, this form is (Mohammad et al., 2016)

$$\xi = \frac{Gg - Gr - gr + rr}{rr}, \tag{1.18}$$

where Gg, Gr, gr, and rr are the normalised numbers of group–galaxy, group–random, galaxy–random and random–random pairs respectively. This can be projected in the same way as the galaxy auto-correlation function.

As well as exploring the clustering of groups directly, this can be used to explore the clustering of groups relative to the underlying matter distribution. Galaxies and groups are known to be biased relative to the distribution of dark matter (Kaiser, 1984), and this bias can be used to compare different samples, as well as having applications for cosmology. Bias can be calculated for any clustering measure, and in the case of the projected cross-correlation w_p^{AB} between samples A and B it is derived from

$$w_p^{\mathrm{AB}}(r_\perp) = b_{\mathrm{A}}(r_\perp) b_{\mathrm{B}}(r_\perp) w_p^{\mathrm{DM}}(r_\perp), \tag{1.19}$$

where w_p^{DM} is the projected dark matter correlation function and b_{A} and b_{B} are the bias measures for the two samples.

The biases measured from the cross-correlation are not necessarily the same as those from the auto-correlations of the same samples. In particular, for the group–galaxy clustering we consider in this thesis, on small scales the group bias derived from this equation remains positive, although there would be no group–group pairs. On larger scales the cross- and auto-correlation biases will be similar as they both measure the clustering relative to the matter distribution across a wider region, but will have a scaling factor due to the different bias of the second population in the cross-correlation.

1.2.2.4 Marked correlation functions

Marked correlation functions were introduced in Sheth & Tormen (2004) to explore the environmental dependence of galaxy clustering, and were further developed by Sheth et al. (2005) and Skibba et al. (2006). These rely on weighted correlations, where each pair is multiplied by an associated weight when included in the pair counts. In the case of projected correlation functions the marked correlation M_w is given by (Skibba et al., 2006)

$$M_w(r_\perp) = \frac{r_\perp + W_p(r_\perp)}{r_\perp + w_p(r_\perp)}, \tag{1.20}$$

where $r_\perp$ is the projected separation, w_p is the unweighted projected two-point correlation function and W_p is the weighted two-point correlation function.

1.2.2.5 Integral constraints

Finally, we note that when considering clustering in small volumes, an integral constraint becomes important when calculating the correlation function. The volume integral over the sample region of the estimator of $\xi(r)$ is by definition zero, and this results in deviations in the correlation function on large scales in small volumes. To account for this the integral constraint needs to be added to each estimated $\xi(r)$. The integral constraint is calculated as the volume integral of $\xi(r)$ out to the maximum distance used.

Roche & Eales (1999) fit angular correlation functions $w(\theta)$ with functions of the form $w(\theta) = A(\theta^{-0.8} - C)$ and add the derived value of C to the projected correlation to estimate the true correlation. This same method can be used for correlation functions computed as a function of r. An alternative method from Maddox et al. (1996) approximates the integral constraint from the variance of the galaxy overdensity between different observed fields.

1.2.2.6 Cosmology dependence

Before moving on from the discussion on the clustering of galaxies, it is worth noting that this may be affected by the assumed underlying cosmology. The first order effect of this will be a dependence on the expansion of the Universe throught the Hubble parameter, h, which we minimise by plotting all distances in units of h^{-1} Mpc. Secondary effects will be present due to different values of Ω_m, which also alters the expansion of the Universe, and σ_8, which changes the amplitude of the correlation functions (e.g. Tinker et al., 2012). However, these effects will primarily manifest at higher redshifts than those considered in this thesis.

In Fig. 1.2 we show the comoving distances for redshifts up to $z = 0.267$ in each of the different cosmologies assumed for the observations and simulations we use (these are explained in the sections below[1]). It can be seen in the lower panel that the choice of cosmology has an effect of at most about 1% by $z = 0.267$. This applies for the line-of-sight distance plotted, and for the transverse distance between galaxies—which equals the plotted distance multiplied by the angular separation on the sky. We note that uncertainties of this order are much smaller than the differences we find later in this

[1]The cosmology of the Millennium simulation shown here is that of the rescaled version used in L-GALAXIES.

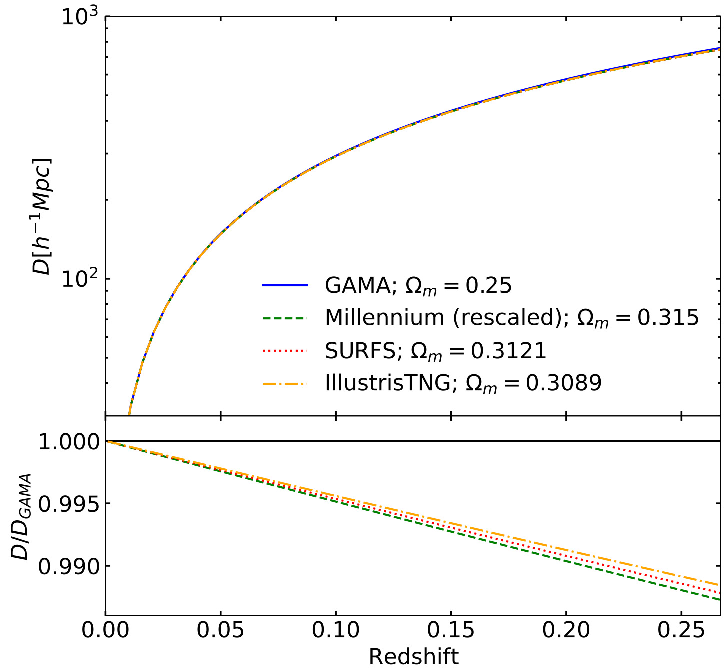

Figure 1.2: Comoving distance for redshifts up to 0.267 for the different cosmologies used in this thesis. The upper panel shows the comoving distance as a function of redshift in each cosmology, while the lower panel shows the ratios to the comoving distance in the $\Omega_m = 0.25$ cosmology assumed for GAMA.

thesis from the numerical methods and baryonic physics used, and so we assume that the cosmology has a minimal impact on the results in the remainder of our work.

1.2.3 Two-point functions: profiles of galaxy groups

On the scale of galaxy groups, an alternative to the two-point correlation function is the group profile, which expresses the number of satellite galaxies as a function of distance from the central. This is the simplest way of considering the distributions of satellites in the groups, as it only uses the single measurement of radial separation. Similarly to the correlation function, the profile can be considered in two or three dimensions.

The profile is closely related to the cross-correlation between groups and galaxies, but contains slightly different information. Whereas the cross-correlation is computed with respect to all galaxies, showing the relation between the groups and the background density field, the profile gives the shape of the subhalo and satellite distributions of the halo, as it contains only satellites associated with the group.

1.3 Galaxy surveys

To determine the statistical properties of the galaxy population in the Universe, galaxy surveys are used. Here we consider spectroscopic surveys which observe large numbers of galaxies with the intention of obtaining their spectra. These galaxy spectra can then be used to determine the properties of the galaxies, including age, chemical composition and star formation rate. Additionally, and crucially for studies of clustering and galaxy groups, these spectra can be used to determine accurate redshifts for the galaxies, although these will include the effect of redshift space distortions.

It is important to note that galaxy surveys do not give perfect measurements as generating properties from galaxy spectra is subject to modelling uncertainties in the fittings used, and that the finite volume of galaxy surveys means that they are affected by cosmic variance, due to sampling only part of the large-scale structure. Further, observations are normally performed to a certain minimum observed brightness in a chosen waveband. This cutoff in the galaxies observed can make it complicated to produce volume-limited samples, those where we can be confident that all galaxies with particular properties are detected out to a given redshift.

Over the past few decades the magnitude limits and number of galaxies explored by surveys have progressively improved. One of the first large surveys that was able to determine the statistical properties of the group and galaxy populations, including clustering, was the Two Degree Field Galaxy Redshift Survey (2dFGRS, Colless et al., 2001) which observed over 200,000 galaxies across 1,500 square degrees.

Following this, the Sloan Digital Sky Survey (SDSS, York et al., 2000) has been one of the most important surveys in furthering our understanding of the Universe. This is based around observations in five photometric filters *ugriz* centred on optical wavelengths. The SDSS main galaxy sample contains around a million galaxies with $m_r < 17.77$ in more than 8,000 square degrees of the sky. This has been used to produce results for many statistical properties, including stellar mass functions (Baldry et al., 2008; Li & White, 2009) and two-point correlation functions (Zehavi et al., 2011).

SDSS has been well suited to determining statistical properties, but one disadvantage for works looking at galaxy groups is that SDSS spectra in dense regions are limited due to fibre collisions, which restrict the proportion of galaxies for which redshifts can be obtained. This is due to the minimum angular separation on the sky which two fibres in the instrument can be pointed at without interfering with each other. Groups are particularly impacted by this due to the close proximity of the galaxies in them.

1.3.1 The GAMA survey

The Galaxy And Mass Assembly survey (GAMA, Driver et al., 2009, 2011; Liske et al., 2015; Baldry et al., 2018; Driver et al., 2022b) is a joint European-Australasian project which combines spectroscopic observations from the Anglo-Australian Telescope with complementary data from other surveys. It provides a spectroscopic sample of galaxies with a high completeness in all environments and has followed SDSS in calculating the statistics of the galaxy population it observed.

GAMA observed a much smaller sky area than 2dFGRS and SDSS, but observes galaxies at two magnitudes deeper than SDSS. The GAMA-I survey comprised three equatorial fields, each of area 12×4 degrees, with a Petrosian magnitude limit of

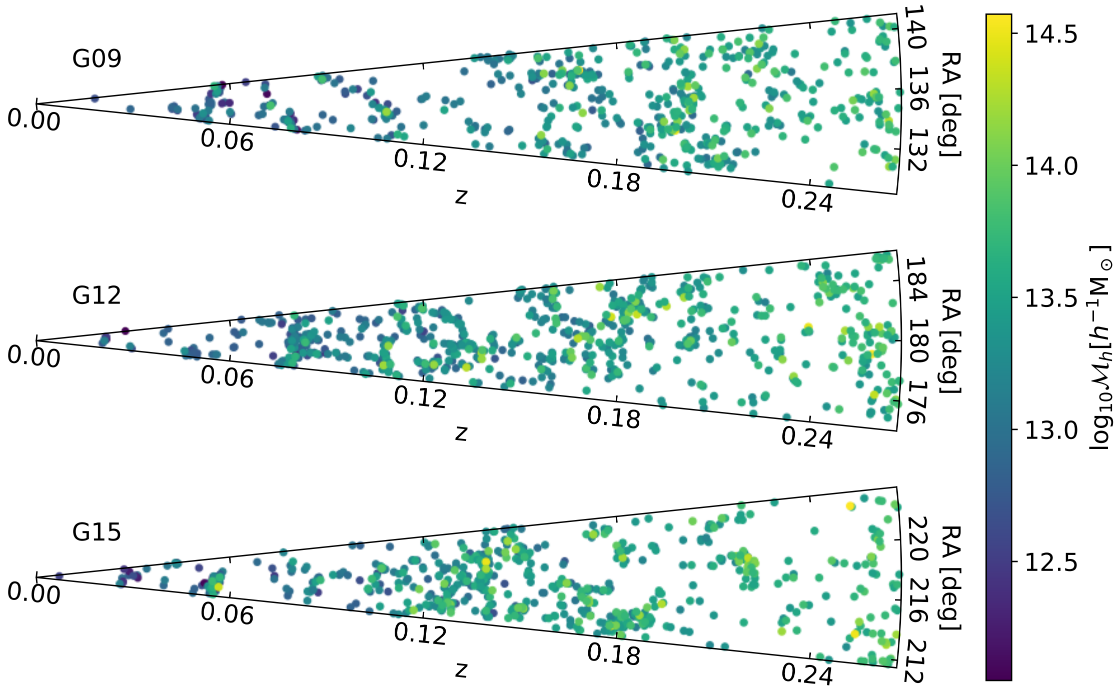

Figure 1.3: Locations of GAMA groups with at least 5 members in RA-redshift space, for $z < 0.267$. The groups are coloured based on their estimated mass.

$m_r < 19.4$. This was updated in GAMA-II to increase the area of each field to 12×5 degrees and the magnitude limit to $m_r < 19.8$. Then most recently the final GAMA DR4 data release (Driver et al., 2022b) changed the main photometry from that of SDSS to that of the Kilo-Degree Survey (KiDS, Kuijken et al., 2019), unifying the three equatorial regions with a fourth region and altering the galaxy magnitudes slightly.

Importantly for this thesis, GAMA specifically aimed for a high spectroscopic completeness, measuring spectra for nearly all galaxies in all environments, making it ideal for exploring galaxy groups. While SDSS is limited by fibre collisions, GAMA worked around this problem by making repeated observations of dense regions including groups to determine spectroscopic properties of a much greater proportion of the galaxies in them. Overall, GAMA has a completeness of over 96% for galaxies with up to 5 neighbours within 40 arcsec (Liske et al., 2015).

Statistical properties have been explored in a number of works using the GAMA samples. The galaxy stellar mass function from GAMA-I was determined by Baldry et al. (2012) and this has been updated for more recent data releases by Wright et al. (2017) and Driver et al. (2022b). Covariances in the Baldry et al. (2012) mass function are considered by Benson (2019). Luminosity functions in the bands used by SDSS have been found by Loveday et al. (2012, 2015) and across the full 11 GAMA bands from the far ultra-violet to the near infra-red by Driver et al. (2012). More recently, the GAMA *r*-band luminosity function was improved at the faint end in Karademir et al. (2022) by the addition of data from KiDS.

This high spectroscopic completeness, including of close pairs (Robotham et al., 2010), makes the survey suitable for examining clustering down to small scales, and this has been done by Farrow et al. (2015). Further, as it has been designed to observe groups of galaxies, group catalogues have been produced from it by Robotham et al. (2011). The locations of these groups in the GAMA lightcone are shown in Fig. 1.3. It can be seen that groups of lower mass are only detected at low redshift, and that groups tend to cluster together within the large-scale structure.

The group catalogues of Robotham et al. (2011) were produced using a friends-of-friends (FoF) algorithm, grouping galaxies based on their projected and line-of-sight separations. This FoF algorithm was calibrated and tested by applying it to mock catalogues, optimising for a high completeness and purity where the true groups are recovered without introducing spurious extra groups or additional group members. The tests determined that the properties of recovered groups are robust but that the smaller groups ($N_{\rm gals} \leq 4$) are less reliable. These groups have been used to extract properties of the dark matter haloes that host them, including the halo masses. Scaling relations for the masses have been calibrated against weak lensing (Viola et al., 2015; Han et al., 2015; Rana et al., 2022), and one of the more reliable measures is that of Viola et al. (2015), equation 37,

$$\frac{M_{\rm 200m}}{10^{14}h^{-1}{\rm M}_\odot} = (0.95 \pm 0.14)\left(\frac{L_{\rm grp}}{10^{11.5}h^{-2}{\rm L}_\odot}\right)^{(1.16\pm0.13)}, \tag{1.21}$$

which estimates the group mass $M_{\rm 200m}$ from the total group luminosity $L_{\rm grp}$.

1.3.2 Clustering and radial profiles from surveys

Galaxy distributions are a standard measurement made from galaxy surveys, used for exploring both astrophysics and cosmology. We describe a few of these results here.

When looking at the two-point correlation function of galaxies, stronger clustering is seen for brighter, more massive and redder galaxies. This was seen in 2dFGRS by Norberg et al. (2001), in SDSS by Zehavi et al. (2005, 2011) and in GAMA by Farrow et al. (2015). The projected galaxy correlation functions for GAMA that were calculated in Farrow et al. (2015) are explored in bins of galaxy stellar mass, luminosity and redshift, showing some weak evidence of evolution of the clustering strengths. The correlation functions from GAMA are shown to be reasonably well fit by power laws and are in agreement with SDSS.

More recently clustering in GAMA has been explored using marked correlations by Sureshkumar et al. (2021, 2022), where it is seen that stellar mass is the best tracer of environment, while close pairs do not typically have high star formation rates.

The clustering of groups and the group–galaxy cross-correlation has been explored in fewer works. In SDSS these are examined in Wang et al. (2008) to explore their dependence on group mass and member galaxy colours, finding stronger clustering for more massive groups and redder galaxy populations. Berlind et al. (2006) also show that on small scales the group–galaxy cross-correlation increases, before flattening due to either a core to the groups or mis-centring. The use of the clustering of groups to derive bias and redshift space distortion parameters is discussed in Mohammad et al. (2016).

While group clustering has only been considered in a few works, the distribution of satellite galaxies around centrals has frequently been considered. At the largest cluster masses the profiles showing the radial positions of satellite galaxies within groups from SDSS have been explored by Hansen et al. (2005), and by Budzynski et al. (2012) who explore the dependencies of profiles on properties including halo mass and satellite luminosity. More recently, the profiles of observed cluster galaxies have also been found by Adhikari et al. (2021) and Shin et al. (2021), and the distributions of galaxies around smaller groups, similar to the Milky Way, have been explored by several works (e.g. Carlsten et al., 2020; Mao et al., 2021; Font et al., 2021).

Across the wider SDSS galaxy sample, radial profiles have been considered in several works including Watson et al. (2012) who find that the most luminous satellites do not trace the dark matter profile, Guo et al. (2012) who explore the luminosity dependence further, and Wang et al. (2014) who explore the colour dependence. Satellite radial distributions have not previously been determined from GAMA, but Kafle et al. (2016) calculated the masses of satellites at different radial separations, showing no significant change in mean mass with distance. This shows there is negligible evidence of mass segregation in the GAMA survey, a tendency for satellite galaxies of different masses to be preferentially at different distances from the group centre. This trend is however controversial, as other studies have found evidence of mass segregation in groups (e.g. Roberts et al., 2015; Kim et al., 2020).

1.4 Simulating galaxy formation

The complexity of galaxy formation presents many challenges when simulating the Universe. In particular, the finite resolution of any simulation requires assumptions on the effects of unresolved small-scale effects. Despite these challenges, the latest models and simulations have been shown to accurately reproduce many of the properties of the Universe.

A variety of simulation methods are used, ranging from dark matter-only (DMO) simulations which model a universe where matter interacts only by gravity (e.g. Springel et al., 2005; Boylan-Kolchin et al., 2009), to zoom-in simulations of the baryonic processes in individual galaxies (e.g. Grand et al., 2017; Hopkins et al., 2018).

In this thesis we use DMO simulations and two methods of modelling the inclusion of baryons which produce visible galaxies. Semi-analytic models (SAMs, e.g. Henriques et al., 2015; Somerville et al., 2015; Lacey et al., 2016; Lagos et al., 2018) model baryonic processes as an addition to DMO simulations, while hydrodynamical simulations (e.g. Crain et al., 2015; Schaye et al., 2015; Nelson et al., 2019a) begin with a combination of dark matter and baryons and evolve them together.

1.4.1 Dark-matter only simulations

The simplest, and longest established, method of simulating the Universe is to use gravity-only N-body methods, originating with Holmberg (1941). N-body methods are now used for dark matter-only simulations.

The usual method of producing DMO simulations is to choose a cosmology and then begin with initial conditions of particles displaced by perturbations generated (often at $z = 127$) from the approximation of Zel'Dovich (1970). The subsequent evolution of these dark matter particles is then determined by the gravitational force between them, calculated with a code such as GADGET (Springel et al., 2021) containing methods to accelerate the computation. Finally, the outputs from these N-body simulations consist of the locations of the dark matter particles at a series of defined timesteps, referred to as snapshots.

DMO simulations exist for a variety of resolutions and box sizes, these being chosen to balance the requirements between resolving small structures and having statistically significant numbers of objects. The Millennium simulation (Springel et al., 2005) remains one of the most suitable for cosmological simulations of galaxy formation, having a volume of $(500h^{-1}\mathrm{Mpc})^3$ and 2160^3 particles. However, in recent years many other simulations have been performed, such as the SURFS suite (Elahi et al., 2018) which we use in addition to Millennium.

1.4.1.1 Clustering and profiles in DMO simulations

DMO simulations and the haloes and subhaloes that can be identified in them have been shown to accurately reproduce the large-scale structure of the Universe as on the largest scales they contain clusters, filaments and voids in a similar manner to the real Universe. Quantitatively, they have been shown to reproduce the halo mass function inferred from observations (e.g. Eke et al., 2006) and theoretically motivated models (e.g. Murray et al., 2018), as well as the theoretical clustering of matter on large scales (e.g. Springel et al., 2005).

However, some of the small-scale structure is not representative of the Universe. Using DMO simulations it is consistently seen that the subhalo profile in the inner region of haloes is flatter than the observed galaxy profile (e.g. Angulo et al., 2009; Vogelsberger et al., 2014b; Bose et al., 2020). This then affects the clustering of subhaloes when compared to that of galaxies.

1.4.1.2 Halo finders and merger trees

Galaxies cannot readily be placed directly into the N-body outputs of DMO simulations, and are usually taken to be associated with the subhaloes. In order to compare DMO simulations to observed galaxies it is therefore necessary to extract haloes and subhaloes from the DMO particles.

Haloes are derived from the N-body outputs using halo finder tools such as SUBFIND (Springel et al., 2001) and VELOCIRAPTOR (Elahi et al., 2019a). Halo finders are often based on the use of a FoF algorithm in either three-dimensional position space or six-dimensional position-velocity space to group particles. The simulations used in this thesis all involve FoF methods, although there are other methods of determining haloes, such as spherical overdensity estimates (e.g. Hadzhiyska et al., 2022) which

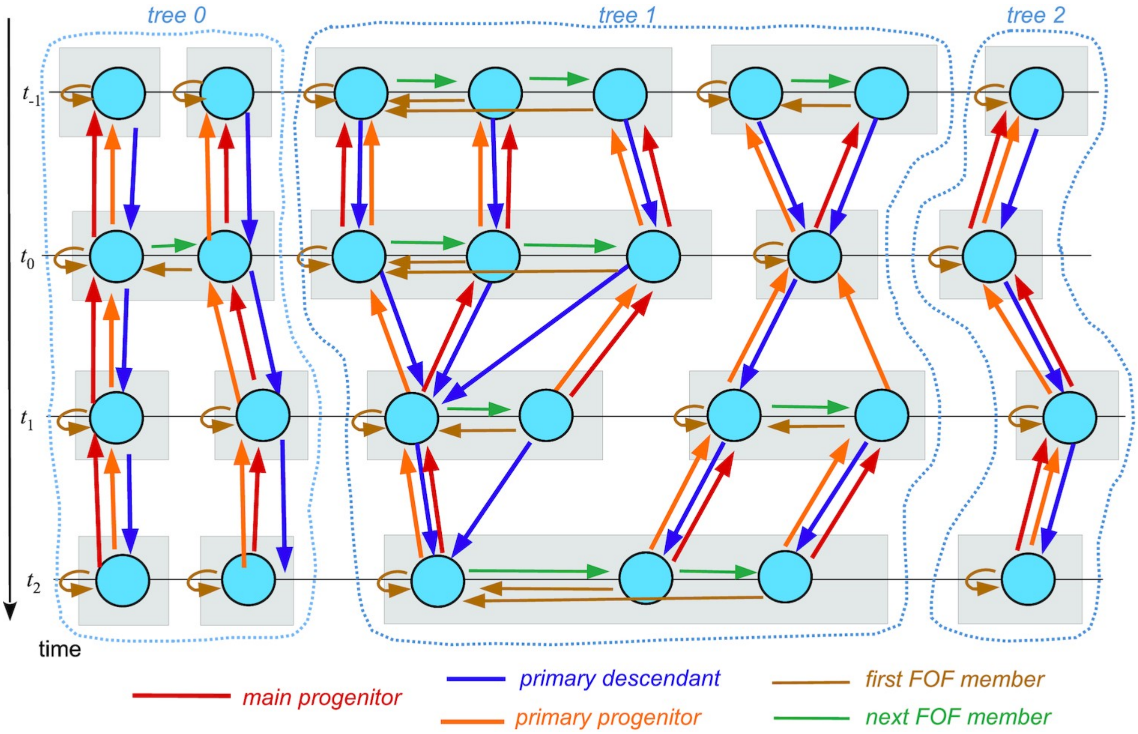

Figure 1.4: Example of a halo merger tree structure, reproduced from Springel et al. (2021, Fig. 35). With time increasing going down the page, this shows the relationships between subhaloes, including groups and mergers, as well as the connections to progenitors and descendants.

assign particles within spheres centred on the high-density regions to haloes. The haloes produced by halo finders form hierarchical structures, with subhaloes contained within the larger haloes, down to a minimum mass determined by the minimum number of grouped particles allowed to be a subhalo.

The evolution of these haloes and subhaloes is determined by looking at different output snapshots, and halo merger trees are found by connecting the structures across these snapshots. Fig. 1.4 shows an example of a merger tree structure, reproduced from Springel et al. (2021). This shows the subhaloes as circles, grouped together in boxes representing haloes. Different rows show different snapshot outputs, and the arrows show connections between the different subhaloes, including the progenitors and descendants that define the subhalo evolution and mergers. When tracing the evolution of a subhalo, trees define there to be only one descendant. This descendant is the subhalo at the following snapshot which shares the most particles with the initial subhalo, but Fig. 1.4 shows this assumption does not always accurately represent the evolution. It can also be seen that the grouping of subhaloes can vary between snapshots and there can be inconsistencies in the connections between snapshots.

As with the determination of haloes, there are a variety of codes and methods for calculating the merger trees associated with output snapshots and haloes (e.g. Springel et al., 2005; Rodriguez-Gomez et al., 2015; Elahi et al., 2019b). These do not always lead to the same outputs from N-body simulations, as shown by the merger tree comparison project in Srisawat et al. (2013) and Wang et al. (2016). Such differences include changes in the definition of the central halo of a group, the splitting of haloes, and problems associated with the temporary disappearance of a halo. These problems are almost unavoidable with current tree methods, and are a source of uncertainty in the simulation results we present in this thesis, but they may in future be resolved by the ideas presented in Roper et al. (2020), waiving the minimum mass requirement and allowing trees to branch into graphs.

1.4.1.3 Subhaloes and orphan satellites

Further problems with haloes and merger trees are encountered when the evolution and survival of satellite subhaloes is examined.

The DASH sequence of works (van den Bosch et al., 2018; van den Bosch & Ogiya, 2018; Ogiya et al., 2019) find that up to half of substructures are missing due to artificial disruption effects. This is due to the discreteness of the simulations and the force softening which is required to prevent spurious results for close particles. However, Green et al. (2021) argue that this artificial disruption is less important than resolution effects for radial biases of the locations of substructures. Additionally, Gao et al. (2004) argue that simply improving the simulation resolution does not resolve the problem of missing or inaccurate substructures, as it is still possible for subhalo masses to decrease to the point where their evolution should be affected by the baryonic components. These baryonic components of the galaxies within the haloes are shown by Zolotov et al. (2012) to be capable of altering the survival of substructures.

The uncertain disruption, resolution issues and baryonic effects lead many works to argue that when mapping between dark matter-only subhaloes and satellite galaxies, extra 'orphan' satellites are required to account for the subhaloes which are missing in the DMO simulations (e.g. Kitzbichler & White, 2008; Guo et al., 2011; Moster et al., 2018; Bose et al., 2020; DeRose et al., 2021). The requirement for orphans in a semi-empirical galaxy model is discussed by Behroozi et al. (2019) who argue that without orphans the stellar masses of the other satellites would need to be increased to reproduce observational constraints, and that this is not possible given most satellites are quenched and not star-forming.

The detection of substructures by the subhalo finder is also important when considering orphans, with Onions et al. (2012) showing that the ability to detect subhaloes varies between different structure finders and Gómez et al. (2022) showing this can influence the number of orphans required by a galaxy formation model. Haggar et al. (2021) argue that the orphans are objects that the subhalo finder has been unable to detect in DMO simulations as their density is not sufficiently different from the background halo, but that they are nonetheless separate structures that can host galaxies.

Overall, we see that there are several reasons that have been proposed for the origin of the orphan satellites. They may represent objects that have been stripped or disrupted in the DMO run, but which would remain bound due to the baryons in a full-physics run; they may be a numerical effect caused by artificial disruption or the ability of the substructure finder to detect objects; or they could be a resolution effect, caused by attempting to include galaxies that cannot be resolved.

The true picture is likely to be a combination of these effects. In essence they are all variations on the same central idea: DMO simulations are an incomplete picture of the Universe.

1.4.1.4 Adding galaxies to DMO simulations

The incompleteness of DMO simulations also means they cannot themselves be used for comparisons with observed galaxies and their distributions as they contain none of the luminous material we observe. In order to make these comparisons, several methods exist that populate dark matter haloes with galaxies.

The simplest methods are halo occupation distributions (HODs, e.g. Berlind & Weinberg, 2002; Artale et al., 2018; Zehavi et al., 2018; Hadzhiyska et al., 2020), which simply provide estimates of the number of galaxies in a halo. Dependent only on the halo mass, these may place a central galaxy in the halo and, if so, then any number of satellite galaxies can also be included. Satellite galaxies are often distributed spatially according to the dark matter density profile of the halo, either sampling the particle distribution or by making the assumption that the halo follows the NFW profile.

A slightly more advanced method is to use subhalo abundance matching methods (SHAMs, e.g. Conroy et al., 2006; Behroozi et al., 2010; Guo et al., 2016; Contreras et al., 2021), which match galaxies to subhaloes. Similarly to HODs, these usually depend only on the subhalo masses, but they can be modified to include secondary dependencies as well. Requiring galaxies to be in subhaloes provides a potential advantage in that the locations of the satellites are then pre-defined, and their properties connected to the subhalo mass, but in their simplest form they still require a one-to-one mapping between satellite galaxies and DMO subhaloes.

The next level of detail is provided by semi-empirical models such as UniverseMachine (Behroozi et al., 2019) and EMERGE (Moster et al., 2018). These include empirically derived models to generate basic properties of galaxies such as star formation rates, usually making use of the assembly history and mass growth of the haloes over time.

Finally, the inclusion of further physical models leads to the most sophisticated method to populate galaxies into dark matter haloes, semi-analytic models (SAMs). These include the evolution of galaxies by seeding them at early times and proceeding forwards in timesteps from there. SAMs are the models which we concentrate on in this thesis.

1.4.2 Semi-analytic galaxy formation models

The principle aim of SAMs is to take the dark matter haloes from an N-body simulation and perform the baryonic physics using simple physical models with empirically derived parameters. Commonly used examples of SAMs which we include in this thesis are L-GALAXIES (Henriques et al., 2015), GALFORM (Lacey et al., 2016) and SHARK (Lagos et al., 2018), although these are only a few from a large assortment of available models (e.g. Cora et al., 2018; Croton et al., 2016; Somerville et al., 2015). This variety of models is further complicated as most models have multiple versions, for example the list of major releases of L-GALAXIES over the last 15 years runs to 6 different models (De Lucia & Blaizot, 2007; Guo et al., 2011, 2013a; Henriques et al., 2013, 2015, 2020).

Specifically, in the following descriptions and throughout this thesis, we focus on the Henriques et al. (2015) version of L-GALAXIES and the Lagos et al. (2018) version of SHARK. Later we also make use of some mocks created with the Bower et al. (2006) version of GALFORM.

When connecting galaxies to haloes, the galaxies in a SAM are split into centrals and satellites, which may evolve differently. It is common to further divide the satellites into those attached to dark matter subhaloes and any which may be left over after their subhalo has been disrupted or stripped. Centrals are usually referred to as Type 0s, satellites in subhaloes as Type 1s, and satellites without subhaloes as Type 2s or 'orphans'.

1.4.2.1 SAM physical models

The main constituent of SAMs is a set of physical models for galaxy evolution. The parameters of these models have to be constrained against observations, as they generally cannot be determined analytically. The standard way of constraining these parameters is to manually alter them to give predictions that match particular observables, but this can be done in a more sophisticated way with the Markov Chain Monte Carlo (MCMC) methods introduced by Kampakoglou et al. (2008) and Henriques et al. (2009). The observations used as constraints for SAM physics vary, but the stellar mass function of galaxies is usually the primary observable used. While other observable quantities are also used, it is beneficial to leave some unused so as to provide testable predictions from the models.

The most basic requirement of a SAM is an estimate for the mass of gas contained in dark matter haloes, and a model to convert the gas into stars. Beyond this, black holes are seeded in galaxies and grow by accreting gas, and these can subsequently influence the gas distribution of galaxies through active galactic nuclei (AGN) feedback. It was shown early in the development of SAMs, including by Efstathiou (2000) and Benson et al. (2003), that both AGN and supernovae feedback are essential requirements to reproduce observed stellar mass and luminosity functions, as they limit the available gas in galaxies, and consequently the star formation rate.

These processes create a cycle for the gas distribution around haloes. Hot gas initially accretes onto haloes, where it may cool and form stars. Feedback processes then inject energy into the remaining gas, ejecting it from the halo. This causes a suppression of star formation, but gas may be reincorporated back into the haloes allowing the cycle to continue.

This cycle for the gas and stars is the minimum requirement of a SAM, but many more processes occur that should be included. Examples are chemical enrichment due to metals forming in stars, the modelling of both atomic and molecular hydrogen gas, and effects specific to galaxy disc and bulge components. It is also necessary to model galaxy mergers and effects due to group environments, both of which we discuss below.

One important aspect for comparing SAMs to observations is the generation of galaxy luminosities. This requires a model for the stellar populations of the galaxies, such as that of Bruzual & Charlot (2003) or Maraston (2005), which can be combined with the star formation rate histories of the galaxies to predict their emitted light. Then to estimate the spectra they would have if observed this needs to be combined with a model for the dust content of the galaxies and the absorption this causes.

1.4.2.2 L-GALAXIES and SHARK

L-GALAXIES is a well-established and extensively developed SAM, originally built upon the Millennium simulation (Springel et al., 2005), and later adapted to simulate lower mass galaxies with the higher resolution Millennium-II simulation (Boylan-Kolchin et al., 2009). A major update to the code was released in Henriques et al. (2015) and a more recent version was produced by Henriques et al. (2020).

The main model includes gas physics, star formation, black hole growth and feedback, and supernova feedback. Additionally, environmental effects are included for satellite galaxies such as gas stripping and tidal disruption. The more recent Henriques et al. (2020) model also includes rings of material in galaxy discs as well as more detailed chemical models. Post-processing methods were added by Henriques et al. (2012) for stellar population synthesis and dust, to generate galaxy luminosities in different filter bands.

The free parameters in L-GALAXIES are chosen using Monte Carlo Markov Chain (MCMC) analysis. This was first incorporated into the SAM by Henriques et al. (2009), and from Henriques et al. (2013) has been used to fit the SAM on a representative sample of merger trees from the Millennium and Millennium-II simulations. This MCMC uses a standard Metropolis-Hastings algorithm (Metropolis et al., 1953; Hastings, 1970), with a flat prior. This works by generating walkers which are able to explore the possible parameter values. For each walker, the process is to select a new point in parameter space, calculate a likelihood for that point, and accept or reject that point using the ratio of the likelihood to that of the previous step. The MCMC for the Henriques et al. (2015) version of L-GALAXIES was used to fit 17 parameters in the model against observations of the stellar mass function at $z = 0, 1, 2, 3$ and the fraction of red galaxies as a function of mass at $z = 0, 0.4, 1, 2, 3$.

The SHARK SAM (Lagos et al., 2018) is a more recent model built upon the SURFS (Elahi et al., 2018) halo catalogues. It is designed to be an open source and modular SAM which can be easily adapted for new models. This contrasts with most other SAMs where the code is either not public (as is the case for GALFORM) or has been developed piecemeal without a clear structure (as is the case for L-GALAXIES).

Being a newer model SHARK is less well-developed but includes the basic required methods of a SAM such as gas cooling and heating, star formation, stellar feedback, black hole feedback, and galaxy mergers.

The parameters in SHARK were chosen by hand to match observations of the stellar mass function at $z = 0$ and 2, as well as the $z = 0$ black hole–bulge mass relation and galaxy mass-size relations.

1.4.2.3 Merging galaxies

Galaxy mergers in SAMs are taken to occur between a central galaxy and one of the associated satellites. Mergers are split into major mergers and minor mergers depending on the mass ratio of the two objects. Major mergers occur when two similarly sized galaxies merge, and these destroy the discs of both galaxies, leading to the formation of a bulge in the centre of the resulting galaxy. Minor mergers occur when one galaxy is much larger than the other, and result in the larger galaxy having a disc and bulge structure. Mergers may cause bursts of star formation and also feed the central super-massive black hole with cold gas which then drives AGN feedback.

The question of when these galaxy merger events occur in SAMs poses a problem. The loss of a dark matter subhalo from the simulation does not necessarily imply that any galaxy within it has undergone a merger. While a few SAMs, such as that of Cattaneo et al. (2017), do include instantaneous mergers, most include Type 2 or orphan satellites to account for the possible extended survival times of galaxies compared to subhaloes.

The extended survival of these galaxies is usually accounted for by estimating the merger time t_{df} based on the properties of the satellite when it becomes a Type 2, and merging it with the central galaxy once this time has elapsed. A variety of models for survival time exist (e.g. Boylan-Kolchin et al., 2008; Jiang et al., 2008; Poulton et al., 2021; Berner et al., 2021), most of which are built on the theoretical model of Chandrasekhar (1943). These models all account for the dynamical friction of the host on the satellite, but many do not account for satellites with a physical extent or the addition of baryons, so they are often adapted with a free parameter that can be tuned.

For the specific cases of the SAMs we use, L-GALAXIES uses a model based on Binney & Tremaine (1987),

$$t_{\mathrm{df}} = \alpha_{\mathrm{DF}} \frac{r_{\mathrm{sat}}^2 V_{200c}}{G M_{\mathrm{sat}} \ln \Lambda}, \tag{1.22}$$

which has a free parameter α_{DF} and depends on the satellite mass M_{sat} and radial position r_{sat}, as well as the host properties through V_{200c} and the Coulomb logarithm $\ln \Lambda = \ln(1 + M_{200c}/M_{\mathrm{sat}})$. SHARK instead uses a formula from Lacey & Cole (1993),

$$t_{\mathrm{df}} = \alpha_{\mathrm{DF}} \frac{\Theta_{\mathrm{orbit}} R_{200c}^2 V_{200c}}{G M_{\mathrm{sat}} \ln \Lambda}, \tag{1.23}$$

and calculates the Coulomb logarithm as $\ln \Lambda = \ln(M_{200c}/M_{\mathrm{sat}})$. We have expressed these two equations in a way that emphasises an overall similarity, but also demonstrates the differences, in particular the inclusion of r_{sat} in the L-GALAXIES method, and the addition of a dimensionless orbital function Θ_{orbit} for SHARK. Θ_{orbit} depends on the energy of the satellite orbit, but in practice it is selected at random from a log-normal distribution in SHARK. The significance of this is that the survival times of satellites in L-GALAXIES depend on the location of the satellite, but are independent of position in

SHARK.

Having established the survival time of a Type 2 satellite at the snapshot its host subhalo is lost, the position of the satellite at subsequent snapshots needs consideration. A common method is to assume the satellite follows the position of the particle which had the greatest binding energy in the subhalo it previously belonged to, referred to as the most-bound particle (e.g. Guo et al., 2011; Pujol et al., 2017). This is the approach taken by the Henriques et al. (2015) version of L-GALAXIES, although a slight modification is applied. It is assumed that the baryonic component of the satellite causes an increase in the dynamical friction force, and so the satellite is displaced radially from the most-bound particle by a factor

$$\frac{r_{\mathrm{sat}}}{r_{\mathrm{MBP}}} = 1 - \frac{\delta t}{t_{\mathrm{df}}}, \tag{1.24}$$

where δt is the time since the galaxy became a Type 2.

SHARK follows another common approach for the locations of Type 2 satellites: distribute the satellites randomly. In SHARK this random distribution is taken to be the NFW profile using the properties of the host halo, and positions selected using the method of Robotham & Howlett (2018).

While the methods used by L-GALAXIES and SHARK are common approaches to dealing with the problem of Type 2 locations, we note that other models have been proposed and used. These include analytically predicting orbits based on the initial properties of the host and satellite, as used by Tollet et al. (2017), Cora et al. (2018) and Jiang et al. (2021), and creating a model that matches the orbits of DMO subhaloes at different resolutions, as done by Delfino et al. (2022).

1.4.2.4 Environmental effects

The evolution of satellites is further complicated by possible environmental effects, which can cause the loss of gas and stars from the satellites. In particular, in L-GALAXIES, once a satellite has become an orphan it is assumed that, if the forces on the galaxy are great enough, it can be broken apart.

Within L-GALAXIES there are two environmental effects that act on satellites. Firstly, tidal and ram pressure stripping of Type 1s by their host halo; these stripping effects gradually cause the removal of the hot gas of the satellite based on the location and mass of the satellite. The tidal aspect of this acts proportionally to the dark matter mass of the subhalo, thus removing all the hot gas by the time the mass reaches zero and the satellite becomes an orphan (Guo et al., 2011).

The second environmental effect occurs after the point at which the satellite becomes an orphan and this removes the remaining components of the galaxy, the cold gas and stars. The main Henriques et al. (2015) model includes an instantaneous disruption method, whereby if an orphan satellite is estimated to pass far enough into the halo density profile, it is completely destroyed and the components of it are dispersed into the intergalactic medium. This is a simplistic model, and a more detailed model has been developed by Henriques & Thomas (2010) and Murphy et al. (2022) where the stars and cold gas are stripped from the satellite gradually.

In SHARK no detailed environmental effects are included for Type 2s. Instead, the model of Lagos et al. (2014) is used, so that when a satellite first becomes a satellite all of the hot gas is instantaneously stripped away and transferred to the central.

1.4.2.5 Clustering and profiles in SAMs

The clustering predictions of SAMs have been widely explored, as these are key large-scale structure observables for which benefits are gained by the larger volume that can be modelled by SAMs compared to the more computationally expensive hydrodynamical simulations we discuss next. However, the inclusion of clustering among the constraints on the free parameters of SAMs has proven a greater challenge.

In works based around individual SAMs the most relevant here are Henriques et al. (2017) which shows projected clustering results from the Henriques et al. (2015) version of L-GALAXIES in stellar mass bins, and Chauhan et al. (2020) which shows clustering in SHARK for galaxies selected by HI mass. Both SAMs demonstrate a reasonable agreement with observations, but neither exactly matches the observations. By comparing to Guo et al. (2013a), Henriques et al. (2017) are able to conclude these predictions are affected by supernova feedback and gas reincorporation.

A number of works have also compared clustering predictions between SAMs. The most detailed of these is Pujol et al. (2017), part of the SAM comparison project begun in Knebe et al. (2015), which provides direct comparisons between 12 SAM and HOD variants by running them all on the same halo catalogue. By comparison of both three-dimensional clustering and radial profiles, they conclude that the differences in the modelling of orphan satellites is the primary cause of the scatter between SAM and HOD predictions on small scales. The merging of satellites is also identified as the main cause of differences in clustering between models in Contreras et al. (2013), which compared a range of variants of the L-GALAXIES and GALFORM SAMs.

Wang et al. (2014) compare profiles from an earlier version of L-GALAXIES against SDSS, and also show that the profiles on the smallest scales are dominated by Type 2 satellites. Further comparisons are done with SDSS using the GALFORM SAM by Guo et al. (2013b), showing the SAM does not match the colour dependence to the SDSS profiles.

The most complete way to explore the dependence of clustering on SAM parameters would be to use clustering as a constraint in the fitting of the free parameters. However, the two-point structure of clustering does not lend itself to calculations on subsets of SAM outputs, as is required for MCMC fitting. The one major attempt to use clustering is that of van Daalen et al. (2016), who endeavour to get around the problem of clustering in small volumes by using the halo model to predict clustering for samples of galaxies. This allows them to perform MCMC parameter analysis, finding the satellite merger timescale and the parameters associated with supernovae feedback are altered the most by the use of clustering constraints.

1.4.3 Hydrodynamical simulations and the effect of baryons

The most comprehensive method of simulating galaxy formation is the use of cosmological hydrodynamical simulations such as IllustrisTNG (Nelson et al., 2019a) and EAGLE (Crain et al., 2015; Schaye et al., 2015). These simulate the baryons and dark matter simultaneously, solving both the equations of gravity and hydrodynamics. This means that they include the interactions between the baryonic and dark components of the Universe in a manner that is impossible in simulations built upon DMO methods. Fig. 1.5, reproduced from Vogelsberger et al. (2020), shows some examples of hydrodynamical simulations, as well as some of the DMO simulations which SAMs are built upon. It can be seen that the large-scale structure is similar for hydrodynamical and DMO methods, but on small scales they differ. This is most clearly seen for the small hydrodynamical zoom simulations which can produce realistic images of galaxies.

While hydrodynamical simulations, by including the baryons with the dark matter, are expected to be the most detailed and accurate simulations currently available, they are still not free from uncertainties in the modelling. It is important to note that the particle masses in the simulation are large, often millions of stellar masses, and for example the stellar particles are equivalent to large objects such as star clusters. Similarly the minimum spatial resolution that can be resolved may represent a significant fraction of the size of a galaxy. Physics at smaller scales and masses must be accounted for using subgrid models, which are often similar to the empirical models used in SAMs. The details of these models are uncertain and they require calibration to produce results comparable to observed galaxies. As explained in Vogelsberger et al. (2020), the mechanisms used for feedback processes are particularly unclear and can significantly impact the outcomes of the simulations.

1.4.3.1 IllustrisTNG

In this thesis we use the IllustrisTNG simulations (TNG, Marinacci et al., 2018; Naiman et al., 2018; Nelson et al., 2018, 2019a,b; Pillepich et al., 2018b, 2019; Springel et al., 2018) These are a recent set of cosmological magnetohydrodynamical simulations which have been run at a variety of resolutions. They are an improved version of the Illustris simulations (Vogelsberger et al., 2014a,b; Genel et al., 2014; Sijacki et al., 2015), to resolve issues with the feedback in the original model causing discrepancies with observations compiled in Nelson et al. (2015).

The main TNG simulations consist of 9 simulations, split into 3 different size boxes, each with 3 different resolutions. These are detailed in Table 1.1. There are also dark matter-only simulations to match each of the 9 TNG simulations. Of particular note are the highest resolution simulation, TNG50-1, and the largest simulation, TNG300-1. In TNG50-1 galaxies of lower masses are resolved and the internal structure of galaxies can be explored, while TNG300-1 has a box size comparable to some DMO simulations and so samples the large-scale structure in a more statistically significant manner.

The physical models of TNG are detailed in Weinberger et al. (2017) and Pillepich et al. (2018a), and include star formation, gas radiative processes, chemical enrichment

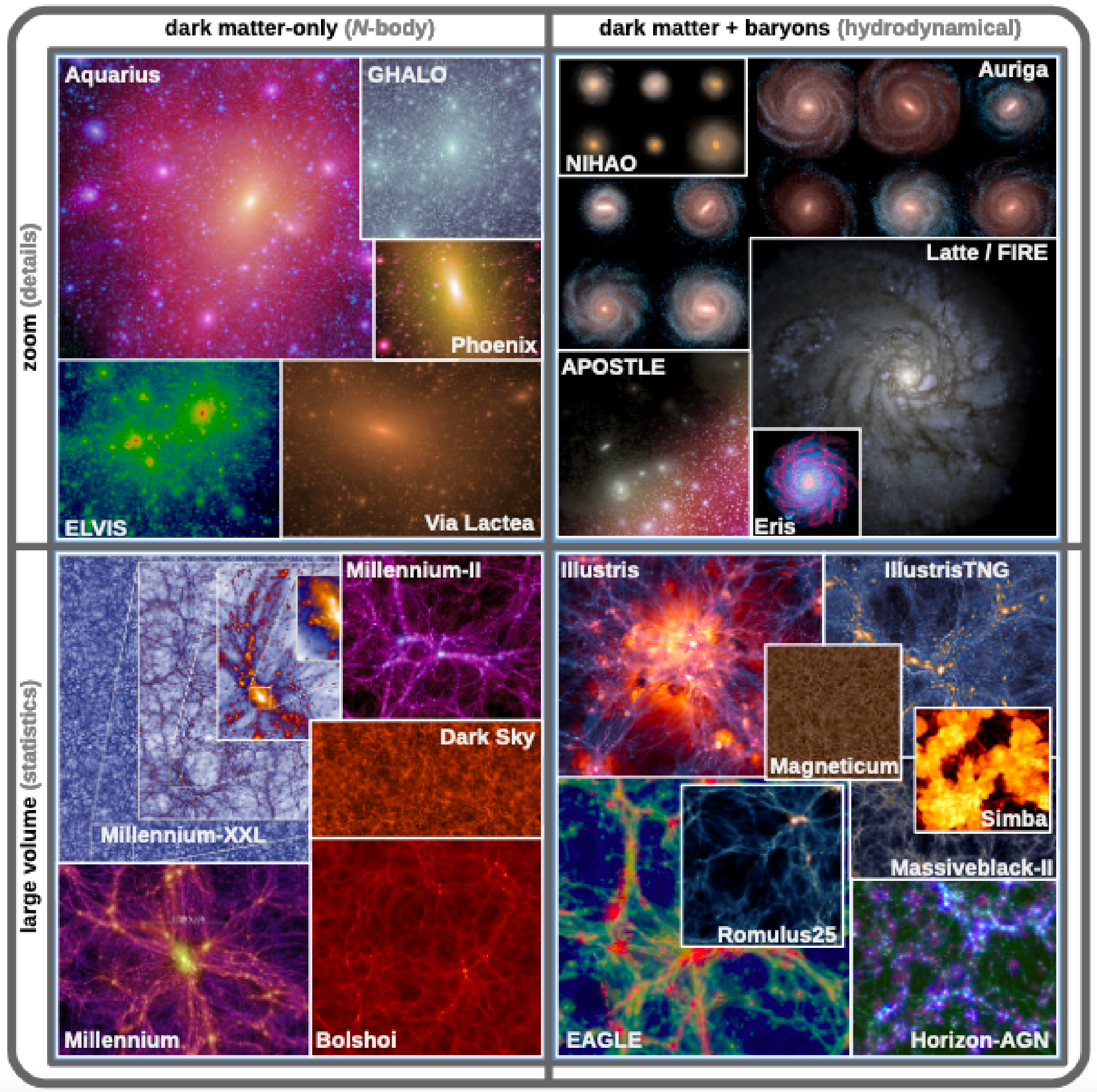

Figure 1.5: A comparison of some examples of galaxy formation and dark matter simulations, reproduced form Vogelsberger et al. (2020, Fig. 1). Cosmological and zoom simulations are shown, for both hydrodynamical and DMO methods. Some of the simulations we use in this thesis are shown in the lower half of this figure: the Millennium and Millennium-II DMO simulations and the IllustrisTNG hydrodynamical simulation.

Table 1.1: Details of the IllustrisTNG simulations, giving the particle masses of the full-physics simulations and their dark matter-only equivalents.

Name	$L_{\rm box}$ [h^{-1} Mpc]	$M_{\rm bary}$ [$h^{-1}\mathrm{M}_\odot$]	Hydro $M_{\rm DMO}$ [$h^{-1}\mathrm{M}_\odot$]	DMO $M_{\rm DMO}$ [$h^{-1}\mathrm{M}_\odot$]
TNG50-1	35	5.7×10^4	3.1×10^5	3.7×10^5
TNG50-2	35	4.6×10^5	2.5×10^6	2.9×10^6
TNG50-3	35	3.7×10^6	2.0×10^7	2.3×10^7
TNG100-1	75	9.4×10^5	5.1×10^6	6.0×10^6
TNG100-2	75	7.6×10^6	4.0×10^7	4.8×10^7
TNG100-3	75	6.0×10^7	3.2×10^8	3.8×10^8
TNG300-1	205	7.6×10^6	4.0×10^7	4.8×10^7
TNG300-2	205	5.9×10^7	3.2×10^8	3.8×10^8
TNG300-3	205	4.8×10^8	2.5×10^9	3.0×10^9

and black hole growth. Feedback effects from the stars and black holes in the simulations occur in the form of supernovae and active galactic nuclei.

1.4.3.2 Effects of baryons

The key difference between hydrodynamical simulations and other methods such as SAMs is that the impact of baryonic physics on galaxy formation and the structure of the Universe can be directly investigated. This has lead to studies being done of the effect of baryons on haloes in many hydrodynamical simulations.

One of the key studies is that of Sawala et al. (2013), who find that baryonic physics reduces both the mass and abundance of structures with masses $\lesssim 10^{12}\mathrm{M}_\odot$. Chua et al. (2017), using the original Illustris simulations, also show baryons reduce the abundance of low mass subhaloes. However, other studies such as Schaller et al. (2015) and Castro et al. (2021) show a reduction in abundance for all masses. Despali & Vegetti (2017) argue that the apparently inconsistent reductions, and some differences they show in the radial distribution of subhaloes, are due to the range of feedback mechanisms used in simulations. Additionally, the variety of reductions in masses seen in different studies may be partly attributable to the choices made about the selection of subhaloes.

However, it can be hard to distinguish the effects of the baryonic physics from the impacts of the numerical methods used for the hydrodynamics. Jia et al. (2020) found that adding only the hydrodynamics required for gas particles is enough to alter the abundance of substructures, and this will therefore account for some of the differences between dark matter-only and hydrodynamic simulations.

Another effect of baryons, seen in studies such as Schaller et al. (2015), is the alteration of the radial distributions of the different components of the haloes, caused by the presence of stars. Baryons have been seen to change the shapes of haloes, including in Illustris by Chua et al. (2019), but there are two different effects involved. In the inner regions of haloes the baryons can cause contraction (Gnedin et al., 2004) but the feedback processes associated with baryons can also eject matter from the centre (Duffy et al., 2010).

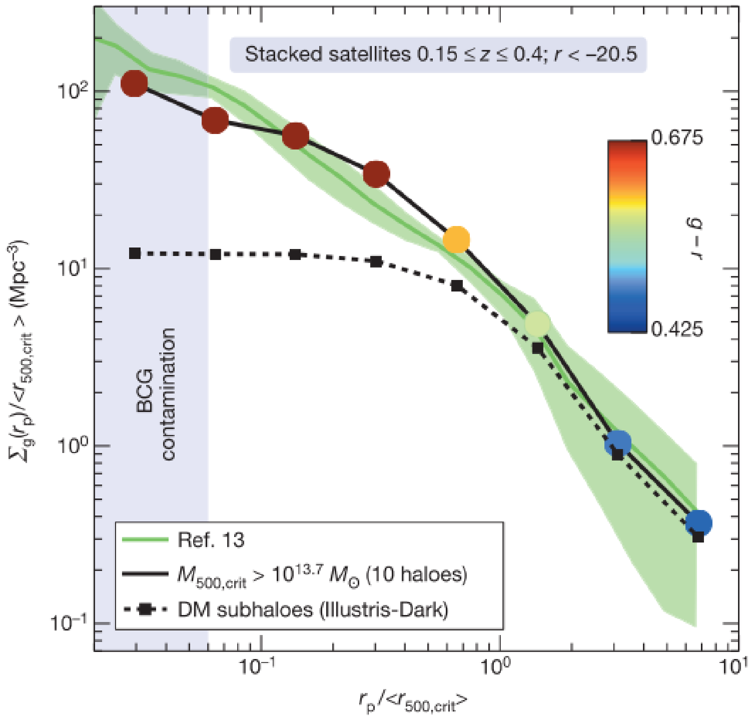

Figure 1.6: Radial distribution of satellite galaxies in clusters from the Illustris simulation, reproduced from Vogelsberger et al. (2014b, Fig. 2). The solid black line shows the satellite profile, and is in agreement with the green band, which shows the results of Budzynski et al. (2012). The dotted line shows the distribution of subhaloes in the equivalent DMO simulation, which has a much flatter profile.

1.4.3.3 Clustering and profiles in hydrodynamical simulations

Hydrodynamical simulations have been limited by box size and obtainable resolution when considering the large-scale structure of the Universe, but recently the increasing size and complexity of the simulations has made it possible to generate predictions for galaxy clustering.

The clustering in the TNG100 and TNG300 simulations is explored in Springel et al. (2018). A reasonable agreement is shown compared to SDSS, except for when galaxies are split by colour. This is suggested to be the result of not applying dust corrections for their colours. One of the most successful clustering predictions from other hydrodynamical simulations is in the EAGLE simulations by Artale et al. (2017), reaching a similar level of agreement as IllustrisTNG, with results consistent with observations except for red galaxies.

The distribution of satellite galaxies from the centre of their host halo has been considered by Vogelsberger et al. (2014b) in the earlier Illustris simulation. Fig. 1.6 is reproduced from that work and shows that satellites closer in to the centre are redder and that luminous satellite galaxies have an enhanced number density on small scales compared to the distribution of subhaloes in the dark matter-only simulation.

Nagai & Kravtsov (2005) showed that adding in some of the gas dynamics and star formation processes involved in galaxy formation results in this enhancement over the distribution of DMO subhaloes, and brings simulations into reasonable agreement with observations, but that this does depend on the subhalo selection used. Similar enhancement of galaxies compared to DMO subhaloes is also seen in Weinberg et al. (2008), where it is shown to cause an enhancement in the correlation function on small scales, and in the subhalo distributions around clusters in the THETHREEHUNDRED project by Haggar et al. (2021).

In the IllustrisTNG simulations radial profiles are considered by Bose et al. (2019), where the galaxies are seen to follow the NFW profile of matter more closely than they follow the distribution of subhaloes selected by mass in the dark matter-only run. Further, they show that if dark matter-only subhaloes are instead selected by the maximum value of the peak circular velocity at any point in their history, then a close match to the galaxy profile can be obtained.

1.5 Thesis outline

In this thesis we use the galaxy surveys and simulations we have discussed above to explore the distribution of galaxies within and around groups. To achieve this we make use of small-scale clustering and satellite galaxy radial profiles. The outline of this thesis is as follows.

In Chapter 2 we compare predictions from the L-GALAXIES and SHARK SAMs against results from the GAMA survey, with a focus on how well they are able to reproduce the clustering of galaxies. We examine which aspects of the models influence the clustering, finding that on small scales the modelling of 'orphan' satellites is most important, while large scales are mainly determined by the halo catalogue. We confirm this with some simple modifications to the satellite radial distributions in SHARK.

As part of this study we measure the stellar mass function and luminosity functions of the galaxies in the SAMs, and we adapt the luminosity post-processing methods from L-GALAXIES to work on SHARK, allowing direct comparison of these methods. We also discuss the occupation of haloes of different masses by galaxies with differing properties, and the impact of the tuning of the SAMs.

In Chapter 3 we present Riggs et al. (2021), an exploration of the group clustering in the GAMA survey. We calculate the group–galaxy cross-correlation for GAMA to explore the small-scale group profile and the large-scale bias around groups, and we also calculate the first results for marked correlation functions using groups.

We find the marked clustering statistics depend strongly on the group masses, but have only weak dependence on galaxy mass, suggesting there is little mass segregation. We compare these GAMA results to predictions from IllustrisTNG and L-GALAXIES. IllustrisTNG matches GAMA well for most measurements but L-GALAXIES over-predicts the mass dependence of the cross-correlation, which we ascribe to inaccuracies in the modelling of the physics affecting satellite galaxies.

In Chapter 4 we present Riggs et al. (2022), looking at the radial distribution of satellite galaxies around groups in the IllustrisTNG simulations and the GAMA survey.

We compare the TNG satellite profiles to the distributions of matched subhaloes in the equivalent dark matter-only simulations, seeing that there is an enhanced satellite density on small scales in the full-physics simulations. This is due to the full-physics satellites residing closer to the halo centre and having longer survival times.

We use these differences to derive models to account for the effect of baryons on the positions of satellite galaxies in SAMs. For the satellites which have DMO counterparts, we find that they reside closer to the central in the full-physics simulations, and that this can be modelled with a power law. Satellites without DMO counterparts are distributed radially in a manner that can be fit with a log-normal distribution, and we also develop a model for their radial motion.

Following this, we test the application of these models to L-GALAXIES and SHARK in Chapter 5. In both SAMs we find that our models provide some improvement in the predicted satellite galaxy distributions and galaxy clustering when compared to GAMA. However, for L-GALAXIES these changes impact the other predictions of the SAM such that it needs recalibrating, and we show that this recalibration leads to faster mergers and altered star formation rates.

Finally, we give our conclusions from this thesis and discuss the outlook for future works in Chapter 6.

2

Comparing semi-analytic galaxy formation models against the GAMA survey

S. D. Riggs, J. Loveday

Abstract

We compare the semi-analytic galaxy formation models (SAMs) L-GALAXIES and SHARK against the Galaxy and Mass Assembly (GAMA) survey. We consider the stellar mass function, luminosity functions from *FUV* to *K*-band, and the projected two-point correlation function. To understand the differences in these, we compare the occupation of haloes by galaxies of different stellar masses and luminosities, and also examine the distributions of satellite galaxies within haloes.

We find that the tuning of SHARK places high-mass galaxies in less massive haloes than L-GALAXIES, meaning that SHARK produces galaxy distributions in disagreement with GAMA when galaxies are split by halo mass. The accuracy of the clustering predictions varies with the underlying N-body simulation and the galaxy selection criteria, but we find that L-GALAXIES consistently predicts a greater small-scale clustering amplitude than SHARK.

We conclude that the halo catalogue matters for clustering predictions, particularly on scales above $0.5h^{-1}$Mpc; smaller scales are dominated by the effects of orphan satellite galaxies that have lost their dark matter subhalo and are spiralling in to merge with their associated central galaxy. Our work indicates that clustering predictions from the SHARK model could be improved by merging orphan satellite galaxies later, and that in both SAMs small-scale clustering predictions require a more detailed model for the positions of the orphan satellites.

2.1 Introduction

Galaxy formation involves a complex mixture of many processes, which many simulations have attempted to reproduce in order to understand the underlying physics. The two most sophisticated simulation methods are hydrodynamical simulations (e.g. Crain et al., 2015; Schaye et al., 2015; Pillepich et al., 2018b) and semi-analytic models (SAMs, e.g. Henriques et al., 2015; Somerville et al., 2015; Lacey et al., 2016; Lagos et al., 2018). Hydrodynamical simulations consider the dark matter and baryons simultaneously, providing insight into the interactions between them, but are computationally expensive to run. SAMs are simpler and evolve galaxies on a pre-computed dark matter N-body simulation. They contain more free parameters that must be tuned, but they allow rapid testing in large volumes of a range of different simple models for the processes involved in galaxy formation. This makes them a powerful tool for investigating these processes. In this work we explore predictions from two SAMs, the Lagos et al. (2018) version of SHARK and the Henriques et al. (2015) version of the Munich galaxy formation model L-GALAXIES.

Large spectroscopic galaxy surveys are important for constraining and testing galaxy formation models, and we compare these SAM predictions to observational results from the Galaxy And Mass Assembly survey (GAMA, Driver et al., 2009, 2011; Liske et al., 2015). GAMA provides a spectroscopic sample of galaxies that is highly complete in all environments. In comparison to the Sloan Digital Sky Survey (SDSS, York et al., 2000) main galaxy sample, GAMA is two magnitudes deeper and has much better spectroscopic completeness, although at the cost of reduced sky coverage.

The parameters of the galaxy formation physics in SAMs have to be constrained against such observations, as it is not possible to produce theoretical values for them *a priori*. The stellar mass function (SMF) of galaxies is the first observable that any model should reproduce, and most SAMs constrain their parameters to give the best possible fit to the SMF. However, luminosity functions (LFs) provide a more direct comparison to observations of real galaxies, and so it is also important to reproduce these.

In addition to the overall SMF and LFs, it is interesting to consider how galaxies with different masses and luminosities are distributed in haloes of different masses. Recently Vázquez-Mata et al. (2020, hereafter VM20) compared SMFs in different mass haloes between GAMA, L-GALAXIES and two hydrodynamical models, finding similar trends in central galaxy properties but significantly less dependence of satellite galaxy properties on halo mass in the simulations than in GAMA.

Galaxy clustering is also a key prediction of galaxy formation models, although most SAMs do not include clustering among their constraints, with the Markov Chain Monte Carlo (MCMC) methods introduced by Kampakoglou et al. (2008) and Henriques et al. (2009) only once having been adapted to include clustering. This was done in the work of van Daalen et al. (2016), who concluded that the parameters most strongly affecting the two-point correlation function are those affecting merger times and supernovae feedback, and suggested that clustering will be a fruitful additional measurement to test and constrain models.

While not often used as a constraint, galaxy clustering binned by galaxy stellar mass has been frequently examined in the outputs from SAMs, including by Henriques et al. (2013), Kang (2014) and Campbell et al. (2015). The Henriques et al. (2015) version of L-GALAXIES has its projected galaxy clustering examined by Henriques et al. (2017), who show that the most significant effects on the predicted two-point correlation function are from supernova feedback and gas reincorporation models. Contreras et al. (2013) provide a detailed comparison of clustering in several versions of the Munich and Durham SAMs, and conclude that the merging of satellite galaxies is the biggest cause of differences between models. Comparing those SAMs avoids some differences associated with the N-body simulation, as they both use the Millennium (Springel et al., 2005) N-body simulation, but that still leaves some degeneracy between the effects of the halo merger tree construction and the galaxy formation models.

The most comprehensive exploration of galaxy clustering in different SAMs is that of Pujol et al. (2017), who run several SAMs on the same dark matter halo catalogue. This follows the work of Knebe et al. (2015), where it is shown that using the same halo catalogue for different SAMs can produce large differences in the stellar mass functions and other observables due to the different tuning used for each SAM.

Pujol et al. (2017) identify the modelling of 'orphan' satellite galaxies, also referred to in the models as Type 2 galaxies, as one key element of clustering predictions. These are satellite galaxies which have lost their associated dark matter subhalo. This occurs when the subhalo becomes sufficiently disrupted that it is no longer detected by the halo finding algorithm, and so any galaxy contained within that subhalo becomes an orphan. The subsequent modelling of these galaxies varies between SAMs, with some instantly merging the galaxy with the central galaxy of the host halo, and others following orbits generated analytically, or from the most-bound particle of the disrupted subhalo.

Increasing the simulation resolution allows for the exploration of galaxies with smaller stellar masses, but does not solve the problem of orphan galaxies (Gao et al., 2004). If the dark matter mass of a subhalo drops below that of its baryons, the orbit found by just considering the dark matter will become inaccurate. In L-GALAXIES, galaxies where that happens are treated as orphan satellites for their subsequent evolution.

Small-scale problems affected by satellite galaxies are also found in Farrow et al. (2015) when mock catalogues from the Lacey et al. (2016) and Gonzalez-Perez et al. (2014) versions of the Durham SAM are compared against GAMA projected correlations.

Our work adds to this, considering clustering in volume-limited samples from two different SAMs. We present the first comprehensive clustering results from SHARK and compare against L-GALAXIES to test the SHARK model and explore reasons for the differences in their predictions. We compare both SAMs against the GAMA spectroscopic galaxy survey, as the high completeness of GAMA for close pairs (see Robotham et al., 2010) is a significant improvement upon SDSS for examining small-scale clustering. We expand upon the results of Pujol et al. (2017), looking at galaxy clustering as a function of both stellar mass and luminosity, and considering the effect that different halo catalogues can have on the results. Through the addition of luminosity-dependent clustering we compare against a more direct result from the observations, where it is much easier to derive a volume-limited sample for luminosities than for stellar masses.

This paper is organised as follows. In Section 2.2 we introduce the GAMA survey and the relevant details of the SAMs we use, and then in Section 2.3 we explain our methods. Section 2.4 gives our results for stellar mass and luminosity functions, and Section 2.5 for two-point correlation functions. We present a discussion of the impact of the model for orphan satellite positions in Section 2.6 and conclude in Section 2.7.

2.2 Data and simulations

2.2.1 GAMA survey

The data we use for our comparisons comes from the GAMA spectroscopic galaxy survey. The GAMA-I survey comprised three equatorial fields, each of area 12×4 degrees, with a Petrosian magnitude limit of $r < 19.4$. This was updated in GAMA-II to increase the area of each field to 12×5 degrees and the magnitude limit to $r < 19.8$. The high spectroscopic completeness, including of close pairs (see Robotham et al., 2010), makes the survey suitable for examining clustering down to small scales.

We primarily use results from GAMA-II, but also compare to GAMA-I results in the form of the SMF of Baldry et al. (2012) and the LFs of Driver et al. (2012) from the far ultra-violet to the near infra-red.

We calculate projected two-point correlation functions for volume-limited samples from GAMA-II. The details of these samples are given in Table 2.1. Our bin selections match those of Farrow et al. (2015), with the exception of the lowest stellar mass bin where Farrow et al. (2015) use a wider bin of $8.5 < \log_{10}(\mathcal{M}_{\star}/h^{-2}\mathrm{M}_{\odot}) < 9.5$. Samples split by stellar mass use the masses derived in Taylor et al. (2011) and are volume-limited using the same method as VM20. Briefly, the number density of galaxies with different stellar masses is calculated as a function of redshift, and the turnover points $\mathcal{M}_{\star}^{t}$ in density are fit by a polynomial,

$$\log \mathcal{M}_{\star}^{t} = 1.17 + 29.69a - 22.58a^{2}, \tag{2.1}$$

where $a = 1/(1 + z)$. Galaxies are only included in samples selected by stellar mass if their mass exceeds the value of this polynomial at their redshift.

2.2.2 Dark matter halo catalogues

In this work we use four dark matter N-body simulations with box sizes ranging from 40 h^{-1}Mpc to almost 500 h^{-1}Mpc. The largest simulation we use is Millennium (MR, Springel et al., 2005), which together with Millennium-II (MRII, Boylan-Kolchin et al., 2009), allows the exploration of the formation of galaxies with stellar masses from $10^{7}h^{-1}\mathrm{M}_{\odot}$ upwards. In the Henriques et al. (2015) version of L-Galaxies these have been updated to the Planck Collaboration et al. (2014) cosmology of $\Omega_{\Lambda} = 0.685$, $\Omega_{M} = 0.315$, $\Omega_{b} = 0.0487$, $H_0 = 67.3\ \mathrm{km\,s^{-1}Mpc^{-1}}$, $n_s = 0.96$ and $\sigma_8 = 0.829$, using the

Table 2.1: GAMA clustering sample selection criteria with mean redshifts, masses and r-band luminosities. We also give the selection criteria and power-law fits for comparable samples from Farrow et al. (2015), assuming a power law spatial correlation function $\xi(r) = (r/r_0)^{-\gamma}$.

	Volume-limited sample				Comparable sample from Farrow et al. (2015)		
$M_r - 5\log_{10}h$ range	Mean $M_r - 5\log_{10}h$	Redshift limits	Mean redshift	$N_{\rm gal}$	Redshift limits	r_0	γ
$[-18, -17]$	-17.47	$[0.002, 0.078]$	0.058	3,084	$[0.02, 0.14]$	3.68	1.81
$[-19, -18]$	-18.48	$[0.002, 0.121]$	0.091	8,888	$[0.02, 0.14]$	4.57	1.74
$[-20, -19]$	-19.47	$[0.002, 0.181]$	0.137	23,903	$[0.02, 0.14]$	5.35	1.70
$[-21, -20]$	-20.42	$[0.002, 0.267]$	0.197	35,611	$[0.14, 0.24]$	5.39	1.78

	Volume-limited sample				Comparable sample from Farrow et al. (2015)		
$\log_{10}(\mathcal{M}_\star/h^{-2}\mathrm{M}_\odot)$ range	Mean $\log_{10}(\mathcal{M}_\star/h^{-2}\mathrm{M}_\odot)$	Redshift limits	Mean redshift	$N_{\rm gal}$	Redshift limits	r_0	γ
$[9.0, 9.5]$	9.23	$[0.002, 0.053]$	0.040	545	$[0.02, 0.05]$	3.28	2.24 †
$[9.5, 10.0]$	9.74	$[0.002, 0.100]$	0.075	3,232	$[0.02, 0.14]$	5.84	1.77
$[10.0, 10.5]$	10.23	$[0.002, 0.162]$	0.122	11,699	$[0.02, 0.14]$	5.93	1.82
$[10.5, 11.0]$	10.68	$[0.002, 0.26]$	0.189	14,083	$[0.14, 0.24]$	6.37	1.93

† Farrow et al. (2015) use a wider bin $8.5 < \log_{10}(\mathcal{M}_\star/h^{-2}\mathrm{M}_\odot) < 9.5$

Table 2.2: Box sizes and resolutions of the N-body simulations used in the SAMs.

Name	Box size $[h^{-1}\mathrm{Mpc}]$	Number of particles	Particle mass $[h^{-1}\,\mathrm{M}_{\odot}]$	Snapshots
Millennium (MR)	480.28	2160^3	9.61×10^8	64
Millennium-II (MRII)	96.06	2160^3	7.69×10^6	68
SURFS L40N512	40.00	512^3	4.13×10^7	200
SURFS L210N1536	210.00	1536^3	2.21×10^8	200

method of Angulo & Hilbert (2015). Our smallest simulation is the L40N512 simulation from the SURFS set of simulations (Elahi et al., 2018). We choose to use this for some of our analysis as it has the highest resolution of the SURFS simulations, but we primarily make use of the larger L210N1536 box from them. The SURFS simulations were run with the Planck Collaboration et al. (2016) cosmology of $\Omega_\Lambda = 0.6879$, $\Omega_M = 0.3121$, $\Omega_b = 0.0491$, $H_0 = 67.51\ \mathrm{km\,s^{-1}Mpc^{-1}}$, $n_s = 0.9653$ and $\sigma_8 = 0.815$. We show in Table 2.2 the resolution of each simulation used, showing Millennium and Millennium-II after scaling to Planck Collaboration et al. (2014) cosmology.

In this work, we assume that the small differences in assumed cosmology between SURFS and Millennium will not have significant effects on our conclusions; this is justified as Guo et al. (2013a) see only small differences at low redshifts when changing cosmologies in L-GALAXIES. However, the structures within the catalogues will not be the same as they have been constructed differently. Haloes and subhaloes in the Millennium and Millennium-II simulations were extracted using the SUBFIND (Springel et al., 2001) substructure finder and joined together into trees with LHALOTREE (Springel et al., 2005). The SURFS haloes have been found using the VELOCIRAPTOR (Elahi et al., 2019a) halo finder and trees were constructed from these using the TREEFROG (Elahi et al., 2019b) code. This is expected to lead to differences in the galaxies produced by the SAMs on the different halo catalogues—Lee et al. (2014) show that the growth of galaxies depends on the halo merger trees used.

We show in Fig. 2.1 the subhalo mass function of the simulations, as differences between subhalo mass functions at the high- and low-mass ends have an impact on our later results. The uncertainty regions show the standard deviation from dividing each catalogue into 8 subvolumes. It can be seen that there are fewer high-mass subhaloes in SURFS and Millennium-II than in Millennium, but that Millennium has a higher cut-off threshold at the low mass end.

2.2.3 L-GALAXIES

To produce galaxies from the halo catalogues we first use the Henriques et al. (2015) form of L-GALAXIES. This uses the Millennium and Millennium-II simulations, but we also investigate using the SURFS simulations as the input. However, we have not recalibrated the galaxy formation parameters in L-GALAXIES for the SURFS simulations, and so we expect some loss of accuracy of the results compared to those from Millennium. The parameter values we use are those of Henriques et al. (2015), which have been fit using

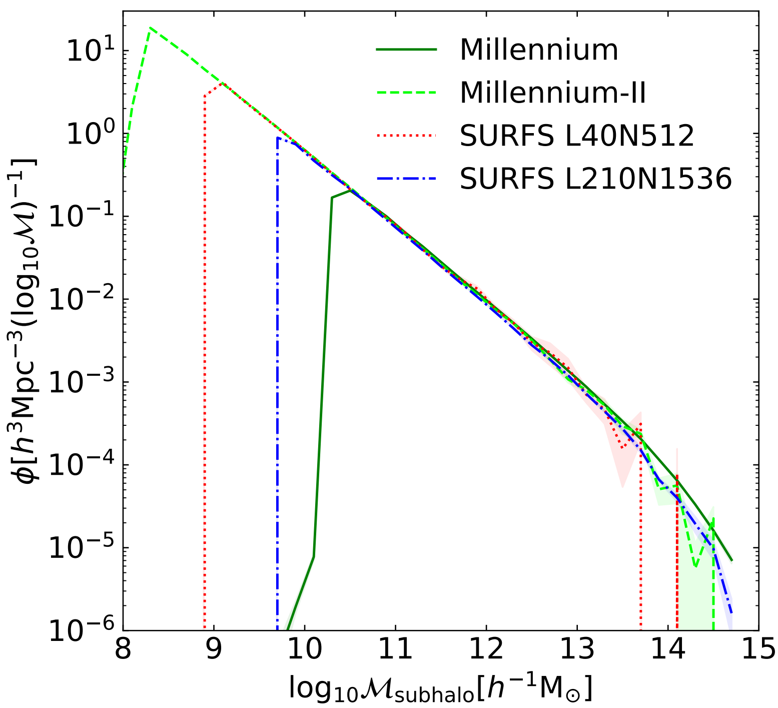

Figure 2.1: Comparison of the subhalo mass functions of the simulations in Table 2.2 at redshift zero.

MCMC against the observed galaxy SMF and the observed fraction of passive galaxies out to redshift 3 for the output from the Millennium and Millennium-II simulations.

In order to run L-GALAXIES on SURFS we had to adjust the halo catalogues slightly. For each defined group of subhaloes in the SURFS catalogues we choose the most massive subhalo in a group to be the central halo. This is necessary as L-GALAXIES requires information on the mass ordering of subhaloes during mergers, which we needed to compute for SURFS. We set the masses of the SURFS haloes to be the sum of the masses of all the subhaloes within the group.

We also change the magnitude of the subhalo spins, following the method employed in SHARK. Spin parameters λ are selected randomly from a log-normal distribution with mean 0.03 and width 0.5, and the subhalo spin J_s is then calculated with (Mo et al., 1998)

$$J_s = \lambda \frac{\sqrt{2}G^{2/3}}{(10H(z))^{1/3}} \mathcal{M}_s^{5/3}, \tag{2.2}$$

where $\mathcal{M}_s$ is the subhalo mass. Spin components are then assigned, maintaining the direction of the original spin. It can be seen this is necessary from Fig. 2.2, where the spin parameters for SURFS L40N512 subhaloes are compared to one subvolume of Millennium. In both cases the subhalo masses are restricted to the range $10.3 < \log_{10}(\mathcal{M}_s/h^{-1}\mathrm{M}_\odot) < 11.3$ and it can be seen that the SURFS subhaloes have greater values of λ and of maximum circular velocity, V_{max}. Such different distributions suggest differences and perhaps problems with the halo finders used. We also show the subhalo spins when selected randomly from a log-normal distribution, which brings the

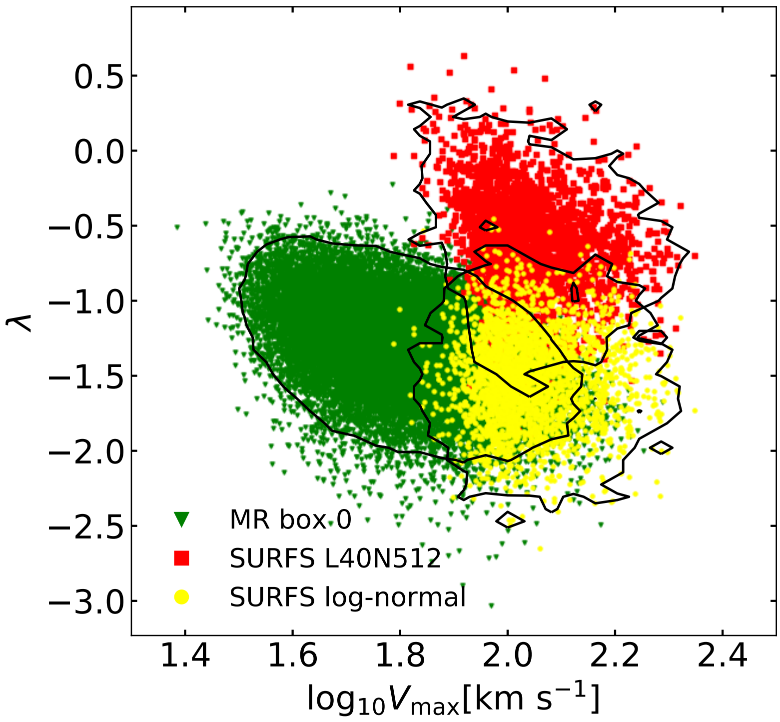

Figure 2.2: Scatter plot of the spin parameter λ against maximum circular velocity $V_{\rm max}$ for subhaloes with $10.3 < \log_{10}(\mathcal{M}_s/h^{-1}{\rm M}_\odot) < 11.3$ in the first subvolume of the Millennium simulation (green triangles), the SURFS L40N512 simulation (red squares) and for SURFS L40N512 when λ is selected from a log-normal distribution as described in the text (yellow circles). Black lines show contours at density 0.15 of the maximum in each case to make comparison easier in the overlapping regions.

values of λ into better alignment with those of Millennium. While this does not correct the difference in $V_{\rm max}$, we choose to use this method for consistency with the SHARK model.

The orphan satellites in L-GALAXIES, important for galaxy clustering, are followed using the position of the most-bound particle in the halo last identified with the galaxy. The radius of the orbit is also decayed over time by a factor of $(1 - \delta t/t_{\rm df})$ compared to that of the most-bound particle, where δt is the time since the galaxy became an orphan and $t_{\rm df}$ is the dynamical friction time. When $\delta t = t_{\rm df}$ the orphan galaxy is merged to the associated central galaxy.

When running on the SURFS simulations, most-bound particle positions are not contained in the halo catalogues so, as in Pujol et al. (2017), the radial positions of orphan satellites are decayed over time by $2 \times \sqrt{1 - \delta t/t_{\rm df}}$ from the position at which they become an orphan. This formula is included in the standard Henriques et al. (2015) implementation of L-GALAXIES for instances where most-bound particles are unavailable. It was designed to approximate the effects of dynamical friction on the satellites, modifying the formula used with most-bound particles. This reduces the differences found by Angulo et al. (2014) in the two-point correlation function on scales less than 0.4 h^{-1}Mpc with and without most-bound particles. However, this formula instantaneously doubles the radial distance from the central at the point when a satellite becomes an orphan, and the reason for this formula change is partly due to differences in the implementation of the methods within the code, leading to different outcomes of the satellite disruption mechanism. It needs to be kept in mind during the later analysis that L-GALAXIES is treating orphan galaxies slightly differently between the Millennium and SURFS simulations.

In addition to galaxies without dark matter subhaloes, L-GALAXIES also models galaxies where the stellar mass exceeds the dark matter subhalo mass as orphans. This approximation is made as for these cases the dynamics of the subhalo will have been strongly affected by the stars.

2.2.4 SHARK

We also consider the galaxies output from the SHARK SAM, version 1.2.1, on the SURFS simulations. We use the parameters of Lagos et al. (2018) which have been tuned by hand against observations, including the galaxy stellar mass function out to redshift 2 and the black hole–bulge mass relation at redshift 0.

The orphan satellites in SHARK are treated in a simpler way than in L-GALAXIES, placing them in a Navarro et al. (1997, hereafter NFW) profile adopting the properties of the host halo using the method of Robotham & Howlett (2018).

A further difference between the SAMs is that SHARK contains no inbuilt galaxy luminosity calculations, whereas L-GALAXIES does. This does not prevent luminosities being generated from SHARK, as star formation histories are recorded, but it does add an extra layer of post-processing. The existing method of post-processing is the VIPERFISH code of Lagos et al. (2019), which connects SHARK outputs to the PROSPECT spectral fitting code (Robotham et al., 2020). We use the default model of Lagos et al. (2019), referred to there as EAGLE-τ RR14, which uses Charlot & Fall (2000) dust model parameters from the parametrisation of Trayford et al. (2020), and dust to metals ratio of Rémy-Ruyer et al. (2014). As a comparison to this, we also adapt the luminosity post-processing routines of L-GALAXIES to run on the SHARK star formation histories. In order to do this, we re-bin the star formation histories into the bins generated by L-GALAXIES, making the simplest assumption that star formation is constant within a bin for the late-time bins in SHARK which are subdivided in converting to L-GALAXIES bins.

The advantage of the method we have adapted from L-GALAXIES is a much shorter running time. Approximate computation times for the VIPERFISH and L-GALAXIES methods running on 1/64 of the SURFS L40N512 simulation on 1 core of a laptop are 5 minutes compared to 2 seconds, although we note the VIPERFISH code can be run in parallel to decrease the run times.

On the other hand, the VIPERFISH code has a major advantage in that it can reproduce luminosity functions in the far infra-red, as shown in Lagos et al. (2019). The methods used in L-GALAXIES are unable to produce accurate luminosity functions beyond the near infra-red and so there is a significant benefit to using the VIPERFISH code with SHARK. However, for the remainder of this work we will only consider wavelengths up to K-band where direct comparisons between the models can be made for the SAMs.

2.3 Methodology

2.3.1 Luminosity and stellar mass functions

We calculate LFs and SMFs for all galaxies in the simulations and also for galaxies divided into bins of host halo mass. To generate uncertainties for these we divide each simulation into 8 subvolumes and calculate the standard deviation between these.

LFs and SMFs in halo mass bins are designed to match to the results of VM20, using the same halo mass bins used there for the IllustrisTNG hydrodynamical simulation. Halo masses for GAMA are calibrated to reproduce the mass within an overdensity 200 times the mean density of the Universe, but for the SAMs the masses correspond to the mass within 200 times the critical density of the Universe. This definition is used for the SAMs as it is the only one available from SHARK, but we have checked with L-GALAXIES (where both mass definitions are available) that the mass used has only a minimal effect on the results we show.

We use the same fitting functions as VM20. Central galaxies are fit with log-normal functions ϕ_c (Yang et al., 2008, 2009) of the form

$$\phi_c(M) = \phi_c^{\star}\exp\left[-\frac{(M-M_c)^2}{2\sigma_c^2}\right], \tag{2.3}$$

with peak height $\phi_c^\star$, central value M_c and width σ_c. M represents magnitude or $\log_{10}$ mass, respectively for LFs and SMFs.

Satellite galaxies are fit with Schechter functions ϕ_s, as these were found in VM20 to provide the best fits to the GAMA data. These have the form

$$\phi_s(L)dL = \phi_s^\star\left(\frac{L}{L^\star}\right)^{\alpha}\exp\left[-\left(\frac{L}{L^\star}\right)\right]d\left(\frac{L}{L^\star}\right), \tag{2.4}$$

for normalisation $\phi_s^\star$, characteristic mass or luminosity $L^\star$ and faint-end slope α. L represents luminosity or stellar mass, respectively for LFs and SMFs. We fit the satellite galaxy LFs and SMFs over the same ranges used in VM20: $-24 < M_r - 5\log_{10}h < -16$ and $9 < \log_{10}(\mathcal{M}_\star/h^{-2}\mathrm{M}_\odot) < 12.5$.

2.3.2 Two-point correlation functions

When calculating clustering results for GAMA we first estimate the two-dimensional correlation function $\xi(r_\perp, r_\parallel)$; the excess probability above random of finding a group and a galaxy separated by $r_\parallel$ along the line of sight (LOS) and $r_\perp$ perpendicular to the LOS. This is calculated using the estimator of Landy & Szalay (1993),

$$\xi(r_\perp, r_\parallel) = \frac{1}{RR}\left(DD\left(\frac{n_R}{n_D}\right)^2 - 2DR\left(\frac{n_R}{n_D}\right) + RR\right), \tag{2.5}$$

where n_D is the number of galaxies in the observations, n_R the number of galaxies in the random catalogue and DD, DR and RR give the counts of pairs of galaxies in the data catalogue, between the data catalogue and a random catalogue, and in the random catalogue respectively.

The random catalogue of points is needed to model any selection effects in the galaxy sample. We use the same survey mask described in section 2.3.1 of Loveday et al. (2018), and generate angular coordinates using MANGLE (Hamilton & Tegmark, 2004; Swanson et al., 2008). Radial coordinates are drawn at random from a distribution uniform in comoving volume modulated by the density-evolution factor $10^{0.4Pz}$ (Loveday et al., 2015, equation 5), where we assume $P = 1$.

In order to calculate correlation functions from the SAMs we use the correlation function calculator CUTE (Alonso, 2012). This calculates three-dimensional correlation functions which we project, then we calculate uncertainties using 8 jackknife samples. The CUTE code provides a specific form, CUTE_box, to run on periodic boxes. In the periodic box case the two-point correlation is estimated as

$$\xi(r) = \frac{DD(r)}{RR(r)} - 1, \tag{2.6}$$

with the random pair count calculated as

$$RR(r) = n_D^2 \frac{v(r)}{V}, \tag{2.7}$$

where V is the total box volume and $v(r) = \frac{4}{3}\pi((r+dr)^3 - r^3)$ is the volume of a spherical shell of radius *r* and thickness *dr* (Alonso, 2012).

To overcome the effects of redshift space distortions, we then calculate the projected correlation function w_p according to (e.g. Coil, 2013)

$$w_p(r_\perp) = 2\int_0^{R_{\max}} \xi(r_\perp, r_\parallel)dr_\parallel \tag{2.8}$$

for GAMA and using

$$w_p(r_\perp) = 2\int_0^{R_{\max}} \xi\left((r_\perp^2 + y^2)^{1/2}\right)dy \tag{2.9}$$

for the SAMs, where the correlation function is projected along the line-of-sight direction onto the perpendicular separation direction $r_\perp$. In practice this integral is performed to a cutoff distance $R_{\max}$, which we choose to be $25h^{-1}$Mpc. The cutoff distance for the SAMs is dictated by the smallest box size we use; and for consistency we use the same for GAMA. The cutoff distance used has only a small effect on our results, as shown for GAMA in appendix B of Loveday et al. (2018).

However, the use of this integral ignores the effect of residual redshift-space distortions (e.g. van den Bosch et al., 2013), which may bias our results at large radii to be low. This will be degenerate with the integral constraint problem where, due to the small volumes of some of the simulations used, an integral constraint biases the results when calculating the correlation function. The volume integral of the estimator of $\xi(r)$ over the sampled volume is by definition zero, which causes the correlation function to deviate from the true value for small simulation boxes and surveys. To account for this we add the integral constraint I to each estimated $\xi(r)$, where I is the volume integral of $\xi(r)$ out to the maximum correlation distance used.

We estimate the volume integral of the binned correlation function ξ_i in the simulations by

$$I = \frac{\Sigma_i(\xi_i RR_i)}{\Sigma_i RR_i}, \tag{2.10}$$

using random pair counts RR_i (Roche & Eales, 1999).

For the GAMA data, we estimate the integral constraint by assuming that w_p has a power law behaviour. Following (Roche & Eales, 1999), we fit w_p with a function of the form

$$w_p(r_\perp) = Ar_\perp^{-B} - C, \tag{2.11}$$

and add the derived value of C to the projected correlation to estimate the true correlation.

2.4 Stellar mass functions and luminosity functions

2.4.1 Stellar mass function

We show in Fig. 2.3 the comparison between the SMFs of the SAMs we have run. Uncertainties, given by the standard deviation between 8 subsamples in each simulation, are seen to be highest for the runs on the SURFS L40N512 simulation, as expected from the small box size.

We only show the L-GALAXIES–Millennium SMF for its range of validity, $\mathcal{M}_\star > 10^9 h^{-2}\mathrm{M}_\odot$, where it provides a reasonable match to GAMA data. This is a reflection of the previous MCMC tuning of L-GALAXIES to combined datasets including the Baldry et al. (2012) SMF used here, although the SAM prediction is slightly below the observational results at masses around $10^{10.7}h^{-2}\mathrm{M}_\odot$. L-GALAXIES–Millennium-II is shown across the full mass range, and we note that the curve is similar to the one produced when running L-GALAXIES on the SURFS L40N512 box, which has a similar resolution. These two simulations have halo mass functions which drop below Millennium at a similar mass, $\log_{10}(\mathcal{M}_{\mathrm{subhalo}}/h^{-1}\mathrm{M}_\odot) \approx 13.5$, as shown in Fig. 2.1, resulting in a similar deviation in SMF. SHARK fits the GAMA data within uncertainties across most of the mass range shown, which is expected as it has been tuned by hand using the SURFS simulations, although on SURFS L210N1536, SHARK produces slightly more of the most massive galaxies than are seen in Baldry et al. (2012). This is due to tuning, as the Wright et al. (2017) SMF used to tune SHARK slightly exceeds the Baldry et al. (2012) SMF at the high-mass end.

At the high mass end it is clear that L-GALAXIES produces fewer galaxies than SHARK when both are run on the SURFS simulations. This implies that, for the same halo mass,

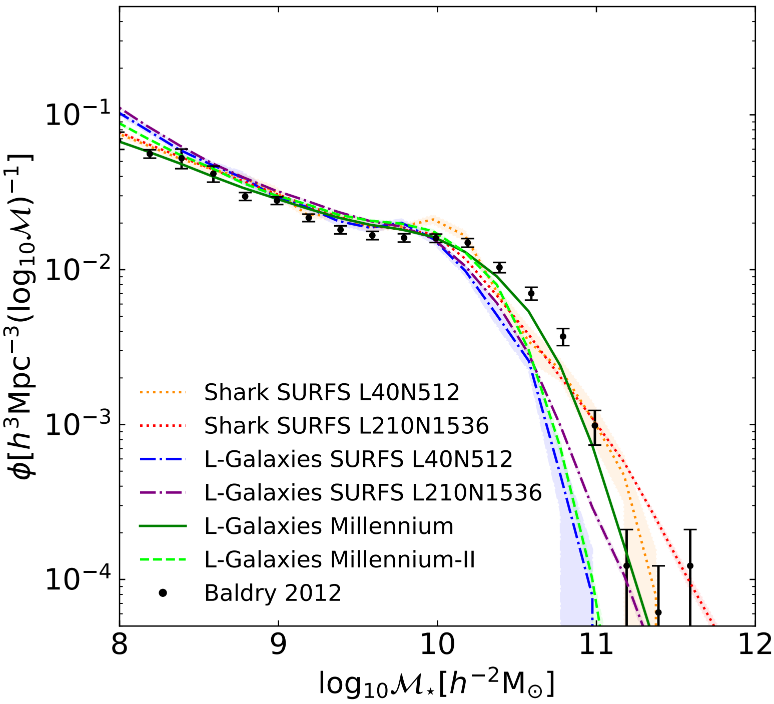

Figure 2.3: Comparison of the SMF from the SAMs at redshift zero. We show L-GALAXIES run on the Millennium (green solid), Millennium-II (lime dashed), SURFS L40N512 (blue dot dashed) and SURFS L210N1536 (purple dot dashed) simulations. SHARK runs on the SURFS L40N512 and SURFS L210N1536 simulations are shown with orange and red dotted lines respectively. Uncertainties are estimated by the standard deviation between 8 subboxes. GAMA results from Baldry et al. (2012) are shown in black.

SHARK produces higher mass galaxies than L-GALAXIES. Considering that the SURFS L40N512 box in particular is under-representative of massive haloes, it is perhaps to be expected that SAMs based on it cannot replicate the high mass end of the SMF. This would imply the masses of the galaxies formed by L-GALAXIES are more accurate.

Some deviation is seen at the low mass end as well. However, this is again likely to be predominantly due to tuning. SHARK is tuned to the GAMA SMF of Wright et al. (2017), which is very similar to the Baldry et al. (2012) values shown here at the low mass end. However, a combined dataset additionally including SDSS data from Baldry et al. (2008) and Li & White (2009) is used for tuning L-GALAXIES, and this dataset displays the upturn below $10^9 h^{-2}\mathrm{M}_\odot$ seen in the L-GALAXIES runs here.

2.4.2 Luminosity functions

We compare LFs produced by the simulations against GAMA LFs from Driver et al. (2012). Uncertainties are computed as the standard deviation between 8 subsamples, as with the SMF. We measure LFs in the GALEX *FUV* and *NUV* ultra-violet bands, SDSS *ugriz* bands and the UKIDSS *YJHK* infra-red bands, and show a selection of these in Fig. 2.4.

In the infra-red UKIDSS *YJHK* bands, accurate predictions are made by all the models

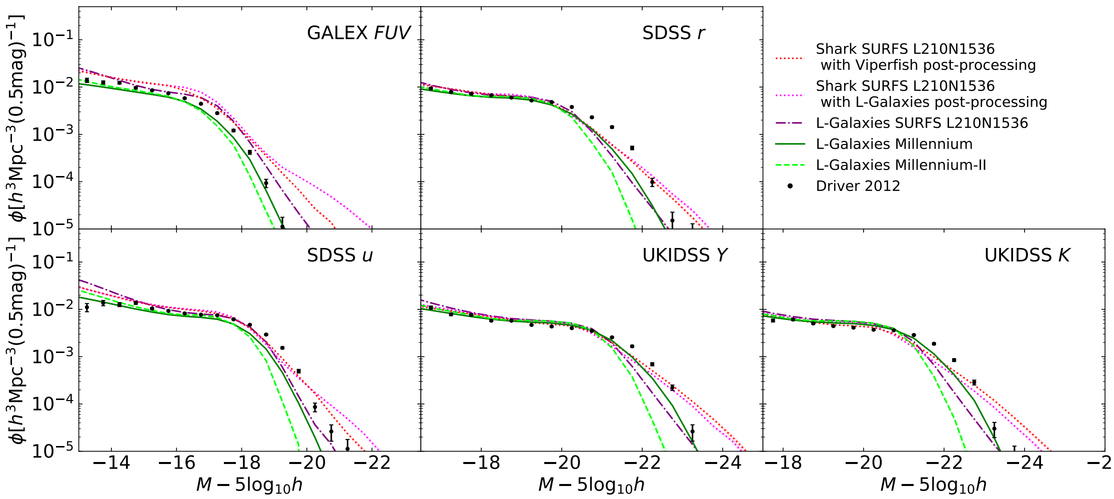

Figure 2.4: Comparison of the LFs at redshift zero in a selection of the available GAMA bands between L-GALAXIES running on the Millennium (green solid), Millennium-II (lime dashed) and SURFS L210N1536 (purple dot dashed) simulations, and SHARK running on the SURFS L210N1536 simulation, post-processed using VIPERFISH (red dotted) or the methods of L-GALAXIES (magenta dotted). GAMA data from Driver et al. (2012) is shown as black points.

except for the brightest galaxies. K-band luminosity is known to be closely correlated with stellar mass at low redshifts and so the level of agreement merely reflects that the models have been tuned to reproduce the SMF.

Moving down in wavelength to the SDSS *riz*-bands, the agreement between each model and the GAMA data remains fairly consistent, except L-GALAXIES–Millennium slightly under-predicts the numbers of the brightest galaxies. These trends continue moving into the SDSS u-band except for an increasing density of bright galaxies relative to GAMA seen in the models run on the SURFS L210N1536 box.

Then in the GALEX bands, both SAMs predict a greater number density of brighter galaxies from SURFS L210N1536 than is present in GAMA. As L-GALAXIES–Millennium matches GAMA well, this may suggest later halo growth in SURFS L210N1536 than Millennium, leading to a greater number of bright, young stars. The over-prediction of the number densities of galaxies in the *FUV* band by SHARK matches the conclusions of Lagos et al. (2019), although our results slightly exceed the values shown there due to different parameter values and we see over-prediction across almost the entire magnitude range shown.

We have found the LFs from SHARK to be nearly identical in all bands, whether using VIPERFISH or the post-processing methods of L-GALAXIES, except at short wavelengths. Fig. 2.4 shows a small difference in the u band at the brightest end and then an increased difference in the *FUV* at the brightest end. The similarity across most bands is surprising, as while both SAMs have dust models based around Charlot & Fall (2000), the parametrisation is performed differently. However, one effect of the dust models is visible, as they will alter the absorption of short wavelengths and consequently be part of the cause of differences in the *FUV*.

Table 2.3: Halo mass bins and limits (column 1) for the SMFs and LFs split by halo mass. Columns 2 and 3 give mean redshifts and mean halo masses for the GAMA samples of VM20. Columns 4–6 give mean halo masses for our matched samples at the corresponding redshifts. The halo mass bins used for GAMA differ slightly from those of the SAMs, and these are listed below the table.

Halo mass range	Redshift	Mean halo mass ($\log_{10}\mathcal{M}_h[h^{-1}\mathrm{M}_\odot]$)			
($\log_{10}\mathcal{M}_h[h^{-1}\mathrm{M}_\odot]$)		GAMA	L-GALAXIES MR + MRII	L-GALAXIES L210N1536	SHARK L210N1536
$[12.8, 13.3]^\dagger$	0.12	13.03	13.00	13.00	13.00
$[13.3, 13.7]$	0.19	13.50	13.47	13.47	13.47
$[13.7, 14.1]$	0.26	13.88	13.86	13.85	13.85
$[14.1, 14.8]^\ddagger$	0.32	14.37	14.29	14.28	14.27

GAMA halo mass ranges differ to give similar mean masses: † $[12.0, 13.3]$; ‡ $[14.1, 15.2]$

The difference in the short wavelength bands between the post-processing methods may also be a problem related to the star formation histories, as the *FUV* band in particular is dependent on the binning of star formation histories near the output redshift. The greater number of snapshots in the SURFS simulations compared to Millennium should be beneficial for this, but it is possible that the snapshot subdivision used in L-GALAXIES at low redshifts is specifically tuned to Millennium. It may also imply that our approximation of dividing the star formation uniformly across the bins when changing the binning scheme is overly simplistic. However, the similarity of the two post-processing methods across the other bands validates the use of the L-GALAXIES post-processing method with SHARK.

2.4.3 SMFs and LFs in haloes

When calculating the SMF and LF for galaxies in haloes of different masses, we use only the larger L210N1536 box of the SURFS simulations, as there are too few large haloes in the L40N512 box. Similarly, instead of using Millennium and Millennium-II separately, we use Millennium for galaxies with $\log_{10}(\mathcal{M}_\star/h^{-2}\mathrm{M}_\odot) > 9.5$ and $M_r - 5\log_{10} h < -19.5$, and Millennium-II otherwise. We make comparisons here against the GAMA results of VM20 using the four halo mass bins given in Table 2.3, and the SMF of L-GALAXIES with Millennium and Millennium-II was also incorporated into VM20. We report here the trends in the fitting parameters, and give the tables of parameter values in Appendix 2.A for direct comparisons. We note that we assume the covariance matrices of the SMFs and LFs are diagonal, which may cause biased parameter estimates (see Smith, 2012), but that this is consistent with the method used in VM20.

2.4.3.1 SMF trends

The SMFs show the expected pattern of centrals at typically higher masses than satellites, seen in Fig. 2.5. The centrals are well fit by log-normal functions for L-GALAXIES on Millennium and Millennium-II, but both SAMs on SURFS L210N1536 show some deviation, with central galaxies present at lower masses than expected. As low mass

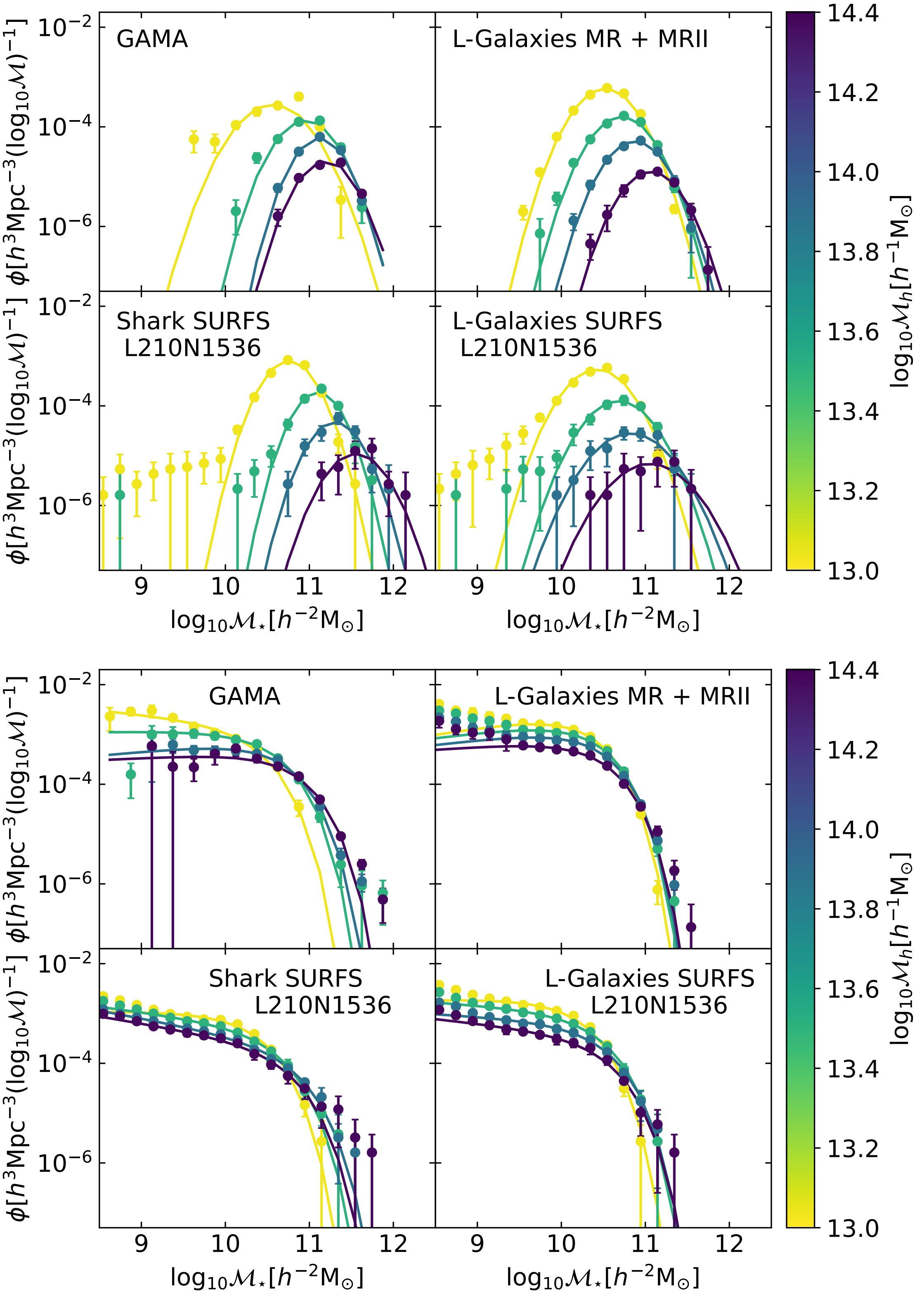

Figure 2.5: SMFs of galaxies split by halo mass for L-GALAXIES and SHARK, with GAMA data from VM20. Central galaxies with log-normal fits are shown in the upper panel and satellite galaxies with Schechter fits are shown in the lower panel. For clarity we only plot bins containing 2 or more galaxies.

central galaxies are found in both SAMs for SURFS and some central galaxies are not the most massive galaxy in their halo we suggest that the central subhalo and the growth history of it have in some cases been misidentified when making the merger trees.

The parameter values for the log-normal fits to the central galaxies in both SAMs show a clear increase in M_c, as seen in the GAMA (VM20) results. No trend in σ_c is seen for the SAMs in contrast to a broadening at low halo masses in GAMA. Similar parameter values are found for L-GALAXIES on both halo catalogues, although with large uncertainties on SURFS L210N1536, and these reasonably agree with the observations. On the other hand, SHARK shows enhanced values of the characteristic mass M_c compared to GAMA, caused by the tendency of SHARK to populate low-mass haloes with higher mass galaxies which we noted in Section 2.4.1.

The simulated satellites are poorly fit by the Schechter fits, as these drop too fast at the high stellar mass end and do not show the upturn in the L-GALAXIES SMF at low masses. However, if these fits are used, L-GALAXIES shows little variation in fit except an increased amplitude in low mass haloes, in contrast to GAMA where the characteristic mass increases in line with halo mass. On the other hand, SHARK agrees much better with GAMA, showing a characteristic mass that increases for more massive haloes.

2.4.3.2 LF trends

The LFs all show that within each halo mass bin, brighter galaxies are generally centrals and fainter galaxies satellites, as shown in Fig. 2.6. All the simulations have central galaxy LFs that are reasonably well-fit by a log-normal distribution, but they all show an excess of fainter centrals relative to the fit.

The parameter trends for central galaxies are similar to those seen for SMFs, particularly SHARK which again shows a shift to brighter (and more massive) galaxies relative to GAMA. L-GALAXIES LFs have similar characteristic magnitudes to GAMA but are wider, This is partly driven by a weaker relation between stellar mass and luminosity in L-GALAXIES, but there could also be effects due to the use of luminosity-based halo mass estimates in GAMA, perhaps with insufficient scatter between halo mass and central galaxy luminosity.

Schechter functions for satellite galaxy LFs give reasonable fits for L-GALAXIES but under-predict the number of bright galaxies for SHARK. Both SAMs display a trend for an increase in characteristic magnitude and a slight decrease in faint-end slope α with increasing halo mass. Particularly in the higher mass bins, the faint end slope in the SAMs disagrees with GAMA.

2.4.3.3 Summary of halo-dependent SMFs and LFs

For both the SMFs and LFs for galaxies split by halo mass, we see similar best-fit parameters in L-GALAXIES for both the Millennium and SURFS halo catalogues. This helps validate the use of L-GALAXIES on simulations other than Millennium by showing that the masses of galaxies formed are not heavily influenced by the particular N-body simulation used. It also further demonstrates that the lack of massive galaxies

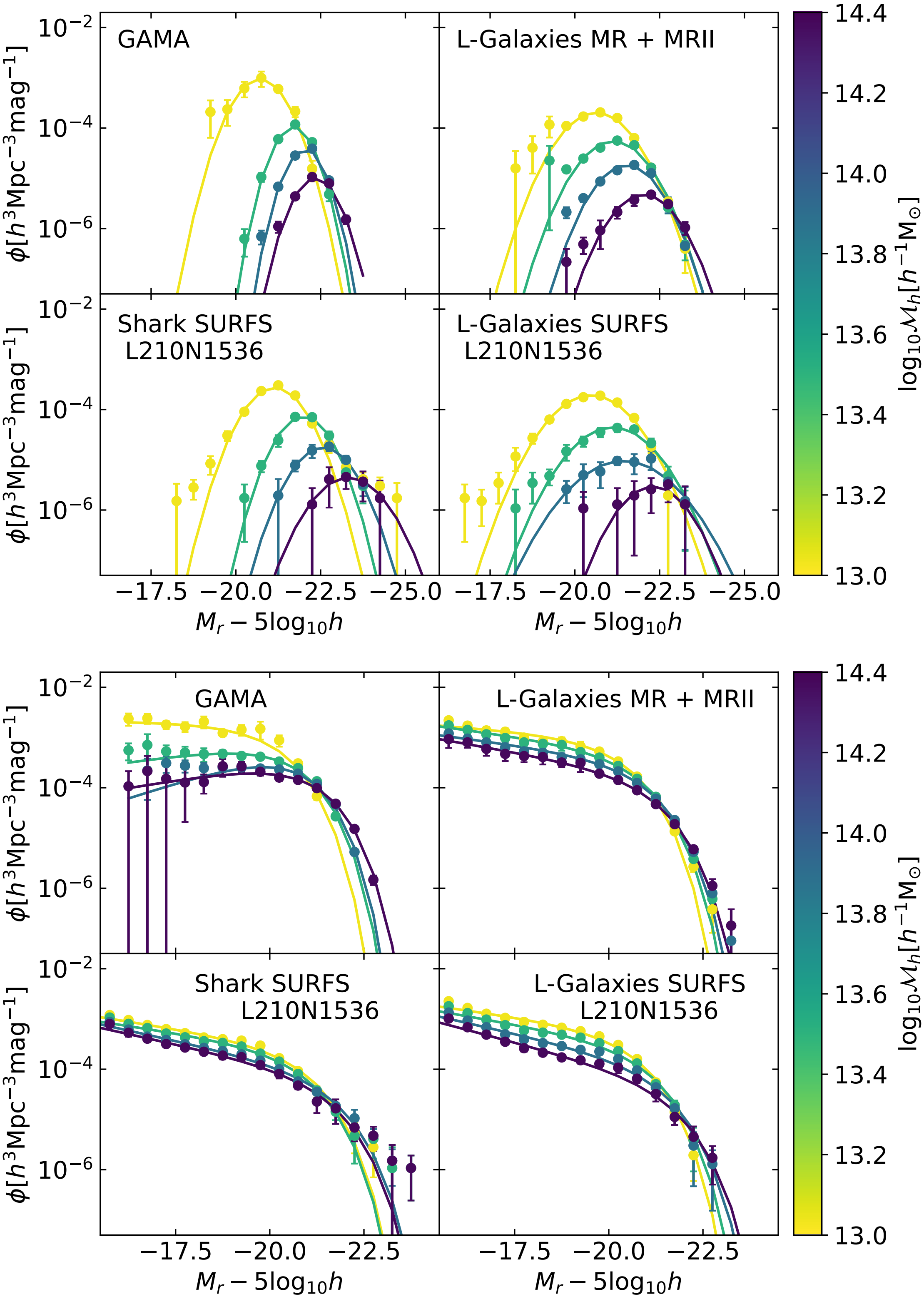

Figure 2.6: r-band LFs of galaxies split by halo mass for L-GALAXIES and SHARK, with GAMA data from VM20. Central galaxies with log-normal fits are shown in the upper panel and satellite galaxies with Schechter fits are shown in the lower panel. For clarity we only plot bins containing 2 or more galaxies.

in the SMF from L-GALAXIES run on the SURFS boxes is due to the boxes being under-representative of massive haloes, and not due to the SAM.

We have found that the modified Schechter fits used for satellite galaxies in the GAMA data are non-optimal for both SAMs. This is due to greater numbers of massive satellite galaxies being predicted by the SAMs compared with GAMA. Further exploration of this may determine whether the SAMs overproduce massive satellites, or if this is an observational bias against massive galaxies, such as the effects of different photometric methods considered in Bernardi et al. (2016, 2017).

2.5 Projected correlation function

2.5.1 Galaxy auto-correlation functions

We compare projected correlation functions against GAMA in four bins of stellar mass and of luminosity, considering for each simulation the snapshot closest to the mean redshift of the GAMA sample for the bin. Here we calculate uncertainties by jackknife between 8 subsamples. For SHARK we use the luminosities calculated with the L-GALAXIES post-processing, although very similar results are expected from the VIPERFISH post-processing. While the *r*-band luminosity functions produced in these bins by the two post-processing methods are almost identical, we use the L-GALAXIES post-processing method here as it gives a fairer comparison by minimising any post-processing aspect of differences in the correlation functions between the SAMs.

Calculating the projected two-point correlation function in stellar mass bins, as shown in Fig. 2.7, all models are seen to reproduce the general trends of the GAMA data. In the three higher mass bins, bins ($9.5 < \log_{10}\mathcal{M}_{\star}[h^{-2}\mathrm{M}_{\odot}] < 11.0$), all simulations display a power law; in the lowest mass bin they all show a change in slope around 0.5 h^{-1}Mpc, approximately the size of a typical group.

L-GALAXIES produces very similar projected correlation functions running on Millennium and Millennium-II, except at small scales in the two higher stellar mass bins, where the stellar mass function begins to drop off for Millennium-II. A reasonable match to GAMA is seen, except in the two higher mass bins the slope appears to be too steep. When running on SURFS L210N1536, L-GALAXIES shows similar results to those on Millennium-II except for the smallest scales in the higher mass bins, where a reduced correlation is seen, which better matches the GAMA results.

The behaviour at separations of a few h^{-1}Mpc is similar with SHARK and L-GALAXIES running on SURFS L210N1536, supporting the idea that correlations at these scales are dependent on the underlying haloes. However, SHARK shows a reduced correlation, mainly at short distances, implying that the distribution of galaxies within haloes differs from L-GALAXIES. In the higher mass bins this brings SHARK into better agreement with GAMA than is seen for L-GALAXIES.

In luminosity bins, shown in Fig. 2.8, the models appear to perform less well than in stellar mass bins, except for the case of L-GALAXIES running on SURFS L210N1536, which at around 0.1 h^{-1}Mpc matches the data within uncertainties in all of these bins.

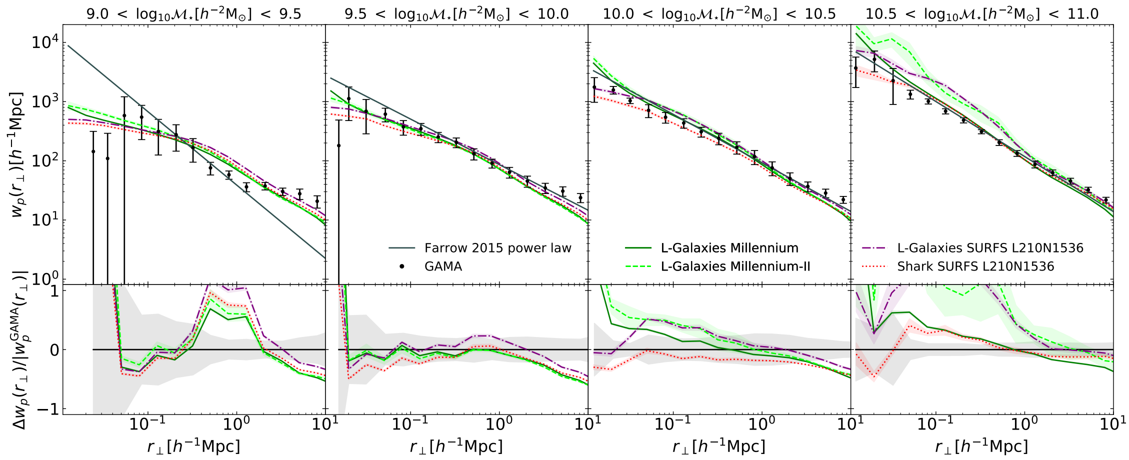

Figure 2.7: The upper panels show the projected two-point correlation function in different stellar mass bins for L-GALAXIES running on the Millennium (green solid), Millennium-II (lime dashed) and SURFS L210N1536 (purple dot dashed) simulations, and SHARK running on the SURFS L210N1536 simulation (red dotted). GAMA results are shown as black points and the power law fits of Farrow et al. (2015) are shown in grey. Note that in the $9.0 < \log_{10}(\mathcal{M}_\star/h^{-2}\mathrm{M}_\odot) < 9.5$ bin we show the power law for a wider bin of $8.5 < \log_{10}(\mathcal{M}_\star/h^{-2}\mathrm{M}_\odot) < 9.5$. The lower panels show the ratio of the simulation correlation functions against the GAMA results in the corresponding upper panel.

This difference in performance between mass- and luminosity-dependent clustering is perhaps indicative of an environmental dependence to the relationship between galaxy stellar masses and luminosities that is not included in the SAM post-processing.

In magnitude bins between $M_r - 5\log_{10} h = -21$ and $M_r - 5\log_{10} h = -19$, SHARK is seen to underestimate clustering on all scales. A similar underestimation is also seen in L-GALAXIES when running on Millennium and Millennium-II in these bins. The results for Millennium and Millennium-II are similar except in the brightest bin, but the difference between these and L-GALAXIES–SURFS L210N1536 must be attributed to the construction of the halo catalogue or the approximations made about the orphan satellites without most-bound particles in SURFS L210N1536.

2.5.2 Central and satellite clustering

In order to understand the differences in the correlation functions, we focus on two mass bins, and compare some of the higher resolution simulations, namely SHARK running on SURFS L210N1536 with L-GALAXIES running on SURFS L210N1536 and on Millennium-II. The bins considered are those with stellar masses between $10^{9.5}h^{-2}\mathrm{M}_\odot$ and $10^{10.5}h^{-2}\mathrm{M}_\odot$.

We show in Fig. 2.9 the contributions to the projected two-point correlation function broken down by central and satellite galaxies: the central and satellite auto-correlation functions and the central–satellite cross-correlation, all divided by the overall galaxy auto-correlation function. The cross-correlation is calculated with CORRFUNC (Sinha & Garrison, 2019, 2020).

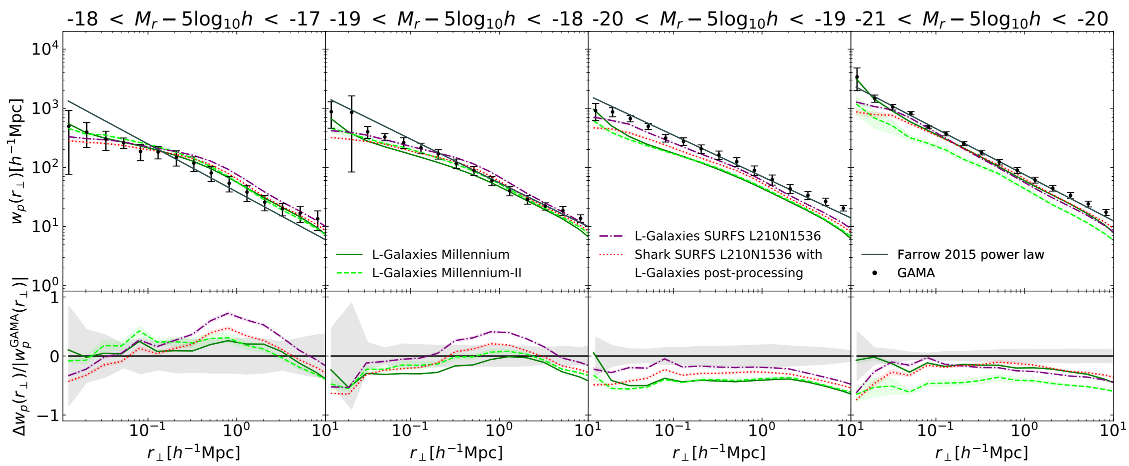

Figure 2.8: The upper panels show the projected two-point correlation function in different luminosity bins for L-GALAXIES running on the Millennium (green solid), Millennium-II (lime dashed) and SURFS L210N1536 (purple dot dashed) simulations, and SHARK running on the SURFS L210N1536 simulation (red dotted). GAMA results are shown as black points and the power law fits of Farrow et al. (2015) are shown in grey. The lower panels show the ratio of the simulation correlation functions against the GAMA results in the corresponding upper panel.

These terms can be connected to the halo model of clustering. The central auto-correlation function contains only two-halo clustering, and is closely related to the clustering of the underlying host haloes themselves. On small scales the central–satellite cross-correlation shows one-halo clustering and is related to the distribution of satellite galaxies in groups, while on larger scales it will contain two-halo terms and is the main contribution to the group–galaxy cross-correlation. However, the satellite auto-correlation is less easily expressed in these terms, as on small scales it is indicative of any exclusion limiting the proximity of satellites in groups, but on large scales it will also contain two-halo terms.

The contributions we plot are scaled by the fractions of centrals and satellites, as

$$w_{GG} = f_C^2 w_{CC} + 2 f_C f_S w_{CS} + f_S^2 w_{SS}, \tag{2.12}$$

where w_{ii} is the auto-correlation of galaxies (G), centrals (C) or satellites (S), w_{CS} is the cross-correlation between centrals and satellites, and f_i is the fraction of centrals or satellites. In Fig. 2.9 the top row shows $f_C^2 w_{CC}$, the middle row $f_S^2 w_{SS}$ and the bottom row $2 f_C f_S w_{CS}$.

We also show on the figure the satellite fractions for each of the simulations within each bin. We see that SHARK produces consistently fewer satellites than L-GALAXIES and we note that L-GALAXIES produces a slightly greater satellite fraction when running on Millennium-II than on SURFS L210N1536. We have also observed that both SAMs running on SURFS produce some galaxies labelled as satellites that are not associated with a central, meaning that the true satellite fractions are lower than the stated values. This is a greater problem for haloes with less massive galaxies, so has only a very

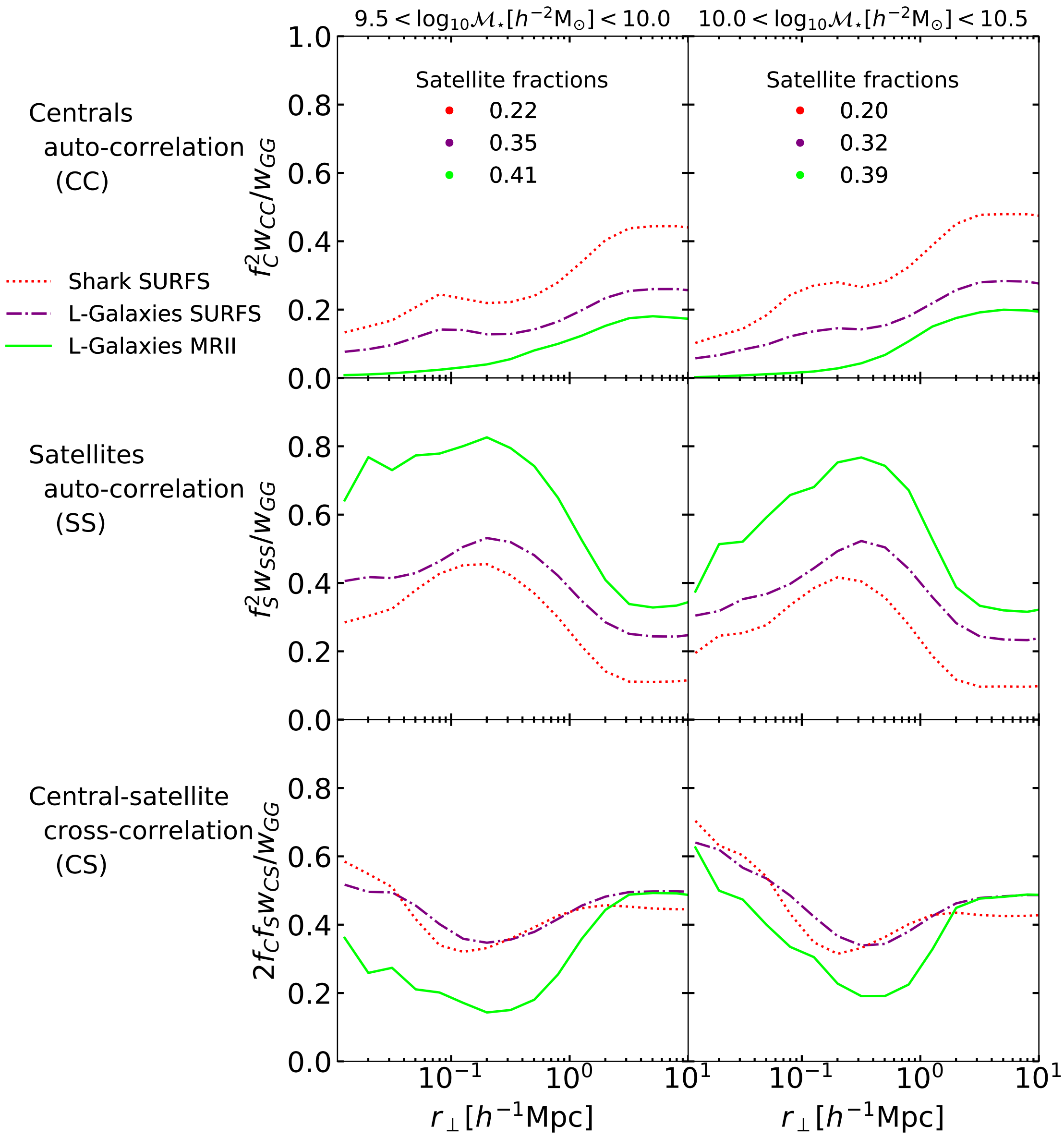

Figure 2.9: Comparison of the projected two-point correlation function between L-GALAXIES running on SURFS L210N1536 (purple dot dashed) and Millennium-II (lime solid), and SHARK running on SURFS L210N1536 (red dotted), broken down into the contributions from centrals and satellites. Two bins selected by stellar mass are shown. The upper panels shows the central galaxy auto-correlations (CC), middle panels show the auto-correlation of satellite galaxies (SS) and the lower panels show the cross-correlation of centrals and satellites (CS). Each line has been multiplied by the central or satellite fractions as described in the text and divided by the total correlation function to show the relative contribution. Satellite fractions are shown in the upper panels, colour-coded by simulation.

small effect in the bins considered here. The cause of this is misidentification of the central subhalo in a group by the halo finder. In some cases, a subhalo hosting a galaxy previously identified as a central becomes a satellite of a halo which has not had time to evolve a central galaxy, therefore producing an isolated satellite galaxy. Note that these are not the same as the orphan satellite galaxies we discuss elsewhere; orphan satellites have no associated dark matter subhalo within their host halo while these isolated satellites have host haloes with no stellar mass at the centre.

The satellite fractions help to highlight some of the differences between the correlation functions. The auto-correlations of central galaxies are seen to be much lower when running L-GALAXIES on Millennium-II than on SURFS L210N1536 in all bins. It therefore seems surprising that the overall correlation function is very similar to that of the other simulations, as we see that in most bins the Millennium-II galaxy auto-correlation function depends almost entirely on the satellite galaxies. In all bins we see that SHARK produces a greater contribution from central galaxy auto-correlations when running on SURFS L210N1536, but this is due to the satellite fraction differences, as the amplitudes of the central galaxy auto-correlations are very similar for the two SAMs running on SURFS L210N1536. This is expected, as larger central galaxies should be formed in the same haloes of the simulation. This means that the differences in the galaxy auto-correlation functions from SURFS L210N1536 must be driven by the differences in satellite galaxy modelling between the SAMs.

The contribution from satellite auto-correlations is always seen to be greater for L-GALAXIES than SHARK, and the domination of satellites on scales $r_\perp \lesssim 1h^{-1}\mathrm{Mpc}$ shows these are responsible for the differences in overall correlation function. At increasing separation, the contribution from the satellites decreases, leaving only the effects of the centrals in different haloes, and, by association, the halo catalogue.

2.5.3 Satellite profiles

To understand the differences in satellite galaxy clustering, we compare the distribution of satellites within haloes. For this we use the SURFS L210N1536 box and Millennium-II for the better resolution they offer. We follow the method of Pujol et al. (2017), but divide by the total number of galaxies to account for the different volumes used:

$$n(r/R_{\mathrm{vir}}) = \frac{N_r}{(4\pi/3)[(r/R_{\mathrm{vir}} + \Delta(r/R_{\mathrm{vir}}))^3 - (r/R_{\mathrm{vir}})^3]N_{\mathrm{tot}}}. \quad (2.13)$$

Here, $n(r/R_{\mathrm{vir}})$ is the satellite profile in radial annular bin from r/R_{vir} to $r/R_{\mathrm{vir}} + \Delta(r/R_{\mathrm{vir}})$, N_r is the number of galaxies in the annulus, R_{vir} is the virial radius of the halo and N_{tot} is the total number of galaxies. The virial radii are calculated from the halo masses, $\mathcal{M}_{\mathrm{halo}}$, from the simulation outputs as $R_{\mathrm{vir}} = (3\mathcal{M}_{\mathrm{halo}}/(4\pi\Delta_{\mathrm{vir}}\rho_c))^{1/3}$, where ρ_c is the critical density, and the overdensity used is $\Delta_{\mathrm{vir}} = 200$.

We show these profiles for the orphan Type 2 galaxies in Fig. 2.10. We show only the Type 2 galaxies as the orbital distances of other satellites (Type 1s) are defined by the subhalo positions and therefore show little difference between the SAMs run on the same

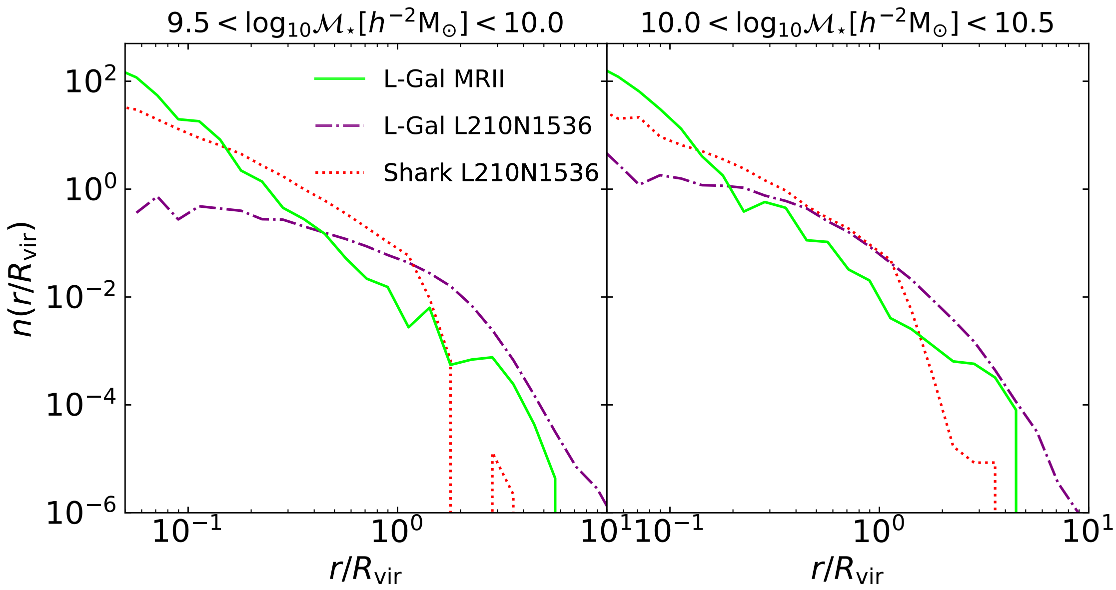

Figure 2.10: Orphan satellite galaxy profiles for L-GALAXIES running on SURFS L210N1536 (purple dot dashed) and Millennium-II (lime solid), and SHARK running on SURFS L210N1536 (red dotted). The profiles shown correspond to the mean density of Type 2 galaxies within haloes as a function of the virial radius of the halo.

halo catalogue.

It can be seen that the orphan satellite profiles for SHARK cut off just above the virial radius in all the selected bins, in contrast to L-GALAXIES which shows Type 2 galaxy profiles that extend to larger radii, both when running on Millennium-II and SURFS. This difference in number and position of the orphan satellites suggests that the satellite fraction differences can be partly attributed to differences in the modelling of orphan satellite orbits, and that the assumption made in SHARK that the orphans follow the NFW profile does not match the more detailed model options in L-GALAXIES. This will then contribute to the differences in correlation functions.

Additionally, it can be seen that within the virial radius both SAMs show slightly reduced orphan satellite profiles when running on SURFS L210N1536 compared to L-GALAXIES on Millennium-II, with both SAMs on SURFS showing a slope change around the virial radius, while L-GALAXIES–Millennium-II displays a profile close to a power law. The main reason for the differences between L-GALAXIES run on the two simulations will be the different methods of tracking the satellites, due to only having most-bound particle positions for Millennium-II. The similarity of the L-GALAXIES profiles at the largest radii plotted suggests the orphans are originating at the same radii (although the positions are instantaneously doubled without most-bound particles) but the different shapes closer to the centre show the subsequent evolution is different with and without most-bound particle orbits. However, profile differences are also likely to be impacted by differences in simulation resolution and halo finder, which will change the mass and location at which a galaxy becomes an orphan.

These differences in projected clustering and satellite profiles depend heavily on

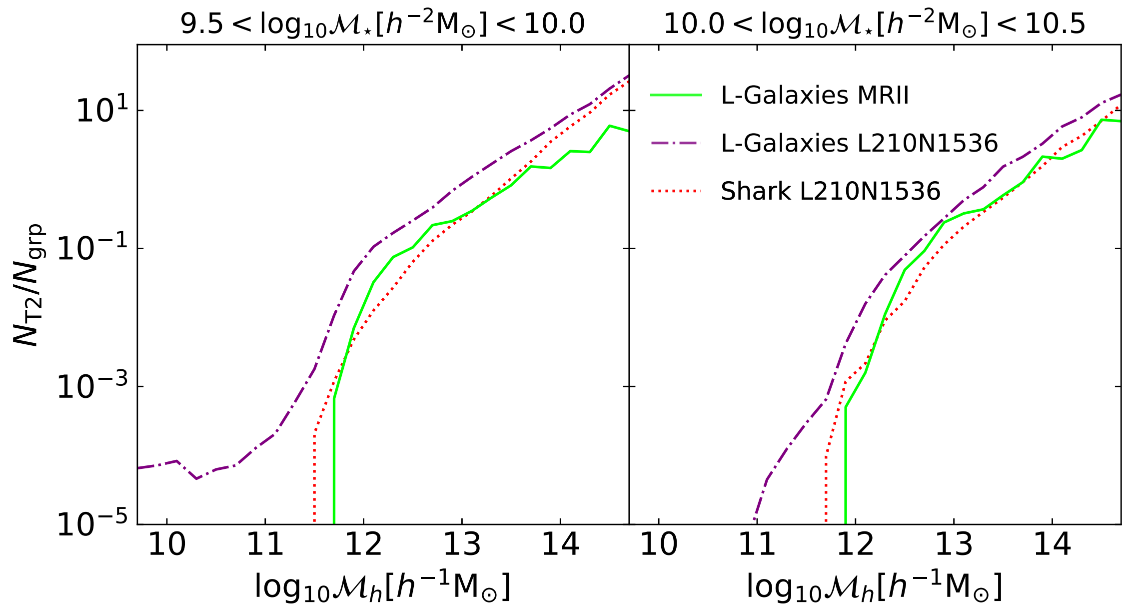

Figure 2.11: Comparison of the halo occupation of orphan satellites between L-GALAXIES running on SURFS L210N1536 (purple dot dashed) and Millennium-II (lime solid), and SHARK running on SURFS L210N1536 (red dotted).

orbital position, so such measurements will be a useful tool to look at the physics affecting satellite galaxies. In particular, it may be possible to use clustering and radial profiles to constrain the dynamical friction that causes satellite orbits to decay, moving the satellites towards the centre of haloes, and the timescales of the resulting galaxy mergers.

2.5.4 Occupation numbers

Finally, we consider the halo occupation of orphan satellites in Fig. 2.11, again using the SURFS L210N1536 and Millennium-II boxes. The occupation number as a function of mass is calculated as the number of galaxies in haloes of a given mass divided by the total number of haloes of that mass in the dark matter simulation. This is complementary to our earlier examination of the SMFs and r-band LFs as a function of halo mass in Section 2.4.3, but focussing on the orphan satellites.

It is seen that L-GALAXIES running on SURFS produces more satellites in low mass haloes than the other simulations. Their absence in SHARK appears to be part of the cause of the lower satellite fraction produced, and may be responsible for the enhanced characteristic masses of satellites seen in Section 2.4.3. It is surprising that the satellite occupation numbers for SHARK in lower mass haloes are consistently very close to those of L-GALAXIES with Millennium-II, given the different halo mass functions and distinct satellite profiles and correlation functions they produce.

2.6 Alterations to orphan galaxy modelling

To further investigate the differences we see in the Type 2 satellites between L-GALAXIES and SHARK, we try implementing the orbital decay model from L-GALAXIES in SHARK. To do this we record the position and dynamical friction time of orphan galaxies at the point the merger clock is started and at any output snapshots move the satellite radially from the starting position by a factor $2\times\sqrt{1-\delta t/t_{\rm df}}$, where δt is the time since the galaxy became an orphan and $t_{\rm df}$ is the initial dynamical friction time. Note that this does not change any of the internal physics of SHARK; we are simply changing the locations of the orphan satellites in the outputs.

Clustering and radial profiles for this modification are shown in Fig. 2.12. Very little change occurs to the clustering, although there is a fractional increase on the smallest scales. The radial profiles show a greater change but comparison to the profiles from L-GALAXIES in Fig. 2.10 explains why this does not lead to clustering amplitude changes. The change of the orphan galaxy positions causes the radial profiles to become more extended, but without the flattening of the inner profile seen in L-GALAXIES. We attribute this to the environmental disruption of satellites close to the centre in L-GALAXIES, which does not occur in SHARK, and also the inclusion in the orphan population of L-GALAXIES of galaxies where the stellar mass has exceeded the dark matter mass. The flatter and more extended profiles of L-GALAXIES suggest the loss of some galaxies at small radii due to disruption, and that the extra orphan condition causes galaxies to become orphans further out in haloes.

The different orphan criteria will have some impact on the numbers of orphans present, but the dramatically reduced number of satellites in SHARK compared to L-GALAXIES shown in Fig. 2.9 suggests the orphans are also merging too fast in SHARK. To explore this, we try changing the `tau_delay` parameter in SHARK when running on SURFS L210N1536. This is a constant prefactor $f_{\rm df}$ in the merger time used for an orphan satellite galaxy in SHARK, based on the merger time formula of Lacey & Cole (1993). Changing this parameter is also justified by the results of van Daalen et al. (2016), who find the merger time has a large effect on clustering in L-GALAXIES, and it is reasonable to assume the same will be the case in SHARK. For our test we increase the value of this parameter from 0.1 to 0.9, selecting this value as being at the opposite end of the range suggested in Lagos et al. (2018).

Increasing the merger time parameter means the number of orphan satellites at low redshifts increases. Central galaxy masses will also be slightly altered as there have been fewer mergers to add mass to both them and their central black hole. This causes a slight increase in the mass function at masses below $10^{10}h^{-1}\mathrm{M}_{\odot}$, and a clear increase in the small-scale clustering, as shown in the upper part of Fig. 2.12. This brings the clustering closer to that of L-GALAXIES, but does not make much impact on the level of agreement with GAMA.

These simple modifications to SHARK demonstrate the strength of the dependence of clustering on only minor changes to the modelling of the orphan satellites. Improvements in the clustering predictions of SAMs therefore requires a much better understanding of

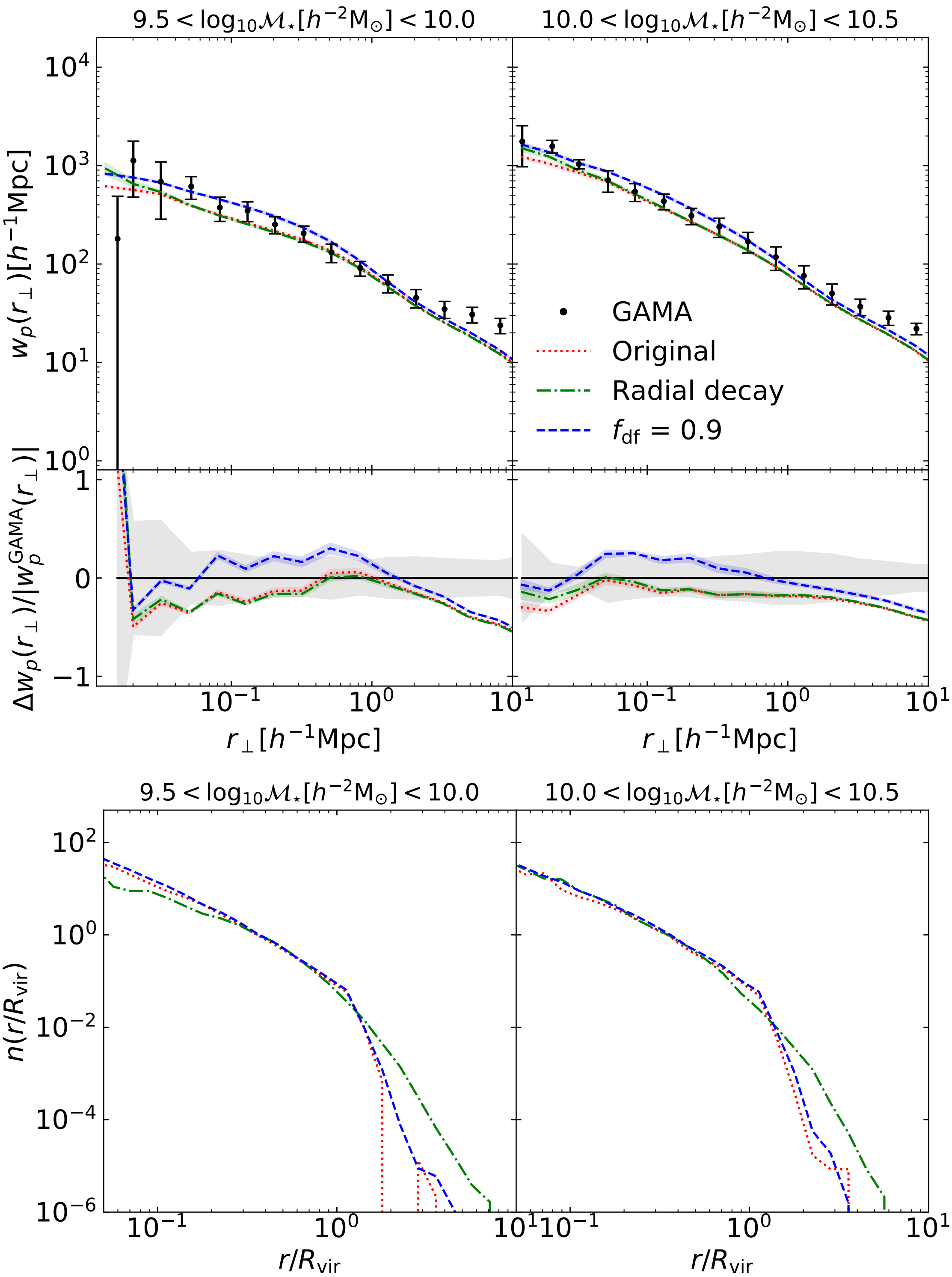

Figure 2.12: Comparison of SHARK running on SURFS L210N1536 (red dotted) with two minor modifications, altering the positions of orphan galaxies based on the merging time (green dot dashed) and changing the merger time scaling factor f_{df} to 0.9 (blue dashed). The upper panels show the projected correlation functions in two bins of stellar mass and the ratios of the projected correlations to GAMA. The lower panels show the radial profiles of orphan satellites in the same stellar mass bins.

the effects of the baryons in galaxies on the positions and infall timescales of satellite galaxies.

2.7 Conclusions

We have compared the semi-analytic galaxy formation models L-GALAXIES and SHARK, and have examined whether they can reproduce the observed SMF, *FUV* to *K*-band LFs and projected two-point correlation functions. We have run SHARK on the SURFS L40N512 and L210N1536 simulations and L-GALAXIES on SURFS L40N512, SURFS L210N1536, Millennium and Millennium-II. We compared the SAMs against the Galaxy and Mass Assembly (GAMA) survey which is highly complete even in high-density regions, and offers improvements upon previous surveys for considering small-scale clustering.

Our main results are as follows:

- The galaxy SMF is accurately reproduced by both SAMs on their native simulation, which is expected as they have been tuned to do so. However, when running on identical simulations, SHARK produces a greater number of galaxies than L-GALAXIES at the high mass end. This is due to the SURFS simulations that SHARK is built on having fewer massive haloes than the Millennium simulation on which L-GALAXIES is based.

- We compared LFs in 11 bands from far ultra-violet to near infra-red and found they differ most between the SAMs at short wavelengths, with SHARK predicting too many bright galaxies in the ultra-violet bands of GALEX. This appears to be partly related to the halo catalogue as L-GALAXIES also has slightly too many bright galaxies when running on the SURFS simulations.

- We have directly compared the methods used by the SAMs to produce luminosities by running both VIPERFISH and the post-processing routines of L-GALAXIES on star formation histories from SHARK. The two methods are seen to produce almost identical results across the 11 bands we have considered, except at the brightest end of the *FUV* band. This consistency over many bands is unexpected given differences in dust modelling parametrisation.

- SMFs and *r*-band LFs for galaxies split by host halo mass show similar trends to GAMA but differ in detail. In particular the SAMs contain more faint and low mass galaxies for a given halo mass than GAMA.

- SHARK generally underestimates the projected two-point correlation function on small scales relative to GAMA, both when binning galaxies by stellar mass and luminosity. At projected separations below 1 h^{-1}Mpc, L-GALAXIES always shows a greater clustering amplitude than SHARK when both are run on SURFS.

- The choice of halo catalogue has a significant effect on the clustering results, mainly above 0.5 h^{-1}Mpc. While higher resolution probes halo interiors with more confidence, the construction of the halo catalogues appears to be a more important factor for clustering, as we found differences in the clustering between L-GALAXIES running on the Millennium and SURFS simulations with similar resolutions.

- Scales smaller than those affected by the halo catalogue are dependent on the astrophysics in the SAMs, with some cross-over in effects on scales between 0.5 and 2 h^{-1}Mpc; we have found the small-scale clustering to be most clearly dependent on the dynamics of orphan satellite galaxies that have lost their subhaloes, supporting the conclusions of Pujol et al. (2017).

The presence of orphan satellites is a result of using N-body simulations without baryons, rather than a true physical effect, but these galaxies have a physical meaning as they are the ones which are allowed to merge with their central by the SAMs. L-GALAXIES produces a much larger fraction of orphan satellites than SHARK, leading to enhanced predictions of galaxy clustering on small scales, where the contribution from satellite auto-correlations is greater. We have also observed that the orphan satellite radial distribution around haloes in SHARK truncates just above the virial radius, whereas in L-GALAXIES orphans are found further out. This is a result of different models for the satellite locations, and will also influence small-scale clustering. However, we have shown that simply incorporating the model for orphan positions in L-GALAXIES into SHARK does not produce the same profiles and clustering, highlighting that the definition of when a galaxy becomes an orphan and the inclusion of environmental effects are also important components of the modelling.

Making use of small-scale clustering will therefore be useful in understanding the physics of galaxy mergers, including looking at dynamical friction timescales that cause the galaxies to spiral inwards. In an initial attempt to make use of this, we have lengthened the time taken for orphan satellites to merge with their central galaxy in SHARK. This increases the small-scale clustering amplitude, and also increases the fraction of galaxies that are orphan satellites. However, improving orphan satellite modelling further would require incorporating an enhanced model for their positions, which we leave for future work.

To improve the fitting of L-GALAXIES to GAMA, adjusting the star formation rates may be required to adjust the relative strengths of mass and luminosity dependent correlation functions. Further changes are likely to focus on the parameters affecting the orphan satellite galaxies but would be best fit using an MCMC approach, similar to that in van Daalen et al. (2016).

We conclude that the L-GALAXIES and SHARK semi-analytic models compare reasonably well, but not perfectly, with GAMA observations. There is room for improvement, particularly around the modelling of orphan satellite galaxies.

Appendices

2.A Halo-dependent SMF and LF fit parameters

We present on the following pages the parameter values of our best fits to SMFs and LFs for galaxies split by host halo mass for L-GALAXIES and SHARK. We also include the parameter values for GAMA from VM20. These fits use the functions described in Section 2.4.3, and the uncertainties given are non-marginalised 1-sigma errors. Mass bins $\mathcal{M}$1–4 are given in Table 2.3.

Table 2.4: Log-normal fits to the SMFs of central galaxies.

	M_c	σ_c	$\log_{10}\phi^{\star}_c$	χ^2/ν
		GAMA		
$\mathcal{M}1$	10.56 ± 0.03	0.30 ± 0.02	-3.54 ± 0.04	$28.5/7$
$\mathcal{M}2$	10.95 ± 0.01	0.25 ± 0.01	-3.84 ± 0.04	$13.2/5$
$\mathcal{M}3$	11.12 ± 0.01	0.22 ± 0.01	-4.20 ± 0.03	$3.5/3$
$\mathcal{M}4$	11.19 ± 0.01	0.24 ± 0.01	-4.67 ± 0.03	$9.5/3$
		L-GALAXIES MR + MRII		
$\mathcal{M}1$	10.52 ± 0.00	0.26 ± 0.00	-3.22 ± 0.00	$70.1/7$
$\mathcal{M}2$	10.72 ± 0.01	0.26 ± 0.00	-3.78 ± 0.01	$20.1/8$
$\mathcal{M}3$	10.87 ± 0.01	0.25 ± 0.01	-4.27 ± 0.02	$6.7/9$
$\mathcal{M}4$	11.07 ± 0.02	0.25 ± 0.02	-4.88 ± 0.04	$2.2/5$
		L-GALAXIES L210N1536		
$\mathcal{M}1$	10.42 ± 0.01	0.28 ± 0.01	-3.26 ± 0.02	$37.5/16$
$\mathcal{M}2$	10.68 ± 0.03	0.29 ± 0.02	-3.89 ± 0.05	$9.6/17$
$\mathcal{M}3$	10.82 ± 0.06	0.33 ± 0.04	-4.54 ± 0.08	$3.0/13$
$\mathcal{M}4$	11.06 ± 0.16	0.34 ± 0.12	-5.15 ± 0.21	$1.0/7$
		SHARK L210N1536		
$\mathcal{M}1$	10.76 ± 0.01	0.23 ± 0.01	-3.08 ± 0.02	$24.0/20$
$\mathcal{M}2$	11.10 ± 0.02	0.21 ± 0.01	-3.70 ± 0.05	$6.8/12$
$\mathcal{M}3$	11.30 ± 0.03	0.23 ± 0.02	-4.31 ± 0.09	$2.4/9$
$\mathcal{M}4$	11.55 ± 0.07	0.26 ± 0.07	-4.95 ± 0.20	$1.3/6$

Table 2.5: Schechter function fits to the SMFs of satellite galaxies.

	$\log_{10}M^{\star}$	α	$\log_{10}\phi^{\star}_s$	χ^2/ν
		GAMA		
$\mathcal{M}1$	10.31 ± 0.04	-1.16 ± 0.09	-3.17 ± 0.07	$7.4/7$
$\mathcal{M}2$	10.51 ± 0.04	-0.98 ± 0.09	-3.27 ± 0.05	$5.2/9$
$\mathcal{M}3$	10.61 ± 0.03	-0.84 ± 0.09	-3.45 ± 0.05	$9.0/9$
$\mathcal{M}4$	10.77 ± 0.04	-0.91 ± 0.11	-3.68 ± 0.06	$22.5/9$
		L-GALAXIES MR + MRII		
$\mathcal{M}1$	10.24 ± 0.01	-0.72 ± 0.02	-2.88 ± 0.01	$33.6/9$
$\mathcal{M}2$	10.32 ± 0.01	-0.79 ± 0.02	-3.04 ± 0.01	$24.2/9$
$\mathcal{M}3$	10.36 ± 0.01	-0.80 ± 0.02	-3.20 ± 0.01	$25.3/10$
$\mathcal{M}4$	10.42 ± 0.02	-0.88 ± 0.03	-3.44 ± 0.02	$27.5/10$
		L-GALAXIES L210N1536		
$\mathcal{M}1$	10.15 ± 0.03	-0.96 ± 0.06	-3.03 ± 0.04	$12.6/8$
$\mathcal{M}2$	10.37 ± 0.05	-1.12 ± 0.05	-3.35 ± 0.06	$2.9/9$
$\mathcal{M}3$	10.43 ± 0.06	-1.10 ± 0.07	-3.57 ± 0.08	$1.9/9$
$\mathcal{M}4$	10.47 ± 0.08	-1.18 ± 0.08	-3.83 ± 0.10	$2.7/10$
		SHARK L210N1536		
$\mathcal{M}1$	10.29 ± 0.04	-0.99 ± 0.06	-3.31 ± 0.05	$6.9/8$
$\mathcal{M}2$	10.53 ± 0.06	-1.22 ± 0.06	-3.66 ± 0.07	$3.2/10$
$\mathcal{M}3$	10.74 ± 0.08	-1.31 ± 0.07	-4.00 ± 0.11	$3.9/10$
$\mathcal{M}4$	10.67 ± 0.14	-1.28 ± 0.09	-4.03 ± 0.15	$5.1/12$

Table 2.6: Log-normal fits to the LFs of central galaxies.

	M_c	σ_c	$\log_{10}\phi_c^\star$	χ^2/ν
		GAMA		
$\mathcal{M}1$	-20.71 ± 0.08	0.55 ± 0.04	-3.01 ± 0.06	3.9/5
$\mathcal{M}2$	-21.70 ± 0.02	0.43 ± 0.01	-3.95 ± 0.03	2.5/3
$\mathcal{M}3$	-22.03 ± 0.02	0.41 ± 0.01	-4.39 ± 0.03	8.6/3
$\mathcal{M}4$	-22.35 ± 0.02	0.47 ± 0.02	-4.97 ± 0.03	3.5/2
		L-GALAXIES MR + MRII		
$\mathcal{M}1$	-20.63 ± 0.01	0.73 ± 0.01	-3.68 ± 0.01	24.9/9
$\mathcal{M}2$	-21.13 ± 0.02	0.71 ± 0.02	-4.25 ± 0.01	38.2/10
$\mathcal{M}3$	-21.52 ± 0.03	0.66 ± 0.02	-4.73 ± 0.02	25.3/7
$\mathcal{M}4$	-22.03 ± 0.07	0.67 ± 0.05	-5.31 ± 0.03	8.5/6
		L-GALAXIES L210N1536		
$\mathcal{M}1$	-20.48 ± 0.04	0.83 ± 0.03	-3.71 ± 0.03	12.3/17
$\mathcal{M}2$	-21.11 ± 0.07	0.85 ± 0.05	-4.35 ± 0.04	7.8/17
$\mathcal{M}3$	-21.43 ± 0.16	1.00 ± 0.11	-5.02 ± 0.07	1.9/12
$\mathcal{M}4$	-22.31 ± 0.29	0.70 ± 0.21	-5.52 ± 0.19	1.8/10
		SHARK L210N1536		
$\mathcal{M}1$	-21.14 ± 0.02	0.62 ± 0.02	-3.55 ± 0.02	40.3/20
$\mathcal{M}2$	-22.00 ± 0.04	0.56 ± 0.03	-4.12 ± 0.04	7.5/15
$\mathcal{M}3$	-22.57 ± 0.07	0.63 ± 0.06	-4.74 ± 0.07	0.8/9
$\mathcal{M}4$	-23.33 ± 0.27	0.73 ± 0.22	-5.34 ± 0.15	0.5/5

Table 2.7: Schechter function fits to the LFs of satellite galaxies.

	$M^\star$	α	$\log_{10}\phi_s^\star$	χ^2/ν
		GAMA		
$\mathcal{M}1$	-19.98 ± 0.13	-1.02 ± 0.11	-2.68 ± 0.10	9.7/8
$\mathcal{M}2$	-20.32 ± 0.08	-0.73 ± 0.10	-3.01 ± 0.04	11.2/9
$\mathcal{M}3$	-20.36 ± 0.05	-0.38 ± 0.08	-3.15 ± 0.02	18.9/0
$\mathcal{M}4$	-20.83 ± 0.05	-0.68 ± 0.08	-3.38 ± 0.02	6.9/11
		L-GALAXIES MR + MRII		
$\mathcal{M}1$	-20.20 ± 0.03	-1.14 ± 0.03	-2.99 ± 0.02	20.5/11
$\mathcal{M}2$	-20.56 ± 0.04	-1.25 ± 0.03	-3.24 ± 0.02	6.6/12
$\mathcal{M}3$	-20.75 ± 0.05	-1.24 ± 0.03	-3.43 ± 0.02	7.5/13
$\mathcal{M}4$	-21.01 ± 0.07	-1.32 ± 0.04	-3.71 ± 0.04	4.7/13
		L-GALAXIES L210N1536		
$\mathcal{M}1$	-20.51 ± 0.06	-1.26 ± 0.02	-3.23 ± 0.03	24.8/12
$\mathcal{M}2$	-20.83 ± 0.09	-1.32 ± 0.03	-3.49 ± 0.04	32.8/12
$\mathcal{M}3$	-21.22 ± 0.14	-1.42 ± 0.03	-3.88 ± 0.08	25.1/13
$\mathcal{M}4$	-21.51 ± 0.20	-1.49 ± 0.05	-4.21 ± 0.11	11.8/13
		SHARK L210N1536		
$\mathcal{M}1$	-20.76 ± 0.10	-1.29 ± 0.03	-3.54 ± 0.05	25.3/12
$\mathcal{M}2$	-20.73 ± 0.12	-1.28 ± 0.04	-3.59 ± 0.06	10.1/13
$\mathcal{M}3$	-21.46 ± 0.20	-1.40 ± 0.04	-4.04 ± 0.10	10.7/13
$\mathcal{M}4$	-21.41 ± 0.37	-1.41 ± 0.06	-4.10 ± 0.16	9.6/13

3

Galaxy and Mass Assembly (GAMA): the clustering of galaxy groups

S. D. Riggs, R. W. Y. M. Barbhuiyan, J. Loveday,
S. Brough, B. W. Holwerda, A. M. Hopkins, S. Phillipps

Abstract

We explore the clustering of galaxy groups in the Galaxy and Mass Assembly (GAMA) survey to investigate the dependence of group bias and profile on separation scale and group mass. Due to the inherent uncertainty in estimating the group selection function, and hence the group auto-correlation function, we instead measure the projected group–galaxy cross-correlation function. We find that the group profile has a strong dependence on scale and group mass on scales $r_\perp \lesssim 1\,h^{-1}$ Mpc. We also find evidence that the most massive groups live in extended, overdense, structures. In the first application of marked clustering statistics to groups, we find that group-mass marked clustering peaks on scales comparable to the typical group radius of $r_\perp \approx 0.5\,h^{-1}$ Mpc. While massive galaxies are associated with massive groups, the marked statistics show no indication of galaxy mass segregation within groups. We show similar results from the IllustrisTNG simulations and the L-Galaxies model, although L-Galaxies shows an enhanced bias and galaxy mass dependence on small scales.

3.1 Introduction

In the standard hierarchical model of galaxy formation, galaxies form in gravitationally collapsed dark matter (DM) haloes which grow by merging with other haloes (e.g. Press & Schechter, 1974; White & Rees, 1978). Consequently, the relative density of observable matter (δ_g, such as galaxies, galaxy groups and galaxy clusters) in a given volume of space is believed to trace the relative density of dark matter, δ_m, in that same space. In the linear bias model $\delta_g = b\delta_m$, where b is known as the *bias* parameter, which will in general be a function of the tracer population, separation scale, and redshift. This linear bias has previously been shown to increase with halo mass (e.g. Mo & White, 1996; Sheth & Tormen, 1999; Sheth et al., 2001; Seljak & Warren, 2004; Tinker et al., 2005).

A direct way to explore the connection between galaxies and their DM haloes is with galaxy group catalogues. The total mass of individual haloes can be estimated using the galaxy motions within them (e.g. Girardi et al., 1998; Eke et al., 2006; Robotham et al., 2011), or by scaling relations based on the luminosity or mass of their constituent galaxies (e.g. Yang et al., 2007; Han et al., 2015; Viola et al., 2015). The galaxy distribution within haloes can be explored directly by group stacking (e.g. Budzynski et al., 2012) or with group–galaxy clustering (e.g. Wang et al., 2008; Mohammad et al., 2016). Group clustering probes intermediate scales compared to the typical galaxy- and galaxy cluster-scales used in most clustering studies, and can be combined with galaxy- and dark matter-clustering to extract estimates of bias.

The mass and colour dependence of the clustering and bias of galaxy groups was investigated for SDSS Data Release 4 (Adelman-McCarthy et al., 2006) by Wang et al. (2008). They found that the clustering strength of groups increases with increasing total group mass and also that groups of comparable mass are more strongly clustered when they contain redder galaxies. Similar results from SDSS were found in the earlier study by Berlind et al. (2006), where a sharp increase in group–galaxy clustering is observed within the typical group scale compared to larger scales. Further, group–galaxy clustering is observed to decrease slightly on scales $r_\perp \lesssim 0.3\,h^{-1}$ Mpc, possibly suggesting the existence of group cores, although clustering measurements on these scales are sensitive to the choice of group centre, a point we discuss further in Section 3.5.1. An increase in clustering strength with increasing group mass has also been shown at slightly higher redshifts using the zCOSMOS survey (Lilly et al., 2007) by Knobel et al. (2012).

While there is a general consensus in previous work on the group clustering increase with group mass at large scale, the details on small scales are less constrained. A key aspect to this is the dependence of the positions of galaxies within groups on the properties of the satellite galaxies. Mass segregation, a tendency for more massive galaxies to be closer to the group centre, is found by, e.g., Presotto et al. (2012); Roberts et al. (2015), but other studies (e.g. von der Linden et al., 2010; Kafle et al., 2016) find no trend in stellar mass with radial distance from group centre. The presence or absence of mass segregation helps constrain the strength of dynamical friction effects within haloes, as satellites infall at large radii (Wetzel et al., 2013) and then move inwards due to dynamical friction.

Standard two-point clustering measurements can be expanded on using marked statistics (Stoyan & Stoyan, 1994; Beisbart & Kerscher, 2000; Sheth & Tormen, 2004; Sheth et al., 2005; Skibba et al., 2006; Harker et al., 2006; White & Padmanabhan, 2009; White, 2016). These have been used to explore the environmental dependence of clustering, with Skibba et al. (2013) finding that small-scale clustering is dependent on local density, and Sheth & Tormen (2004) showing that close pairs of haloes form earlier. Armijo et al. (2018) show that galaxy clustering has an increasing dependence on halo mass on smaller scales. However, this method has not to our knowledge previously been applied to the exploration of group clustering.

The Galaxy and Mass Assembly (GAMA; Driver et al. 2009, 2011; Liske et al. 2015) survey provides an opportunity to reassess the clustering of galaxy groups. GAMA has a smaller area than SDSS, but provides spectroscopic redshifts two magnitudes fainter (Hopkins et al., 2013), and is highly complete, even in the high-density environments of galaxy groups. We thus expect the GAMA group catalogue to be more reliable than group catalogues constructed from SDSS data, and to allow the exploration of group clustering on much smaller scales. The clustering of GAMA galaxies has been shown to increase with luminosity and mass by Farrow et al. (2015). The dependency of galaxy clustering in GAMA on galaxy properties has been explored with marked correlation functions by Gunawardhana et al. (2018) and Sureshkumar et al. (2021), finding that specific star formation rate best traces interactions, and stellar mass best traces environment. Within GAMA groups, Kafle et al. (2016) find negligible mass segregation for satellites. Recently, Vázquez-Mata et al. (2020, hereafter VM20) explored the stellar masses and r-band luminosities of galaxies in GAMA groups, finding brighter and more massive galaxies in more massive groups.

In this paper, we present group–galaxy cross-correlation functions from the GAMA survey; exploring their dependence on scale and group mass. We consider both the large, inter-group, scales which can be compared to results from SDSS, and the smaller, intra-group, scales that are opened up with the high completeness of GAMA. The group–galaxy cross-correlation contains different information in these two scale ranges. On large scales it informs us of the relationship between groups and the underlying matter distribution, while on small scales it contains information about the radial distribution of satellite galaxies within the groups. We further examine the mass and scale dependencies we find by presenting the first application of marked correlations to group clustering. We also compare these correlation functions to results from the IllustrisTNG hydrodynamical simulations (Marinacci et al., 2018; Naiman et al., 2018; Nelson et al., 2018, 2019a; Pillepich et al., 2018b; Springel et al., 2018) and the L-GALAXIES semi-analytic model (Henriques et al., 2015).

The layout of this paper is as follows: in Section 3.2 we describe the data selection from the GAMA survey, mock catalogues and models we compare against; in Section 3.3 we detail the methods used to derive the two-point correlation functions and marked statistics; in Section 3.4 we present our results; and finally in Sections 3.5 and 3.6 we provide a discussion and conclusions. The cosmology assumed throughout is that of a ΛCDM model with $\Omega_\Lambda = 0.75$, $\Omega_\mathrm{m} = 0.25$, and $H_0 = h100$ km s^{-1}Mpc^{-1}. We represent group (halo) masses on a logarithmic scale by $\lg \mathcal{M}_h \equiv \log_{10}(\mathcal{M}_h/h^{-1}\mathrm{M}_\odot)$, where we take $\mathcal{M}_h$ to be M_{200}, defined by the mass enclosed within an overdensity 200 times the mean density of the Universe.

3.2 Data, mocks, and simulations

The GAMA data and mock catalogues used in this analysis are identical to those used in a recent study of the dependence of the galaxy luminosity and stellar mass functions on the mass of their host groups (VM20), although we select groups and galaxies using different mass and redshift cuts. We summarise the most salient features here.

We make use of the GAMA-II (Liske et al., 2015) equatorial fields G09, G12 and G15, centred on 09h, 12h and 14h30m RA respectively. These fields each have an area of 12×5 degrees, Petrosian magnitude limit of $r < 19.8$ mag, and a completeness greater than 96% for all galaxies which have up to 5 neighbours within 40 arcsec; for a more in-depth description see Liske et al. (2015).

3.2.1 Galaxy sample

It is necessary to use a volume-limited sample of galaxies for cross-correlating with groups, as more massive groups are at higher redshift, where galaxies in a flux-limited sample will be more luminous and therefore more strongly clustered. In other words, using a flux-limited galaxy sample, apparent clustering strength would increase with halo mass, even if there was no dependence of halo bias on mass.

We select a volume-limited sample of 42,679 GAMA-II galaxies which have $(K+e)$-corrected r-band Petrosian magnitude ${}^{0.1}M_r - 5\log_{10} h < -20$ mag, with corresponding redshift limit $z_\mathrm{lim} < 0.267$ and mean number density $n = 5.38 \times 10^{-3}\,h^3\,\mathrm{Mpc}^{-3}$. This corresponds to the 'V0' sample of Loveday et al. (2018, hereafter L18)[1], and is chosen to roughly maximise survey volume and number of galaxies. We choose to define the volume-limited sample by luminosity rather than stellar mass, as (i) the parent sample is magnitude limited, meaning that variations in mass-to-light ratio would require much more stringent cuts on mass than on luminosity, and (ii) estimated stellar mass is inherently more uncertain (and model-dependent) than luminosity.

To account for the different redshifts at which galaxies are observed, the intrinsic luminosities of the GAMA galaxies we use have been corrected by the so-called K-correction (Humason et al., 1956). We obtain K-corrections from the GAMA data management unit (DMU) `kCorrectionsv05`; see Loveday et al. (2015) for details on how these were calculated. We K-correct to a passband blue-shifted by $z = 0.1$ in order to minimise the size, and hence uncertainty, in K-correction. Absolute magnitudes

[1] Attentive readers will notice that here we use a slightly higher redshift limit for the same absolute magnitude limit as L18. This is due to an alternative way of defining a 95 percent complete sample. In L18, we take the 95th-percentile of the K-correction of galaxies within $z_\mathrm{lim} \pm 0.01$. Here we take the 95th-percentile of the projected K-correction $K(z_\mathrm{lim})$ of all galaxies with $z < z_\mathrm{lim}$.

Table 3.1: Definition of volume-limited galaxy samples for GAMA data, mocks, TNG300-1 simulation, and L-GALAXIES SAM. The columns are absolute r-band magnitude limit (K-corrected to redshift 0.1 for GAMA, redshift 0.0 for other samples), redshift limit, sample volume, number of galaxies selected, and mean density. GAMA data and mocks cover areas of 180 and 144 degrees^2 respectively. The mock sample was volume-limited to redshift 0.301 before applying the GAMA redshift limit, leading to a slightly higher final number density. TNG300-1 and L-GALAXIES use periodic boxes, and so are volume-limited by nature. The redshifts we quote for them are those of the output snapshot used.

	$M_{\rm lim}$	$z_{\rm lim}$	V $[10^6\,h^{-3}\,{\rm Mpc}^3]$	$N_{\rm gal}$	$\bar{n}$ $[10^{-3}\,h^3\,{\rm Mpc}^{-3}]$
GAMA	-20.00	0.267	7.93	42,679	5.38
Mock	-20.21	0.267	6.35	34,615	5.45
TNG300-1	-19.83	0.200	8.62	46,349	5.38
L-GALAXIES	-20.12	0.180	110.78	596,023	5.38

in this band are indicated by ${}^{0.1}M_r$. We include luminosity evolution by applying a correction of $+Q_e z$ mag, where $Q_e = 1.0$.

The statistics of the GAMA volume-limited galaxy sample, along with those of the mock catalogue and simulations, are summarised in Table 3.1. The GAMA data, mocks and simulations have galaxies with differing K- and e-corrections, and different luminosity functions, but we only need luminosities in order to generate comparable volume-limited galaxy samples. We therefore choose magnitude limits (shown in the second column of Table 3.1), in order to achieve approximately equal number densities (final column), and hence clustering properties. Note that the GAMA mocks were designed to have a luminosity function very close to that of the GAMA data (R11). The different magnitude limits in Table 3.1 most likely reflect differences in the K- and e-corrections assumed, as well as sample variance in the GAMA data (Driver et al., 2011). For reference, the clustering and stellar mass distribution for our GAMA, mock, and simulated galaxy samples are presented in Appendix 3.A.

3.2.2 GAMA groups

The GAMA Galaxy Group Catalogue (G^{3}Cv9) was produced by grouping galaxies in the GAMA-II spectroscopic survey using a friends-of-friends (FoF) algorithm; this is an updated version of G^{3}Cv1 which was generated from the GAMA-I survey by Robotham et al. (2011, hereafter R11). The FoF parameters used for G^{3}Cv9 (hereafter abbreviated to G^{3}C) are identical to those in R11, but applied to the larger GAMA-II galaxy sample. G^{3}C contains 23,654 groups with 2 or more members and overall $\sim$ 40% of galaxies in GAMA are assigned to G^{3}C groups. In this study, we utilise only those groups within the redshift limit $z < 0.267$ of our volume-limited galaxy sample (Table 3.1), and which have five or more member galaxies, as R11 find these richer groups are most reliable. Reducing the threshold on the number of group members increases the number of low-mass groups, but these groups are very unreliable as chance alignments are increasingly included in the group sample. We also require groups in our sample to

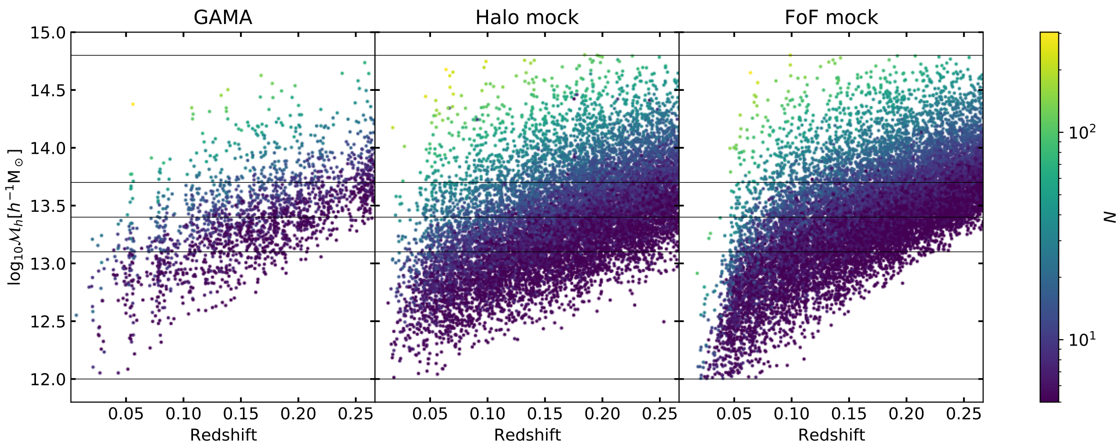

Figure 3.1: Mass–redshift distribution for GAMA and mock groups at $z < 0.267$ with at least 5 members. Groups are colour-coded by the number of group members. The horizontal lines show the division of groups into halo mass bins. Mock groups are shown for all nine realisations of the lightcone.

have `GroupEdge` > 0.9, this removes any where it is estimated that less than 90% of the group is within the GAMA-II survey boundaries. This leaves us with a sample of 1,894 groups with $12.0 < \lg \mathcal{M}_h < 14.8$. We do not attempt to form a volume-limited sample of GAMA groups, as selection effects are complex (see VM20 for a discussion), and to do so would severely limit the number of groups that could be used.

We take the centre of these groups to be the iterative central from R11, found by iteratively removing galaxies from the centre of light until one is left. We choose this as it is found by R11 to be the best estimator of true central, but we discuss the choice of this further in Section 3.5.1.

Halo masses $\mathcal{M}_h$ are estimated from group r-band luminosity (column `LumB`) using the scaling relation for M_{200} of Viola et al. (2015, equation 37), which was calibrated against weak-lensing measurements. The `LumB` column contains total r-band luminosities down to $M_r - 5\log_{10} h = -14$ mag in solar luminosities, corrected by an empirical factor B which has been calibrated against mock catalogues (see R11 section 4.4 for details). The G^{3}C also provides dynamical mass estimates derived via the virial theorem (column `MassA`).

Our choice of luminosity-based mass estimates follows the checks on mass estimate reliability by VM20, who find that the luminosity-based estimates correlate much better with true halo mass than dynamical mass estimates (VM20 Fig. 1).

We show the mass–redshift distribution of our selected GAMA groups in the left-hand panel of Fig. 3.1. Due to the $r < 19.8$ mag flux limit of GAMA-II and our requirement for groups to contain at least 5 members, low-mass groups are less likely to be detected at higher redshifts, and the groups that are detected generally have fewer observed members.

We subdivide the groups into four mass bins as defined in Table 3.2, chosen as a compromise between bins of fixed mass range and comparable group numbers. As seen in VM20, the central galaxy luminosity is greater for more massive groups, with our mass bins $\mathcal{M}1$–4 having central galaxy mean absolute magnitudes of ${}^{0.1}M_r - 5\log_{10} h = -20.48$, -21.12, -21.48, and -21.87 respectively. We note that this means that the $\mathcal{M}1$ centrals have a lower mean luminosity than our volume-limited galaxy sample, which has a mean ${}^{0.1}M_r - 5\log_{10} h = -20.59$, and so the $\mathcal{M}1$ groups are expected to be slightly less clustered than the galaxy sample.

3.2.3 Mock catalogues

We compare our results with predictions from two sets of mock group catalogues for the GAMA-I survey (catalogues updated to the GAMA-II survey are currently being developed). These catalogues were produced using lightcones from the GALFORM (Bower et al., 2006) semi-analytic galaxy formation model run on the Millennium dark matter simulation (Springel et al., 2005). For more details on these mocks we refer the reader to R11.

The first set of mocks are `G3CMockHaloGroupv06`, which we refer to as *halo mocks*. This contains the dark matter haloes in the simulations, with their positions and masses $\mathcal{M}_{\mathrm{Dhalo}}$. The definition of $\mathcal{M}_{\mathrm{Dhalo}}$ differs slightly from M_{200}, but Jiang et al. (2014) and R11 find they are median unbiased relative to each other, so we can use $\mathcal{M}_{\mathrm{Dhalo}}$ as an estimate of M_{200}. The second set of mocks are `G3CMockFoFGroupv06`, which we refer to as *FoF mocks*. The groups in this are generated with the same FoF algorithm as GAMA, and masses $\mathcal{M}_{\mathrm{lum}}$ estimated using the same Viola et al. (2015) luminosity scaling relation. Comparing results from these two mock group catalogues thus allows us to assess the impact on estimated halo clustering of redshift-space group-finding and luminosity-based mass estimation. For halo and FoF mock groups that share a common central galaxy, Fig. 3.2 compares $\mathcal{M}_{\mathrm{lum}}$ with $\mathcal{M}_{\mathrm{Dhalo}}$. The upper panel shows all groups with $N_{\mathrm{FoF}} \geqslant 5$ (and implicitly $N_{\mathrm{halo}} \geqslant 2$ to be counted as a group), while the lower panel shows groups with $N_{\mathrm{FoF}} \geqslant 5$ and $N_{\mathrm{halo}} \geqslant 5$. From the lower panel it is apparent there is reasonable agreement of $\mathcal{M}_{\mathrm{lum}}$ to $\mathcal{M}_{\mathrm{Dhalo}}$ (within one standard deviation) for groups that have sufficient members to be included in our halo catalogue sample. However, it is clear from the upper panel that there is a population of groups which have their membership, and therefore mass, overestimated in the FoF mocks. Through the rest of this work, for consistency with our GAMA selection, we use all groups in the FoF mock with $N_{\mathrm{FoF}} \geqslant 5$, so the groups with overestimated mass are included. In the halo mock we select all groups with $N_{\mathrm{halo}} \geqslant 5$, representing the sample we would have if the FoF group finder perfectly assigned galaxies to groups.

The central and right-hand panels of Fig. 3.1, showing the mass-redshift relation for all selected mock groups, further shows that the luminosity-based masses have a stronger redshift dependence than the true halo masses. The mass overestimation appears to be greater at high redshift. However, at redshifts $z \lesssim 0.04$ the FoF mock groups mostly have low masses, suggesting galaxies are missed from the outskirts of the more extended groups at low redshift. We expect this to imply a similar trend in group mass misestimation with redshift will also be present in the groups from GAMA.

Mock galaxies are taken from the galaxy catalogue associated with the mock

Table 3.2: Group bin names and log-mass limits, number of groups, mean log-mass, and mean redshift for GAMA-II data, intrinsic mock haloes, FoF mock groups, TNG300-1 simulation haloes and L-GALAXIES SAM haloes. Note that the values given for mocks are averages across the 9 realisations used. TNG300-1 and L-GALAXIES are results from single snapshots down-sampled to select groups comparable to GAMA.

		GAMA			Halo Mocks			FoF Mocks			TNG300-1		L-GALAXIES	
	$\lg \mathcal{M}_{h,\mathrm{limits}}$	N	$\overline{\lg \mathcal{M}}$	$\overline{z}$	N	$\overline{\lg \mathcal{M}}$	$\overline{z}$	N	$\overline{\lg \mathcal{M}}$	$\overline{z}$	N	$\overline{\lg \mathcal{M}}$	N	$\overline{\lg \mathcal{M}}$
$\mathcal{M}1$	[12.0, 13.1]	380	12.87	0.10	352	12.86	0.11	346	12.80	0.10	414	12.84	5,276	12.84
$\mathcal{M}2$	[13.1, 13.4]	547	13.26	0.15	383	13.25	0.16	401	13.26	0.15	383	13.25	4,986	13.25
$\mathcal{M}3$	[13.4, 13.7]	566	13.54	0.19	366	13.54	0.19	523	13.55	0.19	405	13.54	5,127	13.55
$\mathcal{M}4$	[13.7, 14.8]	401	13.93	0.20	306	13.97	0.20	430	13.96	0.21	461	13.98	6,263	14.00
Total	[12.0, 14.8]	1,894	13.41	0.16	1,407	13.39	0.17	1,699	13.43	0.17	1,663	13.42	21,652	13.44

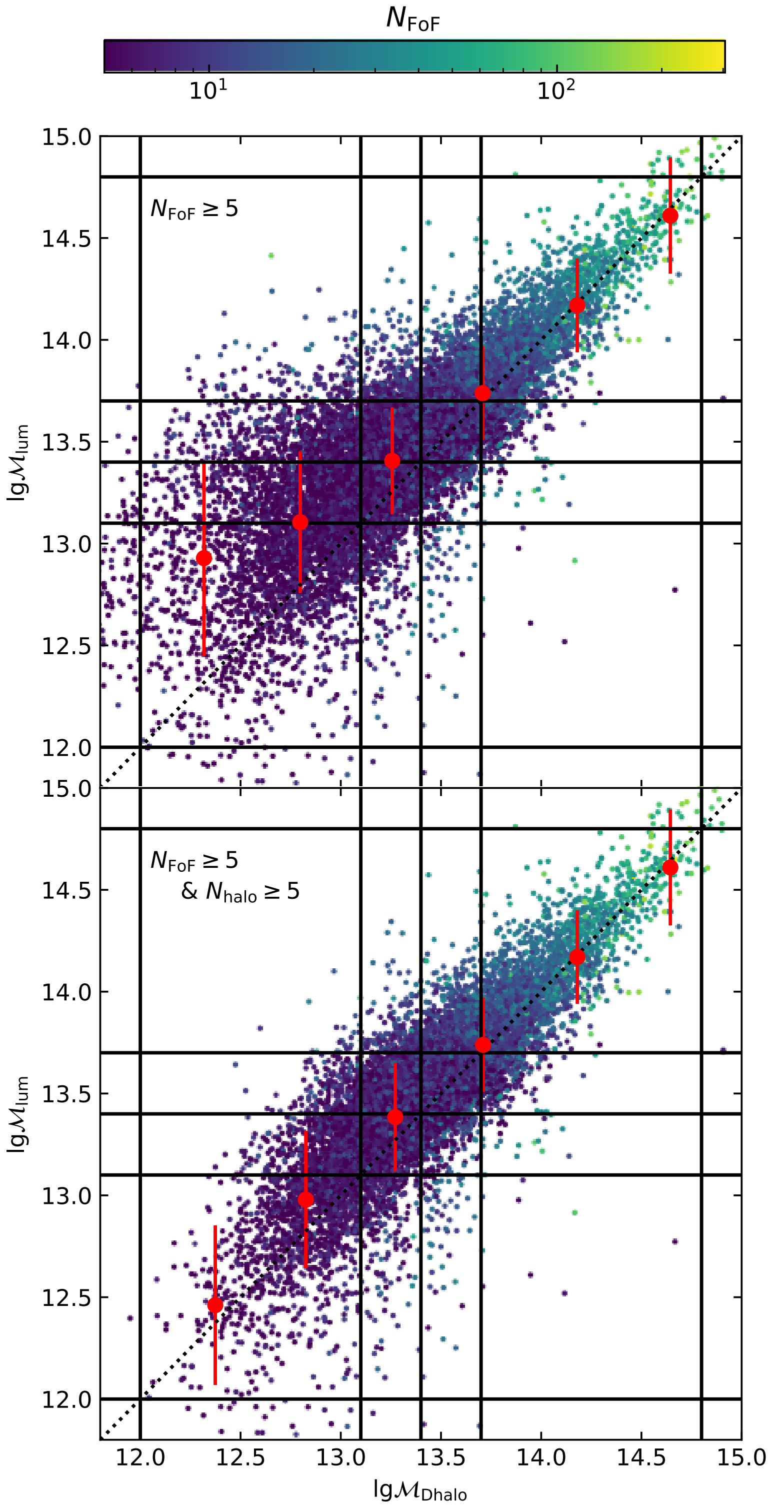

Figure 3.2: Comparison of luminosity-based ($\lg \mathcal{M}_{\mathrm{lum}}$) estimates of mock group mass, against true mock halo mass ($\lg \mathcal{M}_{\mathrm{Dhalo}}$), colour-coded by group membership, for groups at redshifts $z < 0.267$. The upper panels show groups selected by their visibility in the FoF mocks ($N_{\mathrm{FoF}} \geqslant 5$), while the lower panels show only those groups visible in both mocks ($N_{\mathrm{FoF}} \geqslant 5$ and $N_{\mathrm{halo}} \geqslant 5$). The red error-bars show the mean and standard deviation of $\lg \mathcal{M}_{\mathrm{lum}}$ in 0.5 dex bins of $\lg \mathcal{M}_{\mathrm{Dhalo}}$. The horizontal and vertical lines delineate the halo mass bins used in this analysis.

groups we use, `G3CMockGalv06`. We K-correct the absolute magnitudes to redshift zero with the K- and e-corrections specified in section 2.2 of R11. Due to differences with GAMA K- and e-corrections, we set the galaxy magnitude limit by trial-and-error to give approximately the same mean volume-limited number density as the GAMA galaxy sample. This results in a sample with a limiting absolute magnitude ${}^{0.0}M_r - 5\log_{10} h < -20.21$ and limiting redshift $z_{\rm lim} < 0.301$. The typical masses of observed galaxies and groups increase with redshift, and so to ensure that the mock samples are comparable to the observations, we then restrict our mock sample to the GAMA redshift limit of $z_{\rm lim} < 0.267$. The details of our final mock galaxy sample are given in Table 3.1.

We estimate uncertainties on mock clustering from the scatter between nine realisations of the GAMA-I survey equatorial regions. Each of these realisations consists of three 12×4 degrees regions; which are 20 per cent smaller in area (and so also volume) than the equatorial fields we use from GAMA-II. Galaxy stellar masses are not included in these mocks so we cannot explore the dependence of the marked correlation on galaxy mass in the mocks.

3.2.4 Random catalogues

A random sample of points is needed to model any selection effects in the galaxy sample (our choice of cross-correlation estimator in Section 3.3.1 means that the selection function of group samples is not needed). We use the same survey mask described in section 2.3.1 of L18, and generate angular coordinates using MANGLE (Hamilton & Tegmark, 2004; Swanson et al., 2008). Radial coordinates are drawn at random from a uniform distribution in comoving volume with a modulation factor of $10^{0.4Pz}$, the density-evolution factor of Loveday et al. (2015, equation 5), taking $P = 1$. We generate 10 times more random points than galaxies.

In Fig. 3.3 we show galaxy redshift distributions for GAMA, the average across the nine mocks, and random samples (with the number of randoms divided by 10 to match the data samples). The random number counts accurately reproduce the GAMA redshift distribution except for fluctuations due to large-scale structure (c.f. Loveday et al., 2015, Fig. 7).

3.2.5 Comparison models

In addition to comparisons with GAMA mock catalogues, we also compare our results with predictions from the IllustrisTNG hydrodynamical simulations (Marinacci et al., 2018; Naiman et al., 2018; Nelson et al., 2018, 2019a; Pillepich et al., 2018b; Springel et al., 2018) and the Henriques et al. (2015) version of the L-GALAXIES semi-analytic model. For each of these, we select galaxies at a snapshot close to the GAMA mean redshift, selecting $z = 0.20$ in IllustrisTNG and $z = 0.18$ (the closest snapshot to $z = 0.20$) in L-GALAXIES, and set the absolute magnitude limit of the galaxy sample in order to give the same approximate number density as the GAMA volume-limited sample, viz., $n = 5.38 \times 10^{-3}\, h^3\, \mathrm{Mpc}^{-3}$.

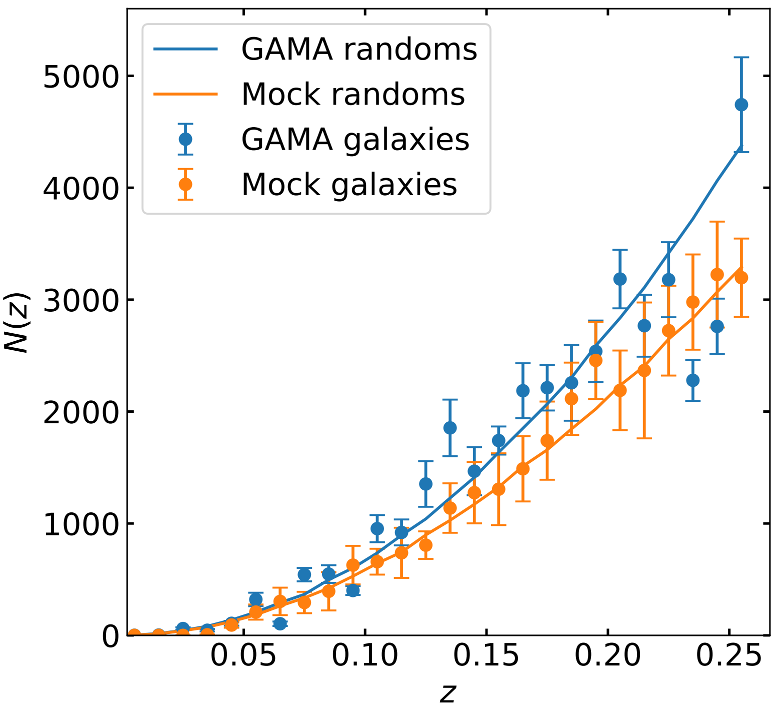

Figure 3.3: Comparison of galaxy redshift distributions for GAMA, the average across the nine mocks, and the random samples. Random counts have been divided by 10 to account for the larger number of random points generated. Uncertainties on GAMA and random counts are found by jackknife between 27 regions in RA, and on the mock counts by the scatter between 9 realisations. The offset in the number of galaxies between GAMA and the mocks is due to the larger area of GAMA (180 degrees^2 compared to 144 degrees^2).

For IllustrisTNG, we use the highest resolution simulation at the largest box-size of 300 Mpc (205 h^{-1} Mpc for $h = 0.6774$), TNG300-1. Haloes are selected by M_{200} (`Group_M_Mean200`) using the mass limits in Table 3.2. For galaxy masses we select the stellar component (type 4) of the `SubhaloMassInRadType` field, which gives the stellar mass within twice the stellar half mass radius. Following the recommendation of Pillepich et al. (2018b), we multiply these by a factor of 1.4, appropriate for haloes in the mass range $12 < \lg \mathcal{M}_h < 15$. We use the dust-corrected luminosities derived from dust model C of Nelson et al. (2018) when selecting the volume-limited galaxy sample.

For L-GALAXIES, we use the Henriques et al. (2015) version with the Millennium (Springel et al., 2005) N-body simulation. Haloes are again selected by M_{200} and the total stellar mass of the galaxies is taken.

To avoid including galaxies below the resolution limits of the TNG300-1 and L-GALAXIES simulations, we select only galaxies with $\log_{10}(\mathcal{M}_\star/\mathrm{M}_\odot) > 9.0$.

To provide comparable group samples, we need to allow for the fact that the periodic-cube (i.e. volume-limited) simulations contain many more low-mass groups than the flux-limited GAMA data and mocks. We describe here our approach to the group selection; in Appendix 3.B we validate our method and demonstrate the consequences of not applying it.

Since we are measuring only group–galaxy cross-correlation functions, we do not require the simulated groups to have an accurate group auto-correlation. Further, while we would ideally create lightcones from the simulated galaxies to provide fair comparisons to GAMA, the mock catalogues already inform us of the potential issues with the GAMA group finding methods, and the creation of lightcones introduces its own uncertainties such as potential duplication of galaxies from the relatively small IllustrisTNG box and the difficulty of interpolating the locations of galaxies between snapshots (e.g. Kitzbichler & White, 2007; Merson et al., 2013). Therefore, rather than attempt to create lightcones from the simulations, we simply down-sample the simulated groups to match the mass distribution of selected GAMA groups. We do this by estimating the probability of finding each halo[2] within the GAMA volume. In our GAMA sample we have set $N_{\rm FoF} \geqslant 5$, and so the halo selection probability is dependent on the fifth brightest galaxy in the halo. To calculate this probability and select simulated groups we use the following procedure for each halo:

1. Identify the absolute magnitude of the fifth brightest galaxy in the halo.
2. Calculate the luminosity distance (and corresponding comoving distance) at which this galaxy would have an observed magnitude of $m_r = 19.8$ mag, the GAMA limit.
3. Calculate the volume of the GAMA lightcone out to this comoving distance.
4. Divide by the total volume of our GAMA sample to get the selection probability.
5. Multiply selection probabilities by 0.95 to account for the use of a 95% complete sample based on *K*-corrections in GAMA (we do not attempt to model *K*-corrections for simulated galaxies).
6. Assign a random number to the halo and include the halo in our sample if this is less than the selection probability.

3.2.6 Comparison of group samples

Statistics for the groups selected in GAMA, the mocks and the comparison models are tabulated in Table 3.2. To complement this, the group mass distributions are shown in Fig. 3.4.

The GAMA group masses display a strongly peaked distribution, with more groups in $\mathcal{M}2$ and $\mathcal{M}3$ than the other bins. Comparing the halo and FoF mock groups, it is clear from the table that the FoF algorithm is systematically overestimating the numbers of groups for the two higher mass bins. The slightly lower mean mass of $\mathcal{M}1$ FoF versus halo groups is likely due to the fact that $\mathcal{M}_{\rm lum}$ is systematically underestimated for low redshifts where these low-mass haloes are found (see Fig. 3.1). For higher-mass haloes, $\mathcal{M}_{\rm lum}$ correlates well with $\mathcal{M}_{\rm Dhalo}$ (see Fig. 3.2), and so it seems likely that the higher

[2]The terms 'halo' and 'group' are used interchangeably when discussing the TNG and L-GALAXIES simulations.

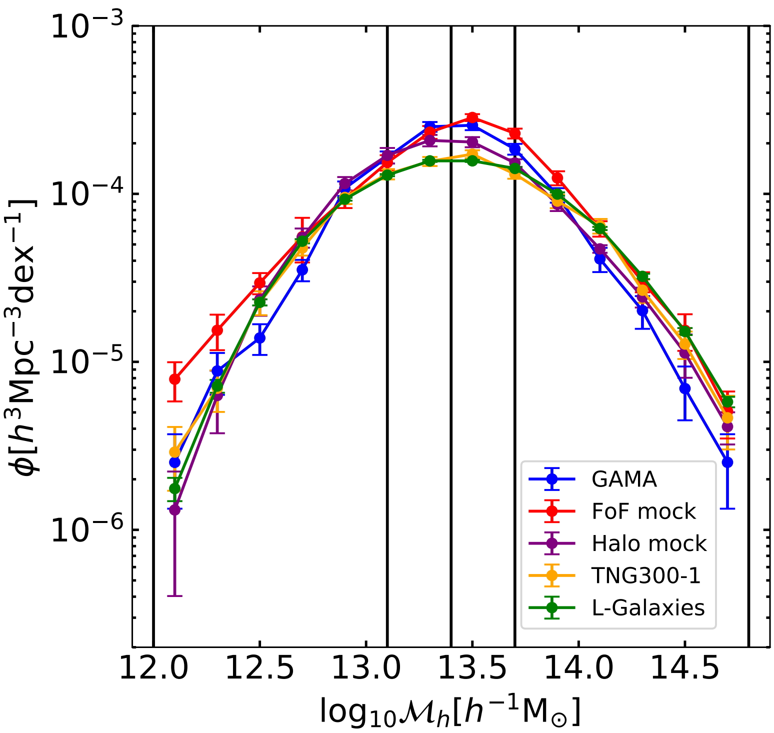

Figure 3.4: Distribution of group (halo) masses in our sample for GAMA, the two mock catalogues, TNG300-1 and L-GALAXIES. The plotted uncertainties are jackknife values between 27 regions for GAMA and simulations, and the scatter between 9 realisations for the mocks. The vertical lines delineate the halo mass bins used in this analysis.

numbers of larger-mass FoF groups is due to the FoF algorithm aggregating lower-mass haloes into one system.

Comparing the FoF mock groups with the GAMA groups, it is clear that the mock groups in the lowest mass bin tend to be of slightly lower mass than the corresponding GAMA groups, and of higher mass than the GAMA groups in the highest mass bin. It also appears that relatively there are slightly more high- than low-mass groups in the FoF mocks. These differences should be borne in mind when comparing results from GAMA data and mock catalogues.

TNG matches the halo mock well on both the mean group masses and the mass distribution of selected haloes. The only apparent difference is in the relative numbers of groups in bin $\mathcal{M}4$ compared to the other bins, with TNG showing a greater relative number. This demonstrates the success of our group selection in TNG, which has the predominant effect of removing low mass groups.

L-GALAXIES matches the halo mock mean group masses and follows very similar trends to TNG. It can be seen from Fig. 3.4 that the mass distribution is almost identical to that from TNG, except for a slightly greater number of haloes at the highest mass end.

3.3 Measuring the correlation function

We estimate the galaxy auto-correlation function and group–galaxy cross-correlation functions in bins of halo mass, as well as marked correlation functions, in which we weight groups and/or galaxies by their estimated mass.

We use CORRFUNC (Sinha & Garrison, 2019, 2020) to calculate pair counts for the clustering statistics. When plotting correlation functions, we always plot w_p against the *mean separation* of galaxy pairs in each bin, rather than the centre of each (log-spaced) bin.

3.3.1 GAMA data and mock catalogues

In order to overcome the effects of redshift space distortions in the lightcones, we start by estimating the two-dimensional group–galaxy cross-correlation function $\xi_{Gg}(r_\perp, r_\parallel)$ and galaxy auto-correlation function $\xi_{gg}(r_\perp, r_\parallel)$; the excess probability above random of finding a group and a galaxy (cross-correlation) or two galaxies (auto-correlation) separated by $r_\parallel$ along the line of sight (LOS) and $r_\perp$ perpendicular to the LOS. These separations are calculated using the standard method (e.g. Fisher et al., 1994) for pairs of objects with position vectors $\boldsymbol{r}_1$ and $\boldsymbol{r}_2$. The separation is given by vector $\boldsymbol{s} = \boldsymbol{r}_2 - \boldsymbol{r}_1$ and the vector to the midpoint of the pair from an observer at the origin by $\boldsymbol{l} = (\boldsymbol{r}_1 + \boldsymbol{r}_2)/2$. The separations in the LOS and perpendicular directions are then given by $r_\parallel = |\boldsymbol{s}.\hat{\boldsymbol{l}}|$, with $\hat{\boldsymbol{l}}$ being the unit vector in the direction of $\boldsymbol{l}$, and $r_\perp = \sqrt{\boldsymbol{s}.\boldsymbol{s} - r_\parallel^2}$.

Raw pair counts are obtained using CORRFUNC, then normalised to account for the relative total numbers of groups, N_G, galaxies, N_g, and random points, N_r. The normalised galaxy–galaxy, gg, group–galaxy, Gg, group–random, Gr, galaxy–random, gr, and random–random, rr, pair counts are then used to calculate the correlation functions. Specifically, these are obtained by dividing the raw pair counts in each separation bin by N_g^2, $N_G N_g$, $N_G N_r$, $N_g N_r$, and N_r^2 respectively.

The pair counts may additionally be weighted by group and/or galaxy mass in order to obtain marked correlation functions, and hence explore the dependence of clustering on group and galaxy mass. The random points, which follow the selection function of the galaxy sample, are generated as described in Section 3.2.4. A total of 426,790 random points are generated, 10 times the number of galaxies in the sample.

The galaxy auto-correlation $\xi_{gg}(r_\perp, r_\parallel)$ is estimated using the standard Landy & Szalay (1993) estimator,

$$\xi_{gg}(r_\perp, r_\parallel) = \frac{gg - 2gr + rr}{rr}, \tag{3.1}$$

while $\xi_{Gg}(r_\perp, r_\parallel)$ is estimated with the cross-correlation form (Mohammad et al., 2016) of this estimator,

$$\xi_{Gg}(r_\perp, r_\parallel) = \frac{Gg - Gr - gr + rr}{rr}. \tag{3.2}$$

As discussed in Hang et al. (2022), in principle this equation should include terms involving a random catalogue of groups as well as of galaxies. However, our form of the cross-correlation estimator containing only one random catalogue will be valid providing the two populations are similar. In the case of the groups and galaxies we use, they have the same sky footprint (although groups may be missing near the edges of the fields). The line-of-sight distribution differs, but the effect of this is small as we are considering a very low redshift sample. In Appendix 3.C we show that, even with extreme examples of artificially introduced group selections, the cross-correlation results are not altered.

The two-dimensional group–galaxy cross-correlation functions for our four mass bins of GAMA groups with our volume-limited sample of galaxies, are shown in Fig. 3.5. At small projected separations, $r_\perp \lesssim 5\,h^{-1}\,\mathrm{Mpc}$, the clustering is seen to be stretched along the LOS direction ($r_\parallel$-axis). This is increasingly apparent in higher mass bins. At larger projected separations, the LOS clustering signal is compressed.

The projected auto- and cross-correlation functions, $w_p(r_\perp)$, are obtained by integrating the observed two-dimensional correlation function $\xi(r_\perp, r_\parallel)$ along the LOS direction $r_\parallel$:

$$w_p(r_\perp) = 2\int_0^{r_{\parallel\max}} \xi(r_\perp, r_\parallel) dr_\parallel. \tag{3.3}$$

We use a limit of $r_{\parallel_{\max}} = 40\,h^{-1}\,\mathrm{Mpc}$; following the results of Loveday et al. (2018, appendix B).

To estimate uncertainties on the clustering results from GAMA we use jackknife sampling. We use 27 regions in RA and calculate error bars as the square root of the diagonal terms in the covariance matrix calculated from these regions. For the mock catalogues 9 different realisations are available and we estimate uncertainties using the scatter between these.

The jackknife sampling we use is designed to reproduce the cosmic variance between independent regions. This accurately reproduces the uncertainty on large scales, and on small scales can be interpreted as an upper bound on the variation between groups.

3.3.2 Simulations

TNG and L-GALAXIES use periodic boxes with no redshift space distortions, and so we can directly calculate the three-dimensional correlation function $\xi(r)$ using the simplified formula

$$\xi(r) = \frac{DD}{RR} - 1, \tag{3.4}$$

with the normalised data pair count DD (Gg for the cross-correlation, gg for the auto-correlation) and random pair count RR. We again make use of CORRFUNC to calculate the data pair counts, normalised by total galaxy and group numbers as above.

Due to periodic boundary conditions, no random catalogue is needed. Instead, the normalised random pair count is calculated as

$$RR = \frac{v(r)}{V}, \tag{3.5}$$

where V is the total box volume and $v(r) = \frac{4}{3}\pi((r+dr)^3 - r^3)$ is the volume of a spherical shell of radius *r* and thickness *dr* (Alonso, 2012).

The real-space three-dimensional correlation function $\xi(r)$ is then converted to a

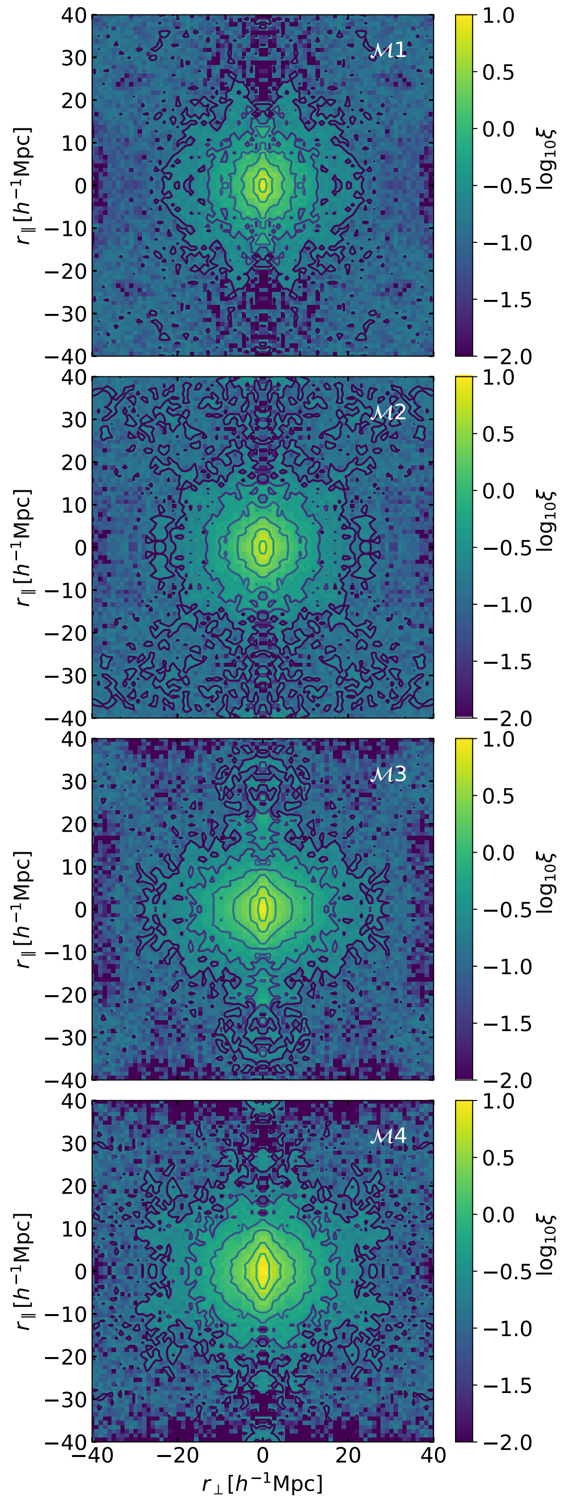

Figure 3.5: The two-dimensional group–galaxy cross-correlation functions $\xi(r_\perp, r_\parallel)$ for our four bins of group mass. We show the clustering signal reflected about both axes to make it easier to see the distortions introduced by the peculiar velocities of galaxies around groups. Contour levels are the same as Li et al. (2006), going up from $\xi = 0.1875$ to $\xi = 48$ in factors of 2.

projected correlation function using

$$w_p(r_\perp) = 2\int_0^{y_{\max}} \xi\left((r_\perp^2 + y^2)^{1/2}\right) dy = 2\int_{r_\perp}^{r_{\max}} \frac{r\xi(r)}{\sqrt{r^2 - r_\perp^2}} dr, \tag{3.6}$$

to produce a quantity directly comparable to the GAMA measurements. We perform this integral over an interpolation of the $\xi(r)$ and we again use an upper integration limit of $r_{\max} = 40\,h^{-1}$ Mpc. It is pointed out in van den Bosch et al. (2013) that this integral may be biased on large scales relative to clustering calculated from observations, but we do not attempt to correct for this as we are mostly interested in small scales.

To calculate uncertainties in the results for the simulation boxes we perform jackknife sampling by dividing the box into 27 subboxes and excluding these one at a time. We then give error bars as the square root of the diagonal elements of the covariance matrix. Jackknife sampling breaks the periodicity of the box, and should therefore require a random catalogue. However, we continue to use equation 3.5 for random pair counts, and account for the changed random–random term by scaling the $\xi(r)$ value in each jackknife region by the ratio of the overall $\xi(r)$ in the box against the mean $\xi(r)$ from the jackknife regions.

3.3.3 Marked correlation

The marked correlation M_w is calculated from the unweighted projected two-point correlation function w_p and weighted projected two-point correlation function W_p in all cases using (Sheth et al., 2005; Skibba et al., 2006)

$$M_w(r_\perp) = \frac{r_\perp + W_p(r_\perp)}{r_\perp + w_p(r_\perp)}. \tag{3.7}$$

Uncertainties on marked correlations would be overestimated if we simply combine the errors on W_p and w_p (see Skibba et al. 2006). Therefore we calculate the marked correlation for each of our jackknife samples separately and estimate the uncertainty from these.

3.3.4 Bias

We make use of two bias measures in our analysis. The first is the relative bias of the group sample compared to the galaxy sample, which we define as

$$b_{\rm rel}(r_\perp) = \frac{w_p^{\rm Gg}(r_\perp)}{w_p^{\rm gg}(r_\perp)}. \tag{3.8}$$

This accounts for different galaxy auto-correlation amplitudes between samples, although it does retain some dependence on the galaxy sample.

The second bias measure we use is that relative to dark matter. We define the galaxy bias $b_{\rm g}$ using

$$w_p^{\rm gg}(r_\perp) = b_{\rm g}^2(r_\perp) w_p^{\rm DM}(r_\perp), \tag{3.9}$$

and the corresponding group bias $b_{\rm G}$ with

$$w_p^{\rm Gg}(r_\perp) = b_{\rm G}(r_\perp) b_{\rm g}(r_\perp) w_p^{\rm DM}(r_\perp). \tag{3.10}$$

Note that in this notation the relative bias from equation 3.8 becomes $b_{\rm rel} = b_{\rm G}/b_{\rm g}$.

For the dark matter auto-correlation, $w_p^{\rm DM}$, we use the Millennium simulations, the Millennium (Springel et al., 2005) $\xi(r)$ on scales $r > 1\,h^{-1}\,$Mpc and Millennium-II (Boylan-Kolchin et al., 2009) on smaller scales, which we project from $\xi(r)$ to $w_p(r_\perp)$ by interpolating $\xi(r)$ and using equation 3.6, the same method we used for the simulation correlations.

The group bias we measure from the cross-correlation will not equal the one we would obtain if we were able to compute a group auto-correlation function. On small intra-group scales, the group auto-correlation goes to -1 as there are no group–group pairs, but the cross-correlation remains positive and so gives a different bias. On larger scales the bias from this cross-correlation will be similar to that from the auto-correlation, although subject to a scaling associated with any remaining dependence on the galaxy population.

3.4 Results

3.4.1 FoF versus halo mocks

We first compare clustering results obtained using the FoF and halo mocks in Fig. 3.6. We see that in mass bins 3 and 4, the FoF mock group clustering is in very good agreement with that of the halo mocks, despite the large excess of FoF groups in these mass bins (Table 3.2). However, for the lower mass bins, particularly $\mathcal{M}1$, the FoF group clustering is underestimated on very small scales, $r_\perp \lesssim 0.2\,h^{-1}\,$Mpc, and very slightly overestimated on scales $0.5 \lesssim r_\perp \lesssim 2\,h^{-1}\,$Mpc. It seems likely that the low mass FoF groups may be contaminated by chance projections of isolated galaxies, thus reducing the small-scale clustering signal. Insofar as the mock catalogues are representative of the GAMA data, we can infer that the GAMA results are likely to be reliable in mass bins 2–4, but that those for $\mathcal{M}1$ should be treated with some scepticism.

To check the effects of the group finding on the marked correlation, we show the group mass marked correlation for the FoF and halo mocks in Fig. 3.7. We see that on small scales the mocks agree, but on scales $r_\perp \gtrsim 0.1\,h^{-1}\,$Mpc the FoF marked correlation is lower. This is around the size of a compact group, and is perhaps due both to spurious FoF groups (created by chance alignments) being isolated from other galaxies, and also to more extended groups being missed by the FoF group finder. We expect this trend to be representative of GAMA, and so the GAMA marked correlation may also be biased low on these scales.

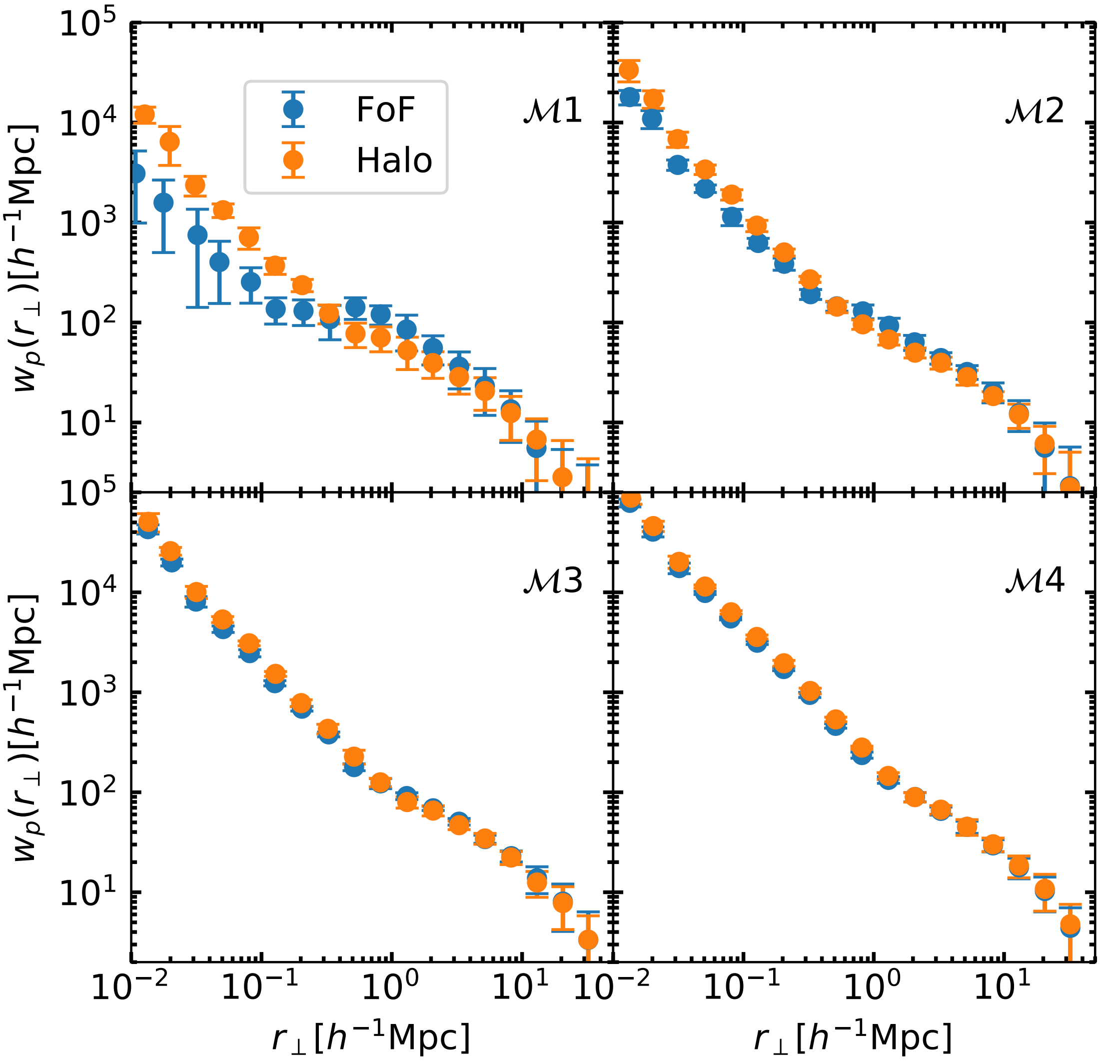

Figure 3.6: Group–galaxy cross-correlation functions for the mock catalogues. Orange symbols show results using the halo mocks, blue symbols show results obtained using FoF mocks.

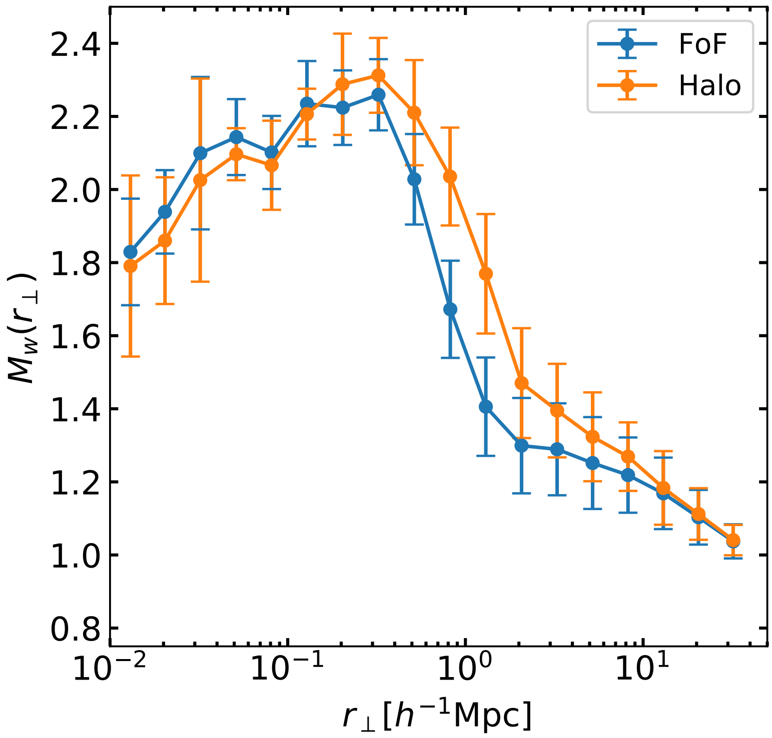

Figure 3.7: Marked correlation for the mock catalogues, using group mass as the mark. Orange symbols show results using the halo mocks, blue symbols show results obtained using FoF mocks.

3.4.2 Group clustering and bias in mass bins

3.4.2.1 GAMA and mocks

Fig. 3.8 shows the GAMA projected group–galaxy cross-correlation functions for each group mass bin (top), along with the bias relative to the galaxy sample (middle), and the bias relative to a DM-only simulation (bottom). Left, middle and right panels show comparison results from the halo mocks, TNG, and L-GALAXIES respectively. Both bias estimates are highly dependent on scale and group mass on intra-group scales, $r_\perp \lesssim 1\,h^{-1}\,$Mpc. On larger scales, the biases are relatively constant (within the error bars) for each mass bin, but there is still a slight trend for bias to increase with mass.

On scales $r_\perp \approx 0.1\,h^{-1}\,$Mpc, GAMA relative group bias ($b_{\rm rel}$ from equation 3.8; middle panels) increases rapidly with group mass, from $b \approx 0.8 \pm 0.2$ for $\mathcal{M}1$ groups to $b \approx 5 \pm 1$ for $\mathcal{M}4$ groups. The strong halo-mass dependence of the GAMA small scale clustering seen here is to be expected, as on scales $r_\perp \lesssim 1\,h^{-1}\,$Mpc, the cross-correlation signal will be dominated by galaxies within each respective halo (intra-halo clustering) and group membership increases with halo mass.

Comparison in Fig. 3.6 of the FoF and halo mocks on these scales suggests that the apparent below-unity bias of $\mathcal{M}1$ groups in GAMA is partly an artefact of the group-finding algorithm, although it also reflects a lack of bright galaxies in these small groups. The halo mock bias in the middle-left panel of Fig. 3.8 is consistent with unity for $\mathcal{M}1$ groups at $r_\perp \approx 0.1\,h^{-1}\,$Mpc, although it drops below unity above this,

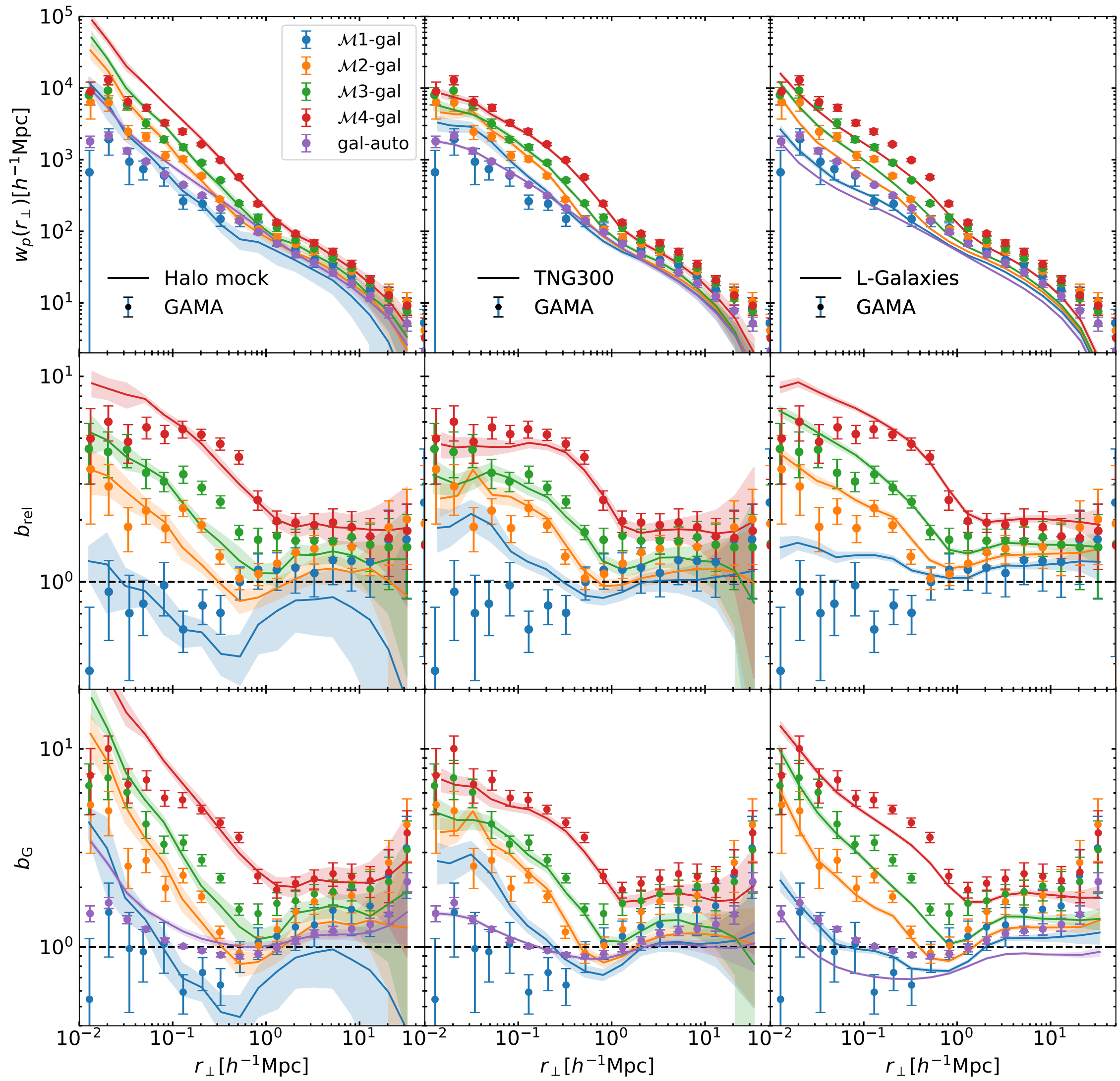

Figure 3.8: Top panels: The projected group–galaxy cross-correlation functions for our four bins of group mass as indicated. Also shown is the galaxy auto-correlation function. Middle panels: Relative bias of the projected group–galaxy cross-correlation to the galaxy sample, obtained by dividing the group–galaxy cross-correlation by the galaxy auto-correlation. Bottom panels: Bias of the projected group–galaxy cross-correlation and galaxy auto-correlation relative to the dark matter auto-correlation function of the Millennium simulations. In all panels, symbols and error bars show the GAMA results; lines of corresponding colour show results from the halo mock in the left panels, the Illustris TNG300-1 simulation in the central panels, and L-GALAXIES in the right panels.

reaching a minimum at $r_\perp \approx 0.5\,h^{-1}\,\mathrm{Mpc}$, indicating the spatial extent of these smaller groups. As with other mass bins, the mock galaxies in $\mathcal{M}1$ groups seem to be too centrally-concentrated.

On larger scales (1–5 $h^{-1}\,\mathrm{Mpc}$), the dependence of relative bias on group mass in GAMA is weaker, although the bias of the highest mass bin is still 2–3 times that of the lowest mass groups. By scales of $r_\perp \approx 10\,h^{-1}\,\mathrm{Mpc}$, the biases of each mass bin are consistent within the uncertainties.

On the largest scales $r_\perp \gtrsim 10\,h^{-1}\,\mathrm{Mpc}$, the relative bias remains constant in each bin within uncertainties but the GAMA auto- and cross-correlation functions are seen to have slightly greater amplitude than those of the mocks. This perhaps indicates small differences in the galaxy populations used, but these scales are also the most affected by the projection of the clustering signal, so we cannot draw any firm conclusions on these scales.

When turning to bias relative to the dark matter auto-correlation (b_g and b_G from equation 3.10; lower panels), the bias for GAMA is seen to increase down to the smallest scales we plot for the galaxies and the groups in bins $\mathcal{M}2$–4. As with the bias relative to the galaxies, $\mathcal{M}1$ GAMA groups show a bias of about unity on the smallest scales not seen in the halo mock, which is likely to be a result of the group-finding algorithm.

The halo mocks substantially over-predict the bias on small scales. On intra-halo scales the relative bias (middle panels) is seen to increase roughly as a power-law with decreasing $r_\perp$, rather than displaying a flattening as seen in GAMA. This becomes even more apparent in bias relative to the dark matter (lower panels), with an even steeper increase when moving to smaller scales. This suggests inaccuracy in the physics defining satellite galaxy occupations and positions in the mocks, with satellites being placed too close to the centre on average. This is perhaps unsurprising given the uncertainties in the modelling of satellite mergers when the dark matter subhalo they are associated with disappears (see e.g. Pujol et al., 2017).

3.4.2.2 TNG300 and L-GALAXIES

In Fig. 3.8, we also show corresponding results from the Illustris TNG300-1 simulation and the L-GALAXIES semi-analytic model, each around the mean GAMA redshift $z = 0.2$.

TNG results are shown as solid lines in the central column of panels. The TNG galaxy auto-correlation function (purple line) is in very close agreement with GAMA on scales $r_\perp \lesssim 5\,h^{-1}\,\mathrm{Mpc}$, although slightly below that of the mock, and the TNG halo–galaxy cross-correlation functions show a similar characteristic inflection to GAMA around $r_\perp \approx 0.5$–$1\,h^{-1}\,\mathrm{Mpc}$; the transition from the intra-halo to the inter-halo regime. In the higher mass bins, $\mathcal{M}3$ and $\mathcal{M}4$, the amplitude of the cross-correlations is also in agreement with GAMA on smaller scales within uncertainties. In $\mathcal{M}1$, and to a lesser extent in $\mathcal{M}2$, for which GAMA results are suspect, TNG shows a greater cross-correlation on scales $r_\perp \lesssim 0.3\,h^{-1}\,\mathrm{Mpc}$ than GAMA. This is clearest moving to the smallest scales, $r_\perp \lesssim 0.05\,h^{-1}\,\mathrm{Mpc}$, where it leads to convergence of $\mathcal{M}1$–$\mathcal{M}3$ results as $\mathcal{M}1$ and $\mathcal{M}2$ continue to rise while $\mathcal{M}3$ and $\mathcal{M}4$ flatten off.

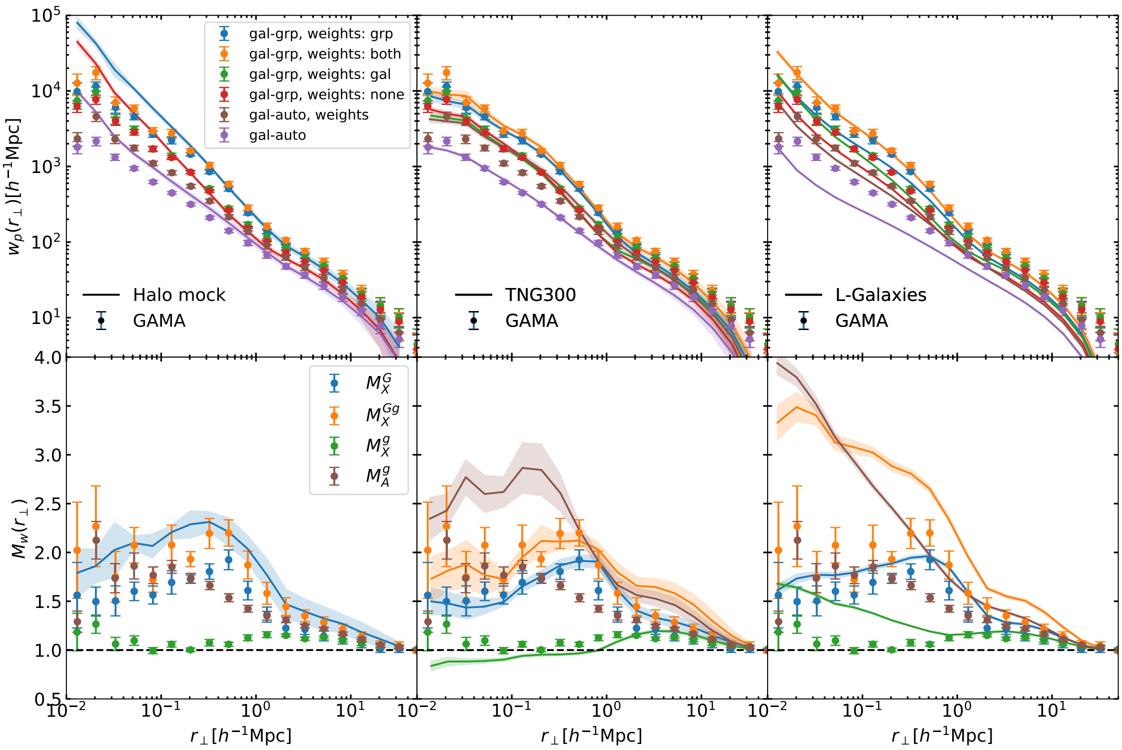

Figure 3.9: Top panels: The projected group–galaxy cross-correlation functions for all groups, weighted by galaxy and group masses as indicated. Also shown is the galaxy auto-correlation function both unweighted and using galaxy masses as weights. Bottom panels: Marked cross-correlations using galaxy masses (M_X^g), group masses (M_X^G), and both masses (M_X^{Gg}) as marks, along with the stellar-mass marked galaxy auto-correlation (M_A^g). In all panels, symbols and error bars show the GAMA results; lines of corresponding colour show results from the halo mock in the left panels, the Illustris TNG300-1 simulation in the central panels and L-GALAXIES in the right panels.

Solid lines in the right-hand panels of Fig. 3.8 show results for L-GALAXIES. Both the galaxy auto-correlation and halo–galaxy cross-correlations fall below the GAMA results. The relative biases in L-GALAXIES show the trend seen in the halo mock of a continuing increase down to the smallest scales and greater amplitude than GAMA, suggesting the same issues in the two SAMs. However, the group bias in the lower panels agrees well with GAMA on scales $r_\perp \gtrsim 0.1\,h^{-1}$ Mpc, implying some of the discrepancy is connected to the galaxy sample. This difference in the dependence on the galaxy properties between L-GALAXIES and GAMA becomes clearer in the marked correlations discussed below. On larger scales, L-GALAXIES shows the halo mass dependence of bias continuing beyond $r_\perp = 5\,h^{-1}$ Mpc, showing the most massive groups are at the centre of denser regions extending further than those of smaller groups, in agreement with GAMA.

3.4.3 Marked correlation functions

3.4.3.1 Marked cross-correlation

The upper panels of Fig. 3.9 show projected correlation functions weighted in the various ways indicated. Lower panels show marked group–galaxy cross-correlation functions using group mass (M_X^G), galaxy mass (M_X^g), and both masses (M_X^{Gg}) as weights, as well as the marked galaxy auto-correlation function (M_A^g). We weight by linear mass in order to enhance the differences between the marked statistics, although the use of log-mass weights does not qualitatively change our results (see Sheth et al. 2005 for a discussion on re-scaling marks). In Appendix 3.D we show, using rank-ordered marks, that the specific values of the weights do not affect our conclusions.

The GAMA group-mass marked cross-correlation function (M_X^G, blue symbols) peaks at scales $r_\perp \approx 0.5\,h^{-1}\,$Mpc, declining gradually to smaller scales, and somewhat more rapidly on larger scales until $r_\perp \approx 2\,h^{-1}\,$Mpc, beyond which M_X^G declines more gradually. The halo mock (blue line) shows similar trends to GAMA data, but with M_X^G about 20 percent higher. The peak in M_X^G around $r_\perp \approx 0.5\,h^{-1}\,$Mpc is indicative of the typical projected radii of our galaxy groups. It is also consistent with the bias results of Fig. 3.8, where the relative strengths of the group biases differ most around this scale, due to the below-unity bias of $\mathcal{M}1$ groups and large bias of $\mathcal{M}4$ groups.

The GAMA galaxy-mass marked cross-correlation function (M_X^g, green points) is systematically greater than unity only on inter-group scales, $r_\perp \gtrsim 0.5\,h^{-1}\,$Mpc. We are unable to measure M_X^g for the GAMA mocks, as galaxy masses are not available. When both galaxy and group masses are used as weights (M_X^{Gg}, orange points), a slight additional enhancement is seen relative to M_X^G, indicative of the most massive groups having an enhanced number of massive satellite galaxies.

M_X^G measurements from both the TNG and L-GALAXIES simulations show general agreement with GAMA. TNG agrees with GAMA within uncertainties on almost all scales, but is below the mocks on scales $r_\perp \lesssim 1\,h^{-1}\,$Mpc. L-GALAXIES on the other hand agrees well on all scales with the halo mock, and is generally above but just consistent with the GAMA results. The very close agreement between L-GALAXIES and the halo mock may be a result of both being built upon the Millennium simulation.

When marking with galaxy masses, TNG shows $M_X^g < 1$ on scales $r_\perp \lesssim 0.5\,h^{-1}\,$Mpc, meaning the most massive satellite galaxies are not found near the group centres. Yet when both group and galaxy masses are used (M_X^{Gg}), an enhancement relative to M_X^G is seen on all scales. This is consistent with the conclusion from GAMA that the most massive groups also contain the most massive satellites, but this dependency extends out slightly further in TNG, to $r_\perp \approx 10\,h^{-1}\,$Mpc.

L-GALAXIES shows a galaxy-mass marked cross-correlation M_X^g greater than unity, especially on scales $r_\perp \lesssim 1\,h^{-1}\,$Mpc where M_X^g is seen to increase as scale decreases, meaning massive satellites are always closely associated with the group centre. The same trend is seen and enhanced even further when both group and galaxy masses are used as marks (M_X^{Gg}). This is consistent with the high small-scale bias we observed for L-GALAXIES, yet very different from the GAMA result, suggesting that the satellite galaxies in L-GALAXIES are typically more massive. This is in accord with the finding in VM20 that the modified Schechter functions appropriate for GAMA satellite galaxies under-predict the number of massive satellites in L-GALAXIES.

3.4.3.2 Marked auto-correlation

For GAMA, L-GALAXIES and TNG, we also show the (stellar mass) marked galaxy auto-correlation (M_A^g, brown symbols or lines), which helps in understanding some of the differences in the group–galaxy cross-correlations. GAMA shows no systematic scale-dependence (but large scatter) in M_A^g on scales $r_\perp \lesssim 0.2\,h^{-1}\,$Mpc, but then declines systematically on larger scales, always lying below M_X^{Gg}. This makes sense, as M_A^g indirectly contains group information through the presence of central galaxies, although these will have lower masses than the groups.

TNG on the other hand shows a marked auto-correlation M_A^g which peaks on scales 0.1–0.5 $h^{-1}\,$Mpc and decreases slightly on smaller scales. The large enhancement compared to GAMA and the TNG cross-correlation functions is likely to be due to the apparent over-dependence of central galaxy mass on group mass in TNG reported by VM20. The decreasing dependence on the smallest scales is consistent with the trends in M_X^g, and shows that the most massive galaxies have a slight tendency to avoid group centres.

L-GALAXIES shows a very different trend that the most massive galaxies are very close together, with M_A^g still increasing at $r_\perp \approx 0.01\,h^{-1}\,$Mpc. This matches the cross-correlation result and also appears consistent with a slight trend in Henriques et al. (2017) for the auto-correlation to be below SDSS in lower mass bins and above in higher mass bins. This is likely to be the result of the supernova feedback used, as van Daalen et al. (2016) find that the feedback strength affects the relative proportions of satellite galaxies of different masses.

The general picture found from the marked correlations is one of agreement in the group mass dependence of clustering, but disagreement in the galaxy mass dependence. While the group mass dependence is a significant success in the positioning of galaxies within groups in both TNG and L-GALAXIES, massive galaxies appear to be too clustered, especially in L-GALAXIES.

3.5 Discussion

To put our results into context we discuss here the choice of group centre, which is the main caveat to our work, and compare against previous works.

3.5.1 Choice of group centre

In this work we have considered group–galaxy cross-correlation functions in GAMA down to scales smaller than the typical group size, so our results depend heavily on the choice of group centre. We check here for effects due to possible misidentification of

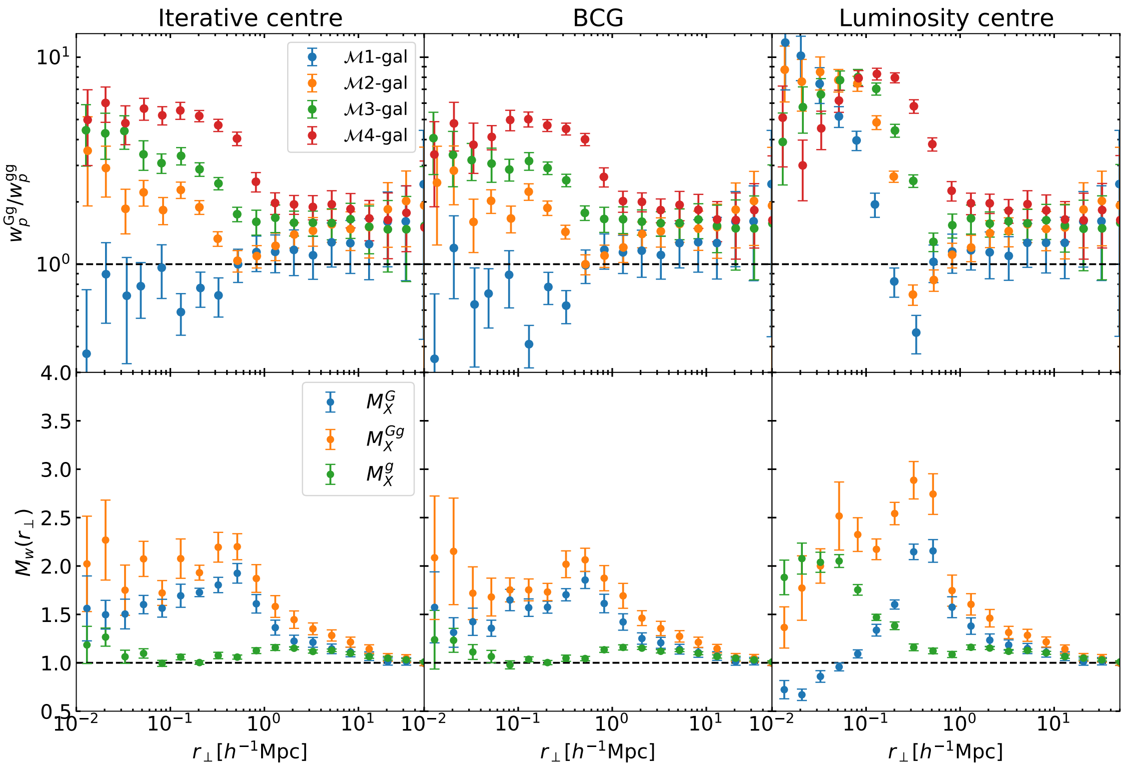

Figure 3.10: Effect of choice of GAMA group centre on our results. Upper panels show the relative bias $b_{\rm rel}$ of the projected group–galaxy cross-correlation to the galaxy sample, and lower panels show the marked correlation using galaxy masses (M_X^g), group masses (M_X^G), and both masses (M_X^{Gg}) as marks. The left panels shows the iterative group centre, the middle panels the brightest central galaxy, and the right panels the centre-of-light of the group.

group centre by using the three different definitions of group centre described in section 4.2.1 of R11.

R11 found the most reliable group centre to be the one we have used throughout this work, the iterative centre. This was found by iteratively removing the galaxy furthest from the centre-of-light of all remaining galaxies in the group, until only one galaxy remains. The position of the final galaxy is taken to be the group centre. In most cases this is the same as the second definition of group centre, the brightest central galaxy (BCG), taken to be the brightest galaxy in the group. The third definition of group centre corresponds simply to the group centre-of-light, which does not in general coincide with a galaxy. Using mock catalogues, R11 showed the iterative centre to match the true centre in $\sim 90\%$ of cases, while the BCG showed large offsets in some cases, and the centre-of-light only matched the true centre for groups where all members are detected.

To explore the effect of group centre choice on our results, we show in Fig. 3.10 the relative bias $b_{\rm rel}$ of the four group mass bins and the marked cross-correlations for the three definitions of group centre. On the left we show the iterative centre used elsewhere in this work. This is in most cases the same as the BCG shown in the middle panel, so the results are similar from these two options. However, the iterative centre shows a more consistent picture for different group masses on small scales, while the BCG shows a drop in bias for the most massive groups, suggesting the galaxy at the centre of the gravitational potential of the group has been included in the cross-correlation. The definition of group centre as centre-of-light is shown in the right panel, and this definition shows significant evidence of mis-centring. The bias is seen to be peaked, with the peak at $r_\perp \approx 0.1\,h^{-1}\,$Mpc for the most massive groups, and on smaller scales for less massive groups. The location of this peak is indicative of the mean offset of the central galaxy from the centre-of-light.

A similar outcome is found by considering the marked correlations. Using group mass as the mark, the iterative centre and BCG results are similar, but the centre-of-light definition shows a negative mark on small scales related to the reduction in bias for the more massive groups. When using galaxy masses as marks, the iterative centre and BCG results both show no mark on scales less than the typical group size, but the centre-of-light shows a positive mark, probably indicating the inclusion of the true central galaxy in the cross-correlation.

Based on this, we are in agreement with the result of R11 that the iterative centre we have used is the best reflection of the true group centre, as it does not display the offset in peak bias associated with including the central galaxy in the cross-correlation.

3.5.2 Comparison with previous results

Finally, we compare our results to previous works, and calculate the average bias on large scales.

Our finding of an increase in clustering amplitude with group mass on scales of a few $h^{-1}\,$Mpc agrees with the results from the analysis of SDSS data by Wang et al. (2008). These authors found that the bias relative to the lowest mass bin increases

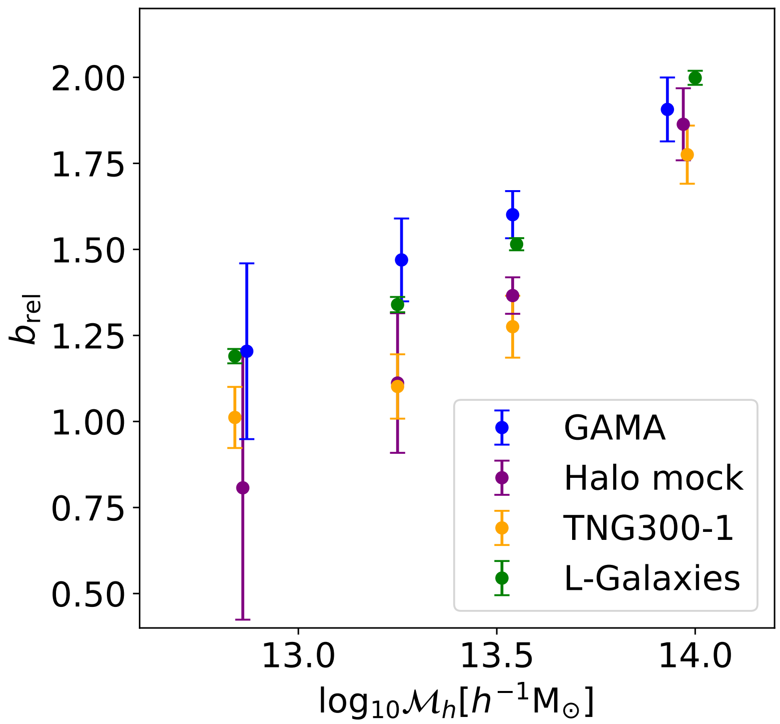

Figure 3.11: Large-scale relative bias, averaged over scales 2–10 h^{-1} Mpc, as a function of halo mass for GAMA, the halo mocks, TNG300-1 and L-GALAXIES. Uncertainties are calculated by jackknife of the average $b_{\rm rel}$ for GAMA, TNG and L-GALAXIES, and by scatter between the 9 realisations for the halo mocks.

quadratically with mass, and we show a similar rise in our relative bias in Fig. 3.11, with bias averaged over scales 2–10 h^{-1} Mpc. This trend is consistent with the results from the simulations, albeit with a slightly higher normalisation. However, due to our use of different, narrower, mass bins than Wang et al. (2008), the uncertainties from GAMA are large, and the bias values are not directly comparable. In addition to the large-scale bias, we show on smaller, intra-group, scales, which were not considered by Wang et al. (2008), that the dependence of clustering amplitude on group mass becomes significantly stronger.

This sharp increase in cross-correlation amplitude within the typical group radius matches the results of Berlind et al. (2006), as does evidence for a flattening of the cross-correlation on scales $r_\perp \lesssim 0.3\,h^{-1}$ Mpc in our GAMA and TNG results. Berlind et al. (2006) attribute this to either a core to the radial profile of satellite galaxies, or to misidentification of the centre. We do not find evidence that the central galaxies are incorrect in our data, so support the explanation of a central core to groups.

The result from the marked correlation functions that massive galaxies are associated with massive groups is not surprising, and consistent with GAMA results from VM20. More interesting is the lack of dependence of the mark on galaxy mass alone within the radii of the smallest groups, in agreement with the results of Kafle et al. (2016) that there is no mass segregation within GAMA groups. This is in contrast to the results from SDSS, most recently in Roberts et al. (2015), that more massive satellites are generally closer to the group centre. Our approach of using the marked correlation is a new method to test for mass segregation, but as our galaxy sample is volume-limited in *r*-band luminosity and not in mass, our results are not directly comparable to these previous studies, and the marked correlations must be interpreted with caution given that stellar masses increase with group mass.

The lack of mass segregation also suggests a breakdown in self-similarity on group scales, as the most massive groups are found to be the most clustered, but this trend does not continue to galaxies within the groups. This suggests that while on inter-group scales the galaxy distribution depends primarily on the dark matter distribution, within groups baryon astrophysics has a significant effect.

3.6 Conclusions

In this work we have presented group–galaxy cross-correlation functions and mass-weighted marked correlations for the GAMA survey, GAMA mocks, the TNG300-1 simulation, and the L-GALAXIES semi-analytic model. We used four group mass bins with $12.0 < \lg \mathcal{M}_h < 14.8$ and cross-correlated with a volume-limited galaxy sample with density $5.38 \times 10^{-3}\, h^3\, \mathrm{Mpc}^{-3}$.

We found that the group–galaxy cross-correlation function (Fig. 3.8) increases systematically with group mass and with decreasing scale below $r_\perp \approx 1\, h^{-1}\, \mathrm{Mpc}$. There is no scale dependence on scales $r_\perp \gtrsim 1\, h^{-1}\, \mathrm{Mpc}$, but the correlation amplitude still increases with group mass, indicating that more massive groups are embedded within extended overdense structures.

Using marked correlations (Fig. 3.9), we saw that the cross-correlation has the strongest group mass dependence at scales $r_\perp \approx 0.5\, h^{-1}\, \mathrm{Mpc}$, the typical group radius (defined as projected separation to the most distant member galaxy from the group centre). No direct dependence on galaxy mass was observed, but the combination of group and galaxy mass causes an enhancement over the use of group mass only. This leads us to conclude that massive satellite galaxies are generally found in massive groups, but do not preferentially lie close to the central galaxy. Note that the central galaxy coincides with the iterative group centre, and so central–group pairs are not included in the group–galaxy cross-correlation functions presented.

3.6.1 Comparison to mocks and simulations

We used the GAMA mock catalogues to explore the effects of systematics in the data, particularly the group mass estimates, and to examine the model used for the mocks. Comparison of mocks using friends-of-friends and halo based group finding methods suggests that the masses may be overestimated at high redshift and underestimated at low redshift, although this only causes differences in the cross-correlation function in our lowest mass bin, $\mathcal{M}1$.

We have also compared our results against the TNG300-1 box from the IllustrisTNG hydrodynamical simulation and to the L-GALAXIES semi-analytic model. In order to provide a fair comparison, we selected groups using a simple model of the GAMA selection function.

The IllustrisTNG hydrodynamical simulation agrees well with our GAMA results in all cross-correlation bins except the lowest mass bin where the GAMA results are least reliable. It also displays very similar marked cross-correlations to GAMA, evidencing accuracy in the distribution of galaxies around groups. The only significant difference between TNG and GAMA we saw is in the marked galaxy auto-correlation, where the enhancement in TNG appears to be the same over-dependence of central galaxy mass on group mass seen in VM20.

The L-GALAXIES model was found to over-predict the mass dependence of the cross-correlation, showing an increasing bias down to the smallest scales considered. This was seen in the marked correlations to be driven by stronger clustering than GAMA of the most massive galaxies, perhaps driven by inaccurate supernova feedback. Together with the difficulties of modelling the infall of satellites without surviving subhaloes, this results in too many galaxies in the inner parts of the haloes. Away from the group centre, L-GALAXIES shows similar group bias to GAMA, demonstrating that the distribution of galaxies in the outer regions of the haloes is realistic.

3.6.2 Future prospects

While the GAMA groups are expected to be more reliable than the SDSS groups used in previous works, due to high spectroscopic completeness and the use of only the most reliable groups with $N_{\mathrm{FoF}} \geqslant 5$, we are limited by the smaller area of the GAMA survey. In future, the Wide Area VISTA Extragalactic Survey (Driver et al., 2019) is expected to be able to produce a much larger sample of galaxy groups and so improve upon our results by reducing the uncertainties and allowing the use of finer mass bins.

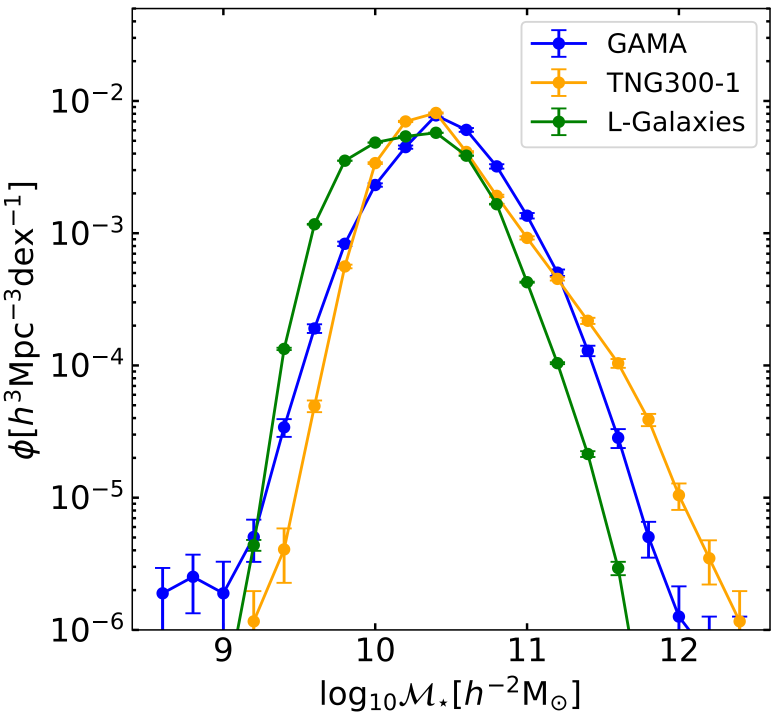

Figure 3.12: Distribution of stellar masses in our galaxy samples from GAMA, TNG and L-GALAXIES. The mock catalogues do not include stellar masses so are not shown.

Appendices

3.A Galaxy sample statistics

We desire our volume-limited GAMA, mock, TNG, and L-GALAXIES galaxy samples to have comparable clustering statistics. In order to achieve this, they were defined to have similar number-densities (Table 3.1). Here we show the stellar mass distributions and auto-correlation functions of these samples.

The distributions of stellar masses in each sample (Fig. 3.12) show some variation. This is not surprising, as the samples are volume-limited in r-band luminosity and not in mass, and so variations in mass-to-light ratio will affect mass-completeness. Compared to the GAMA sample, TNG shows a narrower peak but an over-abundance of the most massive galaxies with $\log_{10}(\mathcal{M}_\star/h^{-2}\mathrm{M}_\odot) \gtrsim 11.2$. L-GALAXIES shows a shift to slightly smaller masses than GAMA.

Fig. 3.13 shows the projected auto-correlation functions of the galaxy samples. On small scales, GAMA and TNG agree well but the mocks show a slightly greater auto-correlation and L-GALAXIES shows a lower auto-correlation. On the largest scales GAMA shows the greatest clustering, but consistent within uncertainties with the mocks.

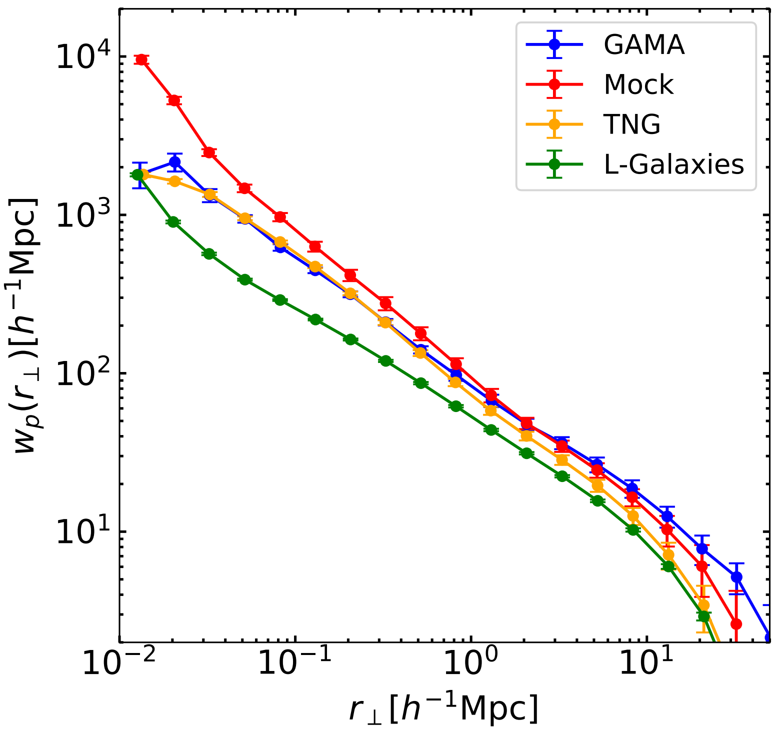

Figure 3.13: Projected auto-correlation functions of our galaxy samples from GAMA, the mock catalogues, TNG and L-GALAXIES.

3.B Group selection in simulations

Here we compare four methods of selecting groups in mass bins from the TNG and L-GALAXIES simulations, and the effect these methods have on estimated relative bias. The four group selection methods compared are:

1. Random sampling to mimic GAMA group selection, the method described in 3.2.5 and used elsewhere in this work.

2. Spatial sampling to mimic GAMA group selection. Here we select groups within a distance from the origin corresponding to the comoving distance at which the fifth brightest member galaxy would have an apparent magnitude of $m_r = 19.8$. This removes the periodicity of the box, and we therefore calculate the correlation function using the full Landy & Szalay (1993) estimator with random galaxies distributed around the box. Uncertainties on this sample are estimated using jackknife between 27 samples of equal volume selected by angle, and are larger than those of the random selection due to the loss of periodicity.

3. Use only of GAMA mass bin limits, without further selection. This results in an over-abundance of low-mass groups in a volume-limited simulation cube compared to GAMA.

4. Adjustment of mass limits to match the mean group masses in GAMA (the method employed in VM20).

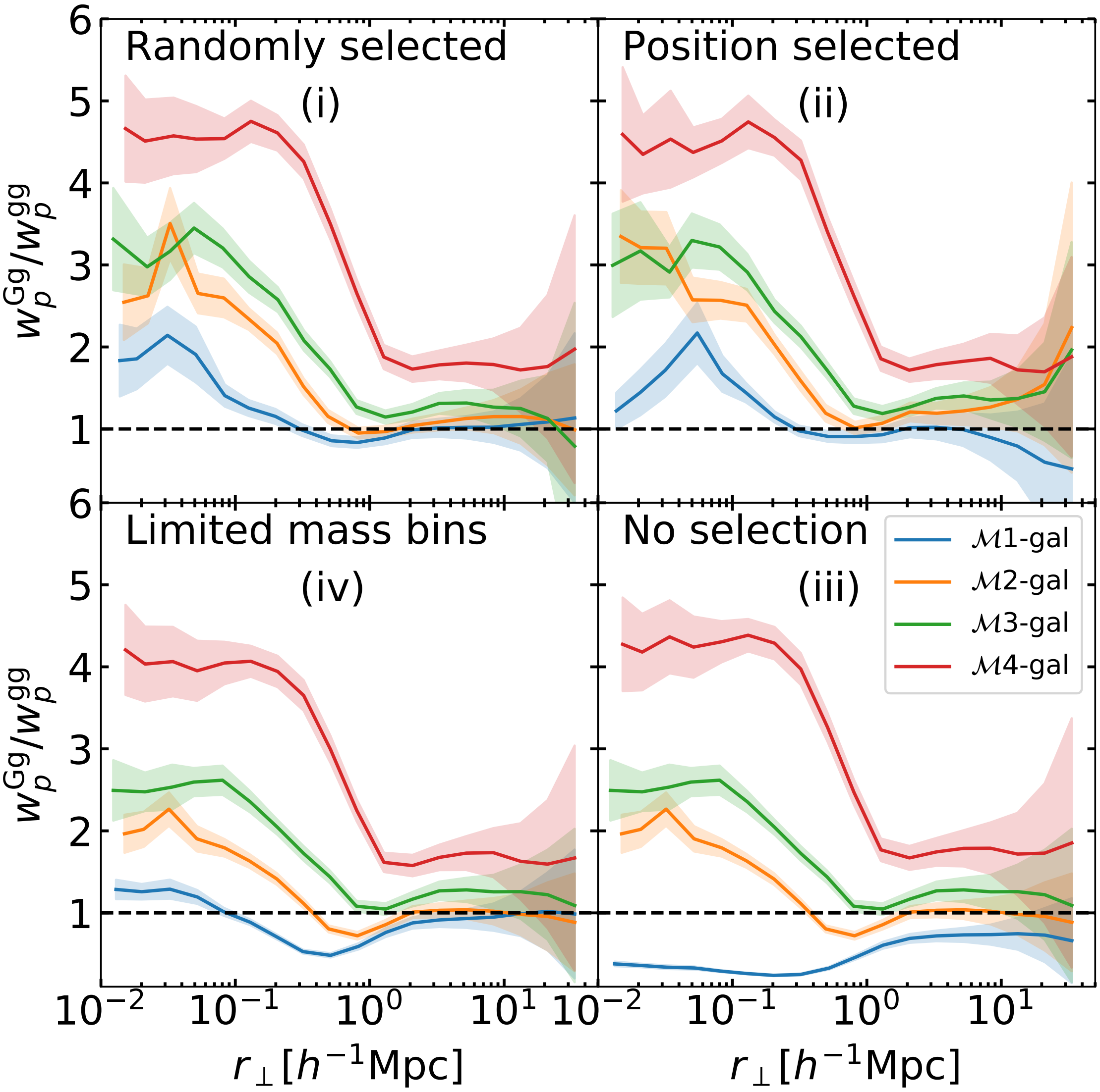

Figure 3.14: Relative bias for the 4 mass bins in the TNG simulations using different selection options for groups. Clockwise from top left, the panels show the four group selections (i)-(iv): upper left, the selection of groups throughout the volume based on galaxy luminosities as used in this work; upper right, a group selection based on galaxy luminosities and radial distance from box origin; lower right, the full group sample in the volume-limited simulation; and lower left, the full group sample with low and high mass groups removed to match GAMA mean masses.

Comparing these different selection methods applied to TNG in Fig. 3.14, the relative bias is consistent between the samples selected using methods (i) and (ii), except for the smallest scales in $\mathcal{M}1$. Bearing in mind that the groups in sample (i) are randomly distributed throughout the TNG data cube, whereas those in sample (ii) lie predominantly closer to the origin, this comparison illustrates that the spatial selection of the groups has only minimal effect on the group–galaxy cross-correlation function, and justifies our choice of random sampling (method i). The differences in very small-scale clustering in $\mathcal{M}1$ likely arise from sampling fluctuations, since the sample (ii) TNG $\mathcal{M}1$ groups are only taken from approximately 10% of the total volume.

Sample (iii), lower-right panel, shows very different results. The addition of many low-mass groups forces the bias for the lower mass bins down, leading to anti-bias on all scales for $\mathcal{M}1$ and near the group edge for $\mathcal{M}2$. This is likely due to the $\mathcal{M}1$ TNG central galaxies in this sample having a mean luminosity ≈ 0.2 mag lower than the comparison galaxy sample. Using sample (iv), lower-left panel, increases the bias for $\mathcal{M}1$ but it still remains below that of sample (i).

The comparison of these selection methods has demonstrated the importance of mimicking the selection function in GAMA and validated our approach to doing so.

3.C Effect of group selection on the cross-correlation

We show here that our GAMA cross-correlation results are not significantly affected by group selection effects. Fig. 3.15 shows the cross-correlation for the $\mathcal{M}4$ bin in the FoF mock with different artificial selection effects introduced.

To check the effects of missing groups near the field edges, we select groups based on the distance from the field centres. This results in a slight increase in cross-correlation amplitude on large scales, but consistent within uncertainties. We also show the effects of selecting low- and high-redshift groups. There are no significant shifts in either case.

The similarity of all the cross-correlations shown here (and similar results are obtained for the other mass bins and the halo mock) demonstrates that our results are robust to the effects of group selection.

3.D Marked correlations by rank

In order to check the effect of our choice of galaxy or group mass as a mark, we perform an alternative marking using the rank ordering method of Skibba et al. (2013).

We sort the masses in ascending order and assign the rank as the position in the sorted list. Results from using these ranks as marks are shown in Fig. 3.16. When compared to the marked correlations using masses shown in Fig. 3.9, it is clear that the amplitude of the marked correlations is reduced when using ranks. However, the qualitative comparison between different weighting options and samples remains the same.

The most notable difference is the TNG galaxy mass-weighted auto-correlation. In that case, using rank orderings brings the mark into agreement with GAMA on most scales, suggesting that the enhanced mark seen in Fig. 3.9 is due to the differences in the shape of the stellar mass function between TNG and GAMA in Fig. 3.12.

The other visible difference is that the cross-correlation weighted by galaxy masses is greater than 1 when using ranks for GAMA and TNG. However, there is no scale dependence, meaning this is not a signal of mass segregation. Instead it appears to confirm the galaxies from our sample which are in the groups have slightly higher masses than the average of the volume-limited sample.

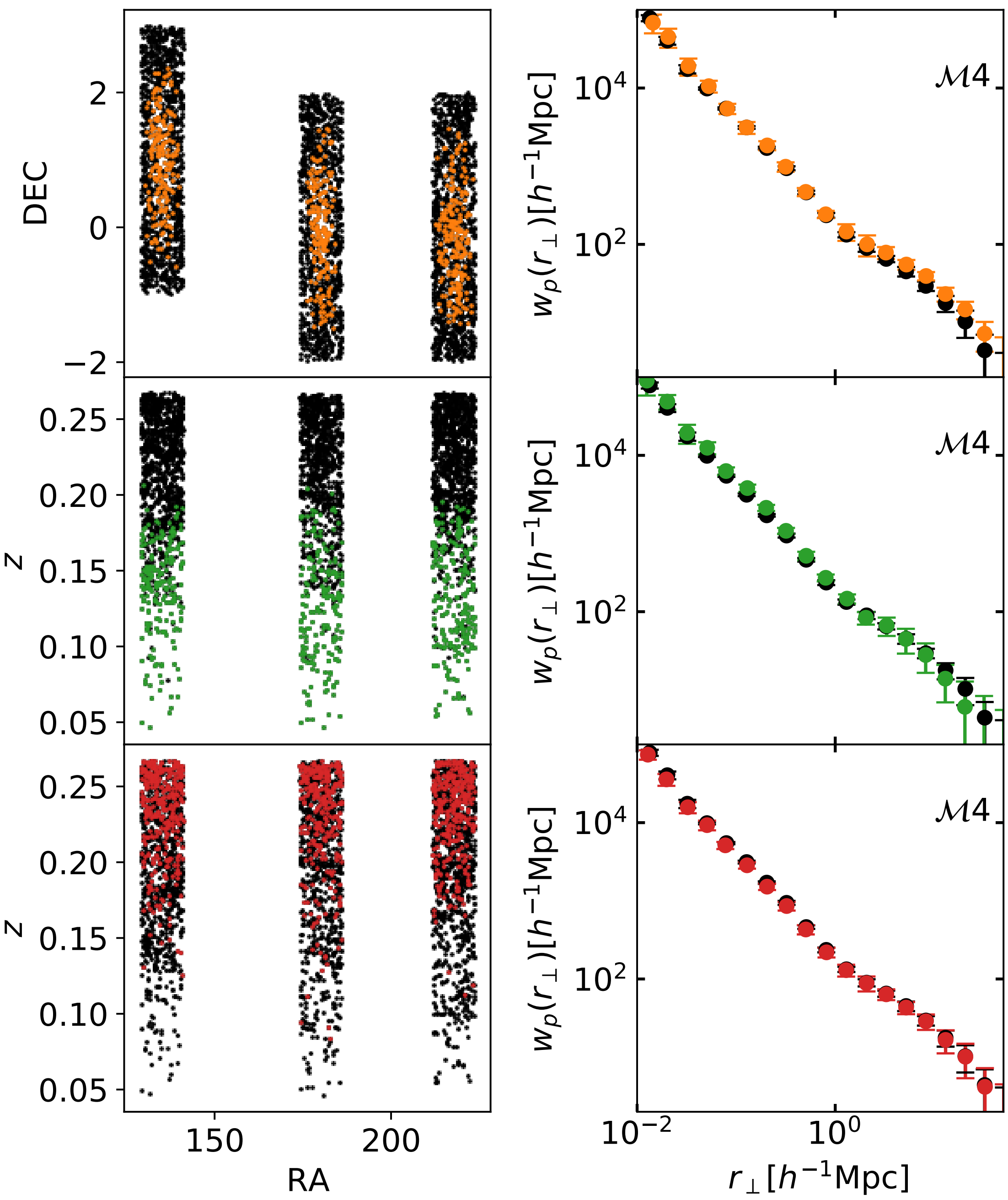

Figure 3.15: The effect of group selection on the group–galaxy cross-correlation function in the FoF mock catalogue for bin $\mathcal{M}4$. Left panels show the selected groups and right panels show the resulting cross-correlation, with black points in all cases showing the full sample. The upper row shows a selection excluding groups near the field edges, the middle panels show low-redshift groups and the lower panels high-redshift groups.

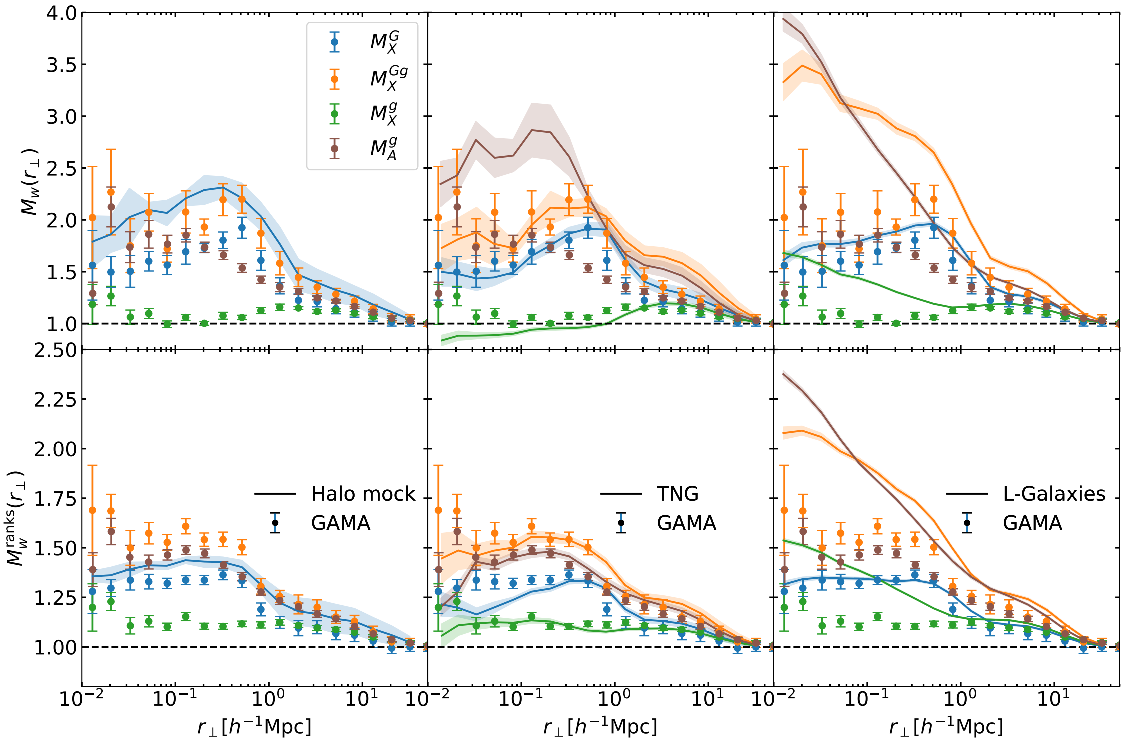

Figure 3.16: Marked correlations using masses and the rank ordering of mass. Upper panels are the same as the lower panels of Fig. 3.9, lower panels show the results from rank ordering the masses. Symbols and error bars show the GAMA results in all panels; lines of corresponding colour show results from the halo mock in the left panels, the Illustris TNG300-1 simulation in the central panels and L-GALAXIES in the right panels.

4

Exploring the effect of baryons on the radial distribution of satellite galaxies with GAMA and IllustrisTNG

S. D. Riggs, J. Loveday, P. A. Thomas,
A. Pillepich, D. Nelson, B. W. Holwerda

Abstract

We explore the radial distribution of satellite galaxies in groups in the Galaxy and Mass Assembly (GAMA) survey and the IllustrisTNG simulations. Considering groups with masses $12.0 \leq \log_{10}(\mathcal{M}_h/h^{-1}\mathrm{M}_\odot) < 14.8$ at $z < 0.267$, we find a good agreement between GAMA and a sample of TNG300 groups and galaxies designed to match the GAMA selection. Both display a flat profile in the centre of groups, followed by a decline that becomes steeper towards the group edge, and normalised profiles show no dependence on group mass. Using matched satellites from TNG and dark matter-only TNG-Dark runs we investigate the effect of baryons on satellite radial location. At $z = 0$, we find that the matched subhaloes from the TNG-Dark runs display a much flatter radial profile: namely, satellites selected above a minimum stellar mass exhibit both smaller halo-centric distances and longer survival times in the full-physics simulations compared to their dark-matter only analogues. We then divide the TNG satellites into those which possess TNG-Dark counterparts and those which do not, and develop models for the radial positions of each. We find the satellites with TNG-Dark counterparts are displaced towards the halo centre in the full-physics simulations, and this difference has a power-law behaviour with radius. For the 'orphan' galaxies without TNG-Dark counterparts, we consider the shape of their radial distribution and provide a model for their motion over time, which can be used to improve the treatment of satellite galaxies in semi-analytic and semi-empirical models of galaxy formation.

4.1 Introduction

In the ΛCDM model of the Universe, galaxies form in dark matter haloes. The dark matter interacts only by gravity, forming structures into which gas collapses to form stars and thus galaxies. However, this gravity-only model of structure is incomplete, as the baryonic physics of the galaxies is known to affect the halo structures in which they reside. One way in which this manifests is in the number and location of substructures, which can host luminous satellite galaxies. This can be explored through the clustering of galaxies or by the radial profiles of satellite galaxy locations within groups.

Much of the importance of understanding the differences between a dark matter-only (DMO) view of the Universe and a full-physics view comes from the use of galaxy formation models built upon DMO simulations. Semi-analytic models of galaxy formation (SAMs; e.g. Henriques et al., 2015; Lacey et al., 2016; Lagos et al., 2018) are one of these. In many SAMs, satellite galaxies are split into two populations: Type 1s and Type 2s. Type 1 satellites reside in resolved dark matter subhaloes, which have not been disrupted, and it is assumed the locations of these are the same as in the underlying DMO simulation. Type 2 satellites, or 'orphan' galaxies, are those which have persisted beyond the lifetime of their host dark matter subhalo (see e.g. Pujol et al. 2017), meaning the locations of these satellites are not available from the simulation itself, and require additional modelling.

These Type 2 satellites are necessary as it has been found that DMO simulations generically have too few subhaloes that would host galaxies in the inner regions of haloes, compared to the number of galaxies seen in observations. For example, this is seen by Angulo et al. (2009), where it is also noted that more massive subhaloes are less centrally concentrated as they experience greater dynamical friction and merge quickly if they are near the centre, and by Bose et al. (2020), who are unable to reproduce the satellite population of the Milky Way from DMO simulations without Type 2 satellites. Further, Behroozi et al. (2019) argue that without orphans the stellar masses of the other satellite galaxies would need to be increased in a manner that is inconsistent with their known evolution. However, Type 2s are often viewed as a resolution issue, and some studies (e.g. Manwadkar & Kravtsov, 2021) have been able to avoid the need for them by using only more massive subhaloes.

On the other hand, cosmological hydrodynamical galaxy simulations allow exploration of the effects of baryons on structures directly. The addition of baryons, hydrodynamics, and galaxy processes changes both the masses (e.g. Sawala et al., 2013; Despali & Vegetti, 2017; Lovell et al., 2018) and the abundances (e.g. Schaller et al., 2015; Chua et al., 2017) of (sub)structures, as well as the distributions (e.g. Marini et al., 2021). In the Illustris simulation, the distribution of satellite galaxies from the centre of their host halo has been considered by Vogelsberger et al. (2014b), where they show that the number density of satellite galaxies is enhanced on small scales compared to subhaloes in a DMO simulation. The distribution of galaxies around clusters is also shown to be different for DMO and full-physics simulations by Haggar et al. (2021), using THETHREEHUNDRED project. They show that DMO simulations both do not have a high enough subhalo density near the cluster centre compared to the full-physics simulations, and have a subhalo density that is too low within groups of satellites which reside at the cluster edge. Further, Nagai & Kravtsov (2005) find that differences between simulations depend on the object selection due to tidal stripping and that the addition of baryons slightly enhances satellite survival. However, baryons can also reduce satellite survival due to disruption by a disc (e.g. Garrison-Kimmel et al., 2017).

The IllustrisTNG cosmological magnetohydrodynamical simulations (TNG, Marinacci et al., 2018; Naiman et al., 2018; Nelson et al., 2018, 2019a; Pillepich et al., 2018b; Springel et al., 2018) are a recent set of simulations consisting of 3 different box sizes, each run at 3 different resolutions. The existence of dark matter-only counterparts to each of these simulations provides the opportunity to explore the effect of baryons on satellite galaxies in more detail and across a greater range of resolutions than has previously been possible. This is particularly true for the highest resolution TNG50 simulation (Nelson et al., 2019b; Pillepich et al., 2019), which is designed to match the resolution of zoom simulations while providing a much greater volume, enabling a detailed look inside simulated galaxies and haloes.

Differences between the full-physics TNG and the DMO TNG-Dark runs have been found in a number of studies, with Chua et al. (2021), Emami et al. (2021) and Anbajagane et al. (2022) finding that the baryons change the properties of haloes, including the shapes. Of most relevance to our study, Bose et al. (2019) show that the distribution of satellite galaxies in the full-physics runs differs from that of subhaloes in TNG-Dark, instead better matching the mass distribution of the host. They also show that the distribution of full-physics satellites can be better reproduced by only considering the few TNG-Dark subhaloes with the highest values of $V_{\rm peak}$, the maximum circular velocity they had at any point in the past.

From an observational perspective, satellite galaxy radial distributions have been inferred in several studies. With the Sloan Digital Sky Survey, Guo et al. (2012) explore the dependence of the profiles on luminosity limits, and Wang et al. (2014) show there is a colour dependence, while Tal et al. (2012) find the distributions can be best fit by including a baryonic contribution near the centre. Budzynski et al. (2012) consider the dependencies of cluster profiles on properties including halo mass and satellite luminosity, comparing the profiles binned by halo mass to some earlier SAMs. This follows the work of Hansen et al. (2005) which additionally looked at the profiles as a function of group size. More recently, cluster profiles were explored by Adhikari et al. (2021), who show differences in the distributions of galaxies of different colours.

The Galaxy and Mass Assembly survey (GAMA; Driver et al. 2009, 2011; Liske et al. 2015; Baldry et al. 2018; Driver et al. 2022b) offers a suitable observational sample of groups to determine the radial distribution of satellites and to compare against simulations, as it has a high completeness in high-density regions. The stellar masses of galaxies in groups has been explored by Vázquez-Mata et al. (2020), and Kafle et al. (2016) find no evidence of variation in satellite galaxy masses with radial position. Recently, Riggs et al. (2021, hereafter RBL21), explored the group–galaxy clustering in

GAMA, finding evidence of a central core to the distribution of galaxies in groups, and a good match between GAMA and TNG clustering results.

In this work we study the locations of satellite galaxies in the TNG simulations and their DMO counterparts, comparing against observational results from the GAMA survey. We do this by using the satellite profile of groups of galaxies, i.e. the number density of satellites as a function of radial separation from the group centre. We examine the differences between full-physics and TNG-Dark a) by selecting satellites above fixed stellar mass limits, b) by identifying their analogue dark-matter subhaloes in the DMO runs, and c) by distinguishing between satellites with and without matched DMO subhaloes. We hence investigate the dependencies of these differences on host and subhalo properties. Finally, we develop models to account for these differences and to correct the satellite locations in DMO simulations. In Section 4.2 of this paper we describe the GAMA and TNG data we use and we explain the methods used to select galaxies and produce profiles; showing the resultant profiles for GAMA, TNG and the TNG-Dark counterparts in Sections 4.3 and 4.4. We provide models for the differences in satellite locations in Sections 4.5 and 4.6 and finally, in Sections 4.7 and 4.8, we discuss our results and provide conclusions.

In this work group (halo) masses are expressed in $\log_{10}(\mathcal{M}_h/h^{-1}\mathrm{M}_\odot)$, taking $\mathcal{M}_h$ to be $M_{200\mathrm{m}}$, the mass enclosed by an overdensity 200 times the mean density of the Universe. We denote the radius of a sphere associated with this overdensity as $R_{200\mathrm{m}}$. We generally express stellar masses from IllustrisTNG in $\log_{10}(\mathcal{M}_\star/\mathrm{M}_\odot)$ using the simulation value of $h = 0.6774$, for consistency with the mass limits given in Pillepich et al. (2018b). The cosmology assumed for GAMA is a ΛCDM model with $\Omega_\Lambda = 0.75$, $\Omega_\mathrm{m} = 0.25$, and $H_0 = h100$ km s^{-1}Mpc^{-1}.

4.2 Data, simulations and methods

4.2.1 GAMA survey

Our group sample from the GAMA survey is derived from the three 12×5 degrees equatorial fields, G09, G12 and G15, of the GAMA-II survey (Liske et al., 2015). GAMA-II has a Petrosian magnitude limit of $r < 19.8$ mag and is well suited to group-finding as it is 96 per cent complete for all galaxies which have up to 5 neighbours within 40 arcsec.

The GAMA Galaxy Group Catalogue (G^{3}Cv9) was produced from the GAMA-II spectroscopic survey using the same friends-of-friends (FoF) algorithm used for GAMA-I by Robotham et al. (2011, hereafter RND11). Group masses are estimates from the total r-band luminosity of the group using the power-law scaling relation for $M_{200\mathrm{m}}$ determined in Viola et al. (2015, equation 37). This scaling relation is consistent with the one recently determined by Rana et al. (2022).

We use the same selection of G^{3}Cv9 groups as RBL21. Groups with 5 or more members are selected, as RND11 find these richer groups to be most reliable. We select these groups if they fulfill the requirements that they are at redshift $z < 0.267$ and have a mass in the range $12.0 \leq \log_{10}(\mathcal{M}_h/h^{-1}\mathrm{M}_\odot) < 14.8$. Additionally, we impose the requirement that `GroupEdge` > 0.9, selecting only those which are estimated to have at least 90% of the group within the GAMA-II survey boundaries. This leaves us with a sample of 1,894 groups with 17,674 galaxies, detailed in Table 4.1.

We select all galaxies within these groups, and identify the centrals using the iterative central from RND11, namely the galaxy which remains after iteratively removing the galaxy furthest from the centre of light of the remaining group members until only one is left. All other galaxies within the groups are then satellites. The iterative centre was shown to be most reliable in GAMA-I by RND11, and RBL21 confirmed this is also the case in GAMA-II. In most cases the iterative central is the brightest galaxy of the group.

4.2.2 Mock group catalogue

To determine systematics within GAMA we use the mock catalogues created for GAMA-I (mocks for GAMA-II are in development). The mock galaxy catalogues consist of 9 realisations of a lightcone created from the GALFORM (Bower et al., 2006) SAM run on the Millennium Springel et al. (2005) DMO simulation. Further details about the creation of these mocks are given in RND11.

Two different catalogues of mock groups have been created from the GALFORM galaxy mocks, allowing us to explore any biases introduced by the group finding algorithm in GAMA:

- The *halo mocks* (`G3CMockHaloGroupv06`) contain the intrinsic dark matter haloes of the Millennium simulation which the mock galaxies reside in.

- The *FoF mocks* (`G3CMockFoFGroupv06`) contain groups derived by applying the same FoF algorithm used for the GAMA groups to the mock galaxies.

Comparing the halo and FoF mocks allows us to explore how accurately the GAMA FoF algorithm detects the intrinsic haloes, providing a way of qualifying the differences between the group finding methods in observations (FoF mock) and simulations (halo mock). This then informs us how directly comparable the GAMA observational sample is to simulations such as TNG.

We select groups from both the halo mocks and FoF mocks using the same criteria as GAMA, requiring redshift $z < 0.267$, halo mass in the range $12.0 \leq \log_{10}(\mathcal{M}_h/h^{-1}\mathrm{M}_\odot) < 14.8$ and at least 5 members.

4.2.3 TNG simulations

We explore the effect of baryons with the IllustrisTNG cosmological magneto-hydrodynamical simulations (TNG, Marinacci et al., 2018; Naiman et al., 2018; Nelson et al., 2018, 2019a,b; Pillepich et al., 2018b, 2019; Springel et al., 2018), and their matching TNG-Dark dark matter-only N-body simulations. The TNG simulations were run using the AREPO code (Springel, 2010) and incorporate the key physical processes of galaxy formation, including gas heating and cooling, star formation and feedback from

Table 4.1: Numbers of groups and galaxies in each mass bin selected from GAMA, the mock catalogues and the GAMA-matched TNG300-1 sample. Values given for the mock catalogues are the mean from the 9 realisations.

		GAMA		Halo Mocks		FoF Mocks		TNG300-1	
	$\log_{10}(\mathcal{M}_h/h^{-1}\mathrm{M}_\odot)$	N_{grps}	N_{gals}	N_{grps}	N_{gals}	N_{grps}	N_{gals}	N_{grps}	N_{gals}
$\mathcal{M}1$	[12.0, 13.1]	380	2,204	352	2,210	346	2,272	368	2,152
$\mathcal{M}2$	[13.1, 13.4]	547	3,646	383	2,890	401	2,775	404	2,941
$\mathcal{M}3$	[13.4, 13.7]	566	4,723	366	3,815	523	4,233	413	3,765
$\mathcal{M}4$	[13.7, 14.8]	401	7,101	306	8,377	430	8,205	467	8,364
Total	[12.0, 14.8]	1,894	17,674	1,407	17,291	1,699	17,486	1,652	17,222

supernovae and black holes. For a full explanation of the processes included we refer the reader to Pillepich et al. (2018a) and Weinberger et al. (2017).

TNG consists of simulations at three different box sizes, each run at a variety of resolutions. We primarily use the runs with the best resolution; TNG50-1 with box size $35\,h^{-1}$ Mpc and baryonic mass resolution $5.7 \times 10^4 h^{-1}\mathrm{M}_{\odot}$, TNG100-1 with box size $75\,h^{-1}$ Mpc and baryonic mass resolution $9.4 \times 10^5 h^{-1}\mathrm{M}_{\odot}$, and TNG300-1 with box size $205\,h^{-1}$ Mpc and baryonic mass resolution $7.6 \times 10^6 h^{-1}\mathrm{M}_{\odot}$. We additionally include the runs at worse resolution in some of our analysis. The second tier of resolution, denoted with -2, has baryonic masses 8 times larger than the -1 runs, and the third tier, denoted with -3, has baryonic masses 64 times larger than the -1 runs.

We select galaxies from these simulations where `SubhaloFlag` equals 1, i.e. objects identified as cosmological in origin (rather than a fragment or substructure formed within an existing galaxy), and where the stellar mass within twice the half mass radius exceeds 10^7, 10^8 and $10^9\mathrm{M}_{\odot}$ for TNG50-1, TNG100-1 and TNG300-1 respectively, limits which correspond to $\approx$ 100 stellar particles. We take the stellar mass of galaxies to be that within twice the half mass radius, and for the total subhalo mass we take the mass of all particles bound to the subhalo.

When comparing against GAMA we use TNG300-1, as this gives the largest sample of high-mass groups. We select galaxies from the simulation snapshot at $z = 0.2$, close to the GAMA mean redshift, and bring the stellar masses into agreement with the TNG100-1 resolution (as well as with GAMA) by multiplying by the resolution correction factor of 1.4 suggested by Pillepich et al. (2018b).

Elsewhere when looking at simulations of differing resolutions we use the snapshots at $z = 0$ and we do not apply resolution corrections as we are interested in the direct simulation outputs, and we mainly instead use the better resolution of TNG50-1 and TNG100-1 to perform more detailed examinations of the satellite galaxies.

Each TNG run has a matching TNG-Dark run with the same box size and resolution. These allow direct comparisons between the outcome of modelling the Universe in DMO and that of including hydrodynamics and galaxy physics to model the baryons.

4.2.4 Group radial profile calculation

Profiles are derived for GAMA as a function of the projected radius $r_{\perp}$, calculated in the standard way (e.g. Fisher et al., 1994). The vector separation of a satellite at position $\boldsymbol{r}_{\rm sat}$ from a group at $\boldsymbol{r}_{\rm grp}$, is given by $\boldsymbol{s} = \boldsymbol{r}_{\rm sat} - \boldsymbol{r}_{\rm grp}$ and the vector to the midpoint of the pair from an observer at the origin by $\boldsymbol{l} = (\boldsymbol{r}_{\rm sat} + \boldsymbol{r}_{\rm grp})/2$. These are used to find the line-of-sight separation $r_{\parallel} = |\boldsymbol{s}.\hat{\boldsymbol{l}}|$, with $\hat{\boldsymbol{l}}$ being the unit vector in the direction of $\boldsymbol{l}$, and this leads to the projected separation $r_{\perp} = \sqrt{\boldsymbol{s}.\boldsymbol{s} - r_{\parallel}^2}$. We do not apply any limits on the line-of-sight distance, instead simply including all galaxies allocated to the groups (although we note that this choice implicitly introduces limits due to the line-of-sight linking condition in the RND11 FoF algorithm).

When measuring projected two-dimensional profiles for TNG we take the projection to occur along the z-axis, but have checked that our results are not sensitive to the choice of projection axis. With TNG we can also measure three-dimensional profiles, which we are unable to do for GAMA. All satellite galaxies which are members of the FoF group are included, and distances measured relative to the centre of the FoF group.

When calculating profiles, we additionally divide the data into bins of group masses, and include two different forms:

Firstly, the average group profiles, which we define as the density of galaxies as a function of physical projected separation from the group centre. This is calculated for each group mass bin by counting the number of satellites in radial bins and dividing by the total number of groups in the mass bin.

Secondly, the normalised profiles, which we define as the density of galaxies using separations as a fraction of the group $R_{200\mathrm{m}}$. The amplitudes of these are divided by the number of galaxies in the mass bin. This can be used to look for differences in the shape of the satellite distribution in different group mass bins, as it normalises out the trend for more massive groups to be more extended and include more galaxies.

We calculate the uncertainties on profiles using jackknife resampling for GAMA and TNG. For GAMA we split the sample into 9 samples in RA, and with TNG we divide the boxes into 8 sub-cubes, showing uncertainties as the square root of the diagonal terms in each covariance matrix. The mock catalogues contain 9 realisations of the GAMA survey, and so we can estimate the uncertainties by using the scatter between the realisations.

4.3 Radial profiles from GAMA and TNG300-1

In this section we examine the satellite distribution of GAMA groups, and compare this against a sample of groups and galaxies from TNG300-1 designed to match the GAMA selection.

4.3.1 Selecting groups from TNG300-1 to match GAMA

When comparing against GAMA data, groups in TNG300-1 are chosen using a modified form of the selection function in RBL21. This modification is necessary as RBL21 only identify if groups have at least 5 visible galaxies, whereas with the simulated data we can in principle identify all the visible galaxies in the chosen groups.

To select the group and galaxy sample we require galaxy luminosities, for which we use the dust-corrected r-band luminosities of dust model C from Nelson et al. (2018). We then perform the following procedure for galaxy and group selection:

1. Find the comoving distance at which each simulated galaxy has an observed magnitude of $m_r = 19.8$ mag.

2. Determine the selection probability by finding the volume of the GAMA lightcone out to this comoving distance and dividing by the total GAMA volume for $z < 0.267$. We additionally multiply the selection probabilities by 0.95 to account for our GAMA redshift limit applying to a sample K-corrected to be 95% complete.

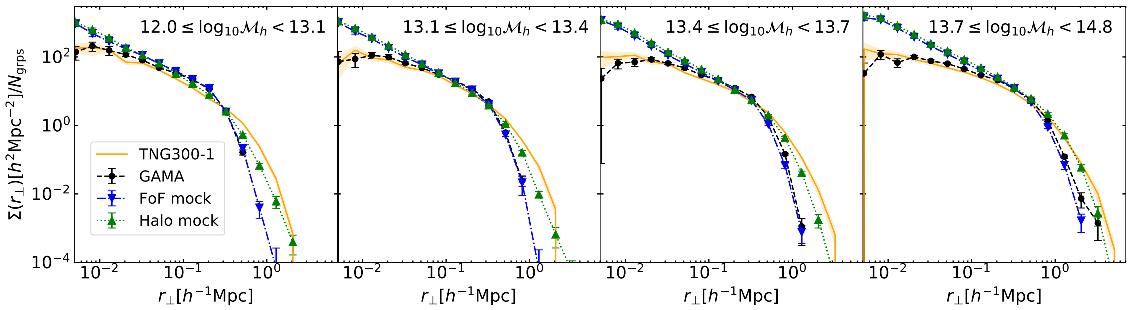

Figure 4.1: Satellite galaxy projected radial profiles in the four mass bins listed in Table 4.1 for selected groups and galaxies from GAMA, the mock catalogues and GAMA-matched TNG300-1. In all panels black circles show the GAMA results, blue downwards triangles the FoF mocks, green upwards triangles the halo mocks and orange solid lines TNG300-1.

3. Assign each simulated group a random probability and select the galaxies whose selection probability is greater than or equal to the random probability assigned to their host group.

4. Include groups (and their constituent visible galaxies) only if at least 5 galaxies have been identified as visible.

We show the mass function of the groups we have selected from GAMA, the mocks and TNG300-1 in Appendix 4.A, demonstrating our group selection method for TNG300-1 reproduces the expected shape of the mass function, although with differences in the detail due to different underlying galaxy populations. Small differences between GAMA and TNG are partly caused by nearby GAMA groups which contain some galaxies below the mass resolution limit of TNG300-1, although we have checked that the inclusion of these does not impact the derived profiles.

4.3.2 Average group profiles

In Fig. 4.1 we show for the first time direct results for radial distributions of satellite galaxies in GAMA groups, calculating the average group profiles in the four mass bins considered. In all the group samples used, increasing group mass leads to a greater number of satellites and wider groups due to halo radius increasing with mass.

The shape of the profiles is such that they are almost flat on the smallest scales, $r_\perp < 0.02\,h^{-1}$ Mpc. With increasing scale there is then a gradual decrease in density until $r_\perp \approx 0.5\,h^{-1}$ Mpc, where a rapid drop is visible.

Comparing with the profiles obtained from the mock catalogues allows us to investigate the effects introduced by the use of the FoF group finder for GAMA. On small scales the profiles are similar for the halo and FoF mocks, with the density increasing to the smallest scales considered. The similarity of the mocks suggests that GAMA is reliable at small halo-centric distances, in agreement with the conclusions of Driver et al. (2022a), as the FoF algorithm accurately reproduces the intrinsic haloes. However, it is noteworthy that the survey mocks and GAMA have a very different behaviour. This is most likely driven by inaccuracies in the locations of orphan satellites in GALFORM (see e.g. Pujol et al., 2017), and this in turn provides further justification for our objective of correcting for issues in mocks based on DMO simulations.

At the turnover radius beyond which the density drops in the $\mathcal{M}1$ bin ($r_\perp \approx 0.2\,h^{-1}\,$Mpc), the FoF mocks have slightly more galaxies that the halo mocks. This is probably due to chance alignments of galaxies on the sky being counted as small groups, as this effect is not present in the higher mass bins, and the GAMA distribution is therefore expected to be similarly boosted slightly on these scales. Beyond this turnover radius, the FoF mocks drop off much faster than the halo mocks in all bins, suggesting the outer edges of the groups are missed by the FoF group finder. At the outer edges, GAMA and the FoF mocks display very similar results, and from this we suggest that the true profile of GAMA groups (that is comparable to simulations) would lie about where that of the halo mocks is on these scales.

Overall the mock comparisons tell us that GAMA profiles should be reliable on scales smaller than the turnover, but likely underestimate the number density at the outer edge of the groups.

The projected satellite galaxy profile of the GAMA-matched TNG300-1 sample is consistent with GAMA on small scales where GAMA is reliable, with the flattening of the profile at $r_\perp \approx 0.02\,h^{-1}\,$Mpc being consistent between the two within uncertainties.

At face value the TNG300-1 profiles are always above the GAMA profiles on large scales ($r_\perp \gtrsim 0.5\,h^{-1}\,$Mpc). However, the differences seen between the halo and FoF mock catalogues show that there are significant differences between the group membership in simulated and observed groups on these scales. As we previously noted, correcting for this difference in methods possibly leads to GAMA profiles which are similar to the halo mocks on large scales. This suggests that the distribution of galaxies around groups in TNG300-1 is similar to the observations across all scales, although with a slight excess of galaxies around the edges of low mass groups.

We note that the flattening of the profiles on the smallest scales in both GAMA and TNG300-1 could be affected by misidentification of the central galaxy in the groups, although we do not see evidence of this. In GAMA previous studies (RND11 and RBL21) find the iterative centrals we use are least impacted by mis-centring, and the central usually corresponds to the brightest galaxy in the group. In TNG the central resides at the centre of potential of the halo and is usually the most massive galaxy in the group. Further, the fact that we see a flattening in both cases, and the consistency between the mocks on these scales, supports the idea that it is a physical effect.

4.3.3 Normalised profiles

We investigate changes in the profile with group mass by normalising the satellite distances by group radius $R_{200\mathrm{m}}$ and the profile amplitude by the total number of satellites.

The normalised profiles for GAMA and the GAMA-matched TNG300-1 sample are shown in Fig. 4.2. We have not included the mocks here as the conclusions from these remain the same as above, that GAMA profiles should be reliable on small scales but

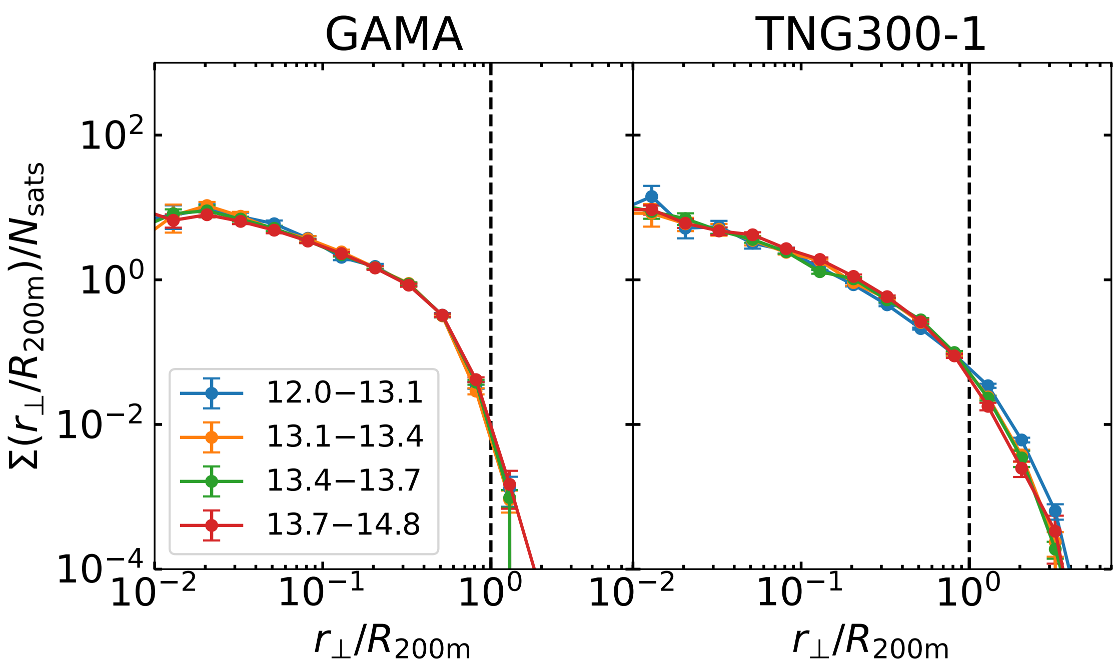

Figure 4.2: Satellite galaxy projected profiles in the four group mass bins for our GAMA group sample and GAMA-matched TNG300-1 sample, calculated as a function of normalised radius and then normalised by the total number of satellites. The vertical dashed lines mark the radius $R_{200\mathrm{m}}$.

drop too rapidly on large scales.

There is no mass dependence visible in the normalised profiles for GAMA, with the profiles being consistent across all scales in the mass bins we use. This suggests a universal shape to the satellite distribution in GAMA galaxy groups, with the number and average radial separation of galaxies depending only on the group mass.

TNG300-1 shows exactly the same result of no group mass dependence to the profile shape. We can also see more clearly here that this trend continues to the edge of the groups.

4.4 Comparing full-physics and DMO distributions

Here we explore the differences between satellite galaxy profiles of groups in TNG and the equivalents from TNG-Dark runs, in order to determine the extent to which baryons adjust the shape of the profile.

4.4.1 Groups and subhaloes from DMO runs

We make use of two methods to extract samples from TNG300-1-Dark to compare to the full-physics run. Here, as we are just comparing between simulation runs, we do not apply the group selection to match GAMA. Instead, we simply select all galaxies with $\mathcal{M}_\star \geq 10^9\mathrm{M}_\odot$ in groups with $12.0 \leq \log_{10}(\mathcal{M}_h/h^{-1}\mathrm{M}_\odot) < 14.8$.

The simplest method to generate a sample of TNG300-1-Dark subhaloes that correspond to the selected luminous satellites is an abundance matching approach. We perform this abundance matching using the maximum circular velocity ($V_{\rm max}$) of each subhalo, as it is expected this will correlate better than halo mass with galaxy properties (e.g. Zehavi et al., 2019). In this case we sort the subhaloes in the dark matter-only simulation by their $V_{\rm max}$, and select those with the greatest $V_{\rm max}$ so we have the same number of dark matter subhaloes as there are galaxies above the resolution limit in the full-physics run.

The second, more comprehensive, method we use is the subhalo SubLink matches of Rodriguez-Gomez et al. (2015), selecting the matching subhalo from the dark matter-only simulation for each of our selected TNG300-1 galaxies. These matches were generated by determining the subhaloes containing the same particles, and calculating a matching score by weighting these particles inversely by their rank ordered binding energy. For each TNG satellite, the TNG-Dark subhalo with the highest matching score is taken to be the best match. This can in some cases lead to multiple TNG galaxies matching to a single TNG-Dark subhalo. We remove these duplicates from the TNG-Dark run so each subhalo is only included once.

However, these duplicates are important for the TNG run as they allow us to split the TNG300-1 satellites into the equivalent of Type 1 and Type 2 satellites in SAMs. Type 1 satellites are those contained in dark matter subhaloes, so all uniquely matched satellites are automatically Type 1s. Type 2 satellites can then be considered as the unmatched TNG satellites. A similar application of matching is used by Renneby et al. (2020).

We use $V_{\rm max}$ to determine the type for duplicated matches at this stage for consistency with the abundance matching method. The matched TNG300-1 galaxy with the highest maximum circular velocity is taken to be the Type 1 (or this may be the central Type 0), while all other matches are allocated as a Type 2 without a matching TNG300-1-Dark subhalo.

These two choices of matching method therefore give us slightly different samples of TNG-Dark subhaloes. In the first selection we have the same number of objects as TNG, but they may not be contained in the same environments, whereas in the second selection the subhaloes we select are known to be comparable to the TNG sample, but the number of objects differs.

4.4.2 Radial profiles in TNG300-1-Dark

In Fig. 4.3 we compare the profiles of satellites in TNG300-1 against those from the matched subhaloes in the TNG300-1-Dark simulation at $z = 0.2$. This is the sample used in Fig. 4.1 but without the group selection method applied.

It is clear that on large scales there is a close agreement between TNG and TNG-Dark. However, at small halo-centric distances, the density of TNG satellites is enhanced over their matched subhaloes in the TNG-Dark simulation (solid blue vs. orange and green dashed curves). In particular, the number density profile of the TNG-Dark subhaloes flattens, while the TNG profile of luminous satellites continues to rise down to smaller scales, albeit at a reduced rate. The two options for selecting subhaloes from the TNG-

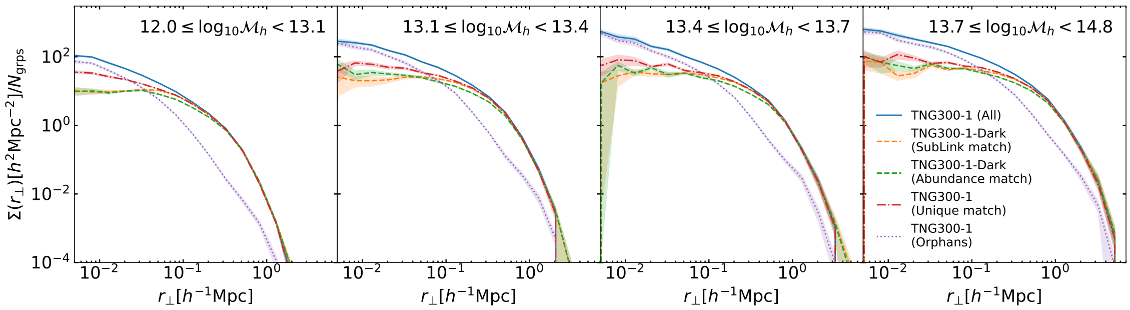

Figure 4.3: Satellite galaxy projected profiles at $z = 0.2$ for TNG300-1 compared to equivalents from the TNG300-1-Dark run. The panels show the same mass bins as given in Table 4.1, but now including all galaxies with $\mathcal{M}_\star > 10^9\mathrm{M}_\odot$ in groups, meaning the amplitude of the TNG300-1 profile has increased relative to Fig. 4.1. Two different methods of selecting matched TNG300-1-Dark subhaloes are used, as explained in Section 4.4.1. We also show the TNG300-1 galaxies split by those which can be matched to TNG300-1-Dark satellites and those which are unmatched (orphans).

Dark simulation are seen to be consistent, with the profiles matching within uncertainties, suggesting this is not just a result of the matching scheme used.

This difference between TNG and TNG-Dark can be attributed to two effects, which we also show in Fig. 4.3. Firstly, there is evidence of an inwards displacement in the TNG simulation, with the directly matched (Type 1) satellites being closer to the centre in TNG. Secondly, there is a population of galaxies that are not uniquely matched to TNG-Dark subhaloes (Type 2s), suggesting that they have been merged or disrupted in the TNG-Dark simulation but not in TNG. Both of these effects primarily affect scales $r_\perp \lesssim 0.1\,h^{-1}$ Mpc, but there is some impact out to at least $r_\perp \approx 0.5\,h^{-1}$ Mpc in the largest groups. Together, these effects suggest baryons enhance both the rate of inwards motion and the survival time of subhaloes that host galaxies.

We note that in all mass bins the dominant effect on the smallest scales is the population of unmatched satellites, and that the contribution due to the inwards displacement of matched satellites decreases as halo mass increases and the groups become wider.

4.4.3 Radial profiles at differing resolutions

To explore the effect of resolution on the profiles in the TNG simulations, we measure the average group profile in each of the TNG50-1, TNG100-1 and TNG300-1 simulations at $z = 0$, and in their TNG-Dark equivalents. While we could compare resolutions by using the different runs at identical box size, we choose to use the largest box available at each resolution to give us a larger galaxy sample, although we show in Appendix 4.B that the same conclusions are reached using different resolutions at the same box size. To enable comparison between the different simulations we apply the same mass limit in each case, $\mathcal{M}_\star \geq 10^9\mathrm{M}_\odot$, although the resulting low number counts for TNG50-1 make comparisons involving it challenging. We show in Appendix 4.C that the choice of mass limit only affects the amplitude of the profile, and that the full-physics runs show very

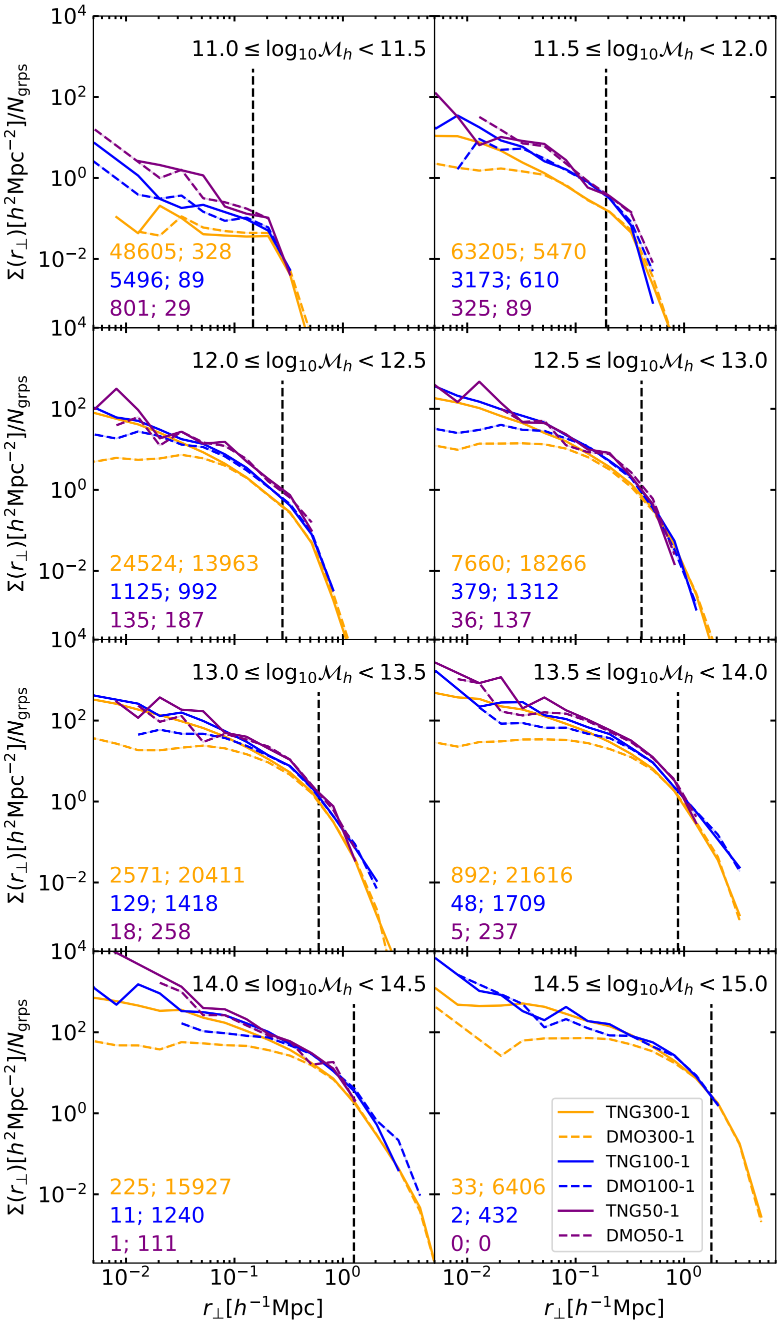

Figure 4.4: Satellite galaxy projected profiles at $z = 0$ for TNG50-1 (purple), TNG100-1 (blue) and TNG300-1 (orange), with their TNG-Dark equivalents in a range of halo mass bins. Galaxies are selected with $\mathcal{M}_\star \geq 10^9\mathrm{M}_\odot$ and halo mass limits are given in $h^{-1}\mathrm{M}_\odot$. The numbers in the lower left of each panel give firstly the number of groups and then the number of satellites in the TNG run presented in the same colour. The vertical dashed lines show the median $R_{200\mathrm{m}}$ of the TNG300-1 groups in that panel.

close agreement when normalised. We have selected TNG-Dark subhaloes which are equivalent to TNG satellites using the SubLink matching.

Fig. 4.4 shows the radial profiles from these samples in bins of host halo mass. In group mass bins of increasing mass we see the profile increases in amplitude and extends to greater radii, as we observed in GAMA.

It is apparent that there is a reasonable consistency between the different TNG simulation resolutions in most group mass bins. The main exception is the least massive bin where the majority of haloes contain no satellites with stellar mass above $10^9\mathrm{M}_\odot$. We also note that the most massive bins are subject to a high uncertainty due to containing very few groups.

The agreement between the distributions of well-resolved satellites at differing resolution matches the conclusions of Grand et al. (2021) with the AURIGA simulations. However, as shown in that work, this consistency is likely to break down for satellites with very few stellar particles.

Looking at the TNG-Dark results, we find the same effect noted before of flatter radial profiles in the centres of groups than in the full baryonic runs, at least for subhaloes matched to satellites with a given minimum stellar mass. However, such flattening varies across simulations, with the DMO profiles becoming flatter at small distances for progressively worse numerical resolution.

The implication of this is that the extent of the differences between TNG and TNG-Dark are affected by the simulation resolution, and that this is driven by differences with resolution across DMO runs—the full-physics runs are in much better agreement across the three resolution levels; see also Fig. 4.21. Instead, the changes in the TNG-Dark profiles for different resolutions are unlikely to be entirely physical and instead may be the result of the numerical disruption effects found by van den Bosch et al. (2018). However, there are still profile differences in TNG50-1, the highest resolution simulation, (and these differences become more apparent if lower mass satellites are also included) so there may be a physical effect at work here too. This could be due to the baryonic feedback, which is known to change the shapes of the haloes (Chua et al., 2021), but could also be related to the baryonic core keeping the satellites more bound and so less prone to disruption (both physical and numerical). This would match the findings of earlier works such as Weinberg et al. (2008). We return to the question of whether the effects we see are physical or numerical in Section 4.7.3.

4.5 Fitting differences between full-physics and DMO runs

Having established that significant differences exist between satellite locations in the full-physics and DMO runs, we now aim to create models to correct for these differences. To create these models we use the runs with the best resolution, TNG50-1 and TNG100-1, as these allow us to explore smaller scales and lower masses with more confidence. Following this we use the runs at worse resolution to explore the dependence of the required correction on simulation resolution.

4.5.1 Splitting Type 1 and Type 2 satellites

We first split the satellite sample into Type 1s (which have a matching TNG-Dark subhalo) and Type 2s (whose subhalo has disrupted or merged in TNG-Dark), with a similar method to that which we used for TNG300-1-Dark in Section 4.4.1.

Using the SubLink matches of Rodriguez-Gomez et al. (2015) we select the matching TNG-Dark subhalo for each full-physics galaxy. Uniquely matched satellites become Type 1s. In the cases where the matches are not unique we assign the best match as the Type 1, and all others as Type 2s. Here, we determine the best match by picking the subhalo which has the highest matching score, as determined by the SubLink matching algorithm.

To clean our sample further, Type 1 satellites are removed if the central and satellite assignment differs between TNG and TNG-Dark, leading to 971 subhaloes being excluded in the case of TNG50-1 (about 6% of the total). The excluded fraction becomes smaller in the simulations with worse resolution. There are a few possible reasons the type (central/satellite) can differ between TNG and TNG-Dark: either the structure formation has occurred differently, the matching scheme is inaccurate, the FoF algorithm has combined two close haloes, or the subhalo has been accreted earlier in one simulation than the other. The majority of the subhaloes we remove have a radial separation from the central exceeding the host $R_{200\mathrm{m}}$, suggesting they have either only just been accreted or are part of neighbouring haloes joined by the FoF algorithm. However, there are a small number closer to the central, suggesting different structure formation or incorrect matching. We do not attempt to correct these matches, instead just excluding these subhaloes.

We also exclude Type 1 satellites where the host halo mass differs enough to suggest that they are attached to different groups. This choice of halo mass difference is somewhat subjective, but we have determined that excluding cases where $|\log_{10}(\mathcal{M}_h^{\mathrm{TNG}}/\mathcal{M}_h^{\mathrm{DMO}})| > 0.15$ removes all clearly different hosts, while allowing for some scatter between the simulations.

For TNG50-1 this gives us a sample size of 6,915 Type 1s, 781 Type 2s and 8,237 central Type 0s with stellar mass $\mathcal{M}_\star \geq 10^7\mathrm{M}_\odot$. This rises in TNG100-1 to 24,759 Type 0s, 16,842 Type 1s and 2,862 Type 2s with stellar mass $\mathcal{M}_\star \geq 10^8\mathrm{M}_\odot$.

4.5.2 Model for Type 1s

We first consider the modelling of the Type 1 satellites, aiming to quantify the expected difference in position between the subhaloes in the TNG and TNG-Dark runs. We describe our model here, before giving the parameters for it in Section 4.5.4.

While the differences in satellite positions between full-physics and DMO runs may depend on any properties of the subhaloes or host haloes, we find a simple model adequately describes the differences. We first present this model, then explore the reasons why we are able to exclude other dependencies.

Our model for the correction to Type 1 positions includes only the *comoving* radial

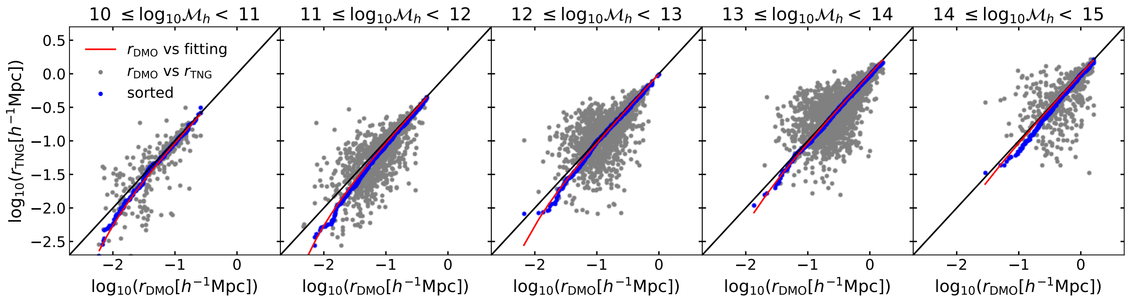

Figure 4.5: Fitting to the difference between matched satellite positions in TNG50-1 and the TNG50-1-Dark run at $z = 0$, with the data split into bins of host halo mass, given in $h^{-1}\mathrm{M}_\odot$, and galaxies shown for $\mathcal{M}_\star > 10^7\mathrm{M}_\odot$. In each panel, the grey background points show the scatter between exactly matched satellites. The blue points then show the result of sorting the positions by distance from the centre. Finally, the red lines show our fit.

distance from the group centre. We model the correction to the position as a power law,

$$\log_{10}(r_{\mathrm{TNG}}/r_{\mathrm{DMO}}) = -(r_{\mathrm{DMO}}/a)^b \tag{4.1}$$

where r_{TNG} is the radial position in the full-physics run and r_{DMO} is the radial position in the DMO run.

To determine the parameter values in this model we first sort the positions of the satellites in ascending order independently for the TNG and TNG-Dark runs, then fit our model to the sorted positions. This is done to produce an overall trend in the position difference.

In doing this we are discarding the true associations between the TNG and TNG-Dark runs, but without sorting the positions we would potentially fit to spurious trends caused by orbital phases. Objects close to the centre in either simulation will be near pericentre, and so a small difference in orbital phase between simulations will result in them being further from the centre in the other. Therefore, without sorting the positions, we would conclude that objects near the centre should always be moved outwards. Similarly, this effect matters when considering possible dependencies on variables which may correlate with radial position.

The position differences between TNG and TNG-Dark satellites, with the results of applying this model in TNG50-1, are shown in Fig. 4.5. Note that while we have split the sample into halo mass bins for this figure, we perform the fitting on the whole data sample together and the fit parameters used are the same in each panel. The grey points show there is a large scatter between the raw positions in the TNG and TNG-Dark runs, but the sorted positions in blue show a clear trend for inwards displacement in the full-physics case. Our fitted results are then shown in red, demonstrating a good match between our model and the sorted data across the full range of halo masses.

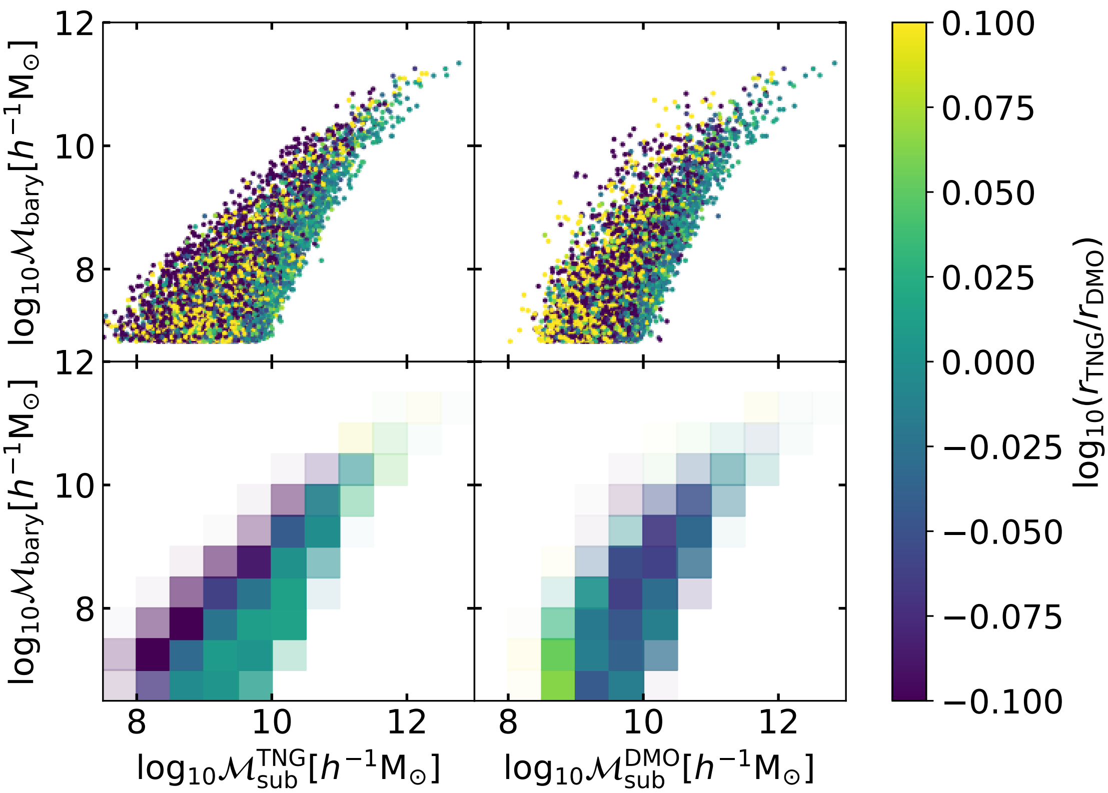

Figure 4.6: Dependence of the position difference of Type 1s on subhalo total mass and baryonic mass at $z = 0$. Left panels show the dependence on subhalo mass in TNG50-1, while the right panels show the dependence using the total subhalo masses of matched TNG-Dark subhaloes. Upper panels show position differences of individual satellites, and the lower panels the binned averages of these.

4.5.3 Dependencies on masses

We now discuss why we are able to exclude other dependencies from our model, despite it being anticipated that the differences between TNG and TNG-Dark may depend both on the properties of the subhalo and those of the host halo. Firstly we note that the aim of our model is to explain the differences between the TNG and TNG-Dark simulations, while also providing a method that can easily be applied to models such as SAMs and HODs. For this reason we do not attempt to include all the possible dependencies in our model (for example dependencies on the star formation rate, colours and gas fraction of galaxies may be challenging to incorporate in SAMs). Additionally, the impact of feedback from active galactic nuclei (AGN) and supernovae on subhaloes may not be consistent between different hydrodynamic simulations, so we do not want to directly consider these effects.

One of the simplest dependencies we expect is with mass, and halo mass, subhalo total mass and subhalo baryonic mass may all have an impact.

In Fig. 4.6 we show the relation between subhalo baryonic mass and subhalo total mass in TNG50-1 and for matched TNG-Dark subhaloes. The colour scaling represents the position difference and shows a large scatter, and this spread increases at low total

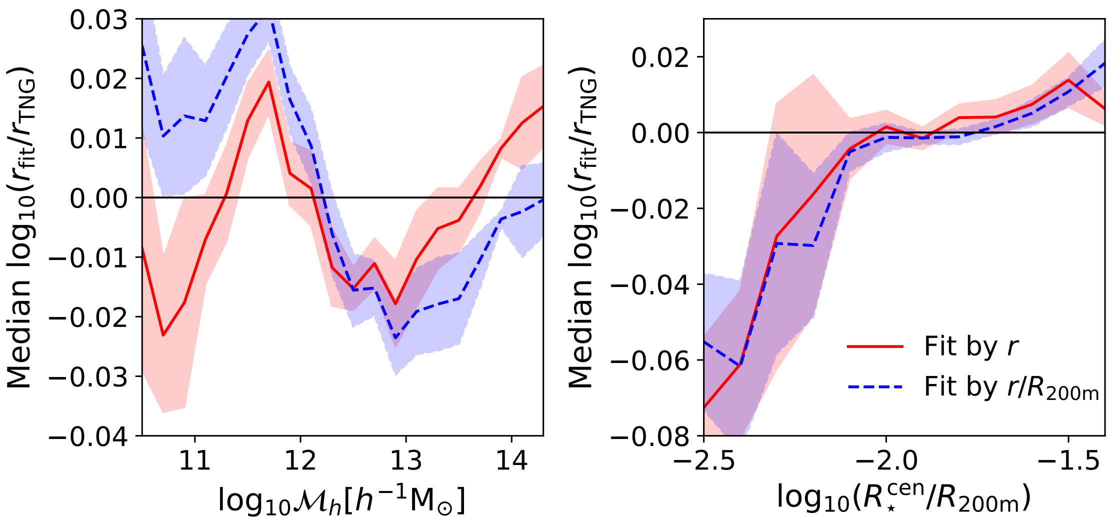

Figure 4.7: Residuals of the Type 1 position fitting model on TNG50-1 at $z = 0$ for galaxies with $\mathcal{M}_\star > 10^7\mathrm{M}_\odot$. The left panel shows the dependence on halo mass, while the right panel shows the dependence on the relative stellar size of the central galaxy.

subhalo masses. To account for this, in the lower panels we split the sample into bins of subhalo mass and colour the bins by the average position difference. On the left, using the TNG subhalo masses, there is a trend for galaxies which have a high baryonic mass for a given total subhalo mass to be closer to the group centre in TNG (having a lower $\log_{10}(r_{\rm TNG}/r_{\rm DMO})$, coloured purple in Fig. 4.6). However, this trend is not present in the right panels, using TNG-Dark subhalo masses. This shows that while the baryonic fraction is related to the reduced halo-centric distances it is likely to be a secondary effect, such that the closer proximity to the centre causes stripping of some of the subhalo dark matter, so increasing the baryon fraction. The secondary nature of this effect, and the lack of this effect in the TNG-Dark panel, means this is not an effect which we need to include in our model.

Fig. 4.5 has already demonstrated that our model works across different halo masses, so we are able to exclude halo mass as an explicit part of our model. However, there is a residual effect of halo mass on the position differences. In the left panel of Fig. 4.7 the median difference between the sorted position in the TNG simulation and our model is plotted. To smooth this we use overlapping mass bins, and the errorbars are calculated using jackkknife. It is clear that there is some halo mass dependent residual. Comparing this to Fig. 4 of Weinberger et al. (2017) shows a very similar trend to that of the difference in halo masses between TNG and TNG-Dark. In that work, this is attributed to the effect of stellar and AGN feedback, and so it is likely our residual is present for the same reasons. In particular, the drop at $\mathcal{M}_h \approx 10^{12}h^{-1}\mathrm{M}_\odot$ is likely due to the onset of feedback from supermassive black holes at this mass scale in TNG.

We also show the comparison here of the outcome of performing our fitting procedure using *normalised* radial distance ($r/R_{\rm 200m}$), rather than the *comoving* radial separation (r). For much of the mass range the discrepancy associated with the two separation options is comparable. However, using normalised distances a clear split is seen, with overestimation in haloes of $\log_{10}(\mathcal{M}_h/h^{-1}\mathrm{M}_\odot) \lesssim 12$, and underestimation in more massive haloes. This gives a slight advantage to using comoving separations in low-mass haloes, with normalised distances only showing a clear advantage for $\log_{10}(\mathcal{M}_h/h^{-1}\mathrm{M}_\odot) \gtrsim 14$. This motivates our usage of comoving separations in our model.

One further dependence can be seen in the right panel of Fig.4.7 where we show the residual as a function of the relative stellar size of the central galaxy in the host halo, defined as the stellar half mass radius divided by the halo radius. While a similar fitting discrepancy is seen using comoving and normalised radii it is likely the stellar size of the central galaxy, which is proportionally smaller in lower mass haloes (see Pillepich et al., 2018b), is also part of the explanation for the residual halo mass dependence seen in the left panel.

4.5.4 Model fitting at different resolutions

We then repeat the fitting procedure in different simulations to investigate the effect of resolution. The upper panels of Fig. 4.8 show the parameters as a function of the dark matter particle mass in the TNG-Dark simulation M_{DMO}, when all resolved galaxies are used in each case. The uncertainties shown are calculated by jackknife between sub-cubes of each simulation.

It is seen that the pivot radius, a, increases, while the power scaling, b, decreases. A linear function of $\log_{10} M_{\mathrm{DMO}}$ is a reasonable fit to both of these parameters. Applying a linear fit we find

$$a = -0.039 + 0.0074 \log_{10} M_{\mathrm{DMO}} \tag{4.2}$$

and

$$b = 0.35 - 0.22 \log_{10} M_{\mathrm{DMO}}. \tag{4.3}$$

The overall correction required is enhanced at worse resolution, as seen in the lower panel of Fig. 4.8. It may be hypothesised that this is due to including haloes and subhaloes of differing masses in each simulation selection. However, the lower panel of Fig. 4.8 also shows the fit does not shift substantially if the better resolution simulations are restricted to only use the most massive galaxies, and therefore this is a true effect of the resolution.

4.5.5 Redshift dependence

Finally, we examine whether our model depends on the redshift at which it is applied. We repeat the fitting of equation 4.1 at a series of snapshots in the run with the best resolution of each box size, and we show the results of this fitting in Fig. 4.9.

In TNG50-1 and TNG100-1 there is no systematic trend visible in the parameters at different redshifts, with the parameters consistent with the redshift zero result in most instances. In TNG300-1 there is a trend for the pivot radius to increase and the power scaling to decrease with redshift, which is largely attributable to the degeneracy in the fitting of the two parameters. Overall, we therefore expect that the fitting parameters we found at redshift zero will be sufficient for any applications at higher redshifts.

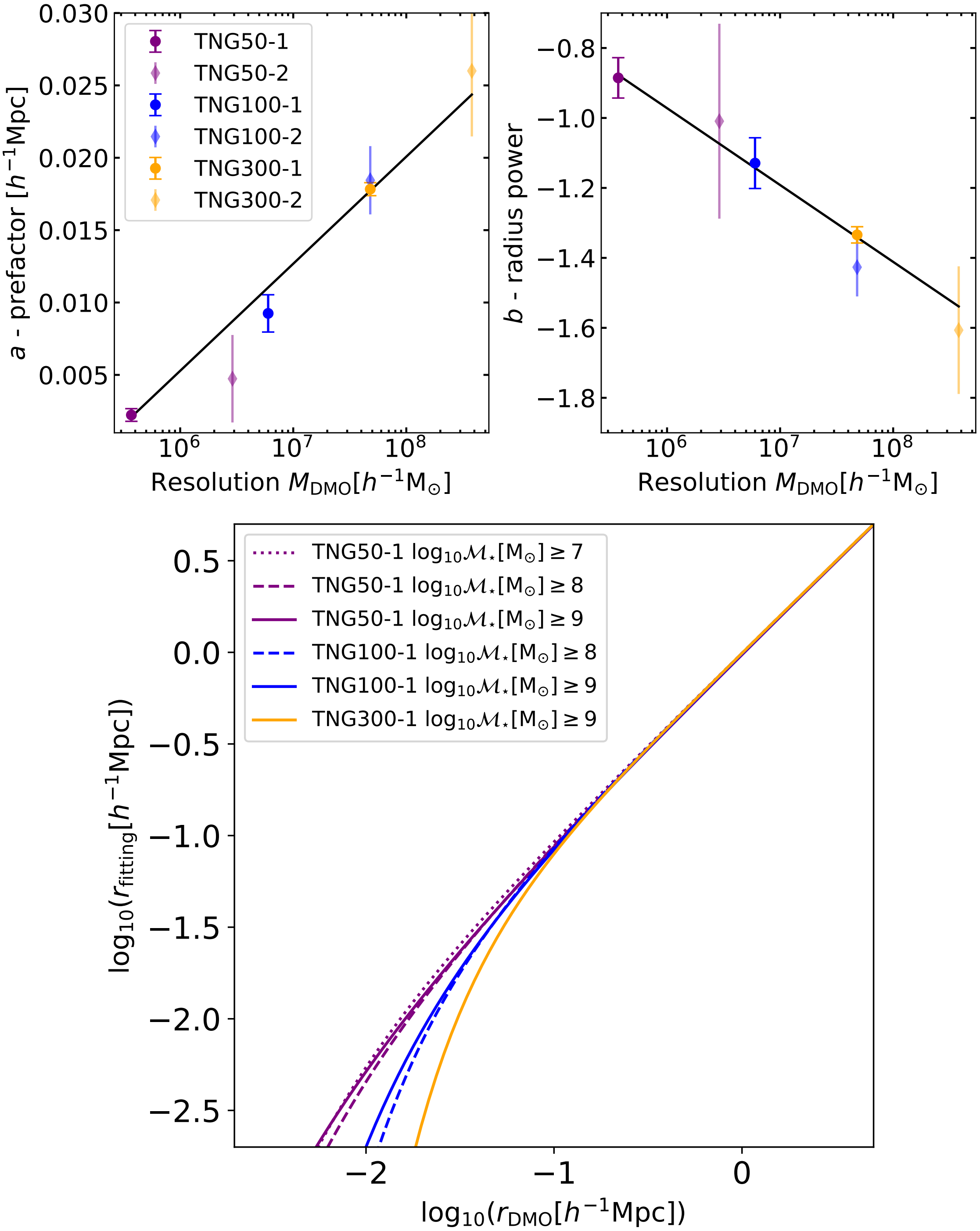

Figure 4.8: Fitting the radial position change of Type 1 satellites for different resolutions at $z = 0$. **Upper panels:** Fitting parameters from equation 4.1 for the Type 1s in different resolution TNG simulations, as a function of the dark matter particle mass used in each TNG-Dark simulation. Galaxies with $\gtrsim 100$ stellar particles are selected from each simulation. **Lower panel:** The radial position of Type 1 satellites in the full-physics simulations as a function of radial position in the DMO simulations for different resolutions and stellar mass limits.

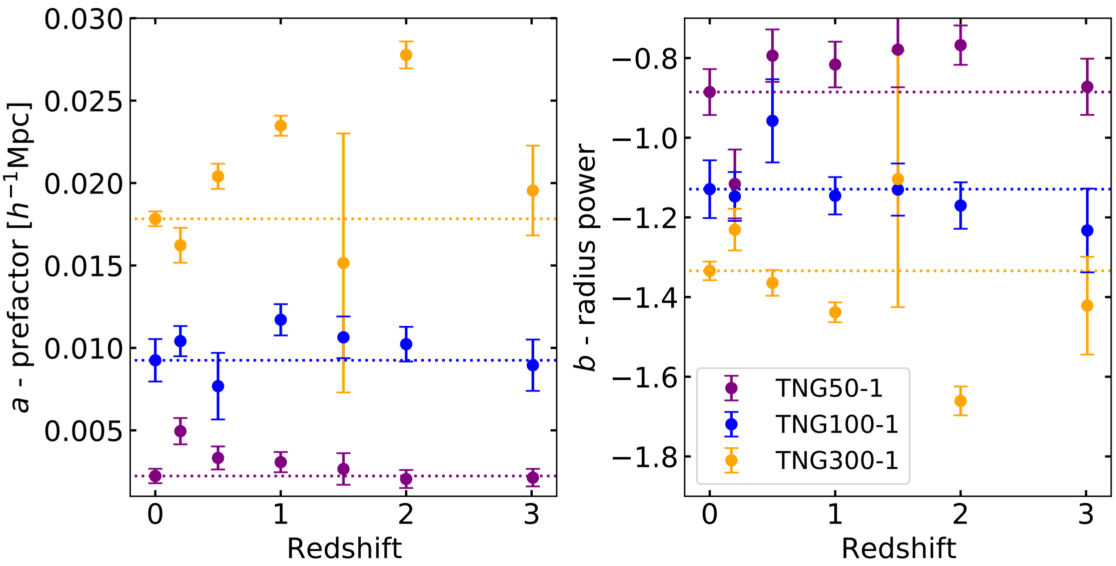

Figure 4.9: The fitting parameters from equation 4.1 for Type 1 satellites as a function of redshift for the run with the best resolution of each box size.

4.5.6 Subhalo mass differences

Our result in Fig. 4.6 that the radius change is related to the subhalo mass from the full-physics simulation but not in DMO suggests a systematic difference in the masses as well as the positions of satellites, as previously found by comparisons of full-physics and DMO simulations by Sawala et al. (2013). Following on from this, we briefly consider here what correction would be required for the masses.

We see in the left panel of Fig. 4.10 that in TNG50 the total mass identified by Subfind (Springel et al., 2001) as belonging to the subhalo is reduced. We speculate that this mass difference may be partly a physical effect due to ram-pressure stripping (e.g. Ayromlou et al., 2019, 2021), but also a numerical effect due to the ability of Subfind to distinguish the structures (e.g. Onions et al., 2012).

We apply a similar fitting for mass change to that which we used for radial position change,

$$\log_{10}(\mathcal{M}_{\rm sub}^{\rm TNG}/\mathcal{M}_{\rm sub}^{\rm DMO}) = -(\mathcal{M}_{\rm sub}^{\rm DMO}/a_{\rm m})^{b_{\rm m}}, \tag{4.4}$$

and follows a power law about a pivot mass $a_{\rm m}$. The red line in the left panel of Fig. 4.10 shows the outcome of fitting this function, successfully reproducing the typical mass difference.

Similarly to the radius change, the mass change could depend on a number of the properties of the subhalo and host halo, as well as simulation resolution. Additionally, we expect a covariance between the mass and radius change. However, to be consistent with the corrections we provide for radius change we again apply only a one-dimensional fitting. This gives us $a_{\rm m} = 2.2 \times 10^{8} h^{-1}{\rm M}_{\odot}$, $b_{\rm m} = -0.55$ for TNG50-1, and $a_{\rm m} = 1.2 \times 10^{9} h^{-1}{\rm M}_{\odot}$, $b_{\rm m} = -0.98$ for TNG100-1.

The resolution dependence is somewhat more complicated than it was for radii. The right panels of Fig. 4.10 show the fitting parameters in different runs. In the runs at the

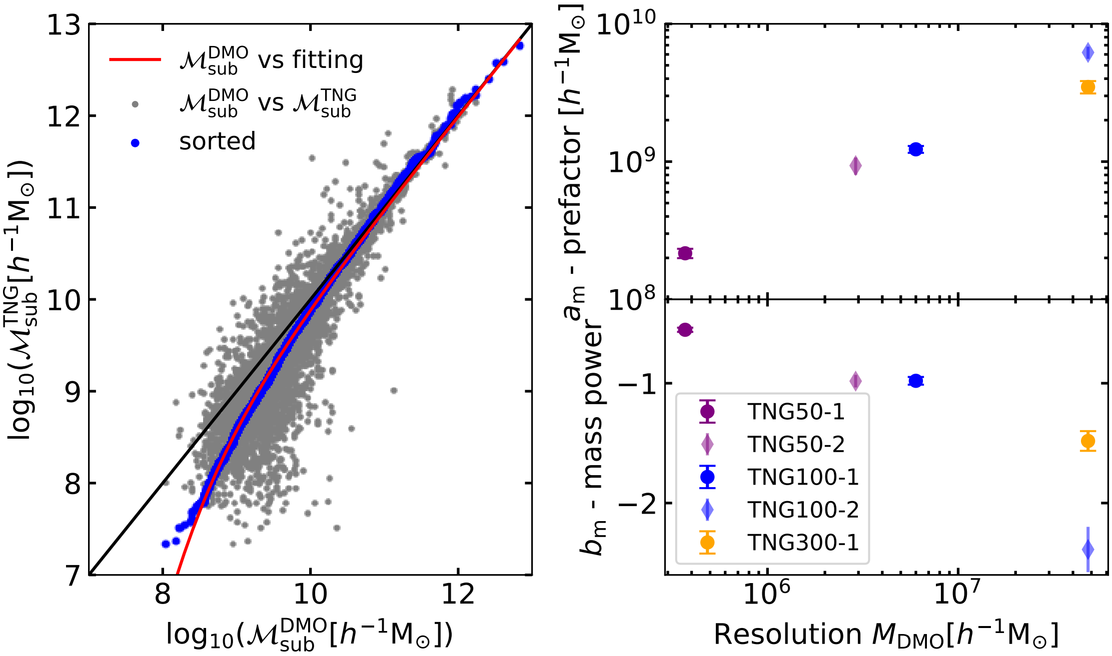

Figure 4.10: Fitting the mass change of Type 1 satellites between the TNG and TNG-Dark runs at $z = 0$. **Left panel:** The difference in mass of satellites of mass $\mathcal{M}_\star > 10^7 \mathrm{M}_\odot$ in TNG50-1 and TNG50-1-Dark. The grey background points show the scatter between exactly matched satellites, blue points show the result of sorting the masses, and the red line the fit. **Right panels:** The dependence of the mass fitting parameters on simulation resolution, each simulation using galaxies with $\gtrsim 100$ stellar particles.

lower end of the $M_{\rm DMO}$ range, a trend is seen for pivot mass $a_{\rm m}$ to increase and power $b_{\rm m}$ to decrease as $M_{\rm DMO}$ increases. However, in the runs with worse resolution (higher $M_{\rm DMO}$) the pivot mass and minimum resolved satellite mass converge, and the fitting method breaks down. For this reason, our results from TNG100-2 and TNG300-1 are not in agreement, and we are unable to fit to TNG300-2.

Consequently, while we note that satellite masses are reduced in the TNG simulation relative to TNG-Dark, and that this change can be approximated by equation 4.4, we do not provide fits for simulation resolution.

4.6 Fitting the locations of unmatched satellites

For the unmatched Type 2 satellites, we want to know their radial locations after they are no longer found in the DMO simulation. Our sample here consists of the residual satellites from the cases where multiple TNG galaxies match to one TNG-Dark subhalo. Note that in our fiducial matching algorithm all TNG galaxies map to a TNG-Dark subhalo, so if the corresponding subhalo in TNG-Dark has already merged into a central, then the mapping will be to that central. As a result, all TNG satellites are included in either the Type 1 or Type 2 sample, except for the small number rejected earlier due to differences in the host halo of the matched subhaloes.

We take two approaches to explore their radial distribution. Firstly, we consider the radial profile of the Type 2s at a single snapshot. Secondly, we look at the radial motion between snapshots.

4.6.1 Radial profiles of unmatched satellites

Positions of Type 2 satellites at a single snapshot can be selected by using fits to their radial distribution. As shown in Fig. 4.3, the Type 2s are generally distributed much closer to the central galaxy than the Type 1s, and this gives a different profile shape.

Rather than fitting to these profiles directly, we fit the cumulative distribution of the number of satellites as a function of distance from the centre. This directly provides a distribution from which satellite positions can be drawn. We examine distances and profiles in three dimensions as we are only considering simulated galaxies.

Desiring a profile from which we can readily draw samples, we find that the cumulative distribution is well fit by assuming the galaxy number counts of Type 2s follow a log-normal distribution

$$N(r/R_{200\mathrm{m}}) = N_{\mathrm{sats}}\mathrm{exp}\left(\frac{-(\log_{10}(r/R_{200\mathrm{m}}) - \log_{10}(r_s/R_{200\mathrm{m}}))^2}{2\sigma^2}\right). \tag{4.5}$$

This implies the number density profile of Type 2s can be determined from this using

$$n(r/R_{200\mathrm{m}}) = \frac{N(r/R_{200\mathrm{m}})}{\sqrt{2\pi^3}4\sigma(r/R_{200\mathrm{m}})^3\ln(10)}, \tag{4.6}$$

where N_{sats} is the total number of satellite galaxies, r is the radial position of the satellite, r_s is a scale radius and σ is the distribution width. We note that an Einasto profile (Einasto, 1965) is also able to fit the data, but that we select the log-normal approach due to the comparative ease of drawing random samples from it.

Applying this fit we find the average parameters for the three simulations are $r_s/R_{200\mathrm{m}} = 0.18$ and $\sigma = 0.43$. We note that due to fitting in terms of $r/R_{200\mathrm{m}}$ this depends on the halo mass estimate used. If, instead of using an overdensity of 200 times the mean density, we use 200 times the critical density then $r_s/R_{200(\mathrm{c})}$ increases to 0.30 but σ does not change.

In Fig. 4.11 we show the outcome of this model fit. In the upper panel we show the cumulative number of satellite galaxies in TNG50-1, TNG100-1 and TNG300-1, and in the lower panel we show the number density profile. We have not set matching mass limits in this case, instead selecting all Type 2s above the stellar mass limit for each simulation and then normalising by the total number and the halo $R_{200\mathrm{m}}$. It is immediately apparent that there is a very similar distribution of Type 2 satellites in the different resolution runs, and these agree well with fits given by equation 4.6. Slight discrepancies in the fits are visible on the smallest and largest scales, particularly in TNG300-1 where the tails are underestimated due to the profile shape differing slightly from that of TNG50-1 and TNG100-1. However, in the range $0.02 \lesssim r/R_{200\mathrm{m}} \lesssim 1$ our fitting is seen to work well for all the simulations.

In Fig. 4.12 we then examine whether the fits depend on halo or stellar mass. We

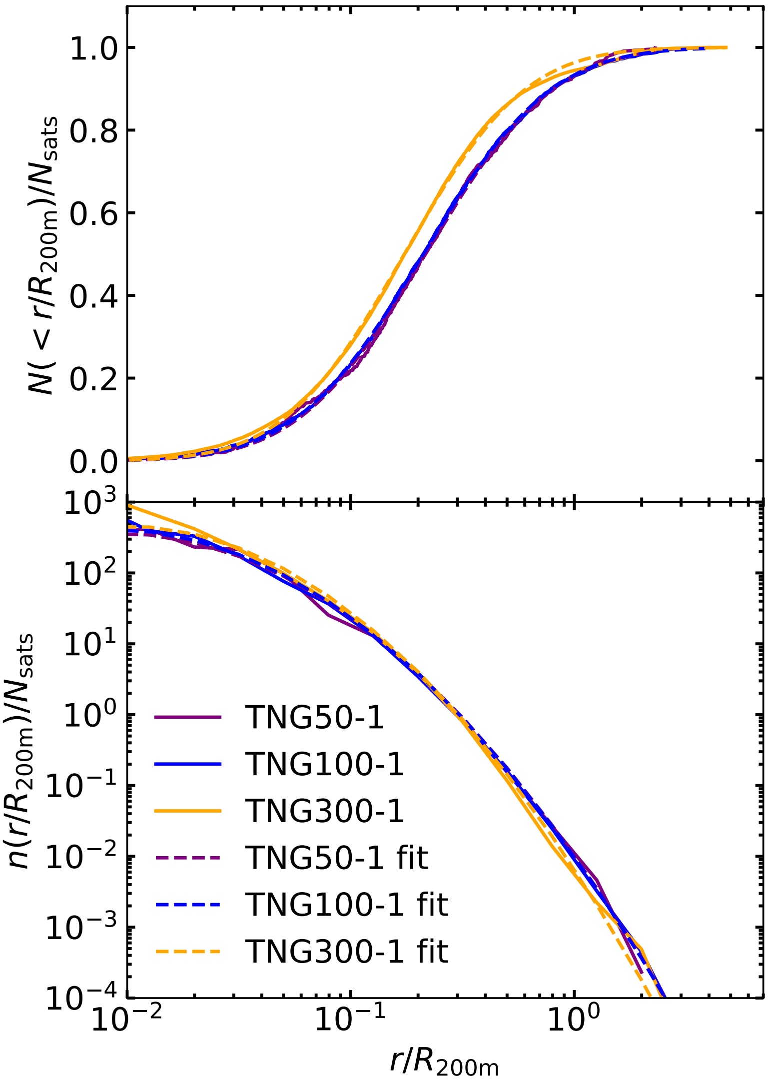

Figure 4.11: Fitting to the distribution of Type 2 satellite galaxies in TNG, as a function of distance normalised by halo radius at $z = 0$. The upper panel shows the cumulative distribution and the lower panel the number density profile. Solid lines show the Type 2 satellites of TNG, and dashed lines show the fits using equation 4.6, which assumes the number counts follow a log-normal distribution.

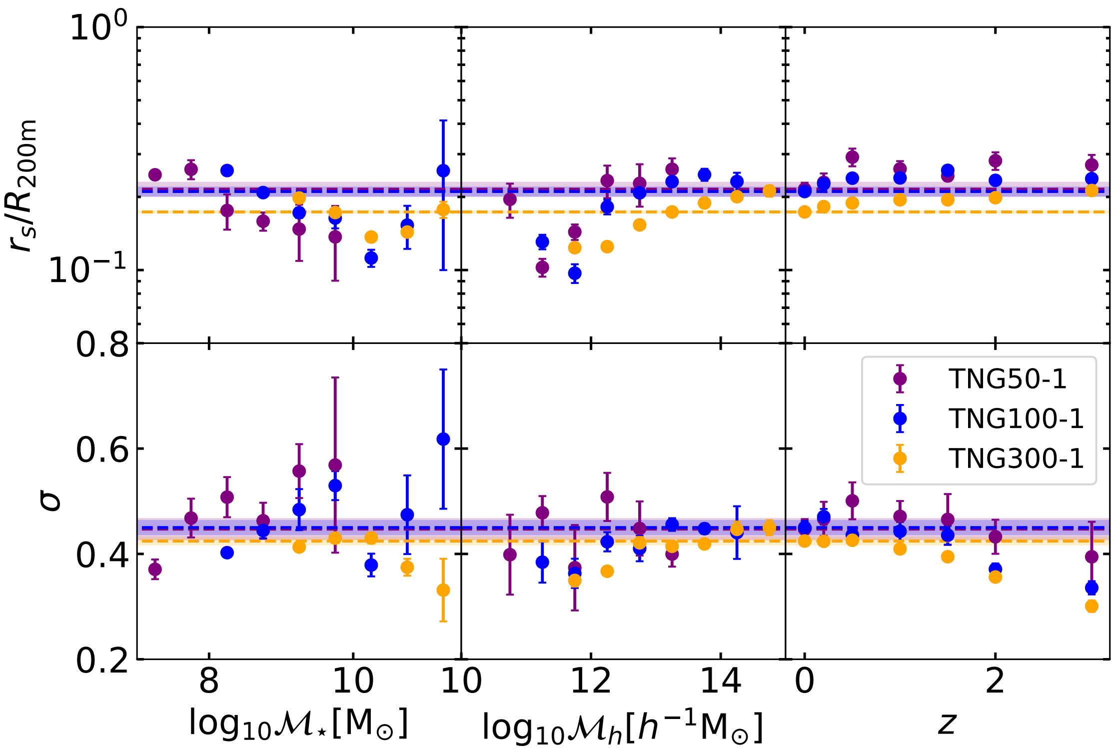

Figure 4.12: The dependency of the parameters of the Type 2 number density profile fits on halo mass, stellar mass and redshift. The $r_s/R_{200\mathrm{m}}$ (upper panels) and σ (lower panels) parameters of equation 4.6 are shown in bins of stellar mass (left panels), halo mass (centre panels) and redshift (right panels) for TNG50-1, TNG100-1 and TNG300-1. The dashed lines show the respective overall fits, as plotted in Fig. 4.11. For clarity we only show bins containing satellites of at least 10 groups.

select Type 2 satellites in evenly spaced bins of halo and stellar mass and recalculate the profile fits in each bin. The changes in the parameters are all relatively small, with a slight reduction in $r_s/R_{200\mathrm{m}}$ in low mass haloes, and for the highest mass galaxies. This consistency is expected from our earlier conclusions that the overall normalised profiles do not depend on halo mass. We do not consider the dependence on subhalo total mass, as this would have no equivalent in the case of SAMs, where these satellites are not contained in subhaloes. Additionally, we show the redshift dependence to this fitting, which leads to a slight reduction of σ at higher z.

In SAMs, the number of Type 2 satellites is known. However, in some simpler empirical models the number of Type 2 satellites would need to be input in order to apply these profiles to DMO simulations. Despite the over-simplifications of halo occupation distribution models (HODs; see e.g. Hadzhiyska et al., 2020), we fit the number of Type 2s per group, $\frac{N_{\mathrm{T2}}}{N_{\mathrm{grp}}}$, with a simple three parameter model,

$$\frac{N_{\mathrm{T2}}}{N_{\mathrm{grp}}} = \left(\frac{\mathcal{M}_h/h^{-1}\mathrm{M}_\odot - M_0}{M_1}\right)^\alpha . \tag{4.7}$$

This model is illustrated in Fig. 4.13. The left panels show the three parameters of equation 4.7 as a function of the stellar mass cut applied to the galaxy sample, $\mathcal{M}_{\star,\mathrm{min}}$, for

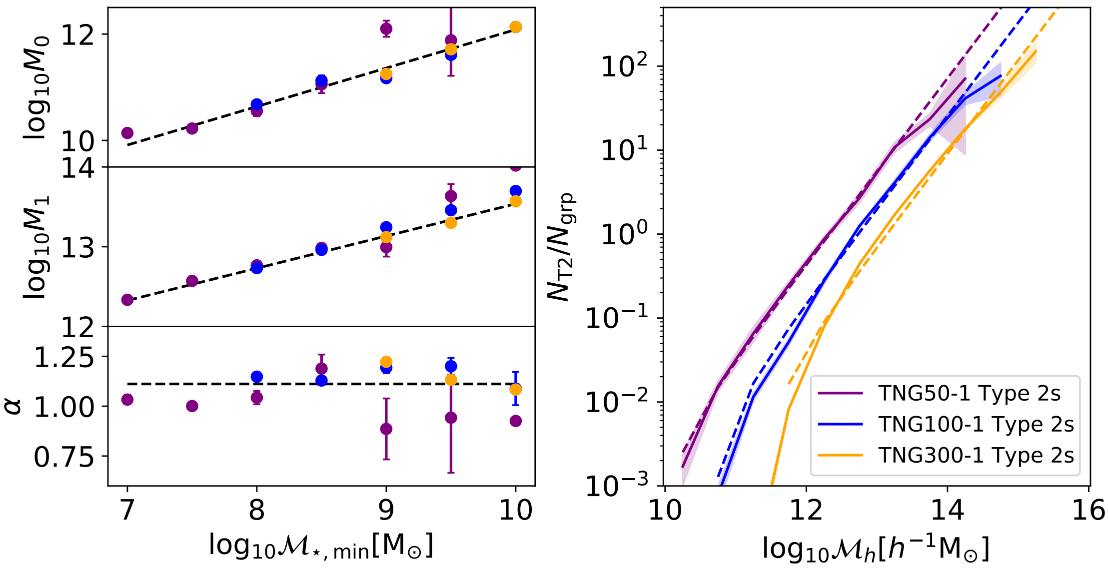

Figure 4.13: The number counts of Type 2 satellites in the TNG simulations at $z = 0$. Left panels show the parameters of equation 4.7 as a function of the stellar mass limit used, fit with the black dashed lines, which are given by equation 4.8. The right panel then shows the number counts in the TNG simulations as solid lines, and the model results as dashed lines. Different mass limits are used for each resolution, giving different numbers of Type 2s: TNG50-1 is shown for $\log_{10}(\mathcal{M}_\star/\mathrm{M}_\odot) \geq 7$, TNG100-1 is shown for $\log_{10}(\mathcal{M}_\star/\mathrm{M}_\odot) \geq 8$ and TNG300-1 is shown for $\log_{10}(\mathcal{M}_\star/\mathrm{M}_\odot) \geq 9$.

TNG50-1, TNG100-1 and TNG300-1. It can be seen that the fits are relatively insensitive to the simulation choice, but there is a dependence on the stellar mass of selected galaxies, which we have fit with the black dashed lines, given by

$$
\begin{aligned}
M_0 &= 10^{4.84}(\mathcal{M}_{\star,\mathrm{min}}/\mathrm{M}_\odot)^{0.724}, \\
M_1 &= 10^{9.50}(\mathcal{M}_{\star,\mathrm{min}}/\mathrm{M}_\odot)^{0.404}, \\
\alpha &= 1.11.
\end{aligned}
\tag{4.8}
$$

This stellar mass dependence is a result of an increased number of satellites per group and the inclusion of satellites in lower mass groups, both resulting from a lower minimum mass threshold. However, the lack of dependence on the simulation resolution is more surprising, as it means that even with improved resolution we are still finding some massive galaxies lose their subhalo to become ‘orphaned’.

The right panel of Fig. 4.13 then shows the number of Type 2 satellites per group, and the fits resulting from equations 4.7 and 4.8. While the number of satellites is reproduced for intermediate halo masses $\mathcal{M}_h \approx 10^{12.5}h^{-1}\mathrm{M}_\odot$, the fitting is less accurate at either end of the mass scale, particularly the most massive haloes have the number of Type 2s over-estimated. As we are only interested in knowing the approximate number of Type 2s, we do not attempt to correct this further.

4.6.2 Modelling Type 2 radial motion

The second approach we consider for determining the location of Type 2 satellites is to trace and model their radial motion. To do this we take all the galaxies we have assigned as Type 2s at redshift zero, and find the difference in position from earlier snapshots. We restrict ourselves to galaxies that remain satellites at earlier snapshots, and which reside in haloes which differ in mass by less than 0.15 dex between snapshots.

We once again use comoving distances in our analysis. We choose to do this as these are the natural units of the simulations, and by using them we avoid the need to account for the changing value of h over time. However, we note that given that groups will not expand at the same rate as the Universe, we could instead use proper distances to minimise the effects of the expansion in our model.

Fitting a relationship between successive snapshots and propagating this over time invites an increasingly large error on each iteration. Instead, we look at the change in radial separation of Type 2s from their host across a range of time steps. Given an initial radial distance at an earlier time, this can then be applied to generate radial distances at later times. By implication, the application of this means the positions of satellites at successive snapshots are not directly related, but instead they are both related to the radial separation at the starting time.

Strictly, we are then concerned only with the radial change since a certain starting time, that at which the satellite was last identified as a Type 1. However, this is very restrictive on the number of satellites available at each snapshot, and has a strong dependence on the criteria used to identify the galaxy type. Instead, we consider the radial change from all snapshots at which the galaxy remains a satellite (Type 1 or Type 2). Regarding the number which remain Type 2s on tracing back from redshift zero, about 90% of the Type 2s are still Type 2s after a single timestep, dropping to 50% after slightly over 2 Gyr (15 snapshots), and decreasing slowly for greater times.

Having found the historical locations of the satellites, we can then consider statistically the distribution of possible radial movements of a galaxy at a given initial position. This allows us to estimate the positions of Type 2s over time by drawing randomly from this distribution.

To find this distribution we first calculate for each galaxy the probability, λ, that a galaxy at the same initial radial distance has experienced more radial motion towards the centre of the group. We calculate this by examining all galaxies starting in a bin of log radial location centred on the selected galaxy with width 0.1 dex, and determining the fraction that move inwards by the same or a greater proportion (equal or lower value of $\log_{10}(r_{\rm end}/r_{\rm start})$), giving a λ value in the range $0 < \lambda \leq 1$.

Due to the small number of Type 2 satellites in TNG50-1, we instead focus on TNG100-1 when developing our model. In Fig. 4.14 we show the radial movement of Type 2 satellites in TNG100-1 between $z = 0.01$ and $z = 0$. We colour the points by their λ value, and highlight in red the ones with $\lambda \geq 0.95$ which we use to fit the upper power law described below. We also show the prediction of the model given below for $\lambda = 0.5$, showing the satellites tend to move slightly inwards on average between these times.

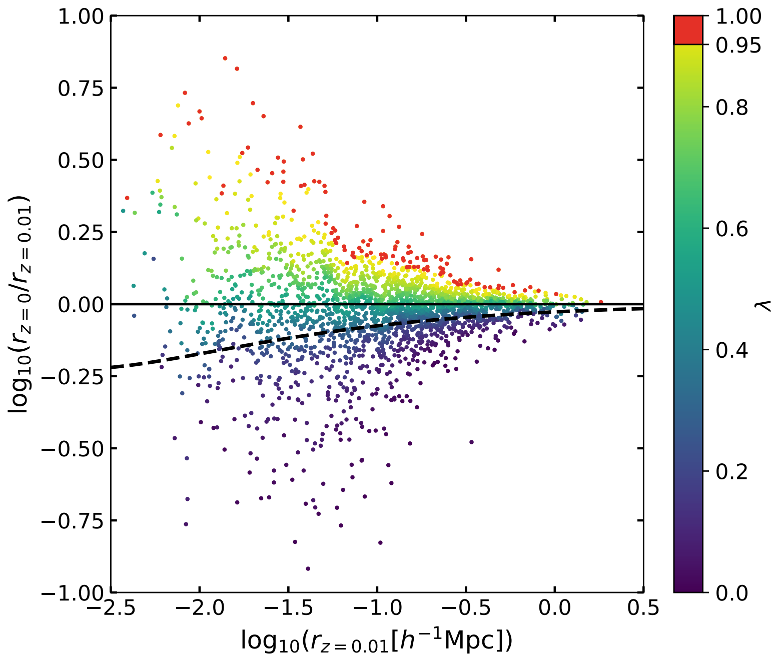

Figure 4.14: Movement of Type 2s between the final two snapshots of the TNG100-1 simulation, $z = 0.01$ and $z = 0$, plotted against their starting location at $z = 0.01$. Galaxies are shown for masses $\mathcal{M}_\star > 10^8\mathrm{M}_\odot$ and colour-coded by the probability of a galaxy at a similar starting location moving further inwards. We highlight in red the ones which move furthest outwards. The black dashed line then shows the prediction of the model given in Table 4.2 for $\lambda = 0.5$.

Typically we see that Type 2 satellites gradually move towards the halo centre over time, but that there is a chance that they move away from the centre. In particular, those which begun close to the centre (and so close to the pericentre of their orbit) are more likely to move outwards.

In order to account for the shape of this distribution, and the possibilities of both outwards and inwards movement, we model this as a sum of power laws. We choose this as it provides a relatively simple model for the entire distribution, whereas fitting in bins of radius would require more parameters, and fitting an overall trend would ignore the spread of orbits the satellites are seen to be following. A power law model was selected as it approximately visually matches the shape of the contours of equal λ, but we note that this is a problem where machine learning methods for analytic expressions might be useful, in a similar manner to Krone-Martins et al. (2014).

Our power law sum consists of an upper power law which describes the maximum outwards movement possible, and a lower power law describing the inwards motion. This may then be expressed in the form

$$\log_{10}(r_{\mathrm{end}}/r_{\mathrm{start}}) = u(t)r_{\mathrm{start}}^{v(t)} - C(\lambda,t)r_{\mathrm{start}}^{D(\lambda,t)}, \tag{4.9}$$

where r_{start} is the initial radial location, r_{end} is the final radial location and t is the time between the snapshots. The first term in this equation is our upper power law, and the second term the lower power law.

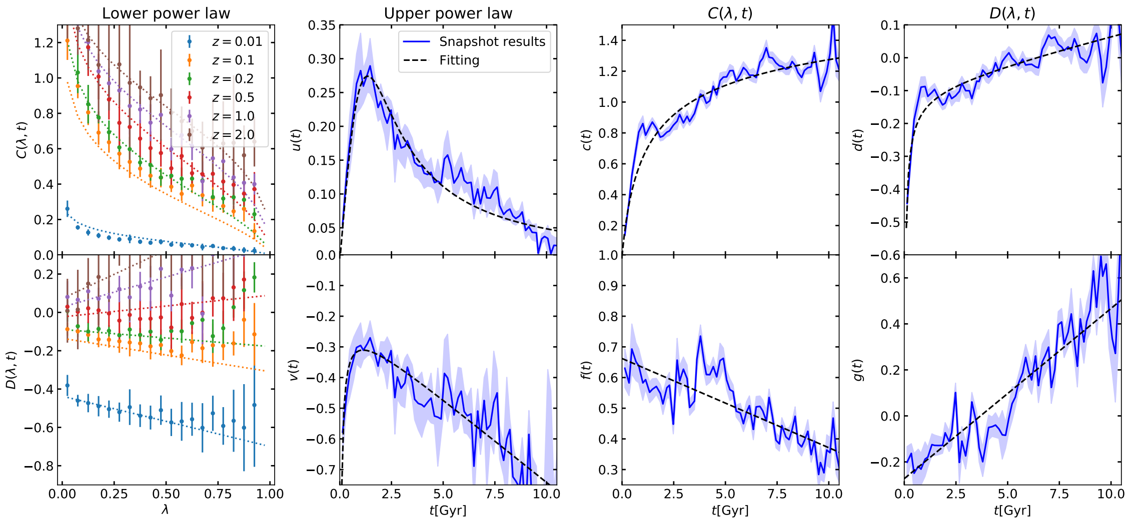

Figure 4.15: Parameters of the model given in Table 4.2 used to fit the movement of $z = 0$ Type 2 satellites between snapshots in TNG100-1. The left panels show the lower power law parameters as a function of the distribution location λ, with different colours showing different starting redshifts and dashed lines showing fittings from Table 4.2. The other panels show the parameters as a function of time between snapshots, with the fittings overplotted as dashed lines.

Our procedure for fitting this is as follows. We fit the galaxies with $\lambda \geq 0.95$ with a single power law ur^v. Then in bins of width 0.05 in λ we fit the lower power law Cr^D. For both of these fittings we use only galaxies at $r_{\rm start} > 0.01\,h^{-1}$ Mpc, to avoid biasing the fit with the very few on the smallest scales which may be affected by the spatial resolution of the simulation.

In the left panels of Fig. 4.15 we show the dependence of the lower power law parameters $C(\lambda)$ and $D(\lambda)$ on the distribution percentile across different time periods. The two components of the lower power law can be fit as a function of the distribution percentile as $C(\lambda, t) = c(t)(-\log_{10}\lambda)^{f(t)}$ and $D(\lambda, t) = d(t) + g(t)\lambda$.

Finally, we fit this as a function of the time between snapshots in Gyr, with $0.136 < t/\mathrm{Gyr} < 10$. The right hand 6 panels of Fig. 4.15 show the dependencies of the parameters on time between snapshots. In considering the time dependence, our primary requirement is that parameters u and c tend towards zero at small times, to give no instantaneous satellite movement (although for times $t < 0.136$ Gyr, shorter than the minimum this model is fit for, it would be more appropriate to just set zero movement). We include the time dependence of the parameters with a summary of the model in Table 4.2.

4.6.3 Interpreting the fitting

Our model has been designed to match the statistical distribution of satellite radial positions. This means that for any individual satellite we are treating the orbital phase as a random variable, and so the motion will not be accurately predicted from the initial location of the satellite, but for the whole population the distribution should be

Table 4.2: Details of the parameters of the model given in equation 4.9, used to fit the movement of Type 2 satellites between snapshots in TNG100-1 with time steps $0.136 < t/\text{Gyr} < 10$. The top half of the table gives the time dependence of the upper power law, and the lower half of the table gives the dependence on time and distribution position λ of the lower power law.

Section	Model	Parameters		
Upper power law	$u(t)r^{v(t)}$			
	$u(t) = \frac{t}{u_1+u_2t^{u_3}}$	u_1= 2.7	u_2= 1.1	u_3= 2.3
	$v(t) = (v_1 + v_2t)(1 + t^{v_3})$	v_1= -0.10	v_2= -0.053	v_3= -0.78
Lower power law	$C(\lambda, t)r^{D(\lambda,t)}$			
$C(\lambda, t) = c(t)(-\log\lambda)^{f(t)}$	$c(t) = \frac{t}{c_1+c_2t^{c_3}}$	c_1= 0.66	c_2= 0.91	c_3= 0.90
	$f(t) = f_1 + f_2t$	f_1= 0.66	f_2= -0.029	
$D(\lambda, t) = d(t) + g(t)\lambda$	$d(t) = (d_1 + d_2t)(1 + t^{d_3})$	d_1= -0.094	d_2= 0.015	d_3= -0.67
	$g(t) = g_1 + g_2t$	g_1= -0.27	g_2= 0.074	

reproduced. It also means that our model parameters have no direct physical meanings, but we can still infer some information from them.

Firstly, considering the parameters at small timesteps, the shape of $C(\lambda, t)$, which has sharp upturn at lower end of the λ range, demonstrates that most satellites do not move far, but that the distribution has a large tail of satellites with substantially greater radial movement, perhaps those on first infall with radial orbits.

Looking at the time dependence, the strengths of the power laws, given by $u(t)$ and $c(t)$, inform us of the relative probabilities of a satellite moving towards or away from the group centre. Across a few snapshots, both $u(t)$ and $c(t)$ increase rapidly, showing the satellites can have large radial movements on their orbits, but the overall population does not have a significant inwards or outwards movement. At greater timesteps, $u(t)$ and $c(t)$ both become smoother, with a gradual decrease in $u(t)$ and an increase in $c(t)$. This shows a transition from the scatter associated with the orbital motion to an average inwards motion for the satellite population.

This switch to an overall infall is also visible in $d(t)$, which tends towards zero at large times, showing that some of the radial dependence is washed out by the overall infall. However, there is still some radial dependence, with $g(t)$ changing sign at large times. This sign change, and the growth of $v(t)$, is indicative of a continued tendency for those satellites which began close to the central to move outwards on average. This is to be expected, as any satellites which began close to the central and moved inwards will have merged into the central, and so not be included in our analysis.

These interpretations show that our model has encapsulated much of the expected satellite motion, and should provide a practical method to predict the overall movement of satellite populations.

4.7 Discussion and caveats

We further explore our results and models here, firstly via some tests of the application of our models and then by discussing the interpretation and caveats of this work.

4.7.1 Testing the Type 2 model for TNG subhaloes

The primary test of the model from Section 4.6.2 is the application of it to the traced locations of the satellites over time. We show in Fig. 4.16 the profiles of satellites at redshift zero in TNG50-1, TNG100-1 and TNG300-1 as solid lines in each panel, selected with $\log_{10}(\mathcal{M}_\star/\mathrm{M}_\odot) \geq 7$ (TNG50-1), 8 (TNG100-1) or 9 (TNG300-1). The dotted lines then show the radial distribution of these same satellites traced back to the redshift of the column. If successful, our model should take the radial positions shown by the dotted line in each panel, and reproduce the solid lines.

The blue shaded region in each panel shows the result of the application of our model specified in Table 4.2. The model was applied 1,000 times, with a different set of random λ values each time, and the shaded regions show the 95% region of the spread of these results. In most cases, it can be seen that our model is successfully generating the distribution of satellites at redshift zero. Discrepancies in our model are most apparent on small scales when it is applied to TNG300-1, likely due to the different halo masses sampled by it. More generally, there is a small tendency to move satellites too close to the centre when starting at higher redshifts.

Fitting our model on Type 2 satellites in TNG50-1, TNG100-1 and TNG300-1 leads to slightly different parameterisations, although the overall trends are similar between them. These different fits are shown in Appendix 4.D. We show using the purple and orange shaded regions the results of alternatively applying the model as fit on TNG50-1 or TNG300-1, demonstrating the comparable results of each.

We may anticipate some halo or stellar mass dependence to these fits, as dynamical friction is a function of both of these (e.g. Binney & Tremaine, 1987). We show in Fig. 4.17 the radial profile in four halo mass bins, starting at three different redshifts. It is apparent that our model achieves reasonable success in every case, although there are some minor discrepancies. In particular the model performs less well for halo masses below $10^{12}h^{-1}\mathrm{M}_\odot$, which is unsurprising given we have fewer Type 2s to fit in those haloes.

Some of the differences are attributable to variation in the distribution locations as a function of halo mass. We find that Type 2s in lower mass haloes are assigned λ values which are on average less than 0.5, while the opposite applies to high mass haloes.

A similar picture emerges for stellar mass, with our model working well for the lower mass satellites which are the most frequent, and slightly less well for higher masses. Therefore we conclude that, while there are mass dependencies, these are small and so our model is able to perform adequately without these extra dependencies.

4.7.2 Testing the full model on TNG300-Dark

The accuracy of the power law model for the inwards displacement of Type 1s given in Section 4.5.2 plus the distributions of Type 2 satellites given in Section 4.6.1 can be tested simply by application to the positions of TNG300-1-Dark subhaloes we selected in Section 4.4.2. To do this we move the Type 1s radially inwards along the vector separating

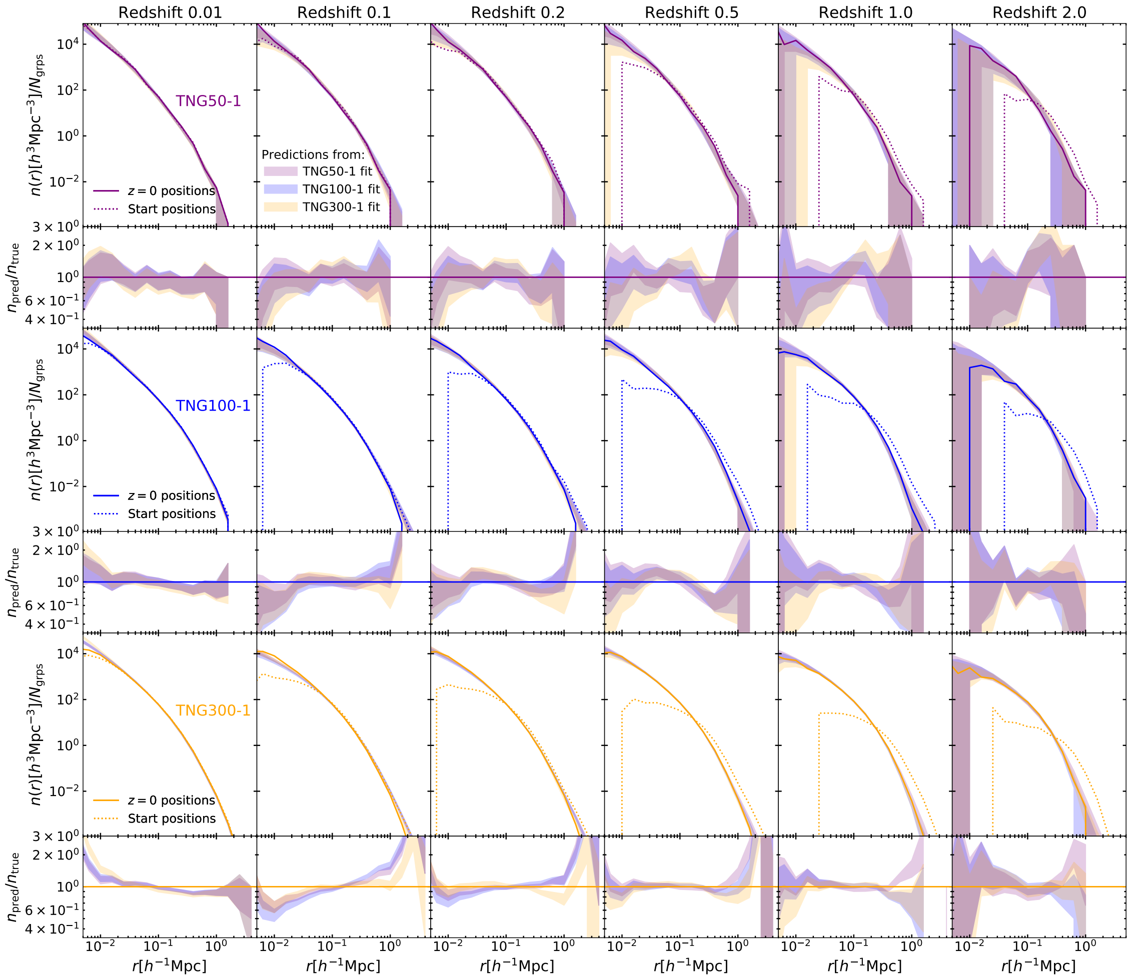

Figure 4.16: Radial distributions of Type 2 satellites in the TNG simulations, before and after applying our model for their radial movement given in Table 4.2. The top two rows show TNG50-1 profiles, middle two rows TNG100-1 profiles and lower two rows TNG300-1 profiles. From left to right the panels show satellites tracked to higher redshifts. The larger panels show the radial profiles, while the smaller panels show the ratio of the predicted profiles to the true profile. We include resolved galaxies in all groups, but show comoving distances as those are the input to our model. In each of the larger panels the dotted line shows the distribution of satellites at the redshift of the column and the solid line shows the distribution of the satellites at redshift zero. The shaded bands in all panels show the 95% region for 1,000 applications of the model predictions at redshift zero. The model predictions are calculated for the satellite locations shown in the dotted lines, with random values of λ, and the different colours show the prediction of the model when fit to the different simulations.

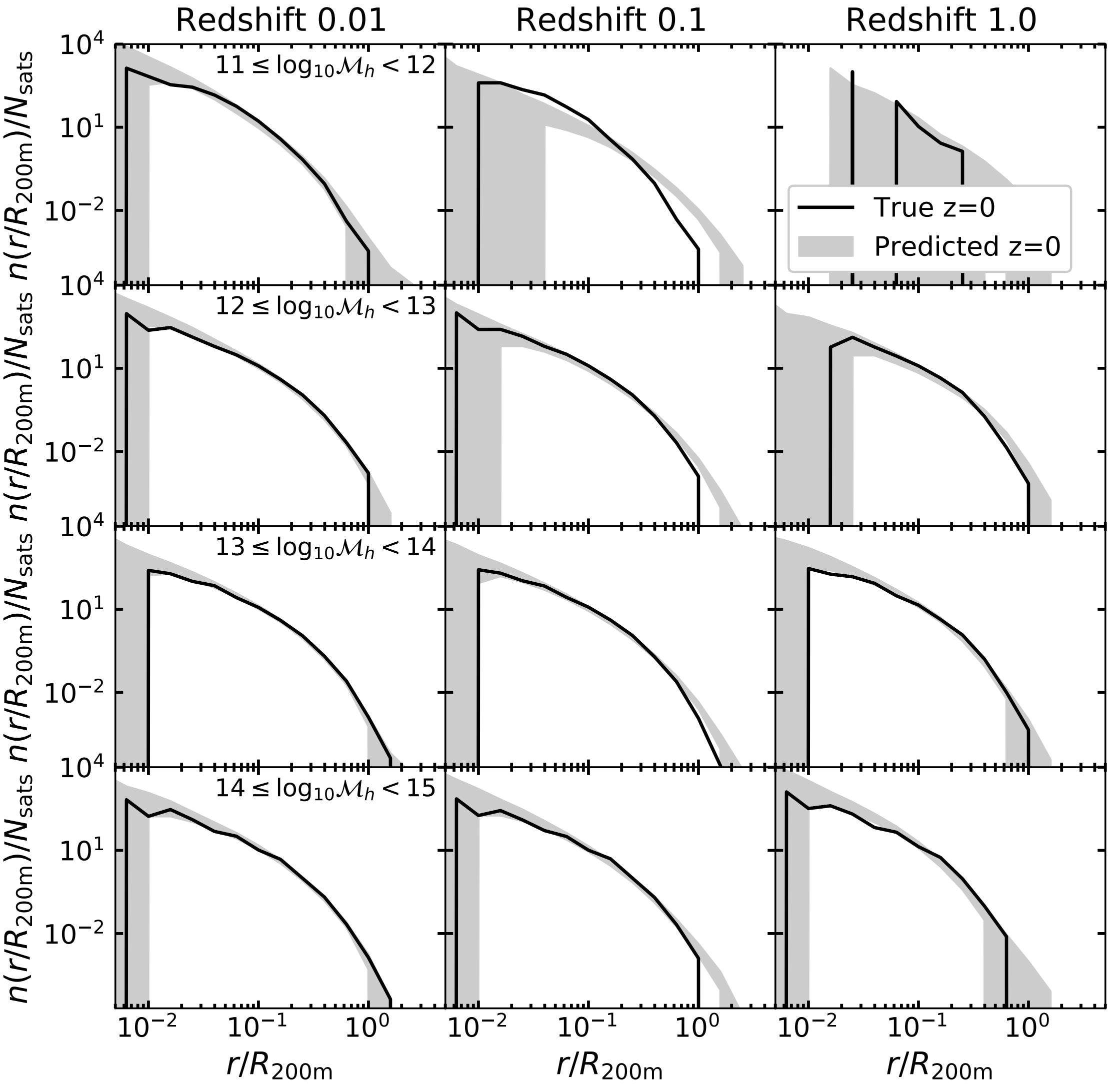

Figure 4.17: The Type 2 profile fits in different group mass bins for TNG100-1. The rows each show a different group mass selection, while the columns show satellites traced back to different redshifts. The solid lines show the redshift zero positions of satellites starting at the specified redshift, and the shaded regions show the 95% spread of the positions predicted by our model over 1,000 applications.

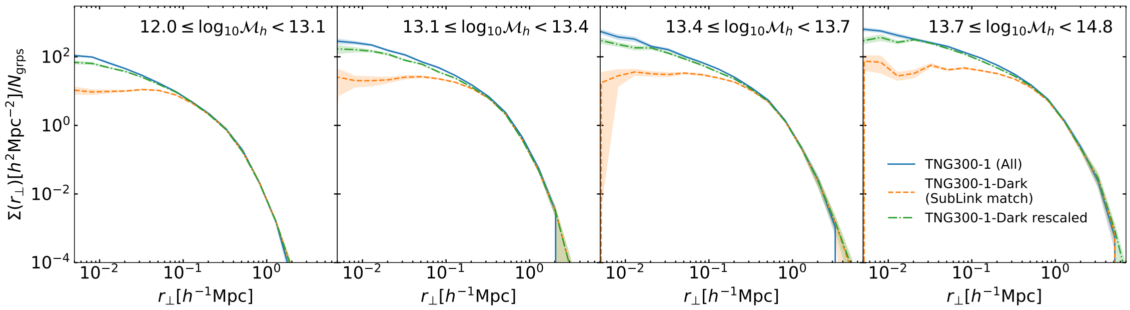

Figure 4.18: The outcome of the application of our model for Type 1 satellites on the TNG300-1-Dark profile at $z = 0.2$, with the addition of the profile for Type 2 satellites, shown as green dot dash lines, compared to the TNG300-1 profile (blue solid lines) and the original TNG300-1-Dark profile (orange dashed lines) from Fig. 4.3.

them from the central, and add Type 2s randomly distributed in a sphere around the central with the log-normal radial distribution given in Section 4.6.1.

In Fig. 4.18 we show the outcome of this test compared to the TNG and TNG-Dark profiles of Section 4.4.2. On scales $r_\perp \geq 0.02\,h^{-1}$ Mpc our model accurately modifies the TNG-Dark simulation to give it the same profile as TNG. On the smallest scales we see a slight underestimation of the number of satellites, which is related to the slightly different small-scale profiles seen amongst the TNG simulations in Fig. 4.11. While we underestimate the profile for TNG300-1 on small scales in both Fig. 4.11 and Fig. 4.18, we expect the simulations with better resolution to be more accurate on small scales—and these were well reproduced in Fig. 4.11—so we do not try and correct the discrepancy remaining here any further.

Overall the Type 1 model and the model for the Type 2 profiles is seen to accurately reproduce the profile from the full-physics simulation. In future work we will test these further, and also evaluate our model for Type 2 radial motion (Section 4.6.2), based on tracing subhaloes across snapshots, by application directly to a semi-analytic model for galaxy formation.

4.7.3 Physical interpretations

By comparing the TNG and TNG-Dark simulations, we showed that there are two primary effects of baryons on the radial distribution of satellites (and subhaloes) in groups.

Firstly, the comparison between satellites and their matched subhaloes in the DMO runs shows that satellites in the full-physics simulations are located at smaller halo-centric distances at the time of inspection than their surviving analogue subhaloes in the DMO simulations. Secondly, the existence of a population of satellites with no DMO matches suggests an increased survival time of satellites in full-physics simulations. These effects are connected, as satellites that spent more time in their current hosts are typically found closer to their host centres (Rhee et al., 2017).

The greater survival time of satellites in TNG can be explained by the inclusion of a baryonic core to the satellites. Many studies (e.g. Smith et al., 2016; Joshi et al., 2019;

Łokas, 2020; Engler et al., 2021) show that tidal stripping acts primarily on the dark matter component of subhaloes, and that the baryonic component is not extensively stripped. This central component can thus be postulated to keep the satellite bound beyond the point it is disrupted in a DMO simulation, in agreement with Nagai & Kravtsov (2005).

This would seemingly be in contrast to the Chua et al. (2017) result that the addition of baryons reduces the survival time, or the conclusion of Bahé et al. (2019) that baryons make little difference to survival times. However, our findings are not necessarily in tension with such results. Importantly, throughout this work we have focused on satellite galaxies above a certain minimum stellar mass and on their analogues in the DMO simulations, whereas Chua et al. (2017), for example, analyse the entire population of subhaloes, whether luminous or not, and also include lower-mass ones. Secondly, our orphan population, i.e. the satellites with no surviving DMO counterparts, is only a small proportion of the total group–galaxy population and is biased towards the centre. Instead, our results therefore seem to suggest that there is a strong radial dependence to the effect of baryons on the survival of satellites. We cannot exclude, but do not think it the case, that some differences across works may be due to different simulations using different astrophysical feedback mechanisms.

Different survival times between works could also be related to the opposite effect to that considered in this work: disruption caused by baryons. A suppression in the number of substructures is known to occur due to the destruction of satellites by baryonic discs (e.g. Garrison-Kimmel et al., 2017; Kelley et al., 2019). Our choice to select only galaxies from the full-physics simulation and then determine their DMO analogues means we do not account for this, but it will affect the relative survival times of full-physics and DMO substructures.

An alternative explanation for the greater survival time we see is provided by Haggar et al. (2021), who argue that the baryonic material in the centre of the subhaloes causes a contraction of the surrounding dark matter distribution, as seen in other works (e.g. Dolag et al., 2009; Adhikari et al., 2021). This leads to a more pronounced density contrast between the subhalo and the host halo, making it easier for the halo finder to detect the subhalo. If the differences are indeed due to the subhalo detection and tracking, then this might in future be resolved by more advanced structure finders such as those of Elahi et al. (2019a) and Springel et al. (2021), and alternative methods such as the merger graphs of Roper et al. (2020).

A similar contraction argument can be used to explain the inwards displacement of full-physics satellites. Baryons change both the concentration (e.g. Bryan et al., 2013; Lovell et al., 2018; Chua et al., 2019) and shape (e.g. Rasia et al., 2004; Lin et al., 2006) of haloes, which can change the location of the satellite galaxies in the potential of the host. Contraction of the halo can then be suggested to lead to the satellite being further out in the potential, and then falling inwards towards the halo centre to balance this. Alternatively, it is possible that the baryons are increasing the drag force experienced by the satellites, causing the orbits to reduce in size (e.g. Gu et al., 2016).

These explanations do not account for the resolution dependence to the position differences. Instead, the resolution dependence of the DMO results implies that the inwards displacement is at least partly a numerical effect of the simulations, perhaps due to gravitational changes associated with the reduced sampling of the distribution of mass in the halo by the particles at poorer resolution.

Such degeneracies in the explanations should be remembered throughout. Overall, when thinking about physical interpretations, we cannot definitively distinguish the physical effects of adding baryons from numerical effects. While we have provided some speculation for the reasons behind differences between full-physics and DMO results, detailed explanations of the causes are beyond the scope of this work and do not affect the empirical correction models we have presented.

4.7.4 Caveats

There are a number of assumptions and resulting caveats in the results and models we have presented in this work. We discuss a few of the more important ones here.

4.7.4.1 Matching scheme

One of the primary sources of potential uncertainty in our work lies in the matching between TNG and TNG-Dark satellites, and the distinction between Type 1 and Type 2 satellites. Due to the differences in structure formation between the full-physics and DMO cases, it is not necessarily clear that matched satellites represent the same structures.

One way of exploring this is by using an alternative matching scheme, and one exists using the LHaloTree method of Nelson et al. (2015). The matches given by this method are bijective, only matching objects where the object with the most matching particles is the same for the TNG-Dark to TNG direction as for the TNG to TNG-Dark direction. This provides a stricter criteria for the matching and leads to a reduced number of matched satellites (Type 1s), particularly near the centre of haloes. This eliminates the need to apply a correction to the locations of Type 1 satellites, but enhances the need for Type 2s. This, together with the abundance matching method we explored earlier, shows that the balance between satellite types can be adjusted, but the differences between the TNG and TNG-Dark profiles remain. For our purposes, as we are interested in the expected positions of satellites placed in DMO subhaloes by a SAM, which is a one-way matching, it is most appropriate for us to use the one-way SubLink matches we have used throughout to select the types. In future, the effect of the matching scheme could be further explored by also comparing to results from the Lagrangian matching scheme of Lovell et al. (2018).

One further comment on the matching is that we found earlier that up to around 6% of galaxies in each simulation are identified as a satellite in TNG or TNG-Dark but as a central in the other. Rather than attempt to correct for this, we have simply excluded these galaxies. We have not, however, removed any other satellites which may be in these groups. Most of these were at large distances from the centre when a satellite, and our analysis is not affected by these objects. This does, however, suggest some differences in either the structure formation or the numerical methods used, particularly the matching scheme and group finder.

4.7.4.2 Other physical effects

While we have attempted to account for the most relevant physical dependencies and processes in our analysis, there are others which we have not included.

For example, while we have considered dependencies on the masses of the hosts and satellites, we have not included additional parameters such as those known to be secondary parameters in assembly bias (e.g. Sheth & Tormen, 2004; Xu et al., 2021). These may include local environment, halo shape and halo maximum circular velocity. Any of these may impact the motion of satellites, but, aiming for simplicity in our models, we choose not to pursue these secondary effects.

Finally, we note that throughout this work we have assumed that all the satellites are directly associated with the central, and that they do not interact with other satellites. This simplification ignores effects known to exist in simulations, including mergers between satellites (Shi et al., 2020), the accretion of groups onto clusters (Haggar et al., 2021), and more generally the pre-processing of satellites in other environments (Donnari et al., 2021). We also note that we have not included any exclusion principle for the satellites, and satellites could therefore lie arbitrarily close to each other when implementing our models.

4.8 Conclusions

In this work we have explored the radial distributions of satellite galaxies in groups in the GAMA survey and in the IllustrisTNG simulations. We have then compared the distributions of satellites between full-physics and dark matter-only (DMO) simulations, and developed models to characterise the differences.

For the GAMA survey, we showed the number density profile of all visible satellites in groups of mass $12.0 \leq \log_{10}(\mathcal{M}_h/h^{-1}\mathrm{M}_{\odot}) < 14.8$ at $z < 0.267$. We saw that an increasing group mass leads to a greater number of satellites and more extended radial distributions. However, normalising by the number of satellites and the group radius showed that there is no mass dependence to the shape of the satellite radial profiles. By comparison to mock catalogues constructed from DMO simulations, we identified that GAMA group profiles are expected to be accurate for small scales, but that satellites on the edges of the groups ($r_{\perp} \gtrsim 1\,h^{-1}$ Mpc), are missed by the group finding algorithm and so the profiles are underestimated.

We selected galaxies and groups from the TNG300-1 simulation to replicate the GAMA sample and showed that the profiles derived from these agree well with GAMA. This agreement demonstrates the accuracy of the satellite population in TNG, and so we can be confident that our subsequent modelling is performed on a realistic sample.

Comparing the full sample of group satellites above fixed stellar mass limits from the TNG simulations to matched subhaloes from the equivalent TNG-Dark runs showed that the satellite profiles are much flatter in the DMO case. We attribute this to two connected effects; an inwards displacement and a longer survival time of the satellites in the full-physics case.

Following this, we developed empirical models to account for these effects. We showed that the reduced halo-centric distances of matched satellites can be accounted for with a simple power-law model, and that a similar model can also reproduce the mass loss of these satellites. We fit the unmatched satellites which have endured longer in the full-physics run via two methods. Firstly, we considered the shape of the radial profile, finding it can be fit by a model of log-normal number counts. Secondly, we considered the radial motion of unmatched satellites over time.

In future work, we intend to apply our models to semi-analytic galaxy formation models, with the aim of improving their predictions of galaxy clustering. From a simulation perspective, an expansion to this work would be to apply the same methods to other simulations, such as EAGLE (Crain et al., 2015; Schaye et al., 2015), and the use of alternative methods to find, track and match subhaloes. Observationally, more reliable profiles of galaxy groups will be produced in future from the Wide Area VISTA Extragalactic Survey (Driver et al., 2019). The use of different group finding algorithms in observational data will also provide improvements, particularly around the edges of groups.

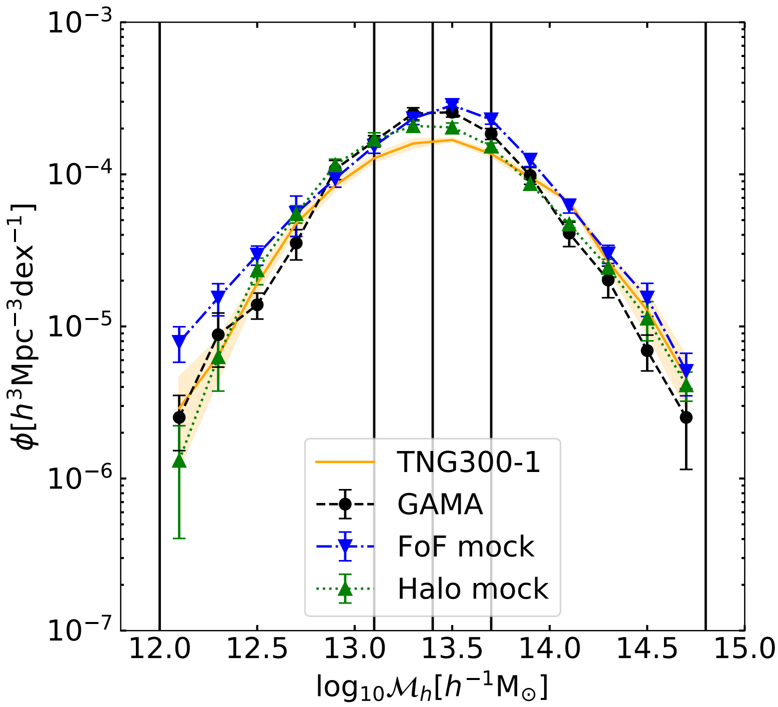

Figure 4.19: Mass function of selected groups in GAMA and the mock catalogues, together with a sample from TNG300-1 designed to approximately match the GAMA selection criteria. Vertical lines show the mass bins we use.

Appendices

4.A Group mass function

We show in Fig. 4.19 the mass distribution of selected groups from GAMA, the mocks and TNG300-1. Groups in TNG300-1 are selected with the method given in Section 4.3.1.

The primary effect of this selection method is to reduce the number of low-mass groups, and so the comparable shapes of the mass distributions of GAMA and TNG300-1 demonstrates the success of our selection method for TNG300-1 groups. Differences in the mass distribution are visible between GAMA and TNG300-1, but these are mostly at masses above the peak, where the selection function has less impact, and so this is more likely related to differences in the underlying group and galaxy populations (see e.g. Vázquez-Mata et al., 2020). Additionally, our earlier result that the halo mass does not affect the profile shape suggests that the differences seen here are unimportant.

4.B Resolution dependence of TNG and TNG-Dark distributions

We show here that the results of Section 4.4.3 still apply if we instead consider different resolutions with the same box size. This minimises the impact of different environments on our results, demonstrating the outcomes are not simply an effect of cosmic variance.

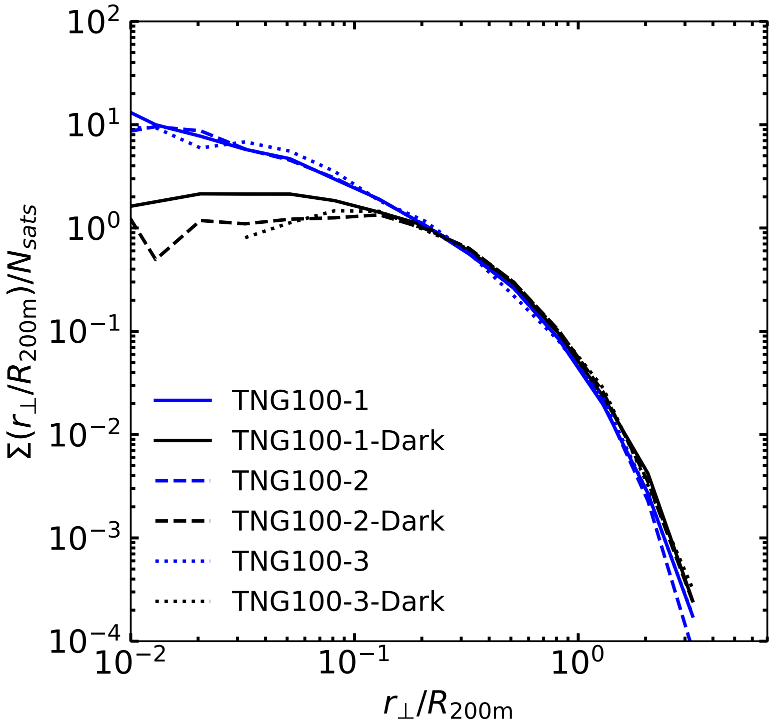

Figure 4.20: Normalised satellite profile of groups of mass $11 \leq \log_{10} \mathcal{M}_h < 15$ and galaxies with $\mathcal{M}_\star \geq 10^9 \mathrm{M}_\odot$ at $z = 0$ in TNG100-1, -2 and -3.

In Fig. 4.20 we show normalised profiles of satellites with $\mathcal{M}_\star \geq 10^9 \mathrm{M}_\odot$ for TNG100-1, TNG100-2 and TNG100-3, each compared against subhaloes from the equivalent TNG-Dark run, matched using SubLink. We see the same results as in Section 4.4.3, i.e. that resolution does not affect the distribution of full-physics satellites, but improved resolution changes the distribution of the matched TNG-Dark satellites. While the results from the worse resolution TNG-Dark runs are noisy, they flatten at larger radii than TNG100-1-Dark, and cut off at larger scales.

4.C Stellar mass dependence of TNG radial distribution

In Fig. 4.21 we show that the normalised satellite profiles in TNG do not depend on the simulation resolution or the stellar mass limit applied. We include TNG50-1, TNG100-1 and TNG300-1, each with a series of increasing minimum satellite masses. No change is seen in the shape of these normalised profiles when these different cuts are applied.

This shows that while the inclusion of lower-mass satellites increases the number of satellites, and so the amplitude of the average group profile, these additional satellites are distributed in the same way as the most massive satellites.

4.D Type 2 model fitting at different resolutions

Here we show the parameterisations of the Type 2 model given in Section 4.6.2 for TNG50-1, TNG100-1 and TNG300-1. For TNG100-1 and TNG300-1 we show in Fig. 4.22 the fits at each snapshot as solid lines with errorbars, and the overall relation with a

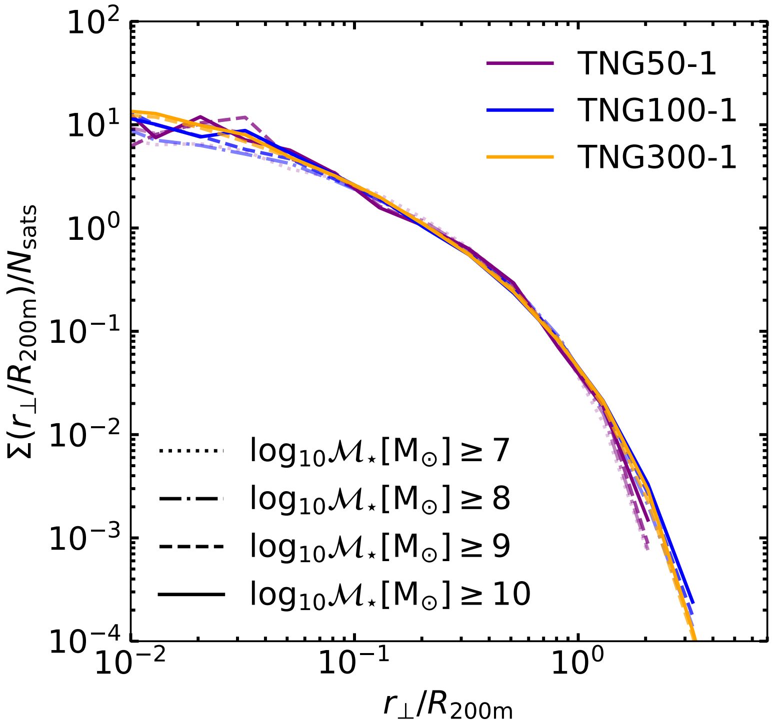

Figure 4.21: Normalised satellite profile of groups of mass $11 \leq \log_{10}\mathcal{M}_h < 15$ at $z = 0$ in TNG50-1, TNG100-1 and TNG300-1, with different stellar mass cuts on the galaxies included.

dashed line of the same colour. With TNG50-1 we only show the overall relation, as the scatter and uncertainties across individual snapshots are large.

It can be seen that the overall trends in the parameters as a function of time are the same for each resolution. However, the exact values vary, particularly at larger timesteps for $v(t)$ and $c(t)$. This is likely to show the covariances between our parameters, and also perhaps an effect of different halo and stellar mass selections in the simulations.

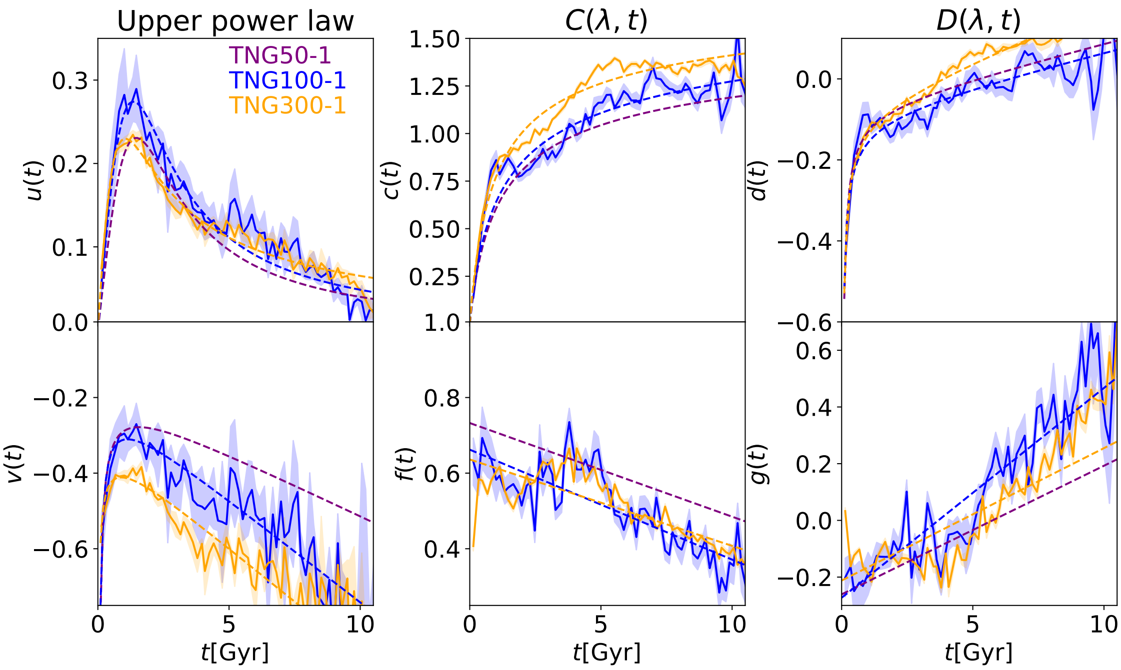

Figure 4.22: Parameters of the Type 2 model as a function of time, for TNG50-1 (purple), TNG100-1 (blue) and TNG300-1 (orange). The solid lines with error bands show the fits for each snapshot, and the dashed lines the fits as a function of time. We do not show the individual snapshot fits for TNG50-1 for clarity, as they have large scatter and uncertainty.

5

Applying satellite position corrections to SAMs

S. D. Riggs, J. Loveday, P. A. Thomas

Abstract

We explore the effects of modifying the radial distribution of satellite galaxies in semi-analytic models of galaxy formation (SAMs) using models derived from the IllustrisTNG simulations. The models used first adjust the positions of satellites in dark matter subhaloes, then place 'orphan' satellites either in a log-normal distribution or in locations empirically derived from their last known position. We implement these models in the L-GALAXIES and SHARK SAMs and examine the resulting galaxy clustering predictions, showing that both models for 'orphan' satellites improve the agreement with the Galaxy and Mass Assembly (GAMA) survey relative to the standard SAM implementations. However, in the case of SHARK we find that the number of galaxies per group is less than in GAMA, making it difficult to compare the radial distributions. In L-GALAXIES we find that the new models for satellite galaxies result in changes to the galaxy stellar mass function, so we recalibrate L-GALAXIES, finding we need to alter the parameters which determine the merger timescales and the star formation in merger-driven starbursts.

5.1 Introduction

In earlier chapters we have shown that the locations of satellite galaxies in groups are very uncertain in semi-analytic models of galaxy formation (SAMs) and other models based on dark-matter only simulations. This is especially true for the 'orphan' Type 2 satellites whose subhalo has merged or been disrupted, leaving an isolated galaxy. This directly affects the radial profiles of groups and the clustering of galaxies, and can also indirectly influence other observables.

The need for Type 2 satellites has been established in a number of works (e.g. Gao et al., 2004; Guo et al., 2011; Behroozi et al., 2019; Bose et al., 2020), although there is less agreement regarding the reasons for needing them. Despite their frequent use, there is no single established method to account for Type 2s. Many different methods have been used to incorporate them into SAMs, and some of these models were compared in Pujol et al. (2017), where it is shown they lead to different predictions from the SAMs. These methods commonly assume that the satellite orbits are determined solely by the constituents and dynamics of dark matter subhaloes in a DMO simulation (e.g. Tollet et al., 2017; Delfino et al., 2022). However, this assumption is poorly justified as the baryonic components can contribute a significant fraction of the total mass of satellites (e.g. Dvornik et al., 2020; Engler et al., 2021), and so the baryons are likely to affect the satellite dynamics.

In an attempt to resolve some of the uncertainty around modelling satellite positions, in Chapter 4 (Riggs et al., 2022, hereafter RLT22) we created models to account for the differences between the locations of satellites in the full-physics IllustrisTNG simulations (TNG, Marinacci et al., 2018; Naiman et al., 2018; Nelson et al., 2018, 2019a,b; Pillepich et al., 2018b, 2019; Springel et al., 2018) and their equivalent subhaloes in the TNG-Dark dark matter-only (DMO) simulations.

In a similar manner to that used in SAMs, we separated the TNG satellite galaxies into Type 1s which are directly matched to subhaloes in the TNG-Dark runs and 'orphan' Type 2s whose equivalent TNG-Dark subhaloes have already merged with another subhalo. The models we developed for these, together with the abbreviations we use for them in this chapter, are as follows:

- The *T1pl* power law model for Type 1s. The Type 1 satellites are closer to the halo centre than their equivalent TNG-Dark subhaloes, and this change can be fit with a power law.
- The *T2lg* model for Type 2 positions. The radial distribution of Type 2s approximately follows a log-normal distribution.
- The *T2rm* model for the radial motion of Type 2s. The radial motion of Type 2s was empirically modelled, using the time since the satellite became a Type 2, the initial radial location, and a uniform random variable.

Following the creation of these models, we now explore the outcome of applying these satellite radial position corrections in SAMs. We do this using L-GALAXIES

(Henriques et al., 2015) and SHARK (Lagos et al., 2018), which are the two SAMs we explored in Chapter 2. The original goal of creating our satellite galaxy models was to improve SAM predictions, and so this chapter provides an important test of whether we have achieved this objective.

In order to test the accuracy of the results from our models we once again compare the SAM outputs to the Galaxy and Mass Assembly survey (GAMA; Driver et al. 2009, 2011; Liske et al. 2015; Baldry et al. 2018; Driver et al. 2022b). In this case we consider the accuracy of the SAMs in predicting the stellar mass function, radial distribution of satellite galaxies, and projected galaxy clustering. We have chosen these observables as the primary aim of our models is to improve the clustering predictions, but it is important to check we do not degrade the accuracy of other predictions, particularly the stellar mass function.

The layout of this chapter is as follows: in Section 5.2 we introduce the modified versions of the SHARK and L-GALAXIES SAMs we use; in Section 5.3 we describe how we compare these against GAMA; we present results from the SAMs in Sections 5.4 and 5.5; and finally we discuss our results in Section 5.6.

5.2 Semi-analytic galaxy formation models

The SAMs with which we test our galaxy position models are the same as those we use in Chapter 2, the Lagos et al. (2018) version of SHARK and the Henriques et al. (2015) version of L-GALAXIES. We run each of the SAMs on their native dark matter halo catalogues. For SHARK this is the SURFS L210N1536 simulation (Elahi et al., 2018) and for L-GALAXIES this is the Millennium simulation (Springel et al., 2005).

Here we remind the reader of the physics affecting satellite galaxies in these SAMs, and then describe the impact that changing the locations of satellites is expected to have.

5.2.1 SHARK satellite physics

The standard version of SHARK contains Type 1 satellites at the locations of subhaloes and Type 2s which have lost their subhaloes. The Type 2s are distributed according to the Navarro et al. (1997, hereafter NFW) profile using the properties of the host halo.

SHARK is the easier of the two SAMs to implement the position corrections in, as the internal physics does not depend on the satellite locations. This means that we are able to change the positions as a post-processing step, and these corrections will not alter any other galaxy properties.

The reason for this lack of internal position dependence is that SHARK does not contain mechanisms for environmental stripping of cold gas and stars from satellites or the possibility of complete disruption of galaxies. It instead only removes the hot gas from satellites, which is done instantaneously when a galaxy becomes a satellite. Additionally, while the time a satellite takes to merge with the associated central does in principle depend on the satellite location, SHARK does not directly include this as it chooses the timescales using a statistical distribution for satellite orbits.

5.2.2 L-GALAXIES satellite physics

The Henriques et al. (2015) version of L-GALAXIES places Type 1 satellites in subhaloes, and tracks Type 2 satellites using the position of the most-bound particle of the subhalo they were last found in. Type 2 satellites are also given a further time-dependent inwards radial displacement that means they reach the centre of the host halo at the time they merge.

In the case of L-GALAXIES, the internal physics of the SAM depends on the locations of the satellite galaxies. The outcome of this is that when applying our models that alter the satellite positions we also adjust the number and properties of the galaxies produced by the model.

The position dependence of the internal galaxy processes manifests in three ways:

1. The stripping of hot gas from Type 1 satellites.
2. The estimate of the merger timescale when a satellite transitions from Type 1 (or occasionally Type 0) to Type 2.
3. The possibility of a Type 2 satellite being disrupted by tidal forces.

The first two of these are affected by the adjustment of the positions of Type 1 satellites, and the last is affected by the model for Type 2 satellite positions.

Further, the final one also depends on modelling of the disruptive forces which satellites are subject to and the implementation of these forces in the SAM. The standard method during a snapshot for L-GALAXIES is to reposition the central galaxy, check for disruption of satellites by estimating their peri-centre radius, then update the positions of the remaining satellites. There are two reasons why it is not clear that this is physically motivated.

Firstly, there is a strong justification for dealing with the satellite motion before checking the disruption condition, as this checks if disruption has occurred by the end of the satellite motion between snapshots, rather than at the previous snapshot. Secondly, using the peri-centre radius implicitly assumes the satellite reaches peri-centre within a single snapshot of the current time. This will not be the case for most satellites—Miki et al. (2021) find that the orbital timescales of satellites around the Milky Way are mostly in excess of a Gyr, which covers several snapshots in the Millennium simulation.

This leads us to adapt the disruption model in L-GALAXIES, as well as adjusting the positions of satellite galaxies. Our modified disruption model makes two changes based on our above arguments. Firstly, we move the time at which disruption may occur to after the satellite positions are updated. Secondly, we calculate the disruption based on the current position of the satellite, rather than an estimated peri-centre radius.

These two changes are expected to have opposite effects on the survival of satellites. Calculating the satellite locations earlier reduces the distance of the satellite galaxy from the central when the disruption condition is checked, increasing the tidal forces that cause disruption, but this is partly counter-acted by using the current radius, as this is by definition not smaller than the peri-centre radius.

Table 5.1: Definition of volume-limited galaxy samples for GAMA data with different magnitude cuts. The columns are absolute r-band magnitude limit K-corrected to redshift 0.1, redshift limit, sample volume, number of galaxies selected, and mean density.

$M_{\rm lim}$	$z_{\rm lim}$	V $[10^6\,h^{-3}\,{\rm Mpc}^3]$	$N_{\rm gal}$	$\bar{n}$ $[10^{-3}\,h^3\,{\rm Mpc}^{-3}]$
-20.00	0.267	7.93	42,679	5.38
-19.00	0.181	2.62	38,492	14.67
-18.00	0.121	0.81	19,063	23.65
-17.00	0.078	0.23	7,550	33.46

We note that the model for disruption used here is the instantaneous model which is used in the standard form of L-Galaxies, and originates from Guo et al. (2011). An alternative gradual stripping model was developed by Henriques & Thomas (2010) and Murphy et al. (2022) which is arguably more physical, but this model was also implemented before the positions are altered.

5.3 GAMA comparison samples

We compare the results from our modified SAM models against the GAMA survey to explore their accuracy. In this section we briefly describe the observational results we compare against and the methods used for these comparisons.

We perform comparisons on the stellar mass function (SMF), the radial distribution of satellite galaxies within groups, and the clustering of galaxies. The SMF is taken from the most recent GAMA release by Driver et al. (2022b), and we also show the earlier GAMA SMF from Baldry et al. (2012). The radial profiles giving the distribution of satellite galaxies are those from RLT22. The groups used for the radial profiles have at least 5 members, masses $12.0 \leq \log_{10}(\mathcal{M}_h/h^{-1}{\rm M}_\odot) < 14.8$ and reside at $z < 0.267$

We define new clustering samples with different densities of galaxies, based on the volume-limited galaxy sample of Riggs et al. (2021). We do this as it allows a comparison of the SAMs with less dependence on the masses of the galaxies output, and thus any changes to these caused by our position models. The samples we use from GAMA are defined in Table 5.1, using a series of cuts in r-band magnitude. The deepest of these samples is the same as the one that we used in Riggs et al. (2021), while the other samples were produced in the same way but using fainter magnitude cuts. To account for the galaxies not all being observed at the same redshift we apply K-corrections to $z = 0.1$ and e-corrections of $+Q_e z$ mag, where $Q_e = 1.0$.

5.3.1 GAMA galaxy auto-correlation

In order to calculate auto-correlation functions from GAMA we need a sample of random points to model any selection effects in the galaxy sample. We follow the same method as Riggs et al. (2021), generating 10 times more random points than galaxies in the survey mask of Loveday et al. (2018). Angular coordinates for these random points are sampled using MANGLE (Hamilton & Tegmark, 2004; Swanson et al., 2008), while the radial coordinates are drawn at random from a uniform distribution in comoving volume modulated by the density-evolution factor of Loveday et al. (2015).

Galaxy auto-correlation functions were generated from these GAMA samples and random catalogues using CORRFUNC (Sinha & Garrison, 2019, 2020). This calculates the two-dimensional auto-correlation along ($r_{\|}$) and perpendicular to ($r_{\perp}$) the line of sight with the Landy & Szalay (1993) operator,

$$\xi(r_{\perp}, r_{\|}) = \frac{gg - 2gr + rr}{rr}, \tag{5.1}$$

for galaxy–galaxy pairs, gg, galaxy–random pairs, gr, and random–random pairs, rr, with each of the pair counts normalised by the number of galaxies and randoms used in them.

These were then projected along the line of sight using

$$w_p(r_{\perp}) = 2\int_0^{r_{\|\max}} \xi(r_{\perp}, r_{\|}) dr_{\|}, \tag{5.2}$$

integrating up to $r_{\|\max} = 40\,h^{-1}$ Mpc.

The GAMA samples with lower volumes are significantly affected by an integral constraint on large scales. To correct for this we follow Roche & Eales (1999) by assuming a power law behaviour for the correlation function,

$$w_p(r_{\perp}) = Ar_{\perp}^{-B} - C, \tag{5.3}$$

to estimate the integral constraint C which we then add to the correlation function.

5.3.2 Comparison methods

Our comparisons of simulations and observations are all performed close to the mean redshift of GAMA, using the snapshot at $z = 0.18$ for L-GALAXIES and at $z = 0.19$ for SHARK. While we note that not all of our GAMA clustering and group samples extend to this redshift, we have checked that choosing lower redshift simulation samples does not alter our conclusions.

To generate comparable samples of groups and galaxies to compare the radial profile to GAMA we use the method of RLT22. This involves allocating a random location in the GAMA lightcone to each simulated group, and then determining how many of the constituent galaxies would have an observed magnitude brighter than $m_r = 19.8$ mag at that distance, and so be visible to GAMA. To match the GAMA selection, groups should only be included if at least 5 of their galaxies are identified as being visible.

For these selected groups, the profiles are then calculated in terms of projected distance to the centre of each simulated halo, taking the projection to occur along the z-axis.

When comparing galaxy clustering, we set absolute magnitude limits in the SAM outputs to produce galaxy samples of the same density as GAMA. The Henriques et al.

(2015) version of L-GALAXIES produces dust-corrected magnitudes directly, so we use those, but SHARK does not compute luminosities. To generate magnitudes for the SHARK galaxies we choose to use the post-processing routines adapted from L-GALAXIES which we set up in Chapter 2.

The clustering of galaxies in the simulations is computed using CORRFUNC as

$$\xi(r) = \frac{gg}{rr} - 1, \tag{5.4}$$

where the normalised random pair counts rr are calculated from the total box volume V and the volume of a spherical shell $v(r) = \frac{4}{3}\pi((r + dr)^3 - r^3)$, of radius r and thickness dr, using

$$rr = \frac{v(r)}{V}. \tag{5.5}$$

This is projected in the standard way,

$$w_p(r_\perp) = 2\int_0^{y_{\max}} \xi\left((r_\perp^2 + y^2)^{1/2}\right) dy = 2\int_{r_\perp}^{r_{\max}} \frac{r\xi(r)}{\sqrt{r^2 - r_\perp^2}} dr, \tag{5.6}$$

with a projection integral limit of $r_{\max} = 40\,h^{-1}\,\mathrm{Mpc}$. We do not apply an integral constraint correction to the simulated results, as the boxes are sufficiently large that this correction is negligible.

5.4 SHARK results

We now proceed to explore the impact of our satellite position corrections on the predictions from the SAMs.

Considering SHARK, the movement of satellite galaxies works as a post-processing step, which does not affect the other properties of the galaxies. This means that we do not need to recalibrate the free parameters of SHARK, as we have not modified any of the other predictions from it. Further, as the masses and luminosities of the galaxies are unchanged, we only need to consider the results for the radial distributions and galaxy clustering.

With SHARK, we compare four different runs of the SAM, progressively implementing the models for satellite galaxies. These are as follows:

- The *Lagos18* run, which uses the unaltered Lagos et al. (2018) version of SHARK.
- The *T1pl* run, which adds only the power law model for moving Type 1 satellites radially inwards.
- The *T1pl+T2lg* run which places the Type 2s in a log-normal distribution as well as moving the Type 1s.
- The*T1pl+T2rm* run which implements the model for radial motion of Type 2s as well as the model for Type 1s.

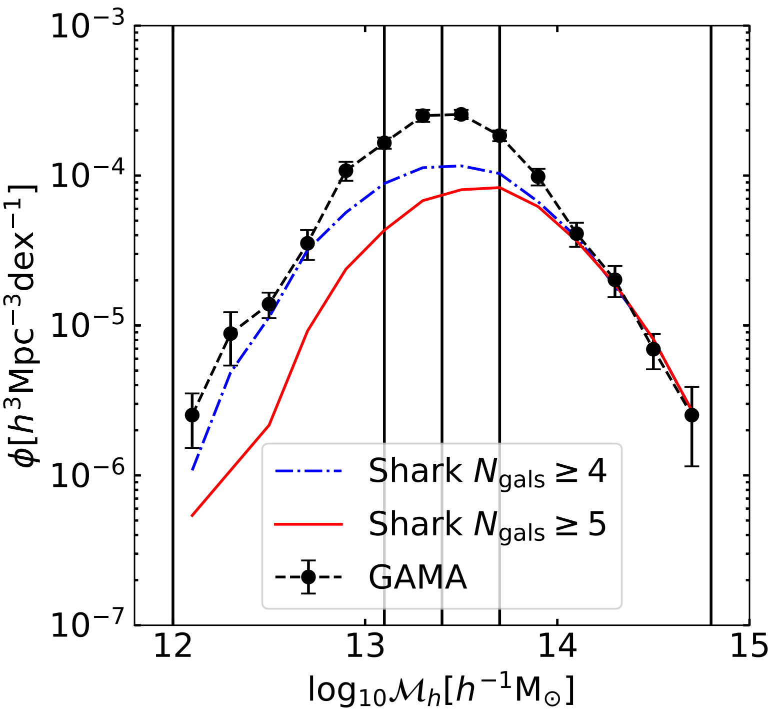

Figure 5.1: The masses of groups in the GAMA survey compared to those selected from the SHARK model. We show sampled SHARK groups with $N_{\mathrm{gals}} \geq 5$, the sample which is designed to match the GAMA selection (GAMA also uses $N_{\mathrm{gals}} \geq 5$), and those with $N_{\mathrm{gals}} \geq 4$, which provides a better match to the GAMA mass distribution.

5.4.1 Satellite radial profiles

We first consider the effect of our models on the radial distribution of satellite galaxies in SHARK. In order to compare these to GAMA we need to select a sample of groups and galaxies that matches the GAMA selection. However, in doing this we encounter a problem, which is illustrated in Fig. 5.1.

If we select groups which have 5 or more galaxies above the GAMA selection limit, which should correspond to the GAMA group sample we use, we sample too few groups with masses $\mathcal{M}_h < 10^{14}h^{-1}\mathrm{M}_\odot$. This suggests that the less massive SHARK groups have too few bright galaxies relative to GAMA, so they are not picked by the selection function.

This is associated with the differences we saw in Chapter 2 between the conditional satellite luminosity functions in SHARK, L-GALAXIES and GAMA. We therefore briefly return here to the Schechter function fittings we performed for the satellite luminosity functions in Chapter 2. In particular we are now interested in the amplitude $\phi_s^\star$ of the Schechter functions, as this will be the leading order term when determining the number of galaxies observed in each group. We show these amplitudes in Fig. 5.2, and it can be seen that they are lower for SHARK compared to L-GALAXIES, equivalent to a statement that SHARK has fewer galaxies per group. Further, both SAMs show lower amplitudes than in GAMA, and this difference approaches an order of magnitude for SHARK. However, we caution that we previously showed the Schechter functions are poor fits to the SAM luminosity functions and that Fig. 5.2 also shows there is a

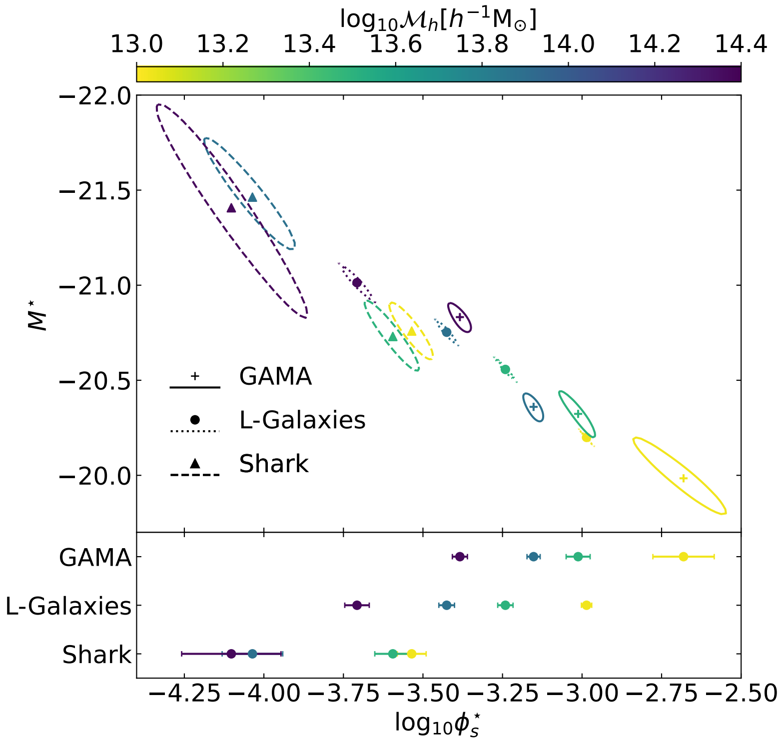

Figure 5.2: Amplitudes of conditional luminosity function parameters for satellite galaxies in GAMA, L-GALAXIES (using Millennium) and SHARK. These are the Schechter function results we calculated in Chapter 2. The upper panel shows 68% contour regions for the amplitude and characteristic magnitude, while the lower panel shows the amplitudes with non-marginalised 1-sigma errors.

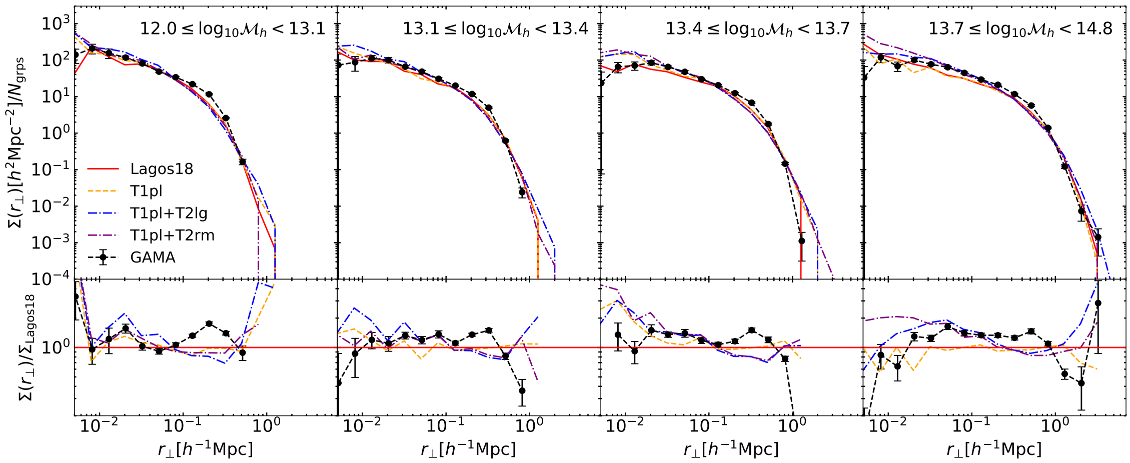

Figure 5.3: Radial distributions of satellite galaxies in the modified versions of SHARK, compared to the GAMA results of RLT22. The upper panels show the average radial profiles of the groups, while the lower panels show the ratio of each of the profiles in the upper panels to that of the Lagos18 run.

significant degeneracy between the amplitude and the characteristic magnitude of the luminosity functions. Relating this back to the group selection used here, the lower SHARK conditional luminosity function amplitudes means fewer galaxies will be visible per group for SHARK than GAMA and so fewer groups are selected.

To generate a sample of groups which better matches the GAMA groups we reduce the minimum number of galaxies required to 4. It can be seen in Fig. 5.1 that this then produces a group number density that is more comparable to GAMA for masses $\mathcal{M}_h \lesssim 10^{12.5}h^{-1}\mathrm{M}_\odot$. While this sample still contains too few groups at $\mathcal{M}_h \approx 10^{13.5}h^{-1}\mathrm{M}_\odot$, any further changes to the selection of groups will require selecting groups using a different method than has been done for GAMA and may alter the radial distributions, so we use this $N_{\mathrm{gals}} \geq 4$ sample.

In Fig. 5.3 we show the comparison of group profiles from SHARK against the RLT22 GAMA results. Due to the relatively low number of groups we have in our sample, the results for the profiles are noisy. It is apparent that all of the models predict the profiles with reasonable accuracy, and that there is not a clear preference for any of them above the others. The models we have implemented show a slightly greater density of satellites for $r_\perp < 0.02\,h^{-1}$ Mpc than the standard SHARK model and, at least in the lower mass bins, this appears to be driven by the movement of the Type 1 satellites.

On larger scales, $r_\perp \gtrsim 0.5\,h^{-1}$ Mpc all the SHARK models appear to agree reasonably with GAMA. However, this is perhaps further evidence that the SHARK groups differ from observed groups as in RLT22 we showed the GAMA profile is likely to be an underestimate on larger scales. The profiles we show here therefore suggest the SHARK groups are not sufficiently spatially extended.

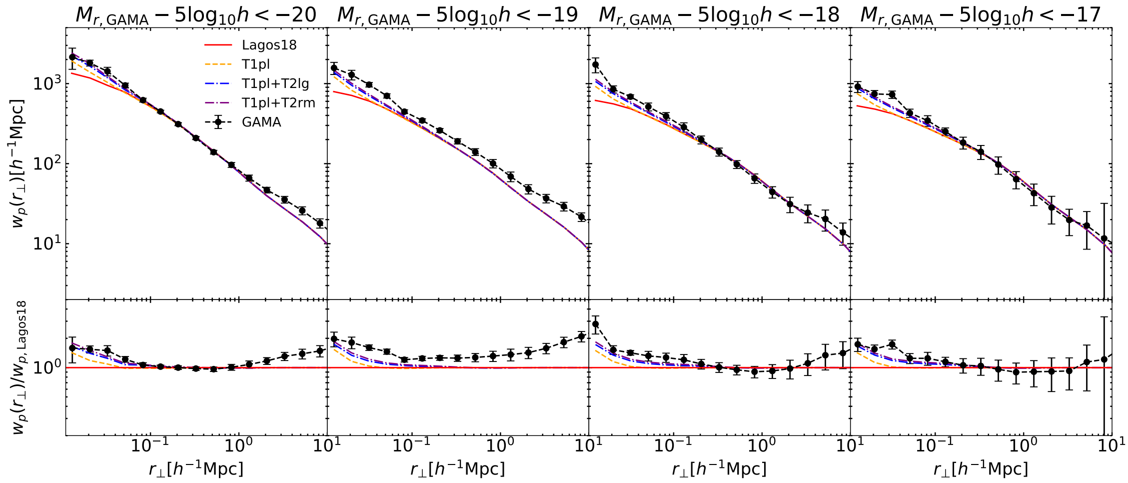

Figure 5.4: Clustering of galaxies in the modified versions of SHARK, compared to the GAMA samples in Table 5.1. The upper panels show the two-point correlation function for samples with different density cuts, and the lower panels show the ratio of these to the results of the Lagos18 run.

5.4.2 Galaxy clustering

In Fig. 5.4 we compare the clustering of our SHARK samples to the results from GAMA. These samples are selected in GAMA using a magnitude limit, and in SHARK by selecting galaxies to match the density of GAMA galaxies in each sample. In the brightest sample the SHARK magnitude limit is close to that of GAMA, at $M_r - 5\log h < -20.03$, but in the samples of lower brightness the magnitude limits match GAMA progressively less well. In the faintest sample we use GAMA has $M_r - 5\log h < -17$ while the SHARK sample has $M_r - 5\log h < -17.77$.

The results in all panels show that the Lagos18 version of SHARK under-predicts the clustering on scales $r_\perp \lesssim 0.1\,h^{-1}\,\mathrm{Mpc}$, but generally provides a good match to the GAMA results on larger scales. This again demonstrates the problem which our models are designed to address, as the small scales are those which are affected by the distribution of galaxies in groups.

Looking at the predictions of our modified forms of SHARK it can be seen that our models have indeed gone some way towards addressing the differences between the clustering in the Lagos18 version and GAMA. The T1pl model shows identical results to the Lagos18 version for $r_\perp \gtrsim 0.04\,h^{-1}\,\mathrm{Mpc}$ but on smaller scales it shows an enhancement of the clustering. This shows that moving the Type 1 satellites inwards has improved the agreement with GAMA.

The two runs using modified Type 2 satellite locations give very similar outcomes, and enhance the clustering further than the T1pl model. This leads them to agree better with GAMA than either the original Lagos18 version or the T1pl model alone. In particular, on small scales, the modified forms do not show the flattening seen in the Lagos18 version, and this effect extends slightly further than in the T1pl model, enhancing the clustering for $r_\perp \lesssim 0.1\,h^{-1}\,\mathrm{Mpc}$ in the two Type 2 satellite models. Overall, it therefore appears that our models for satellite galaxy radial positions have improved the clustering predictions from SHARK.

5.5 L-GALAXIES results

We now consider the outcome of implementing our models in L-GALAXIES. In L-GALAXIES the physics affecting satellite galaxies depends on their position relative to the centre of the host halo, resulting in both the survival time and the stripping of the gas changing when new models for the positions are included. We have also altered the mechanism for satellite galaxy disruption which further impacts the survival of satellites. Ultimately, our alterations lead to changes in the number of galaxies and their masses.

The first test of our models is to run L-GALAXIES with the new models but keeping the parameter values for the SAM as those determined by Henriques et al. (2015). However, the changes we have made to the internal mechanisms of the SAM mean we should also recalibrate the parameters of L-GALAXIES for the new models.

We examine a total of seven different runs of L-GALAXIES on the Millennium simulation. These runs consist of four model versions using the original parameters and recalibrated versions of three of these models. The first model is the unmodified Henriques et al. (2015) version, the baseline against which we compare the modified forms. Secondly, in the *AD* model we adjust the disruption mechanism to occur after the recalculation of satellite positions, and at the current position rather than at the peri-centre. This informs us on the impact of the modified disruption, before we adjust the satellite position model. The final two models implement the models of RLT22 in addition to the adjusted disruption. Both of these runs move the Type 1 satellites radially inwards using the power-law model. The *AD+T1pl+T2lg* model then adds the Type 2s in a log-normal radial distribution, while the *AD+T1pl+T2rm* model implements the empirical model for their radial motion.

In Table 5.2 we list these runs, together with the numbers of galaxies that are produced, and the number of disruptions that occur in each run. Note that the number of disruptions is a count of all occurrences, and so most of these will be of galaxies below the mass resolution of the simulation output.

The number of galaxies output by each run is similar, although we see the recalibration of the models can reduce the number of galaxies by more than 10% in some cases. In contrast, the number of disruptions varies substantially between the models. The alternative disruption mechanism causes an increase in the number of disruptions, and the use of the log-normal profiles for Type 2s increases the disruptions slightly further. However, the use of the radial motion model reduces the number of disruptions, suggesting the galaxies do not fall far enough into the halo potential to be disrupted before they are merged.

Table 5.2: Details of the model versions used for L-GALAXIES, with the number of galaxies output from them and the number of satellites that are disrupted.

Version or modifications	Name	$N_{\rm gals}(\mathcal{M}_\star > 10^9 \rm M_\odot)$	Disruptions
Henriques et al. (2015)	Hen15	4.30 $\times 10^6$	1.07 $\times 10^7$
Adjusted disruption	AD	4.34 $\times 10^6$	1.47 $\times 10^7$
+ Recalibration	recal_AD	3.74 $\times 10^6$	1.13 $\times 10^7$
Type 2 log-normal profile	AD+T1pl+T2lg	4.24 $\times 10^6$	1.77 $\times 10^7$
+ Recalibration	recal_T2lg	3.81 $\times 10^6$	1.53 $\times 10^7$
Type 2 radial motion model	AD+T1pl+T2rm	4.35 $\times 10^6$	0.63 $\times 10^7$
+ Recalibration	recal_T2rm	3.89 $\times 10^6$	0.57 $\times 10^7$

5.5.1 MCMC analysis of L-GALAXIES

To explore the changes that are necessary to the parameters of L-GALAXIES due to our model alterations we run Markov Chain Monte Carlo (MCMC) analysis. This MCMC analysis for L-GALAXIES was developed by Henriques et al. (2009, 2013), and here we simply repeat the approach used in Henriques et al. (2015). This uses observational constraints on the stellar mass function at $z = 0, 1, 2, 3$ and the fraction of red galaxies as a function of mass at $z = 0, 0.4, 1, 2, 3$ to fit the parameters. During the MCMC L-GALAXIES is run on a representative sample of trees from the Millennium and Millennium-II (Boylan-Kolchin et al., 2009) simulations (see Henriques et al., 2013). We do not use the halo model approach used by van Daalen et al. (2016) to fit clustering predictions as we are interested in the clustering outputs from our satellite galaxy models and do not want to adjust the clustering further.

Our objective here is to explore which parameters are altered and how this affects the predictions from the SAM. With this in mind, we do not run the MCMC formally to produce likelihood regions, but instead we simply search for a solution with high likelihoood. We cannot therefore claim to have conclusively determined the optimal solution, but the changes in the parameters and predictions will be informative as to the direction and magnitude of the shifts.

With our models for Type 2 positions we also note that the process is further complicated by the random variables in the Type 2 location models. This results in two levels of stochasticity, one from the MCMC and one from the models, which would make it more challenging to attempt to produce parameter likelihoods.

5.5.2 MCMC parameter results

Before considering the predictions of the modified version of L-GALAXIES, we first look at the new parameter values produced by the MCMC analysis. In Table 5.3 we list the parameters explored in the MCMC, together with the values determined for them in each of the models we use. We also include the parameters of the Henriques et al. (2020) version of L-GALAXIES for reference, although we caution that the meaning of some parameters is slightly different in that version.

In the AD and T2lg models one of the most apparent changes is a reduction of $\alpha_{\rm DF}$, which defines the time taken for satellite galaxies to merge. The merger time is given by

$$t_{\rm df} = \alpha_{\rm DF} \frac{r_{\rm sat}^2 V_{200c}}{G M_{\rm sat} \ln \Lambda}, \tag{5.7}$$

and so it varies linearly with the free parameter $\alpha_{\rm DF}$. The change in $\alpha_{\rm DF}$ occurs as by changing the disruption mechanisms we have increased the number of satellite galaxies being destroyed, so we have altered the balance between satellite galaxies merging or being disrupted. The reduced merger time suggested by the MCMC means that mergers occur faster, and specifically they occur before the disruption condition is met in more instances. However, it is worth noting that the merger time has not dramatically changed between the Hen15 and T2rm models. This implies that in the radial motion model it takes longer for satellite galaxies to move to a radial separation where disruption occurs than it does in our other models, confirming what we saw for the number of disruptions in each model.

The next significant parameter shift, which is present for all of three of our modified models, is a reduction in $\alpha_{\rm burst}$. This parameter defines the strength of the bursts of star formation that occur during galaxy mergers, and the change in this parameter can also therefore be ascribed to the alteration in the disruption and mergers of satellites. The resulting reduction in the stellar mass formed during bursts would lead to less star formation over the entire history of massive galaxies. However, this is balanced by an increase in the in-situ star formation from the higher value of $\alpha_{\rm SF}$, which defines the rate of star formation from cold gas.

The other parameters used in the MCMC do not show trends which are consistent between our model versions. The black hole feedback parameters (second section of Table 5.3) are in most cases close to their values in Henriques et al. (2015). The supernova feedback parameters (third section of Table 5.3) show some shifts for each of the models, with the values changing most clearly for the AD model. Shifts in the supernova feedback parameters are expected, as earlier studies with L-GALAXIES showed they affect satellite galaxies (van Daalen et al., 2016; Henriques et al., 2015), but the inconsistent nature of the shifts and the complexity of the feedback mechanisms makes it hard to provide detailed interpretations of these parameters.

5.5.3 Stellar mass function

The first prediction to consider from L-GALAXIES is the stellar mass function, which has changed due to the dependence of the physical models for environmental effects on satellite galaxy positions. We show the stellar mass density, the stellar mass function multiplied by mass, for the L-GALAXIES runs in Fig. 5.6. In the left panel we show each of the models when run with the Henriques et al. (2015) parameters, while in the right panel we show them using the recalibrated parameters. We choose to plot the mass density function rather than the stellar mass function here to highlight differences around the peak.

As we found in Chapter 2, the Henriques et al. (2015) version of L-GALAXIES

Table 5.3: The parameters explored in the MCMC for L-GALAXIES. The columns give the values from Henriques et al. (2015) and from Henriques et al. (2020), and the best fits determined by the MCMC for each of our modified versions. The parameters in the table are grouped by the processes they contribute to. The top section gives the star formation parameters, the second section the black hole feedback parameters, the third section the supernova feedback parameters, and the final section the parameters associated with satellite galaxies. We mark in bold the parameters from our models that have shifted by more than a factor of 2 from their value in Henriques et al. (2015).

Parameter	Hen15	Hen20	recal_AD	recal_T2lg	recal_T2rm
$\alpha_{\rm SF}$	0.025	0.060	**0.072**	**0.063**	**0.057**
$M_{\rm crit}$	0.24	0.14	**0.58**	0.35	0.48
$\alpha_{\rm burst}$	0.60	0.50	**0.096**	**0.15**	**0.23**
$\beta_{\rm burst}$	1.9	0.38	1.5	1.8	1.7
$k_{\rm AGN}[{\rm M_\odot yr^{-1}}]$	0.0053	0.0025	0.0096	**0.011**	0.0043
$f_{\rm BH}$	0.041	0.066	0.022	0.036	0.041
$V_{\rm BH}[{\rm km\ s^{-1}}]$	750	700	1100	1100	1200
$\epsilon_{\rm reheat}$	2.6	5.6	**1.2**	2.1	1.3
$V_{\rm reheat}[{\rm km\ s^{-1}}]$	480	110	**2200**	640	680
$\beta_{\rm reheat}$	0.72	2.9	0.39	**0.29**	0.73
$\eta_{\rm eject}$	0.62	5.5	0.38	1.1	0.79
$V_{\rm eject}[{\rm km\ s^{-1}}]$	100	220	190	110	65
$\beta_{\rm eject}$	0.8	2.0	**3.8**	1.5	**0.3**
$\gamma_{\rm reinc}[{\rm yr^{-1}}]$	3.0×10^{10}	1.2×10^{10}	2.9×10^{10}	2.6×10^{10}	3.6×10^{10}
$Z_{\rm yield}$	0.046	0.030	0.023	**0.018**	0.024
$M_{\rm rp}[10^{10}{\rm M_\odot}]$	1.2×10^4	5.1×10^4	$\mathbf{5.9 \times 10^4}$	1.7×10^4	9.1×10^3
$\alpha_{\rm DF}$	2.5	1.8	**0.29**	**0.43**	2.3

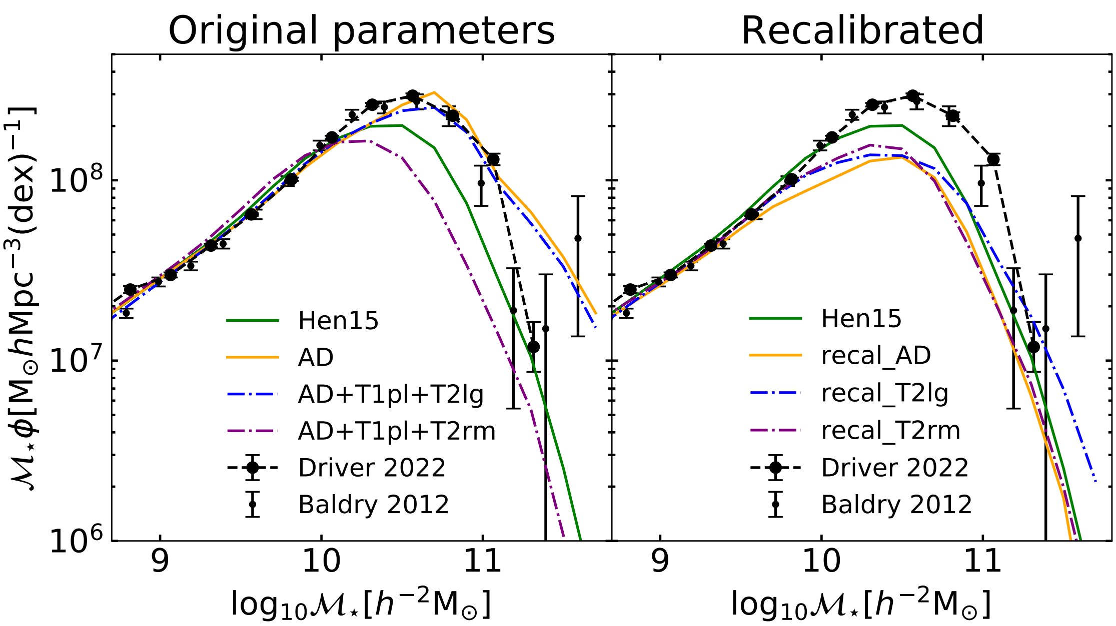

Figure 5.5: Stellar mass density function of the modified versions of L-GALAXIES, compared to GAMA results from Baldry et al. (2012) and Driver et al. (2022b). The left panel shows the outcome of the models using the parameters of Henriques et al. (2015), while in the right panel we show the recalibrated versions.

reproduces the SMF with reasonable accuracy compared to GAMA, although with a slight underestimation at masses $\mathcal{M}_\star \approx 10^{10.7}h^{-2}\mathrm{M}_\odot$.

Modifying the disruption mechanism has a significant effect on the stellar mass function before the recalibration is applied (AD model). The disruption primarily occurs for galaxies with low masses, and it might therefore be assumed the main effect of increased disruption would be to reduce the SMF at low masses. However, while the number of low-mass satellites does change a small amount, differences are instead most apparent at $\mathcal{M}_\star \gtrsim 10^{10.5}h^{-2}\mathrm{M}_\odot$. This increase in the masses of the most massive galaxies occurs because increased disruption means low mass satellite galaxies no longer merge with their central. This reduction in the number of mergers leads to less gas being accreted by the super-massive black hole in the core of the central galaxy, reducing the quenching effect of AGN feedback, and allowing the central galaxy to keep forming stars, increasing the stellar mass.

Looking at the recalibrated version (recal_AD model) it can be seen that the MCMC procedure is able to account for this change in the mass function and almost reproduce the results of the standard Hen15 model. Considering only this low-redshift stellar mass function then the changes due to the MCMC are perhaps not advantageous, as without calibration the AD model matches the peak of the stellar mass function better, although the recalibration does bring the number of galaxies with $\mathcal{M}_\star > 10^{11}h^{-2}\mathrm{M}_\odot$ into better agreement with GAMA. However, the recalibration is not only making use of low redshift stellar masses. The necessity of the changes is therefore likely to suggest an incompatibility whereby the model cannot accurately reproduce both the SMF and the galaxy red fractions simultaneously.

Having established the effect of the disruption mechanism, we can now consider the effect of our models for satellite positions. Firstly, the log-normal model (AD+T1pl+T2lg), which without calibration leads to a similar stellar mass function to that of the AD disruption model. This implies that over the lifetime of a satellite the probability of being disrupted remains about the same as the original model using most bound particles. Secondly, the radial motion model (AD+T1pl+T2rm), which dramatically reduces the number of high-mass galaxies compared to the AD model. This is due to a substantially reduced number of disruptions, probably a result of satellites remaining further from their group centre and never experiencing the full effect of the tidal forces.

While the two new models for Type 2 positions predict very different stellar mass functions before calibration, when the MCMC has been performed they give similar predictions. As we saw for the recal_AD model, the MCMC tends to bring the stellar mass function back towards the Hen15 prediction, and so all the recalibrated models give underestimates compared to the GAMA stellar mass function. Despite the resulting differences with GAMA, it is reassuring that the stellar mass function of the Hen15 model can be reproduced from our adapted version of L-GALAXIES.

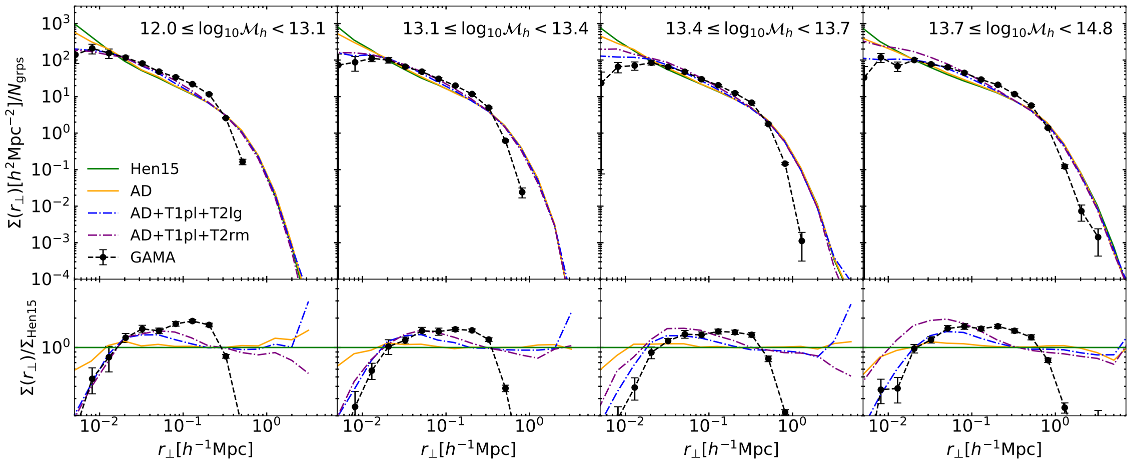

Figure 5.6: Radial distributions of satellite galaxies in the modified versions of L-GALAXIES using the parameters of Henriques et al. (2015), compared to the GAMA results of RLT22. The upper panels show the average radial profiles of the groups, while the lower panels show the ratio of the each of the profiles in the upper panels to that of the Hen15 run.

5.5.4 Satellite radial profiles

We can now directly consider the distributions of satellite galaxies in the groups by comparison to the GAMA profiles of RLT22. To do this we first need to apply the RLT22 selection function to choose a sample of groups and galaxies that is comparable to the GAMA survey. In Fig. 5.2 we showed that the conditional luminosity functions for L-GALAXIES satellites are closer to the GAMA results than for SHARK. This means we do not need to adjust the group selection limit from the RLT22 method, and so select only groups with a number of observed galaxies $N_{\mathrm{gals}} \geq 5$ for L-GALAXIES.

The radial profiles of these GAMA-matched L-GALAXIES samples are shown for the models using the parameters of Henriques et al. (2015) in Fig. 5.6 and for the recalibrated versions in Fig. 5.7. Firstly we note that for all models we find the same problem as RLT22 on scales $r_\perp \gtrsim 0.5\,h^{-1}\,\mathrm{Mpc}$, that the group profiles determined from GAMA are much lower than those of the simulations. However, as shown in RLT22, this is likely to be due to differences in the group finding method, and does not represent a problem with the L-GALAXIES results. On these scales the different L-GALAXIES runs display a similar profile, although the radial movement model generally predicts a slightly reduced number of satellites.

The differences between the models become most apparent on scales $r_\perp < 0.1\,h^{-1}\,\mathrm{Mpc}$. Prior to recalibration, at the smallest scales the Hen15 and AD models display a much greater density of satellites than GAMA. This problem also occurred in the GAMA mock catalogues used in RLT22, and was used there to add justification to the need for new models of satellite positions. Following the recalibration, the AD model agrees better with GAMA on the smallest scales, but at the cost of a reduced amplitude on scales $r_\perp \approx 0.05\,h^{-1}\,\mathrm{Mpc}$ which results in under-prediction compared to GAMA.

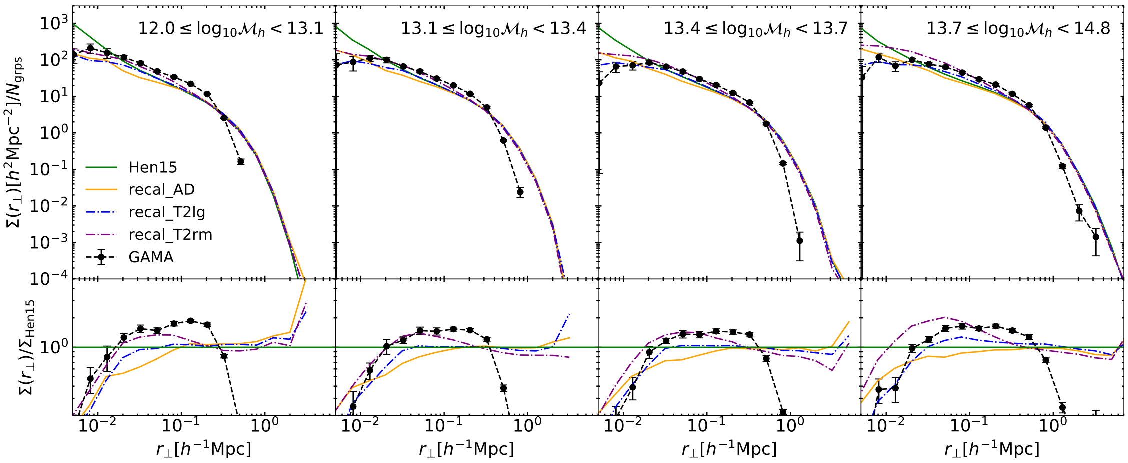

Figure 5.7: Same as Fig. 5.6 but for the recalibrated versions of L-GALAXIES.

In contrast, both of our models for Type 2s show flattening on small scales. Additionally, a sharper turn increases the amplitude compared to the AD model at $r_\perp \approx 0.05\,h^{-1}\,\mathrm{Mpc}$. The recalibration procedure has a relatively minimal effect on the profile predictions from both of the models for Type 2s, leading only to a slight amplitude reduction for the log-normal model.

The log-normal model displays a good match to GAMA, being generally consistent within uncertainties for $r_\perp < 0.03\,h^{-1}\,\mathrm{Mpc}$, the same scales where the original (most-bound particle) model used in the Hen15 version becomes discrepant. This is to be expected, as the log-normal distribution matches the results of TNG by construction. On larger scales the results tend towards those of the Hen15 model.

The more interesting results here are those from the radial motion model, which we were unable to test fully in RLT22. This displays a good match to GAMA for the two lower mass bins, with a similar level of accuracy to the log-normal model. However, it is clear that the differences between this model and GAMA increase as group mass increases. In the highest mass bin, the predicted profile from this model exceeds GAMA, and lies closer to that of the original Hen15 model results. Despite this, the results here are encouraging, as the model is a significant improvement on the Hen15 model at low masses.

5.5.5 Galaxy clustering

Finally, we compare the clustering of the galaxies in each of our L-GALAXIES runs, which is shown in Fig. 5.8. We only show the clustering results for the final recalibrated models as these represent the optimum scenarios, and the clustering predictions do not change significantly when recalibrating the models. When considering the samples selected by density to match GAMA, the same changes in the limiting magnitude occur as we saw in SHARK. In the brightest sample the magnitude limit is about the same as GAMA, whereas the faintest sample has $M_r - 5\log h < -17.59$ for the Hen15 model compared to $M_r - 5\log h < -17$ for GAMA. We note that this may reflect the limited resolution of the Millennium simulation, and perhaps indicates that these samples are less reliable from

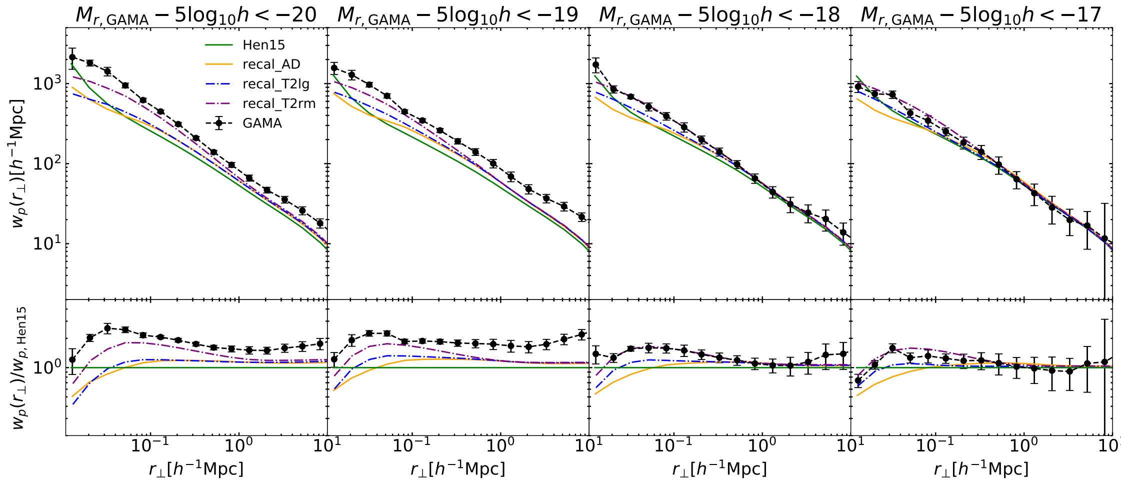

Figure 5.8: Clustering of galaxies in the modified versions of L-GALAXIES, compared to the GAMA samples in Table 5.1. The upper panels show the two-point correlation function for samples with different density cuts, and the lower panels show the ratio of these to the results of the Hen15 run.

L-GALAXIES.

The comparison in the left panel of the Hen15 run and GAMA selected with $M_r - 5\log h < -20$ is identical to the results shown in Fig. A2 of Riggs et al. (2021), and shows that L-GALAXIES predicts a lower clustering amplitude for volume-limited samples than that observed in GAMA. This trend of reduced clustering amplitude for L-GALAXIES continues into the bins of greater density, but the agreement between L-GALAXIES and GAMA improves in the higher density samples.

Similar results are found using the modified disruption, although the clustering amplitude decreases for $r_\perp \lesssim 0.1\,h^{-1}\,\mathrm{Mpc}$. This results in a greater difference in amplitude between L-GALAXIES and GAMA but brings the shape of w_p into better agreement.

The agreement between L-GALAXIES and GAMA improves for our models with modified satellite locations. The log-normal model shows slightly enhanced clustering at $r_\perp \approx 0.05\,h^{-1}\,\mathrm{Mpc}$ compared to the Hen15 run, and on the smallest scales $r_\perp \lesssim 0.02\,h^{-1}\,\mathrm{Mpc}$ it displays the slight flattening which is seen in GAMA, likely related to the flattening seen in the profiles at the centre of groups. However, the clustering is still under-predicted relative to GAMA in most bins. This persists to large scales in the brighter samples, and so will not be due solely to the positioning of satellite galaxies in groups.

The radial motion model shows the best agreement with GAMA. The same effects are seen as in the log-normal model, of enhanced amplitude and small-scale flattening, but the amplitude is changed more significantly. This brings the results into closer agreement with GAMA across all scales, albeit with some underestimation remaining for the brighter samples. Interestingly, in the two faintest samples this model agrees almost perfectly with GAMA at all scales, demonstrating a major success for our model, although we caution that these samples will be the least reliable.

5.6 Discussion and conclusions

In this chapter we have explored the outcome of including the models for satellite positions from Chapter 4 in the L-GALAXIES and SHARK SAMs. These models firstly move the Type 1 satellites, which are contained in subhaloes of the DMO simulations, radially inwards. Then we included two models for the Type 2 satellites, those without DMO subhaloes. One of the models for Type 2s places them randomly in a log-normal radial distribution while the other moves them radially inwards from their starting location with an empirical model.

5.6.1 Summary

Using SHARK we saw that the new models do not significantly change the radial distributions of satellites from the standard model which assumes Type 2s are distributed by the NFW profile, but that the new models do improve the small-scale clustering predictions.

We determined one main problem with the use of these models in SHARK, which is that the number of visible galaxies per group is less than in GAMA. This means the predictions for radial distributions are subject to a large uncertainty, and so while all the models agree reasonably with the GAMA profile, it is difficult to reach definite conclusions about their accuracy. The low numbers of galaxies in groups can be interpreted in a number of ways, as it could be evidence that galaxies are too faint, galaxies merge too quickly, or that the groups are fragmented in the halo catalogue. It is likely that a combination of effects are involved, but the determination of which aspects of the SAM lead to this is beyond the scope of our investigation.

Despite the low numbers of galaxies per group and the similarity of the radial distributions between models, when comparing clustering results between the modified versions of SHARK they all show slightly enhanced clustering for $r_\perp \lesssim 0.1\,h^{-1}\,\mathrm{Mpc}$ compared to the original version. This brings the predictions from the modified versions into better agreement with GAMA. Much of the improvement results from the movement of Type 1 satellites, but the addition of either model for Type 2s does provide further improvements to the agreement with GAMA.

Using L-GALAXIES gives us a more reliable demonstration of the improvements that are possible with our models, and we have shown that the models for updated satellite positions improve the predictions for clustering and group profiles.

In addition to the satellite galaxy models, we also made slight modifications to the mechanism for satellite disruption in L-GALAXIES, causing disruption to occur at the current position rather than an estimated peri-centre. We showed this increases the number of satellites that are disrupted and consequently reduces the amplitude of the satellite radial distribution and galaxy clustering on small scales. This modified disruption is not able to improve the clustering predictions alone, which requires the addition of our modified models for satellite positions. We have shown that the log-normal model gives the most accurate group profiles but continues to underestimate the clustering, while the radial motion model produces the most accurate clustering predictions but does not fit the halo mass dependence of the group profiles.

Finally, we showed that recalibration of L-GALAXIES is necessary as the galaxy masses depend on the satellite galaxy physics. We performed this recalibration using MCMC. The most significant parameter changes this led to were a reduction in the time taken for galaxies to merge, and a decrease in the strength of the starbursts that occur due to these mergers.

5.6.2 Future prospects

Overall, the results we have shown indicate that our models do provide an improvement over the standard methods of including satellite galaxies in SAMs. However, these models can be further explored with L-GALAXIES, and also with other SAMs. In L-GALAXIES we have chosen to use the Henriques et al. (2015) version and follow the MCMC procedure used in that work, but this can be followed up by including the satellite galaxy models in the more recent Henriques et al. (2020) version and using additional MCMC observational constraints. Further, these models should be combined with the more detailed disruption methods of Murphy et al. (2022), and extra parameters can be included in the MCMC analysis, such as the mass ratio used to distinguish between major and minor mergers.

Finally, the models we have presented here can themselves be improved further by accounting for the remaining discrepancies, such as the remaining halo mass dependence to the group profile, and the calibration of them using other hydrodynamical simulations as well as IllustrisTNG.

6

Conclusions

In this thesis we have explored the distributions of galaxies within and around groups in the GAMA survey and in simulations of the Universe. We have shown that in simulations the clustering of galaxies on small scales is mainly determined by the modelling of satellite galaxies, and that there is significant uncertainty around this. Using comparisons between observations and a variety of types of simulation we have explored the satellites of groups and developed models for their distributions.

6.1 Summary of results

In Chapter 2 we compared the semi-analytic galaxy formation models L-GALAXIES and SHARK to results from the GAMA survey. We concluded that while both SAMs show a reasonable agreement with observations, there is room for improvement in both. In particular, we found that the modelling of orphan satellites, which have lost their host subhalo, is a major source of uncertainty for galaxy clustering results.

We first compared SAM predictions for the stellar mass function, luminosity functions and conditional one-point functions to GAMA. As part of this we modified L-GALAXIES to run on the SURFS simulations, and adapted the luminosity post-processing methods of L-GALAXIES to run on SHARK outputs. Using the same halo catalogue for the two SAMs showed that they are calibrated to produce different numbers of massive galaxies due to the different halo catalogues and trees they are built upon. Then by generating luminosities we showed that the VIPERFISH method of generating luminosities for SHARK agrees well with the L-GALAXIES methods for most wavelength bands.

Subsequently, we compared the clustering predictions of the SAMs to GAMA and interpreted this using the radial distribution of orphan satellites in the SAMs. SHARK generally predicts lower clustering amplitudes than L-GALAXIES, and this appears to be driven by lower satellite fractions in SHARK. We identified that clustering on scales $r_\perp \gtrsim 0.5\,h^{-1}\,\mathrm{Mpc}$ is mainly determined by the halo catalogue and that smaller scales depend upon the orphan satellite galaxies.

In Chapter 3 we explored the clustering of galaxy groups in the GAMA survey, using the group–galaxy cross-correlation function and the first use of the marked correlation function with groups. We found that on large scales the bias increases with group mass, and so larger groups are contained in extended structures. On small scales we observed an increase in the amplitude of the relative bias, and a flattening on the smallest scales due to the core of the groups.

The GAMA group clustering results were compared against the IllustrisTNG simulations and L-GALAXIES model to explore the galaxy distributions in these. IllustrisTNG accurately predicts the GAMA results for the group–galaxy clustering, but overestimates the marked galaxy auto-correlation function, which appears to show the scatter in the relation between central galaxy masses and group masses is too small. In contrast, L-GALAXIES exhibits significant discrepancies when compared to GAMA. This is particularly true of the group–galaxy cross-correlation, which has a much greater dependence on galaxy masses in L-GALAXIES than in GAMA, which we suggest is associated with the supernova feedback mechanisms, although the uncertainty in the locations of orphan satellite galaxies also contributes to an excess of galaxies in the inner regions of the groups.

In Chapter 4 we explored the difference in the distribution of satellite galaxies between the full-physics IllustrisTNG simulations and their dark matter-only equivalents. We showed that the radial distributions of satellite galaxies in TNG groups agree well with GAMA near the centre of groups and that the differences between them near the edges of groups are most likely due to the friends-of-friends groups from GAMA missing galaxies. When normalised, the profiles from GAMA and TNG both show no dependence on group mass.

Comparing matched satellites between TNG and TNG-Dark runs we showed that the number density of matched TNG-Dark subhaloes is lower than of full-physics satellites in the centre of haloes. We determined that this is associated with two related effects that occur when baryonic physics is included. These are that satellites in the full-physics simulations are closer to the halo centre and have longer survival times.

We showed that the TNG satellites can be split into the equivalent of Type 1 (DMO-matched) and Type 2 (orphan) satellites in SAMs by utilising matches between TNG galaxies and TNG-Dark subhaloes, and we created models for the positions of each of these satellite types. Comparisons of the directly-matched Type 1 satellites showed that they are displaced inwards in the full-physics simulation in a manner that can be fit with a power law. For the Type 2 satellites, which have no unique TNG-Dark equivalent, we took two approaches, showing that they can be distributed in a log-normal radial number density profile or that their radial motion can be modelled as a function of time and a uniform random variable.

We tested these new models for Type 1 and Type 2 satellites in Chapter 5 by applying them to the L-GALAXIES and SHARK SAMs. We found that our models do improve the predictions for galaxy clustering when compared to results from the GAMA survey. While the two approaches to modelling Type 2 satellites give slightly different outcomes, they are both sufficiently accurate that either offers an accurate model for the satellite distributions.

While exploring these models we saw that the predictions for the stellar mass function from L-Galaxies change when the satellite galaxies models are changed. Therefore we recalibrated the SAM, which demonstrated that the stellar mass function of the Henriques et al. (2015) model can be recovered by changing the parameters which are related to galaxy mergers.

6.2 Outlook

Throughout this thesis we have been working with both observations and simulations which suffer from significant limitations and we have needed to make many assumptions. We end this thesis by discussing a few of these and the prospects for improvements and follow-up studies over the coming years.

In all chapters we have been comparing observations and simulations, and these comparisons could be improved by measuring the properties of the groups and galaxies from the simulations using the same methods as in the observations. This applies particularly to the identification of groups, where making mock lightcone catalogues and applying the group finding method used in the observations would largely eliminate any problems associated with differences in the definitions of haloes and groups. This would make it clearer where there are true differences between the galaxy and group populations of the observations and simulations, and where the divergences we see are from differing methodologies.

The clearest follow-up to the work we did in Chapter 2 would be to incorporate clustering predictions in the observations used to constrain SAM parameters. This would ideally be done using MCMC, but this is challenging due to the volumes needed for clustering calculations. One way around this is to use the halo model, as done by van Daalen et al. (2016). However, our results perhaps offer an alternative approach—use only the smallest scales. We demonstrated that the large scales depend primarily on the halo catalogue, so will not be changed by altering the SAM parameters, and are therefore unnecessary in MCMC. While computing only small scales would prevent the use of the projected clustering $w_p(r_\perp)$, the three-dimensional clustering $\xi(r)$ could be constrained against hydrodynamical simulations such as TNG.

In Chapter 3 one of the primary sources of uncertainty was the group catalogues from GAMA. The main way this can be improved upon will be the use of updated group finding methods. These include newer methods such as those of Tempel et al. (2018) or Tinker (2021) and the addition of photometric data to enlarge the regions in which group finding can be performed (e.g. Wang et al., 2020; Yang et al., 2021). This will also allow the results to be expanded to include groups with fewer galaxies and lower masses.

When considering the differences between satellite galaxies in full-physics and dark matter-only simulations in Chapter 4 we concentrated only on the masses and radial positions of the galaxies. However, these are only some of the properties that may change. Arguably the most important quantity we did not consider is velocity, which baryonic physics is known to affect in some contexts (e.g. Kuruvilla et al., 2020), and the satellite galaxy velocities must be different from the DMO subhaloes as the positions are different. Exploring these velocity differences would be an interesting follow-up study.

Additionally, throughout this thesis but most notably when making the models for satellite galaxy positions, we performed all the calculations assuming that satellites are uniformly distributed in spherical haloes. However, as discussed in Pawlowski (2021), satellites have been shown to be associated with each other in phase-space, forming planes and lopsided distributions. Such effects are not directly accounted for in SAMs (although they may be implicitly present for Type 1s) and improvements upon our models for satellite positions should consider these associations.

At a more general level, the next generation of galaxy surveys will be able to significantly improve upon the observational results we have presented in this thesis. In particular, the upcoming Wide Area VISTA Extragalactic Survey (WAVES, Driver et al., 2019) in the 4-metre Multi-Object Spectroscopic Telescope (4MOST, de Jong et al., 2019) programme will provide a galaxy sample covering $\sim 1,200$ degrees^2 and reaching a Z-band magnitude of ~ 21.1, making it both wider and deeper than GAMA. It will make repeated observations of high-density regions to give a high completeness, so it will be well-suited to studies of galaxy groups. Consequently, the results we have found in this thesis for galaxy clustering, group clustering and satellite radial distributions will be made more reliable.

Other surveys will also provide improvements on our results. The Dark Energy Spectroscopic Instrument (DESI, DESI Collaboration et al., 2016) will provide a sample of similar depth to GAMA across around 14,000 degrees^2. This will produce much more reliable estimates of the clustering on large scales, although it will have a lower completeness on small scales and so not be as suitable for group studies. A further large sample of galaxies will be provided by the Legacy Survey of Space and Time (LSST, Ivezić et al., 2019), which expects to be able to explore properties of galaxy groups across time.

Many of the possible improvements from simulations will come from hydrodynamical simulations continuing to grow in size and complexity over the next few years as the computational resources available for them increases. This growth can be in two different directions: greater volume or improved resolution. The TNG300-1 and TNG50-1 simulations represent steps in each of those directions, but future simulations should be able to make further progress. Both of these improvements are beneficial. Larger boxes will gradually be able to replace HODs and SAMs when making mock galaxy surveys, which should consequently improve the accuracy of the mocks. Then improved resolution will probe the internal structure of the galaxies in more detail, providing more detailed tests of the physics of galaxy formation. In addition, it will be increasingly possible to test this physics and the subgrid models used to approximate it by running many smaller simulations, and it will perhaps also be possible to use these to explore alternative theories of cosmology—testing whether it is possible to disentangle cosmological effects from baryonic physics on small scales.

Despite the improvements in hydrodynamical simulations, when exploring very large regions, such as when creating mock catalogues for galaxy surveys or investigating large-scale cosmological effects, SAMs will still arguably provide the best method for the foreseeable future. Alternatives are being introduced, such as the method of Lovell et al. (2022) which uses machine learning to map galaxies between hydrodynamical and dark matter-only simulations and predict the baryonic component of a dark matter halo. However, SAMs provide a clearer method with which to test the galaxies that could be produced in universes with modified cosmologies, as has been tried by Fontanot et al. (2013), albeit leaving uncertainties around the baryonic physics and the tuning of the models. Furthermore, SAMs still have a fundamental advantage in that they can be used to explore the effects of new physical and empirical models very quickly, as we have explored for satellite galaxies. The uncertainty surrounding much of the astrophysics involved in galaxy formation and evolution means further models will be required, and the need to test these models means SAMs will continue to be a useful tool to explore physical processes in the Universe.

6.3 Final remarks

In this thesis we have explored galaxy clustering on small scales and connected that to the study of galaxy groups. We have shown that this is still a challenging area both to determine from observations and to reproduce with simulations. Whilst there are still many problems and assumptions to resolve, this is a worthwhile field to continue exploring and should provide new insights as larger observational and simulated data products become available over the coming years.

7

Further Acknowledgements

For Chapter 2 we thank Peter Thomas for useful discussions and comments in the preparation of this work. We thank Claudia Lagos for providing the SURFS simulation data and advice on the SHARK SAM. We also acknowledge the anonymous referee who provided comments on this manuscript.

For Chapter 3 we thank Michael Boylan-Kolchin for providing the Millennium and Millennium-II simulation dark matter correlation functions in machine-readable form. We acknowledge the IllustrisTNG team for making their simulation data available. Finally, we thank the anonymous referee for providing helpful comments about the manuscript.

For Chapter 4 we thank Andrew Hopkins for suggestions about the manuscript. We also thank the anonymous referee who provided comments which improved the manuscript.

For Chapter 5 we thank Bruno Henriques for advice on the use and interpretation of L-GALAXIES.

GAMA is a joint European-Australasian project based around a spectroscopic campaign using the Anglo-Australian Telescope. The GAMA input catalogue is based on data taken from the Sloan Digital Sky Survey and the UKIRT Infrared Deep Sky Survey. Complementary imaging of the GAMA regions is being obtained by a number of independent survey programs including GALEX MIS, VST KiDS, VISTA VIKING, WISE, Herschel-ATLAS, GMRT and ASKAP providing UV to radio coverage. GAMA is funded by the STFC (UK), the ARC (Australia), the AAO, and the participating institutions. The GAMA website is `http://www.gama-survey.org/`.

This work used the 2015 public version of the Munich model of galaxy formation and evolution: L-GALAXIES. The source code and a full description of the model are available at `https://lgalaxiespublicrelease.github.io/`. We also used the TNG simulations which are publicly available from the IllustrisTNG repository: `https://www.tng-project.org/`.

I acknowledge the following software packages which were used throughout this thesis: NumPy (Harris et al., 2020), SciPy (Virtanen et al., 2020), Matplotlib (Hunter, 2007), Astropy (Astropy Collaboration et al., 2013, 2018) and h5py (Collette, 2013).

Some of the analysis shown in this thesis was undertaken on the APOLLO computing cluster at the University of Sussex and the ISAAC cluster at the Max Planck Computing and Data Facility.

Finally I acknowledge the support of a Science and Technology Facilities Council (STFC) studentship.

Bibliography

Abbott T. M. C., et al., 2022, Phys. Rev. D, 105, 023520 (Cited on page 2.)

Adelman-McCarthy J. K., et al., 2006, ApJS, 162, 38 (Cited on page 65.)

Adhikari S., et al., 2021, ApJ, 923, 37 (Cited on pages 16, 103, and 136.)

Alonso D., 2012, arXiv e-prints, p. arXiv:1210.1833 (Cited on pages 9, 42, and 78.)

Anbajagane D., Evrard A. E., Farahi A., 2022, MNRAS, 509, 3441 (Cited on page 103.)

Angulo R. E., Hilbert S., 2015, MNRAS, 448, 364 (Cited on page 37.)

Angulo R. E., Lacey C. G., Baugh C. M., Frenk C. S., 2009, MNRAS, 399, 983 (Cited on pages 17 and 102.)

Angulo R. E., White S. D. M., Springel V., Henriques B., 2014, MNRAS, 442, 2131 (Cited on page 39.)

Armijo J., Cai Y.-C., Padilla N., Li B., Peacock J. A., 2018, MNRAS, 478, 3627 (Cited on page 66.)

Artale M. C., et al., 2017, MNRAS, 470, 1771 (Cited on page 29.)

Artale M. C., Zehavi I., Contreras S., Norberg P., 2018, MNRAS, 480, 3978 (Cited on page 20.)

Astropy Collaboration et al., 2013, AAP, 558, A33 (Cited on page 170.)

Astropy Collaboration et al., 2018, AJ, 156, 123 (Cited on page 170.)

Ayromlou M., Nelson D., Yates R. M., Kauffmann G., White S. D. M., 2019, MNRAS, 487, 4313 (Cited on page 122.)

Ayromlou M., Nelson D., Yates R. M., Kauffmann G., Renneby M., White S. D. M., 2021, MNRAS, 502, 1051 (Cited on page 122.)

Bahé Y. M., et al., 2019, MNRAS, 485, 2287 (Cited on page 136.)

Baldauf T., Smith R. E., Seljak U., Mandelbaum R., 2010, Phys. Rev. D, 81, 063531 (Cited on page 10.)

Baldry I. K., Glazebrook K., Driver S. P., 2008, MNRAS, 388, 945 (Cited on pages 13 and 44.)

Baldry I. K., et al., 2012, MNRAS, 421, 621 (Cited on pages 14, 35, 43, 44, 148, and 158.)

Baldry I. K., et al., 2018, MNRAS, 474, 3875 (Cited on pages 13, 103, and 146.)

Behroozi P. S., Conroy C., Wechsler R. H., 2010, ApJ, 717, 379 (Cited on page 20.)

Behroozi P., Wechsler R. H., Hearin A. P., Conroy C., 2019, MNRAS, 488, 3143 (Cited on pages 19, 20, 102, and 145.)

Beisbart C., Kerscher M., 2000, ApJ, 545, 6 (Cited on page 66.)

Benson A. J., 2019, MNRAS, 482, 1062 (Cited on page 14.)

Benson A. J., Bower R. G., Frenk C. S., Lacey C. G., Baugh C. M., Cole S., 2003, ApJ, 599, 38 (Cited on page 21.)

Bergé J., Gamper L., Réfrégier A., Amara A., 2013, Astronomy and Computing, 1, 23 (Cited on page 7.)

Berlind A. A., Weinberg D. H., 2002, ApJ, 575, 587 (Cited on page 20.)

Berlind A. A., Kazin E., Blanton M. R., Pueblas S., Scoccimarro R., Hogg D. W., 2006, arXiv e-prints, pp astro–ph/0610524 (Cited on pages 15, 65, and 91.)

Bernardi M., Meert A., Sheth R. K., Huertas-Company M., Maraston C., Shankar F., Vikram V., 2016, MNRAS, 455, 4122 (Cited on page 50.)

Bernardi M., Meert A., Sheth R. K., Fischer J. L., Huertas-Company M., Maraston C., Shankar F., Vikram V., 2017, MNRAS, 467, 2217 (Cited on page 50.)

Berner P., Refregier A., Sgier R., Kacprzak T., Tortorelli L., Monaco P., 2021, arXiv e-prints, p. arXiv:2112.08389 (Cited on page 23.)

Binney J., Tremaine S., 1987, Galactic dynamics. Princeton, N.J.: Princeton University Press (Cited on pages 23 and 132.)

van den Bosch F. C., Ogiya G., 2018, MNRAS, 475, 4066 (Cited on page 19.)

van den Bosch F. C., More S., Cacciato M., Mo H., Yang X., 2013, MNRAS, 430, 725 (Cited on pages 10, 42, and 80.)

van den Bosch F. C., Ogiya G., Hahn O., Burkert A., 2018, MNRAS, 474, 3043 (Cited on pages 19 and 115.)

Bose S., Eisenstein D. J., Hernquist L., Pillepich A., Nelson D., Marinacci F., Springel V., Vogelsberger M., 2019, MNRAS, 490, 5693 (Cited on pages 30 and 103.)

Bose S., Deason A. J., Belokurov V., Frenk C. S., 2020, MNRAS, 495, 743 (Cited on pages 17, 19, 102, and 145.)

Bower R. G., Benson A. J., Malbon R., Helly J. C., Frenk C. S., Baugh C. M., Cole S., Lacey C. G., 2006, MNRAS, 370, 645 (Cited on pages 21, 70, and 105.)

Boylan-Kolchin M., Ma C.-P., Quataert E., 2008, MNRAS, 383, 93 (Cited on page 23.)

Boylan-Kolchin M., Springel V., White S. D. M., Jenkins A., Lemson G., 2009, MNRAS, 398, 1150 (Cited on pages 16, 22, 35, 81, and 156.)

Bruzual G., Charlot S., 2003, MNRAS, 344, 1000 (Cited on pages 7 and 22.)

Bryan S. E., Kay S. T., Duffy A. R., Schaye J., Dalla Vecchia C., Booth C. M., 2013, MNRAS, 429, 3316 (Cited on page 136.)

Budzynski J. M., Koposov S. E., McCarthy I. G., McGee S. L., Belokurov V., 2012, MNRAS, 423, 104 (Cited on pages 16, 29, 65, and 103.)

Bullock J. S., Boylan-Kolchin M., 2017, ARA&A, 55, 343 (Cited on page 2.)

Calzetti D., Armus L., Bohlin R. C., Kinney A. L., Koornneef J., Storchi-Bergmann T., 2000, ApJ, 533, 682 (Cited on page 7.)

Campbell D. J. R., et al., 2015, MNRAS, 452, 852 (Cited on page 34.)

Carlsten S. G., Greene J. E., Peter A. H. G., Greco J. P., Beaton R. L., 2020, ApJ, 902, 124 (Cited on page 16.)

Castro T., Borgani S., Dolag K., Marra V., Quartin M., Saro A., Sefusatti E., 2021, MNRAS, 500, 2316 (Cited on page 28.)

Cattaneo A., et al., 2017, MNRAS, 471, 1401 (Cited on page 23.)

Chabrier G., 2003, PASP, 115, 763 (Cited on page 7.)

Chandrasekhar S., 1943, ApJ, 97, 255 (Cited on page 23.)

Charlot S., Fall S. M., 2000, ApJ, 539, 718 (Cited on pages 40 and 45.)

Chauhan G., Lagos C. d. P., Stevens A. R. H., Obreschkow D., Power C., Meyer M., 2020, MNRAS, 498, 44 (Cited on page 25.)

Chua K. T. E., Pillepich A., Rodriguez-Gomez V., Vogelsberger M., Bird S., Hernquist L., 2017, MNRAS, 472, 4343 (Cited on pages 28, 102, and 136.)

Chua K. T. E., Pillepich A., Vogelsberger M., Hernquist L., 2019, MNRAS, 484, 476 (Cited on pages 28 and 136.)

Chua K. T. E., Vogelsberger M., Pillepich A., Hernquist L., 2021, arXiv e-prints, p. arXiv:2109.00012 (Cited on pages 103 and 115.)

Coil A. L., 2013, in Oswalt T. D., Keel W. C., eds, , Vol. 6, Planets, Stars and Stellar Systems. Springer, Dordrecht, p. 387, doi:10.1007/978-94-007-5609-0_8 (Cited on pages 8, 9, and 42.)

Colless M., et al., 2001, MNRAS, 328, 1039 (Cited on pages 4 and 13.)

Collette A., 2013, Python and HDF5. O'Reilly (Cited on page 170.)

Conroy C., Wechsler R. H., Kravtsov A. V., 2006, ApJ, 647, 201 (Cited on page 20.)

Contreras S., Baugh C. M., Norberg P., Padilla N., 2013, MNRAS, 432, 2717 (Cited on pages 25 and 34.)

Contreras S., Angulo R. E., Zennaro M., 2021, MNRAS, 508, 175 (Cited on page 20.)

Cora S. A., et al., 2018, MNRAS, 479, 2 (Cited on pages 21 and 24.)

Corbelli E., Salucci P., 2000, MNRAS, 311, 441 (Cited on page 2.)

Crain R. A., et al., 2015, MNRAS, 450, 1937 (Cited on pages 16, 26, 33, and 139.)

Croton D. J., et al., 2016, ApJS, 222, 22 (Cited on page 21.)

DESI Collaboration et al., 2016, arXiv e-prints, p. arXiv:1611.00036 (Cited on page 168.)

van Daalen M. P., Henriques B. M. B., Angulo R. E., White S. D. M., 2016, MNRAS, 458, 934 (Cited on pages 25, 33, 57, 60, 88, 156, 157, and 167.)

Davis M., Peebles P. J. E., 1983, ApJ, 267, 465 (Cited on pages 8 and 9.)

De Lucia G., Blaizot J., 2007, MNRAS, 375, 2 (Cited on page 21.)

DeRose J., Becker M. R., Wechsler R. H., 2021, arXiv e-prints, p. arXiv:2105.12104 (Cited on page 19.)

Delfino F. M., Scóccola C. G., Cora S. A., Vega-Martínez C. A., Gargiulo I. D., 2022, MNRAS, 510, 2900 (Cited on pages 24 and 145.)

Despali G., Vegetti S., 2017, MNRAS, 469, 1997 (Cited on pages 28 and 102.)

Dolag K., Borgani S., Murante G., Springel V., 2009, MNRAS, 399, 497 (Cited on page 136.)

Donnari M., et al., 2021, MNRAS, 500, 4004 (Cited on page 138.)

Driver S. P., et al., 2009, Astronomy and Geophysics, 50, 5.12 (Cited on pages 13, 33, 66, 103, and 146.)

Driver S. P., et al., 2011, MNRAS, 413, 971 (Cited on pages 13, 33, 66, 68, 103, and 146.)

Driver S. P., et al., 2012, MNRAS, 427, 3244 (Cited on pages 14, 35, 44, and 45.)

Driver S. P., et al., 2019, The Messenger, 175, 46 (Cited on pages 93, 139, and 168.)

Driver S. P., et al., 2022a, arXiv e-prints, p. arXiv:2203.08540 (Cited on page 109.)

Driver S. P., et al., 2022b, MNRAS, 513, 439 (Cited on pages 13, 14, 103, 146, 148, and 158.)

Duffy A. R., Schaye J., Kay S. T., Dalla Vecchia C., Battye R. A., Booth C. M., 2010, MNRAS, 405, 2161 (Cited on page 28.)

Dvornik A., et al., 2020, AAP, 642, A83 (Cited on page 145.)

Eddington A. S., 1913, MNRAS, 73, 359 (Cited on page 7.)

Efstathiou G., 2000, MNRAS, 317, 697 (Cited on page 21.)

Einasto J., 1965, Trudy Astrofizicheskogo Instituta Alma-Ata, 5, 87 (Cited on page 124.)

Eke V. R., Baugh C. M., Cole S., Frenk C. S., Navarro J. F., 2006, MNRAS, 370, 1147 (Cited on pages 17 and 65.)

Elahi P. J., Welker C., Power C., Lagos C. d. P., Robotham A. S. G., Cañas R., Poulton R., 2018, MNRAS, 475, 5338 (Cited on pages 17, 22, 37, and 146.)

Elahi P. J., Cañas R., Poulton R. J. J., Tobar R. J., Willis J. S., Lagos C. d. P., Power C., Robotham A. S. G., 2019a, PASA, 36, e021 (Cited on pages 17, 37, and 136.)

Elahi P. J., Poulton R. J. J., Tobar R. J., Cañas R., Lagos C. d. P., Power C., Robotham A. S. G., 2019b, PASA, 36, e028 (Cited on pages 18 and 37.)

Emami R., et al., 2021, ApJ, 913, 36 (Cited on page 103.)

Engler C., et al., 2021, MNRAS, 500, 3957 (Cited on pages 136 and 145.)

Fagioli M., et al., 2018, J. Cosmology Astropart. Phys., 2018, 015 (Cited on page 7.)

Farrow D. J., et al., 2015, MNRAS, 454, 2120 (Cited on pages 15, 34, 35, 36, 51, 52, and 66.)

Fisher K. B., Davis M., Strauss M. A., Yahil A., Huchra J., 1994, MNRAS, 266, 50 (Cited on pages 77 and 107.)

Font A. S., McCarthy I. G., Belokurov V., 2021, MNRAS, 505, 783 (Cited on page 16.)

Fontanot F., Puchwein E., Springel V., Bianchi D., 2013, MNRAS, 436, 2672 (Cited on page 169.)

Friedmann A., 1922, Zeitschrift fur Physik, 10, 377 (Cited on page 2.)

Gao L., De Lucia G., White S. D. M., Jenkins A., 2004, MNRAS, 352, L1 (Cited on pages 19, 34, and 145.)

Garrison-Kimmel S., et al., 2017, MNRAS, 471, 1709 (Cited on pages 103 and 136.)

Geller M. J., Huchra J. P., 1989, Science, 246, 897 (Cited on page 4.)

Genel S., et al., 2014, MNRAS, 445, 175 (Cited on page 26.)

Girardi M., Giuricin G., Mardirossian F., Mezzetti M., Boschin W., 1998, ApJ, 505, 74 (Cited on page 65.)

Gnedin O. Y., Kravtsov A. V., Klypin A. A., Nagai D., 2004, ApJ, 616, 16 (Cited on page 28.)

Gómez J. S., Padilla N. D., Helly J. C., Lacey C. G., Baugh C. M., Lagos C. D. P., 2022, MNRAS, 510, 5500 (Cited on page 19.)

Gonzalez-Perez V., Lacey C. G., Baugh C. M., Lagos C. D. P., Helly J., Campbell D. J. R., Mitchell P. D., 2014, MNRAS, 439, 264 (Cited on page 34.)

Grand R. J. J., et al., 2017, MNRAS, 467, 179 (Cited on page 16.)

Grand R. J. J., et al., 2021, MNRAS, 507, 4953 (Cited on page 115.)

Green S. B., van den Bosch F. C., Jiang F., 2021, MNRAS, 503, 4075 (Cited on page 19.)

Gu L., et al., 2016, ApJ, 826, 72 (Cited on page 136.)

Gunawardhana M. L. P., et al., 2018, MNRAS, 479, 1433 (Cited on page 66.)

Guo Q., et al., 2011, MNRAS, 413, 101 (Cited on pages 19, 21, 24, 145, and 148.)

Guo Q., Cole S., Eke V., Frenk C., 2012, MNRAS, 427, 428 (Cited on pages 16 and 103.)

Guo Q., White S., Angulo R. E., Henriques B., Lemson G., Boylan-Kolchin M., Thomas P., Short C., 2013a, MNRAS, 428, 1351 (Cited on pages 21, 25, and 37.)

Guo Q., Cole S., Eke V., Frenk C., Helly J., 2013b, MNRAS, 434, 1838 (Cited on page 25.)

Guo H., et al., 2016, MNRAS, 459, 3040 (Cited on page 20.)

Hadzhiyska B., Bose S., Eisenstein D., Hernquist L., Spergel D. N., 2020, MNRAS, 493, 5506 (Cited on pages 20 and 126.)

Hadzhiyska B., Eisenstein D., Bose S., Garrison L. H., Maksimova N., 2022, MNRAS, 509, 501 (Cited on page 17.)

Haggar R., Pearce F. R., Gray M. E., Knebe A., Yepes G., 2021, MNRAS, 502, 1191 (Cited on pages 19, 30, 102, 136, and 138.)

Hamilton A. J. S., Tegmark M., 2004, MNRAS, 349, 115 (Cited on pages 42, 73, and 149.)

Han J., et al., 2015, MNRAS, 446, 1356 (Cited on pages 15 and 65.)

Hang Q., et al., 2022, arXiv e-prints, p. arXiv:2206.05065 (Cited on page 77.)

Hansen S. M., McKay T. A., Wechsler R. H., Annis J., Sheldon E. S., Kimball A., 2005, ApJ, 633, 122 (Cited on pages 16 and 103.)

Harker G., Cole S., Helly J., Frenk C., Jenkins A., 2006, MNRAS, 367, 1039 (Cited on page 66.)

Harris C. R., et al., 2020, Nature, 585, 357 (Cited on page 170.)

Hastings W. K., 1970, Biometrika, 57, 97 (Cited on page 22.)

Henriques B. M. B., Thomas P. A., 2010, MNRAS, 403, 768 (Cited on pages 24 and 148.)

Henriques B. M. B., Thomas P. A., Oliver S., Roseboom I., 2009, MNRAS, 396, 535 (Cited on pages 21, 22, 33, and 156.)

Henriques B. M. B., White S. D. M., Lemson G., Thomas P. A., Guo Q., Marleau G.-D., Overzier R. A., 2012, MNRAS, 421, 2904 (Cited on page 22.)

Henriques B. M. B., White S. D. M., Thomas P. A., Angulo R. E., Guo Q., Lemson G., Springel V., 2013, MNRAS, 431, 3373 (Cited on pages 21, 22, 34, and 156.)

Henriques B. M. B., White S. D. M., Thomas P. A., Angulo R., Guo Q., Lemson G., Springel V., Overzier R., 2015, MNRAS, 451, 2663 (Cited on pages xiii, 16, 20, 21, 22, 24, 25, 33, 34, 35, 37, 39, 66, 73, 74, 102, 146, 147, 149, 155, 156, 157, 158, 160, 164, and 167.)

Henriques B. M. B., White S. D. M., Thomas P. A., Angulo R. E., Guo Q., Lemson G., Wang W., 2017, MNRAS, 469, 2626 (Cited on pages 25, 34, and 88.)

Henriques B. M. B., Yates R. M., Fu J., Guo Q., Kauffmann G., Srisawat C., Thomas P. A., White S. D. M., 2020, MNRAS, 491, 5795 (Cited on pages 21, 22, 156, 158, and 164.)

Herbel J., Kacprzak T., Amara A., Refregier A., Bruderer C., Nicola A., 2017, J. Cosmology Astropart. Phys., 2017, 035 (Cited on page 7.)

Hogg D. W., Baldry I. K., Blanton M. R., Eisenstein D. J., 2002, arXiv e-prints, pp astro–ph/0210394 (Cited on page 7.)

Holmberg E., 1941, ApJ, 94, 385 (Cited on page 16.)

Hopkins A. M., et al., 2013, MNRAS, 430, 2047 (Cited on page 66.)

Hopkins P. F., et al., 2018, MNRAS, 480, 800 (Cited on page 16.)

Humason M. L., Mayall N. U., Sandage A. R., 1956, AJ, 61, 97 (Cited on pages 7 and 67.)

Hunter J. D., 2007, Computing in Science & Engineering, 9, 90 (Cited on page 170.)

Ivezić Ž., et al., 2019, ApJ, 873, 111 (Cited on page 168.)

Jarvis M., Bernstein G., Jain B., 2004, MNRAS, 352, 338 (Cited on page 9.)

Jia J.-Y., Gao L., Qu Y., 2020, Research in Astronomy and Astrophysics, 20, 174 (Cited on page 28.)

Jiang C. Y., Jing Y. P., Faltenbacher A., Lin W. P., Li C., 2008, ApJ, 675, 1095 (Cited on page 23.)

Jiang L., Helly J. C., Cole S., Frenk C. S., 2014, MNRAS, 440, 2115 (Cited on page 70.)

Jiang F., Dekel A., Freundlich J., van den Bosch F. C., Green S. B., Hopkins P. F., Benson A., Du X., 2021, MNRAS, 502, 621 (Cited on page 24.)

de Jong R. S., et al., 2019, The Messenger, 175, 3 (Cited on page 168.)

Joshi G. D., Parker L. C., Wadsley J., Keller B. W., 2019, MNRAS, 483, 235 (Cited on page 135.)

Kafle P. R., et al., 2016, MNRAS, 463, 4194 (Cited on pages 16, 65, 66, 91, and 103.)

Kaiser N., 1984, ApJ, 284, L9 (Cited on page 10.)

Kaiser N., 1987, MNRAS, 227, 1 (Cited on page 9.)

Kampakoglou M., Trotta R., Silk J., 2008, MNRAS, 384, 1414 (Cited on pages 21 and 33.)

Kang X., 2014, MNRAS, 437, 3385 (Cited on page 34.)

Karademir G. S., et al., 2022, MNRAS, 509, 5467 (Cited on page 14.)

Kelley T., Bullock J. S., Garrison-Kimmel S., Boylan-Kolchin M., Pawlowski M. S., Graus A. S., 2019, MNRAS, 487, 4409 (Cited on page 136.)

Kerscher M., Szapudi I., Szalay A. S., 2000, ApJ, 535, L13 (Cited on page 8.)

Kim S., Contini E., Choi H., Han S., Lee J., Oh S., Kang X., Yi S. K., 2020, ApJ, 905, 12 (Cited on page 16.)

Kitzbichler M. G., White S. D. M., 2007, MNRAS, 376, 2 (Cited on page 75.)

Kitzbichler M. G., White S. D. M., 2008, MNRAS, 391, 1489 (Cited on page 19.)

Knebe A., et al., 2015, MNRAS, 451, 4029 (Cited on pages 25 and 34.)

Knobel C., et al., 2012, ApJ, 755, 48 (Cited on page 65.)

Krone-Martins A., Ishida E. E. O., de Souza R. S., 2014, MNRAS, 443, L34 (Cited on page 129.)

Kuijken K., et al., 2019, AAP, 625, A2 (Cited on page 14.)

Kuruvilla J., Aghanim N., McCarthy I. G., 2020, AAP, 644, A170 (Cited on page 168.)

Lacey C., Cole S., 1993, MNRAS, 262, 627 (Cited on pages 23 and 57.)

Lacey C. G., et al., 2016, MNRAS, 462, 3854 (Cited on pages 16, 20, 33, 34, and 102.)

Lagos C. d. P., Davis T. A., Lacey C. G., Zwaan M. A., Baugh C. M., Gonzalez-Perez V., Padilla N. D., 2014, MNRAS, 443, 1002 (Cited on page 25.)

Lagos C. d. P., Tobar R. J., Robotham A. S. G., Obreschkow D., Mitchell P. D., Power C., Elahi P. J., 2018, MNRAS, 481, 3573 (Cited on pages 16, 20, 21, 22, 33, 40, 57, 102, 146, and 150.)

Lagos C. D. P., et al., 2019, MNRAS, p. 2096 (Cited on pages 40 and 45.)

Landy S. D., Szalay A. S., 1993, ApJ, 412, 64 (Cited on pages 9, 10, 41, 77, 95, and 149.)

Lee J., et al., 2014, MNRAS, 445, 4197 (Cited on page 37.)

Lemaître G., 1931, MNRAS, 91, 483 (Cited on page 2.)

Li C., White S. D. M., 2009, MNRAS, 398, 2177 (Cited on pages 13 and 44.)

Li C., Jing Y. P., Kauffmann G., Börner G., White S. D. M., Cheng F. Z., 2006, MNRAS, 368, 37 (Cited on page 79.)

Lilly S. J., et al., 2007, ApJS, 172, 70 (Cited on page 65.)

Lin H., Yee H. K. C., Carlberg R. G., Morris S. L., Sawicki M., Patton D. R., Wirth G., Shepherd C. W., 1999, ApJ, 518, 533 (Cited on page 7.)

Lin W. P., Jing Y. P., Mao S., Gao L., McCarthy I. G., 2006, ApJ, 651, 636 (Cited on page 136.)

von der Linden A., Wild V., Kauffmann G., White S. D. M., Weinmann S., 2010, MNRAS, 404, 1231 (Cited on page 65.)

Liske J., et al., 2015, MNRAS, 452, 2087 (Cited on pages 13, 14, 33, 66, 67, 103, 104, and 146.)

Łokas E. L., 2020, AAP, 638, A133 (Cited on page 136.)

Loveday J., et al., 2012, MNRAS, 420, 1239 (Cited on page 14.)

Loveday J., et al., 2015, MNRAS, 451, 1540 (Cited on pages 14, 42, 67, 73, and 149.)

Loveday J., et al., 2018, MNRAS, 474, 3435 (Cited on pages 10, 42, 67, 78, and 148.)

Lovell M. R., et al., 2018, MNRAS, 481, 1950 (Cited on pages 102, 136, and 137.)

Lovell C. C., Wilkins S. M., Thomas P. A., Schaller M., Baugh C. M., Fabbian G., Bahé Y., 2022, MNRAS, 509, 5046 (Cited on page 169.)

Maddox S. J., Efstathiou G., Sutherland W. J., 1996, MNRAS, 283, 1227 (Cited on page 11.)

Manwadkar V., Kravtsov A., 2021, arXiv e-prints, p. arXiv:2112.04511 (Cited on page 102.)

Mao Y.-Y., Geha M., Wechsler R. H., Weiner B., Tollerud E. J., Nadler E. O., Kallivayalil N., 2021, ApJ, 907, 85 (Cited on page 16.)

Maraston C., 2005, MNRAS, 362, 799 (Cited on page 22.)

Marinacci F., et al., 2018, MNRAS, 480, 5113 (Cited on pages 26, 66, 73, 103, 105, and 145.)

Marini I., et al., 2021, MNRAS, 500, 3462 (Cited on page 102.)

de Martino I., Chakrabarty S. S., Cesare V., Gallo A., Ostorero L., Diaferio A., 2020, Universe, 6, 107 (Cited on page 2.)

Merson A. I., et al., 2013, MNRAS, 429, 556 (Cited on page 75.)

Metropolis N., Rosenbluth A. W., Rosenbluth M. N., Teller A. H., Teller E., 1953, J. Chem. Phys., 21, 1087 (Cited on page 22.)

Miki Y., Mori M., Kawaguchi T., 2021, Nature Astronomy, 5, 478 (Cited on page 147.)

Mo H. J., White S. D. M., 1996, MNRAS, 282, 347 (Cited on page 65.)

Mo H. J., Mao S., White S. D. M., 1998, MNRAS, 295, 319 (Cited on page 38.)

Mohammad F. G., de la Torre S., Bianchi D., Guzzo L., Peacock J. A., 2016, MNRAS, 458, 1948 (Cited on pages 10, 15, 65, and 77.)

Moster B. P., Naab T., White S. D. M., 2018, MNRAS, 477, 1822 (Cited on pages 19 and 20.)

Murphy G. G., Yates R. M., Mohamed S. S., 2022, MNRAS, 510, 1945 (Cited on pages 24, 148, and 164.)

Murray S. G., Robotham A. S. G., Power C., 2018, ApJ, 855, 5 (Cited on page 17.)

Nagai D., Kravtsov A. V., 2005, ApJ, 618, 557 (Cited on pages 29, 103, and 136.)

Naiman J. P., et al., 2018, MNRAS, 477, 1206 (Cited on pages 26, 66, 73, 103, 105, and 145.)

Navarro J. F., Frenk C. S., White S. D. M., 1997, ApJ, 490, 493 (Cited on pages 4, 40, and 146.)

Nelson D., et al., 2015, Astronomy and Computing, 13, 12 (Cited on pages 26 and 137.)

Nelson D., et al., 2018, MNRAS, 475, 624 (Cited on pages 26, 66, 73, 74, 103, 105, 108, and 145.)

Nelson D., et al., 2019a, Computational Astrophysics and Cosmology, 6, 2 (Cited on pages 16, 26, 66, 73, 103, 105, and 145.)

Nelson D., et al., 2019b, MNRAS, 490, 3234 (Cited on pages 26, 103, 105, and 145.)

Norberg P., et al., 2001, MNRAS, 328, 64 (Cited on page 15.)

Ogiya G., van den Bosch F. C., Hahn O., Green S. B., Miller T. B., Burkert A., 2019, MNRAS, 485, 189 (Cited on page 19.)

Onions J., et al., 2012, MNRAS, 423, 1200 (Cited on pages 19 and 122.)

Pawlowski M. S., 2021, Galaxies, 9, 66 (Cited on page 168.)

Peebles P. J. E., 1980, The large-scale structure of the universe. Princeton University Press (Cited on page 8.)

Perlmutter S., et al., 1999, ApJ, 517, 565 (Cited on page 2.)

Pillepich A., et al., 2018a, MNRAS, 473, 4077 (Cited on pages 26 and 107.)

Pillepich A., et al., 2018b, MNRAS, 475, 648 (Cited on pages 26, 33, 66, 73, 74, 103, 104, 105, 107, 120, and 145.)

Pillepich A., et al., 2019, MNRAS, 490, 3196 (Cited on pages 26, 103, 105, and 145.)

Planck Collaboration et al., 2014, AAP, 571, A16 (Cited on pages 35 and 37.)

Planck Collaboration et al., 2016, AAP, 594, A13 (Cited on page 37.)

Poulton R. J. J., Power C., Robotham A. S. G., Elahi P. J., Lagos C. D. P., 2021, MNRAS, 501, 2810 (Cited on page 23.)

Presotto V., et al., 2012, AAP, 539, A55 (Cited on page 65.)

Press W. H., Schechter P., 1974, ApJ, 187, 425 (Cited on page 65.)

Pujol A., et al., 2017, MNRAS, 469, 749 (Cited on pages 24, 25, 34, 39, 54, 60, 85, 102, 110, and 145.)

Rana D., More S., Miyatake H., Nishimichi T., Takada M., Robotham A. S. G., Hopkins A. M., Holwerda B. W., 2022, MNRAS, 510, 5408 (Cited on pages 15 and 104.)

Rasia E., Tormen G., Moscardini L., 2004, MNRAS, 351, 237 (Cited on page 136.)

Rémy-Ruyer A., et al., 2014, AAP, 563, A31 (Cited on page 40.)

Renneby M., Henriques B. M. B., Hilbert S., Nelson D., Vogelsberger M., Angulo R. E., Springel V., Hernquist L., 2020, MNRAS, 498, 5804 (Cited on page 112.)

Rhee J., Smith R., Choi H., Yi S. K., Jaffé Y., Candlish G., Sánchez-Jánssen R., 2017, ApJ, 843, 128 (Cited on page 135.)

Riess A. G., et al., 1998, AJ, 116, 1009 (Cited on page 2.)

Riggs S. D., Barbhuiyan R. W. Y. M., Loveday J., Brough S., Holwerda B. W., Hopkins A. M., Phillipps S., 2021, MNRAS, 506, 21 (Cited on pages 30, 103, 148, and 162.)

Riggs S. D., Loveday J., Thomas P. A., Pillepich A., Nelson D., Holwerda B. W., 2022, MNRAS, 514, 4676 (Cited on pages 30 and 145.)

Roberts I. D., Parker L. C., Joshi G. D., Evans F. A., 2015, MNRAS, 448, L1 (Cited on pages 16, 65, and 91.)

Robertson H. P., 1935, ApJ, 82, 284 (Cited on page 2.)

Robotham A. S. G., Howlett C., 2018, Research Notes of the American Astronomical Society, 2, 55 (Cited on pages 24 and 40.)

Robotham A., et al., 2010, PASA, 27, 76 (Cited on pages 14, 34, and 35.)

Robotham A. S. G., et al., 2011, MNRAS, 416, 2640 (Cited on pages 15, 65, 68, and 104.)

Robotham A. S. G., Bellstedt S., Lagos C. d. P., Thorne J. E., Davies L. J., Driver S. P., Bravo M., 2020, MNRAS, 495, 905 (Cited on page 40.)

Roche N., Eales S. A., 1999, MNRAS, 307, 703 (Cited on pages 11, 43, and 149.)

Rodriguez-Gomez V., et al., 2015, MNRAS, 449, 49 (Cited on pages 18, 112, and 116.)

Roper W. J., Thomas P. A., Srisawat C., 2020, MNRAS, 494, 4509 (Cited on pages 19 and 136.)

Sawala T., Frenk C. S., Crain R. A., Jenkins A., Schaye J., Theuns T., Zavala J., 2013, MNRAS, 431, 1366 (Cited on pages 28, 102, and 122.)

Schaller M., et al., 2015, MNRAS, 451, 1247 (Cited on pages 28 and 102.)

Schaye J., et al., 2015, MNRAS, 446, 521 (Cited on pages 16, 26, 33, and 139.)

Schechter P., 1976, ApJ, 203, 297 (Cited on page 7.)

Seljak U., Warren M. S., 2004, MNRAS, 355, 129 (Cited on page 65.)

Sheth R. K., Tormen G., 1999, MNRAS, 308, 119 (Cited on page 65.)

Sheth R. K., Tormen G., 2004, MNRAS, 350, 1385 (Cited on pages 10, 66, and 138.)

Sheth R. K., Mo H. J., Tormen G., 2001, MNRAS, 323, 1 (Cited on page 65.)

Sheth R. K., Connolly A. J., Skibba R., 2005, arXiv e-prints, pp astro–ph/0511773 (Cited on pages 10, 66, 80, and 87.)

Shi J., et al., 2020, ApJ, 893, 139 (Cited on page 138.)

Shin T., et al., 2021, MNRAS, 507, 5758 (Cited on page 16.)

Sijacki D., Vogelsberger M., Genel S., Springel V., Torrey P., Snyder G. F., Nelson D., Hernquist L., 2015, MNRAS, 452, 575 (Cited on page 26.)

Sinha M., Garrison L. H., 2019, in Software Challenges to Exascale Computing. Second Workshop. pp 3–20 (`arXiv:1911.08275`), doi:10.1007/978-981-13-7729-7_1 (Cited on pages 9, 51, 77, and 149.)

Sinha M., Garrison L. H., 2020, MNRAS, 491, 3022 (Cited on pages 9, 51, 77, and 149.)

Skibba R., Sheth R. K., Connolly A. J., Scranton R., 2006, MNRAS, 369, 68 (Cited on pages 11, 66, and 80.)

Skibba R. A., Sheth R. K., Croton D. J., Muldrew S. I., Abbas U., Pearce F. R., Shattow G. M., 2013, MNRAS, 429, 458 (Cited on pages 66 and 97.)

Smith R. E., 2012, MNRAS, 426, 531 (Cited on page 46.)

Smith R., Choi H., Lee J., Rhee J., Sanchez-Janssen R., Yi S. K., 2016, ApJ, 833, 109 (Cited on page 135.)

Somerville R. S., Popping G., Trager S. C., 2015, MNRAS, 453, 4337 (Cited on pages 16, 21, and 33.)

Springel V., 2010, MNRAS, 401, 791 (Cited on page 105.)

Springel V., White S. D. M., Tormen G., Kauffmann G., 2001, MNRAS, 328, 726 (Cited on pages 17, 37, and 122.)

Springel V., et al., 2005, Nature, 435, 629 (Cited on pages 4, 16, 17, 18, 22, 34, 35, 37, 70, 74, 81, 105, and 146.)

Springel V., Frenk C. S., White S. D. M., 2006, Nature, 440, 1137 (Cited on page 5.)

Springel V., et al., 2018, MNRAS, 475, 676 (Cited on pages 26, 29, 66, 73, 103, 105, and 145.)

Springel V., Pakmor R., Zier O., Reinecke M., 2021, MNRAS, 506, 2871 (Cited on pages 17, 18, and 136.)

Srisawat C., et al., 2013, MNRAS, 436, 150 (Cited on page 18.)

Stoyan D., Stoyan H., 1994, Fractals, Random Shapes and Point Fields: Methods of Geometrical Statistics. Wiley, Chichester (Cited on page 66.)

Sureshkumar U., et al., 2021, AAP, 653, A35 (Cited on pages 15 and 66.)

Sureshkumar U., et al., 2022, arXiv e-prints, p. arXiv:2201.10480 (Cited on page 15.)

Swanson M. E. C., Tegmark M., Hamilton A. J. S., Hill J. C., 2008, MNRAS, 387, 1391 (Cited on pages 42, 73, and 149.)

Tal T., Wake D. A., van Dokkum P. G., 2012, ApJ, 751, L5 (Cited on page 103.)

Taylor E. N., et al., 2011, MNRAS, 418, 1587 (Cited on page 35.)

Tempel E., Kruuse M., Kipper R., Tuvikene T., Sorce J. G., Stoica R. S., 2018, AAP, 618, A81 (Cited on page 167.)

Tinker J. L., 2021, ApJ, 923, 154 (Cited on page 167.)

Tinker J. L., Weinberg D. H., Zheng Z., Zehavi I., 2005, ApJ, 631, 41 (Cited on page 65.)

Tinker J. L., et al., 2012, ApJ, 745, 16 (Cited on page 11.)

Tollet É., Cattaneo A., Mamon G. A., Moutard T., van den Bosch F. C., 2017, MNRAS, 471, 4170 (Cited on pages 24 and 145.)

Trayford J. W., Lagos C. d. P., Robotham A. S. G., Obreschkow D., 2020, MNRAS, 491, 3937 (Cited on page 40.)

Vázquez-Mata J. A., et al., 2020, MNRAS, 499, 631 (Cited on pages 33, 66, 103, and 140.)

Viola M., et al., 2015, MNRAS, 452, 3529 (Cited on pages 15, 65, 69, 70, and 104.)

Virtanen P., et al., 2020, Nature Methods, 17, 261 (Cited on page 170.)

Vogelsberger M., et al., 2014a, MNRAS, 444, 1518 (Cited on page 26.)

Vogelsberger M., et al., 2014b, Nature, 509, 177 (Cited on pages 17, 26, 29, and 102.)

Vogelsberger M., Marinacci F., Torrey P., Puchwein E., 2020, Nature Reviews Physics, 2, 42 (Cited on pages 26 and 27.)

Walker A. G., 1937, Proceedings of the London Mathematical Society, 42, 90 (Cited on page 2.)

Wang Y., Yang X., Mo H. J., van den Bosch F. C., Weinmann S. M., Chu Y., 2008, ApJ, 687, 919 (Cited on pages 15, 65, 90, and 91.)

Wang W., Sales L. V., Henriques B. M. B., White S. D. M., 2014, MNRAS, 442, 1363 (Cited on pages 16, 25, and 103.)

Wang Y., et al., 2016, MNRAS, 459, 1554 (Cited on page 18.)

Wang K., Mo H. J., Li C., Meng J., Chen Y., 2020, MNRAS, 499, 89 (Cited on page 167.)

Watson D. F., Berlind A. A., McBride C. K., Hogg D. W., Jiang T., 2012, ApJ, 749, 83 (Cited on page 16.)

Weinberg D. H., Colombi S., Davé R., Katz N., 2008, ApJ, 678, 6 (Cited on pages 30 and 115.)

Weinberger R., et al., 2017, MNRAS, 465, 3291 (Cited on pages 26, 107, and 119.)

Wetzel A. R., Tinker J. L., Conroy C., van den Bosch F. C., 2013, MNRAS, 432, 336 (Cited on page 65.)

White M., 2016, J. Cosmology Astropart. Phys., 2016, 057 (Cited on page 66.)

White M., Padmanabhan N., 2009, MNRAS, 395, 2381 (Cited on page 66.)

White S. D. M., Rees M. J., 1978, MNRAS, 183, 341 (Cited on page 65.)

Wright A. H., et al., 2017, MNRAS, 470, 283 (Cited on pages 14, 43, and 44.)

Xu X., Zehavi I., Contreras S., 2021, MNRAS, 502, 3242 (Cited on page 138.)

Yang X., Mo H. J., van den Bosch F. C., 2003, MNRAS, 339, 1057 (Cited on page 8.)

Yang X., Mo H. J., van den Bosch F. C., Pasquali A., Li C., Barden M., 2007, ApJ, 671, 153 (Cited on page 65.)

Yang X., Mo H. J., van den Bosch F. C., 2008, ApJ, 676, 248 (Cited on pages 8 and 41.)

Yang X., Mo H. J., van den Bosch F. C., 2009, ApJ, 695, 900 (Cited on pages 8 and 41.)

Yang X., et al., 2021, ApJ, 909, 143 (Cited on page 167.)

York D. G., et al., 2000, AJ, 120, 1579 (Cited on pages 4, 13, and 33.)

Zehavi I., et al., 2005, ApJ, 630, 1 (Cited on page 15.)

Zehavi I., et al., 2011, ApJ, 736, 59 (Cited on pages 13 and 15.)

Zehavi I., Contreras S., Padilla N., Smith N. J., Baugh C. M., Norberg P., 2018, ApJ, 853, 84 (Cited on page 20.)

Zehavi I., Kerby S. E., Contreras S., Jiménez E., Padilla N., Baugh C. M., 2019, ApJ, 887, 17 (Cited on page 112.)

Zel'Dovich Y. B., 1970, AAP, 5, 84 (Cited on page 17.)

Zolotov A., et al., 2012, ApJ, 761, 71 (Cited on page 19.)